Micro Four-Point Probe and Micro Hall Effect: Methods for Reliable Electrical Characterization of Ultra-Shallow Junctions

Petersen, Dirch Hjorth

Publication date:
2009

Document Version
Publisher's PDF, also known as Version of record

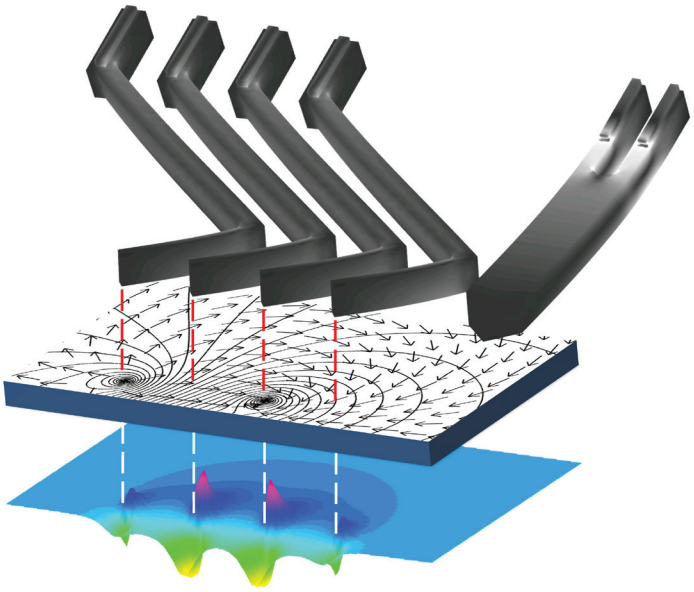

Micro Four-Point Probe and Micro Hall Effect

Methods for Reliable Electrical Characterization of Ultra-Shallow Junctions

Dirch Hjorth Petersen
Ph.D. Thesis December 2009

DTU Nanotech
Department of Micro- and Nanotechnology

Micro Four-Point Probe and Micro Hall Effect

Methods for Reliable Electrical Characterization of Ultra-Shallow Junctions

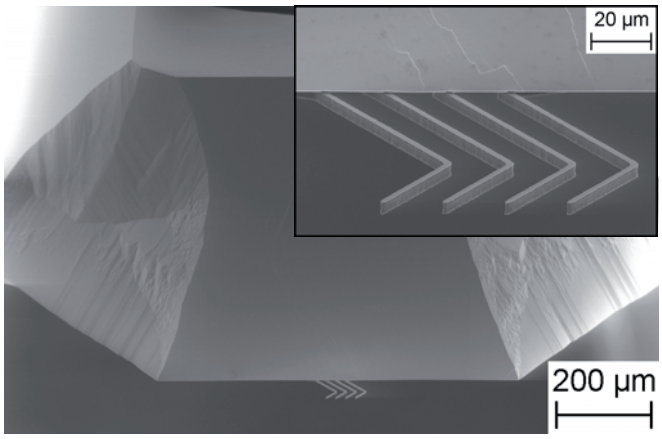

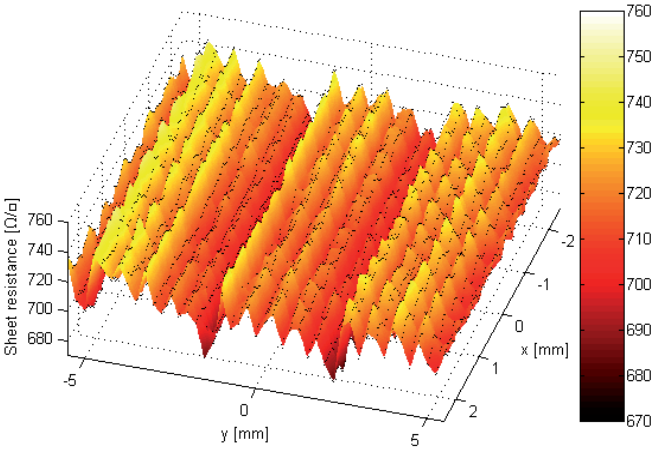

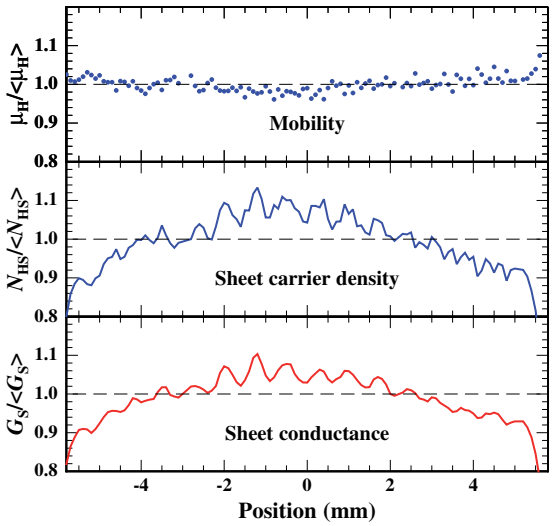

Ph. D. Thesis, Dirch Hjorth Petersen

DTU Nanotech, Technical University of Denmark, Kongens Lyngby, Denmark.

Supervisors:

Peter Bøggild (DTU Nanotech)
Ole Hansen (DTU Nanotech)
Peter F. Nielsen (Capres A/S)
Wilfried Vandervorst (IMEC)

Preface

This Ph.D. project is a joint effort of DTU Nanotech, Capres A/S and IMEC to develop metrology methods for accurate characterization of sheet resistance, sheet carrier density and carrier mobility of ultra-shallow junctions (USJ) using micro four-point probes (M4PP). The thesis consists of a summary of the most important results and a copy of the most relevant published articles to give a complete picture of the M4PP metrology methods developed in this work.

I would like to acknowledge the important contributions of all 96 co-authors (see publications I-XVII and i-xxi) without whom this project would have been both poor and boring. Especially, I wish to thank Peter Bøggild, Ole Hansen (DTU Nanotech) Peter R.E. Petersen, Peter F. Nielsen (Capres A/S), and Wilfried Vandervorst (IMEC) for their efforts to obtain project funding and the financial support from DTU Nanotech, Capres A/S, the Otto Mønsted Fond, the Copenhagen Graduate School for Nanoscience and Nanotechnology (C:O:N:T) and the Danish Research Agency (FTP). This project was greatly supported by contributions from a number of persons; this includes Ole Hansen (DTU Nanotech), who has been a constant source of great inspiration and has provided exceptional help in theoretical calculations as well as paper writing; Rong Lin (Capres A/S), who has been a great support in all aspects of the experimental work with M4PP and always has been available for fruitful discussions; Erik Rosseel (IMEC), who has continuously provided state-of-the-art USJ samples for characterization and provided helpful insight to process related variability; Wilfried Vandervorst, Trudo Clarysse, Janusz Bogdanowicz (IMEC) and Michael I. Current (Current Scientific), with whom I have had numerous inspirational and insightful discussions on USJ metrology; Fei Wang and Torben M. Hansen (DTU Nanotech), who have contributed with great insight into the theoretical aspects of M4PP measurements and especially improving our understanding of M4PP sensitivity; Thor Ansbæk, Frederik W. Østerberg, Henrik F. Dam and Anpan Han (DTU Nanotech), for their exceptional theoretical and/or experimental contributions to improve M4PP metrology; Lars Nørregaard, Hans Henrik Jankjær, Christian Markvardsen, Kristian Nørgaard, Chaker Khalfaoui, Lauge Gammelgaard, Ane Jensen and Daniel Kjær (Capres A/S), for their daily help and discussion related to M4PP measurements; Helle V. Jensen, Yvonne Gyrsting (DTU Danchip), Lise Midjord (Capres A/S) and Inger N. Hansen (DELTA), for their help with M4PP fabrication and packaging; Anders Lei (DTU Nanotech), for his work on implementation of the focused ion beam prototyping method; Özlem S. Sukas (DTU Nanotech), for great discussions on microfabrication and finite element simulations; the Nanointegration group (DTU Nanotech) and the Materials and Components Analysis group (MCA, IMEC), for interesting discussions and collaborative work on side-projects; and last but not least, Peter Bøggild (DTU Nanotech) and Peter F. Nielsen (Capres A/S) for their continues encouragement, support and inspirational discussions.

Kongens Lyngby, December 1st, 2009.

List of acronyms

AI	All inclusive. (MHE method)
CMOS	Complementary metal–oxide–semiconductor.
FIB	Focused ion beam.
F3S	Fast 3*s* separation. (MHE method)
FSS	Fast short separation. (MHE method)
HARP	High aspect ratio probe (fabrication process).
LPCVD	Low-pressure chemical vapor deposition.
M4PP	Micro four-point probe.
MEMS	Microelectromechanical systems.
MHE	Micro Hall Effect.
μ	Carrier mobility. (Also a variable)
N_S	Sheet carrier density. (Also a variable)
poly-SOI	Polysilicon-on-insulator wafer.
RIE	Reactive ion etching.
R_S	Sheet resistance. (Also a variable)
SD	Standard deviation.
SIMS	Secondary ion mass spectroscopy.
STI	Shallow trench isolation.
USJ	Ultra-shallow junction.

Table of contents

Chapter 1

1 Introduction

Metrologies are of key importance for the discovery and understanding of physics, and play a major role in the development of new materials and fabrication techniques. In nano- and microelectronics, the most important material property is electrical conductance, and as CMOS transistors continues to scale, the art of metrology needs to be continuously reevaluated.

Standard electrical characterization of semiconductors has for more than 50 years been performed using four-point probe [1, 2] and van der Pauw [3, 4] techniques to extract sheet resistance (R_S), sheet carrier density (N_S) and carrier mobility (μ) of electrically conducting layers. The four-point probe provides direct measurement of the sample R_S and the van der Pauw technique additionally measures N_S and μ though independent characterization of the Hall scattering factor is necessary for high accuracy [5, 6].

For high performance CMOS production, tight control on process uniformity is important, and for several decades, four-point probe [7, 8] and optically modulated optical reflection (Therma-Probe) measurements [9] have been standard methods for monitoring implant and annealing uniformity [10]. However, in a theoretical evaluation of four-point probe measurements, L.J. Swartzendruber found that the technique was not reliable for accurate characterization of R_S non-uniformities with a length scale similar to the electrode pitch [11]. This was supported in a study by M.I. Current, et al. [12], who reported experimental results on the significant lack of spatial resolution of conventional four-point probes to characterize dose variations when compared to Therma-Probe, that has a sensitive area on the order of 1 μm^2.

Until the introduction of millisecond annealing, the main source of sub-millimeter ranged non-uniformities in N_S was due to variations in the ion implanted dose [13], while conventional thermal annealing typically results in centimeter ranged process variations. Thus, to maintain a high degree of dose uniformity in production, one relies on Therma-Probe measurements, whereas the average dose is best monitored by four-point probe and secondary ion mass spectroscopy (SIMS), while assuming 100 % dose activation [14].

1.1 Ultra-shallow junctions

Ultra-shallow junctions (USJ) are used as source/drain extension in CMOS fabrication. The source/drain extensions are important for reducing the transistor series resistance in the on-current state without causing excessive off-current leakage. The delay in development and introduction of improved USJ process techniques is one of the reasons for the slowdown in high-performance CMOS scaling [15].

In general, ultra-shallow (<20 nm) and sharp junction abruptness is formed by low energy ion implantation of dopants into silicon with subsequent sub-melt millisecond annealing, ideally without dopant diffusion. To obtain a low R_S, the USJ is typically doped beyond the solid solubility, which in combination with the short annealing time only results in partial dopant activation. Thus, to develop adequate USJ fabrication processes, metrologies are necessary to evaluate the degree of dopant activation [XII]. Moreover, the millisecond annealing is a non-equilibrium thermal process with large substrate temperature gradients as the thermal diffusion length L_d scales with the annealing time τ as $L_d \sim \tau^{0.5}$ [XI]. A typical thermal diffusion length for 1 ms annealing of silicon is on the order of 200 μm, thus non-uniformities in dopant activation can be expected at a similar length scale depending on the specific annealing equipment type and design.

Even for uniform USJ, it has during the past decade become evident that conventional four-point probe measurements fail completely to characterize USJ because of junction penetration associated with the high probe pressure [16, 17*, v]. Emerging R_S metrologies solve this by reducing the probe contact pressure [18, 19*] or by non-contact optical methods [20, 21]. Reviews on emerging USJ metrologies are given elsewhere by M.I. Current and J.O. Borland [10] and W. Vandervorst [22].

1.2 Purpose and aim of study

The original scope of this Ph.D. project was to develop micro four-point probe (M4PP) based metrology methods for characterization of micro-scale R_S, Hall Effect and carrier depth profiling of USJ, and to establish a deeper understanding in the use of M4PP metrology on advanced semiconductor materials used by the semiconductor industry.

It can be useful to define some specific goals on measurement requirements. Due to the small dimensions of M4PP, it is a candidate metrology for in-line R_S characterization in scribe-line test pads with dimensions on the order of 50×50 μm^2. This can potentially reduce the number of increasingly expensive monitor/test wafers [19*]. For in-line as well as near-line R_S metrology, a standard deviation (SD) in measurement repeatability and reproducibility of 0.08-0.10 % is expected by semiconductor manufactures, and 0.1 % has been the estimated target throughout this study. For N_S and μ metrology, targets are less stringent. However, to distinguish between micro-scale variations in N_S and μ requires both high spatial resolution and a SD in repeatability smaller

than the variations investigated; for these studies this amounts to a SD in repeatability better than approximately 1 %.

The requirements for the absolute accuracy of electrical characterization are also less stringent, for instance no set of USJ sample standards exist. Thus, calibration is typically done to the most reliable metrology method available. However, the relative accuracy is important for fundamental materials science studies and for process development, e.g. it must be possible to characterize the impact of small changes in implant and annealing conditions. Thus, the relative accuracy must allow for correct interpretation of R_S, N_S and μ variations for a given sample population with small process variations. However, the opposite argument is also valid, that a sample population must include process variations that are detectable with the available metrology methods.

Another important parameter is the measurement time. With increased spatial resolution comes also a demand for more measurement points and reduced measurement time, e.g. for spatial periodic variations of a sample property, it must be possible to characterize more than a period to see the periodic behavior. In this sense, atomic resolution is useless if periodic variations are on the scale of millimeters. In general, it can be stated about metrology, that with improved resolution, speed and accuracy, increasingly better theoretical models for process technology can be developed, but all aspects must be included. As a final remark on the purpose of metrology, I like to quote Michael I. Current[1] who stated: “If you don’t look, you won’t see!”.

1.3 In this thesis

The main content of this thesis revolves around two methods for reliable characterization of USJ; micro-scale R_S characterization with M4PP [19*] and the novel Micro Hall Effect (MHE) technique [V] for accurate characterization of N_S and μ. The thesis summarizes the main results in relation to USJ characterization and includes 17 selected papers which are given as appendices. Additional details are added on subjects relevant for the M4PP R_S and the MHE measurement techniques when not described thoroughly in the reprinted papers [I-XVII]. However, advances in M4PP carrier profiling [23*] is described only in Papers I and XIV and will not be discussed further.

In Chapter 2, the basic theory is briefly presented for the two methods chosen and the focus will be on sensitivity to non-uniformities and electrode position errors. In chapter 3, M4PP fabrication is introduced and solutions implemented for reliable surface detection and vibration tolerance are described. Chapter 4 gives an introduction to advanced data treatment and summarizes the most important experimental results obtained with the two methods on USJ. Finally, an extended outlook and summary is given in Chapter 5.

The bibliography is divided in three; reprinted papers, omitted papers[2] and a reference list. The reference list is not exhaustive and the reader is referred to the reprinted papers and the references herein. Reprinted and omitted publications will be referenced with upper and lower case Roman numerals, respectively, i.e. [I-XVII] for reprinted papers and [i-xxi] for omitted patents/papers. Publications by the author will not be referenced chronological but are grouped by subject for easy overview. Finally, references to papers by the author, prior to this Ph.D. study, are marked by (*).

[1] Presentation at the 16th IEEE International Conference on Advanced Thermal Processing of Semiconductors (RTP 2008, Las Vegas).
[2] Printed conference proceedings also appearing in peer-reviewed journals are omitted from the bibliography to avoid duplicates.

Chapter 2

2 Theory

Thorough analytical descriptions of M4PP R_S and Micro Hall Effect (MHE) measurements are given in Papers IV and V. In this Chapter, an overview of the relevant theory is given along with the fundamental analytical results. Additional analyses for measurements on specific geometries and sample types can be found in Papers I-XIV.

2.1 Definitions

In a four-point measurement a current, I_0, is passed through a conductive sample between two current injection electrodes while the potential difference, V, is measured between the two remaining electrodes. Four-point resistances, $R_i = V/I_0$, may be calculated from six non-trivial combinations of current and voltage electrodes, cf. Fig. 2.1. Here, the subscript i denotes the four-point configuration. Of these six electrode combinations, only five are independent, as it can be shown that $R_A + R_{A'} = R_B + R_{B'} + R_C + R_{C'}$ [I]. In the absence of a magnetic field, this reduces to just two independent combinations as $R_A = R_{A'}$, $R_B = R_{B'}$ and $R_C = R_{C'}$ [V]. Throughout this thesis, the four electrodes are collinear with an equidistant electrode pitch, s.

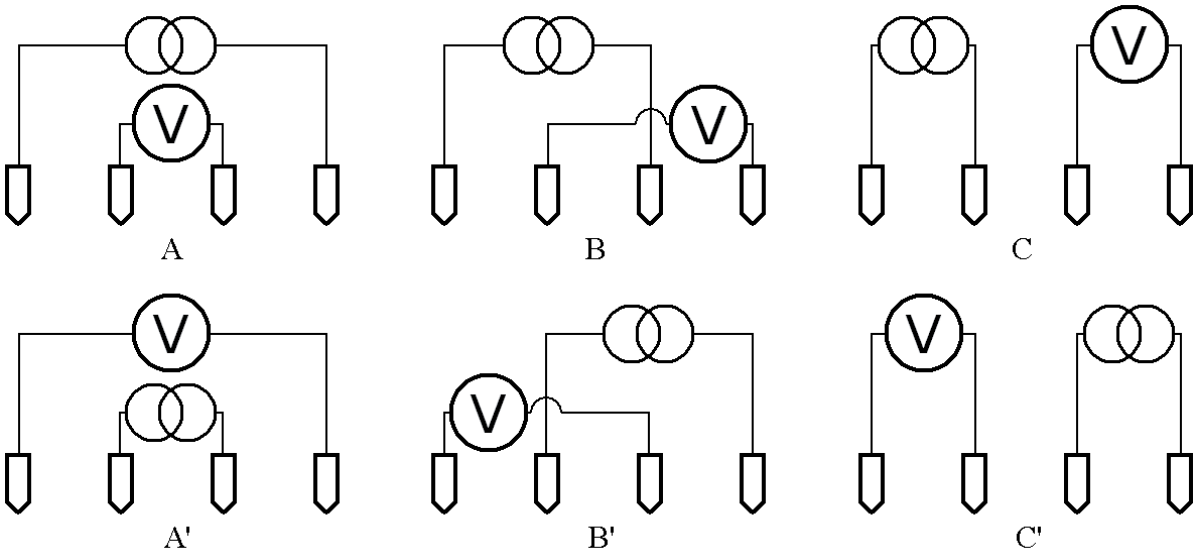

Figure 2.1: Definition of the six configurations with non-trivial combinations of current and voltage electrodes.

In general, we define the sheet resistance as $R_S = (e\mu N_S)^{-1}$ [6], while neglecting minority carriers and assuming a sample to be described as a continuous conductive filamentary sheet. e is the elementary charge, μ is the carrier mobility and N_S is the sheet carrier density. In particular for USJ, a low N_S may affect the assumption of a continuous conductive sheet; this special case is described in the section *Material limitations* of Paper I. Sheet resistance and Micro Hall Effect (MHE) theory for the special case of shallow implant of dopants into a substrate of the same type (e.g. p+/p structure, cf. Paper ix) has not been developed. Also, the influence of contact size have not been evaluated thoroughly, and has been neglected since typically $4R_{contact} >> R_S$, where $R_{contact}$ is the electrode-to-sample contact resistance.

2.2 Sheet resistance

To meet the goal of performing accurate R_S measurements in scribe-line test pads with dimensions on the order of 50×50 μm^2 (as defined in Sect. 1.2), it is important to evaluate possible sources of measurement errors on small pads. Much research in R_S measurements has been done over the past six decades, and references to the most relevant work in relation to measurements on small geometries are given in Chapter 1 and in Paper IV.

In this section, a magnetic flux density of zero is assumed. R_S can be calculated from individual four-point resistance measurements as $R_i = c_i R_S$, where c_i is a sample geometry and configuration specific correction factor. For a conductive infinite sheet c_i may be defined as

$$c_i = \frac{1}{2\pi} \ln \frac{\left|\mathbf{r}_{V-} - \mathbf{r}_{I+}\right| \left\|\mathbf{r}_{V+} - \mathbf{r}_{I-}\right|}{\left|\mathbf{r}_{V+} - \mathbf{r}_{I+}\right| \left\|\mathbf{r}_{V-} - \mathbf{r}_{I-}\right|}, \tag{1}$$

where $\mathbf{r}$ is the position vector of each current and voltage electrode as denoted by subscripts. Assuming a constant correction factor with large relative electrode position errors may result in huge measurement errors. However, in the specific case where the four electrodes are positioned collinear on an infinite sheet, the exact R_S may be calculated from two electrode configurations using the modified van der Pauw equation [24].

$$\exp\left(\frac{2\pi R_A}{R_S}\right) - \exp\left(\frac{2\pi R_B}{R_S}\right) = 1 \qquad (2)$$

This method is generally termed a dual configuration measurement, and it is identical to dual configuration R_S calculated as a function of (R_A, R_C) and (R_B, R_C), respectively.

2.2.1 Insulating boundaries and small pads

A thorough theoretical study of sheet resistance measurements on small samples with dimensions similar to the electrode pitch is presented in Paper IV. From this study it is important to realize that dual configuration measurements performed in the mirror plane of a small sample with uniform R_S is exact even with in-line position errors. Basically it can be interpreted as a van der Pauw measurement of each half of the sample as illustrated in Fig. 2.2.

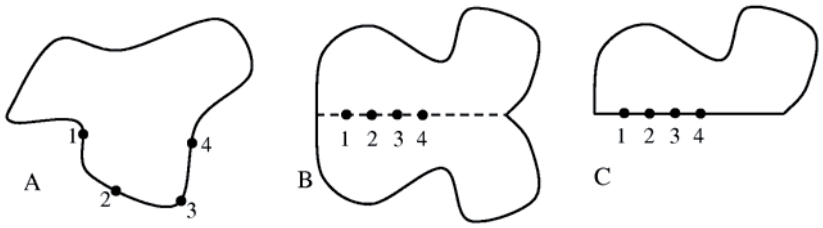

Figure 2.2: (A) Schematic illustration of a van der Pauw measurement. Due to symmetry of the current path, positioning a collinear four-point probe on the mirror plane of a symmetrical sample (B) is equivalent to a van der Pauw measurement on half of the symmetrical sample (C), while only injecting half of the current used in (B). Reproduced from Paper IV.

A single straight boundary also has a mirror plane orthogonal to the boundary. Thus, it is possible to measure the exact R_S even with one electrode touching the boundary. However, when the line of the four contacts is in proximity and parallel to a straight boundary, the calculated sheet resistance differs from the true R_S. Thus, in this case, we substitute R_S in Eq. 1 with the pseudo sheet resistance, $R_P = \chi R_S$, where χ is a geometrical correction function, $0 < \chi \leq 2$ [IV]. For a single straight boundary parallel to the four-point probe, it can be shown that $1 \leq \chi \leq 2$.

Another important result presented in Paper IV, is the area within a square and rectangular pad where the R_P differs from R_S with less than 0.1 %, $|\chi - 1| < 0.1$ %. This is the "sweet spot" where accurate correction-free dual configuration measurements may be performed (cf. Fig. 2.3).

From Fig. 2.3 it is obvious that the ideal orientation to place a four-point probe is parallel to the short edge of a rectangle [IV]. This is a general observation which may be explained using the method of images [25]. The geometrical correction function χ are solved for additional sample geometries and probe rotation in Paper IV. Here, we also find that using a 10 μm pitch M4PP with an alignment error of ±2.5 μm, correction-free R_S measurements may be performed in a square of dimensions 50×50 μm^2 and in a stripe (or long rectangle) of width 35 μm.

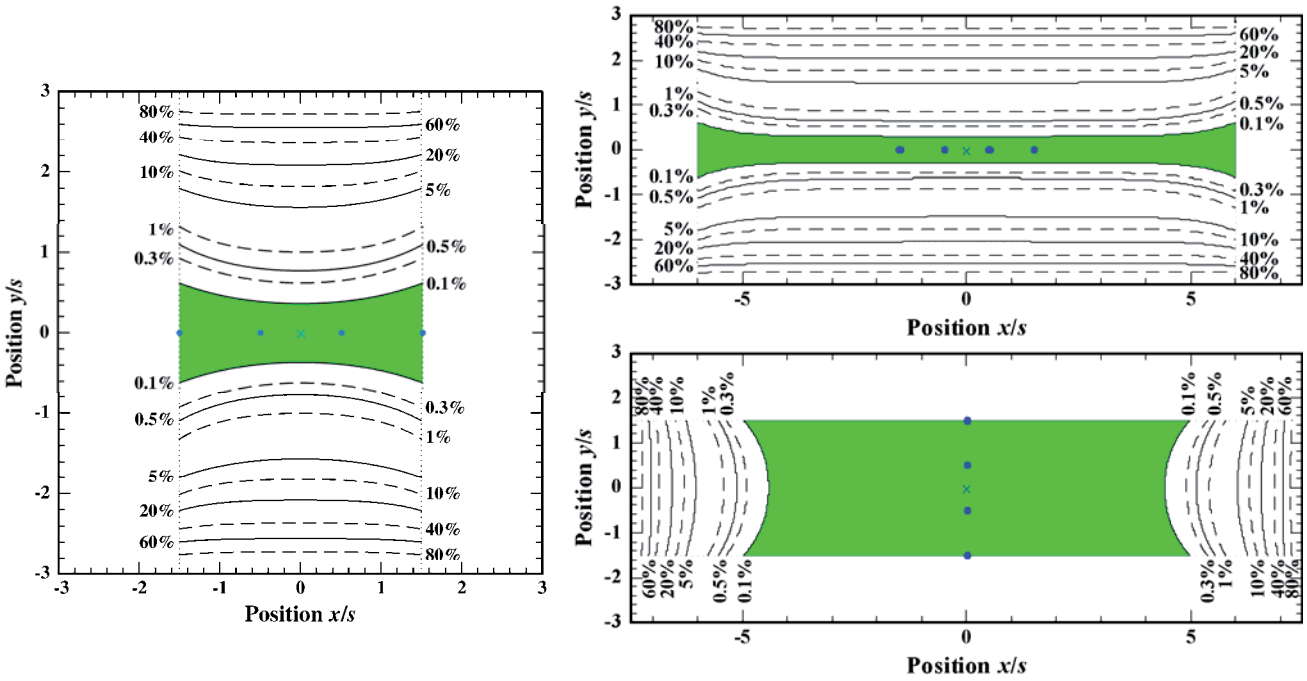

Figure 2.3: The "sweet spot" (green area), where correction-free dual configuration R_S may be measured with an error <0.1 %. The frame of each figure indicates the boundaries of the square ($6s \times 6s$) and rectangles ($15s \times 6s$ and $6s \times 15s$), and the probe location is defined by the center of the four electrodes with a pitch of s. The relative area of the "sweet spot" is largest when the four electrodes are placed parallel to the short side of a rectangle (bottom right). Adapted from Paper IV.

2.2.2 Sensitivity

For a practical R_S measurement, an important issue is the impact of a non-uniform R_S on the measurement result. D.W. Koon et al. [26, 27] found that the R_S can be considered as a non-trivial average of the local sheet resistance $R_{S,L}$. In Paper II we apply a similar approach to numerically evaluate the sensitivity of dual configuration R_S measurements to variations in $R_{S,L}$ using the adjoint system method [28,29] and in Paper IX we verify this result by finite element method (FEM) simulations, respectively. The dimensionless sensitivity [IX] may be defined as

$$S_{R_{S,L}}^{R_S} = \frac{\partial^2 R_S}{\partial R_{S,L} \partial A} \frac{R_{S,L}}{R_S} s^2, \tag{3}$$

where A is the area of the local non-uniformity. Figure 2.4 depicts the dual configuration sensitivity for electrodes placed at (-1.5,0), (-0.5,0), (0.5,0) and (1.5,0). The "spot size" or area of highest sensitivity is roughly circular with a diameter on the order of $2s$, i.e. the sensitivity at the two outermost electrodes is small compared to the inner electrodes.

It should be noted that the sensitivity to inhomogeneities with large variations is non-linear [30]. Also, for small pads with insulating boundaries the current distribution will change and the sensitivity must be reevaluated. In Paper X we show that whereas the distinctive two-peak shape of the sensitivity plot does not change much, the absolute sensitivity may change significantly on confined areas such as a square, rectangle and circle.

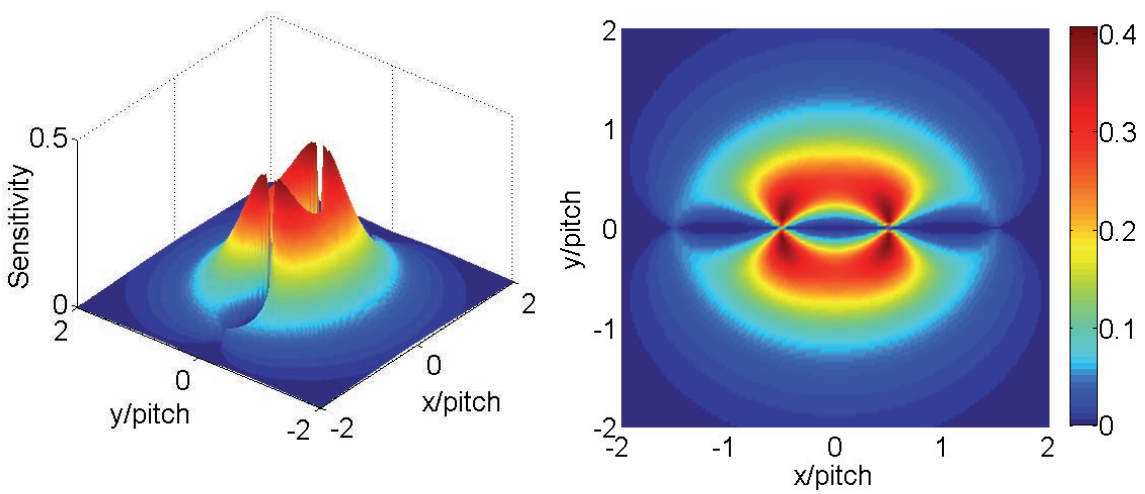

Figure 2.4: Sensitivity of a dual configuration R_S measurement to local variations, $R_{S,L}$. Adapted from Papers I-II.

2.2.3 Spatial frequency transfer function

In general, the resolution of a microscopy technique is limited to the minimum "spot size", e.g. for an optical microscope, this is on the order of the wavelength of light. For samples with 1D periodic R_S variations with a wavelength of λ, the variations may not be measured correctly if the "spot size" is significantly larger than λ. In Paper X we show how the sensitivity to periodic variations may be evaluated using a spatial frequency transfer function, cf. Fig. 2.5.

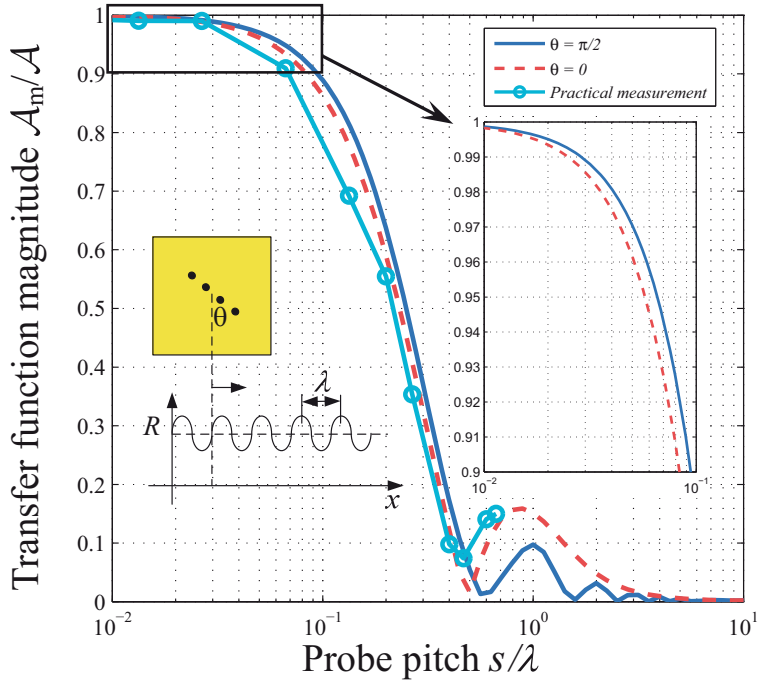

Figure 2.5: Plot of the spatial frequency transfer function for a four-point probe parallel and orthogonal to the 1D spatial R_S variations, respectively. The practical measurements are from Paper II and the figure is adapted from Paper X. Courtesy of Fei Wang.

From the spatial frequency transfer function it is possible to find the accuracy of measured R_S variations as a function of s and λ. For small variations, this can also be used in 2D and for several spatial frequencies using Fourier transform [X]. It can be shown, that with a variation amplitude $\mathcal{A} = 0.100R_S$, a measurement error of less than 1 % on the variation itself is necessary in order to

obtain a total measurement error on R_S of <0.1 %, i.e. the measured amplitude $\mathcal{A}_m > 0.099R_S$. Thus, from Fig. 2.5 we simply find the desired $\mathcal{A}_m/\mathcal{A} = 0.99$ ratio which requires a maximum electrode pitch of $s = \lambda/40$.

2.2.4 Position errors

Statistical analysis of electrode position errors is crucially important for understanding M4PP measurements in general, and all data treatment for M4PP measurements is build on the basis of correct interpretation of position errors. As illustrated in Fig. 2.6 the real positions of the electrode contacts may in practical measurements differ from the ideal positions. It is important to differentiate between static and dynamic position errors which are defined as follows.

> ***Static position errors:*** *When the electrode contact points differ from the ideal positions as illustrated in Fig. 2.6. Static position errors for a collinear four-point probe may be both in-line or off-line and the positions do not change in time.*
>
> ***Dynamic position errors:*** *When two or more electrode configurations are measured sequentially with different static position errors.*

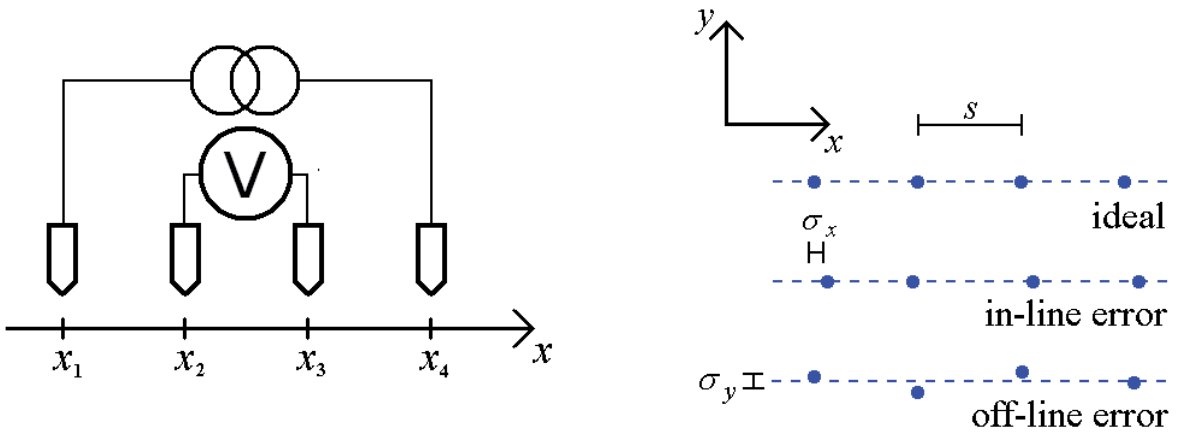

Figure 2.6: (left) Illustration of a four-point probe with electrode positions x_1, x_2, x_3 and x_4 (reprinted from Paper XV). (right) Schematic illustration of in-line and off-line position errors.

Dual configuration measurements are for instance only accurate for static in-line position errors. For a four-point probe with small dynamic position errors, it is possible to estimate the relative standard deviation of the measured four-point resistance, R_i, from the absolute standard deviation of in-line position errors, σ_x [XV].

$$\sigma_{R_i}^{rel} = \frac{1}{R_i}\sqrt{\sum_{n=1}^{4}\left(\frac{\partial R_i}{\partial x_n}\sigma_x\right)^2} = \frac{1}{c_i}\sqrt{\sum_{n=1}^{4}\left(\frac{\partial c_i}{\partial x_n}\sigma_x\right)^2} \qquad (4)$$

Here, the dynamic position errors are assumed to be characterized by equal, normal distribution functions for all four electrode positions x_n, and c_i is given by Eq. 1. The correlations between electrode position errors and four-point resistance are given in Tab. 2.1 for an equidistant four-point probe with electrode pitch, s. This linear model is inadequate for the evaluation of off-line position error which is a second order effect. The off-line error can be evaluated with a parabolic model, but the error is very small and may be neglected for small position errors relative to the electrode pitch.

Table 2.1: Correlation between the standard deviation on electrode positions and the relative standard deviation on measured four-point resistance on an infinite conductive sheet with electrode pitch s.

Configuration	Relative standard deviation
A	$\sigma_{R_A}^{rel} = \frac{\sqrt{5}}{2\ln 2}\frac{\sigma_x}{s} \approx 1.613\frac{\sigma_x}{s}$
B	$\sigma_{R_B}^{rel} = \frac{4\sqrt{5}}{3\ln 3}\frac{\sigma_x}{s} \approx 2.714\frac{\sigma_x}{s}$

The position error correlations given in Tab. 2.1 are useful tools in understanding dynamic position errors and will be used for evaluating a vibration tolerant M4PP in Sect. 3.4.3. The simple relations are also useful for optimizing measurement procedures to achieve the best possible measurement precision as demonstrated in Sect. 4.1.1.

2.3 Micro Hall Effect

Recently, we developed a method for fast and accurate characterization of sheet carrier density N_S and carrier mobility μ [ii, V]. The method differs from conventional van der Pauw measurements since the contacts are placed in the interior of the sample region, not just on the perimeter. In this section, the principle of the Micro Hall Effect (MHE) will first be described, and then an analysis similar to the previous section is given for this slightly more complicated measurement situation.

In Hall Effect [5] measurements, a magnetic flux density is added normal to the sample surface. As a result, the sheet current density $\mathbf{J}_S$ and the electric field $\mathbf{E}$ are no longer parallel, and they must therefore be related by a sheet resistance tensor rather than a scalar sheet resistance [6, V].

$$\mathbf{E} = \begin{pmatrix} R_S & -R_H \\ R_H & R_S \end{pmatrix} \mathbf{J}_S \tag{5}$$

Here, R_S is the sheet resistance and R_H the Hall sheet resistance. From experimental values of R_S and R_H the Hall mobility μ_H and Hall sheet carrier density N_{HS} can be extracted.

$$R_H = \frac{B_z}{ZeN_{HS}} = \frac{r_H B_z}{ZeN_S} \tag{6}$$

$$R_S = \frac{1}{e\mu_H N_{HS}} = \frac{1}{e\mu N_S} \tag{7}$$

Where, B_z is the transverse magnetic field (cf. Fig. 2.7), $Z = \pm 1$ is the charge carrier type, e is the elementary charge and r_H is the Hall scattering factor. The Hall scattering factor is of order one and accounts for the different statistical averaging needed for μ and μ_H [31]. MHE can be measured with a collinear four-point probe in proximity of an insulating boundary as illustrated in Fig. 2.7 [V].

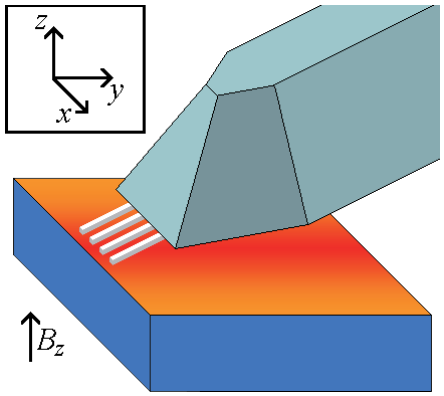

Figure 2.7: Illustration of MHE; a M4PP is positioned close to a straight boundary and a magnetic field is applied normal to the sample surface.

2.3.1 Basic description of Micro Hall Effect

In a magnetic field, a tangential magnetic force (the Lorentz force) acts on the charge carriers causing current rotation. In general, the Hall Effect can be described as an electric field that results from the obstruction of a rotating current at an insulating boundary. Figure 2.8 schematically illustrates the equipotential curves (black lines) resulting from the current flow (red arrows) in an infinite conductive sheet between two current sources. At zero magnetic flux density, the total current flow is the sum of a positive and a negative radial current and the equipotential curves become symmetric, cf. Fig. 2.8(left). When a transverse magnetic field B_z is applied, an additional tangential current contribution will appear, cf. Fig. 2.8(right). The rotating current gives rise to geometrical magnetoresistance [6] but the equipotential curves remain symmetrical.

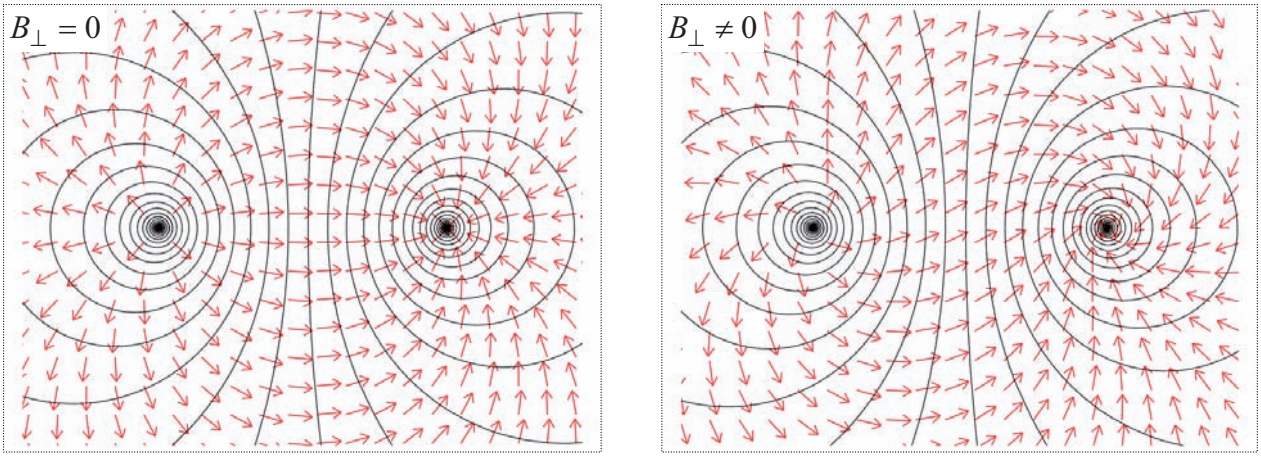

Figure 2.8: Finite element method simulation of the current flow and electric field between two current injection points on an infinite conductive sheet. The equipotential lines are symmetrical for both zero (left) and large (right) transverse magnetic flux density. However, the current flow (red arrows) begins to rotate around the two current injection points at large transvers magnetic flux density.

If the current sources are positioned directly on a boundary as assumed in conventional Hall Effect measurements, cf. Fig. 2.9(left), then the Lorentz force is cancelled along the boundary by an equal opposing force as the current density normal to the boundary remains zero. This result in a small Hall electric field and the equipotential lines become asymmetric. In this case the geometrical magnetoresistance becomes zero. In MHE measurements the current sources are placed in proximity of a boundary, cf. Fig. 2.9(right); this gives rise to an intermediate geometrical magnetoresistance contribution and a small Hall electric field.

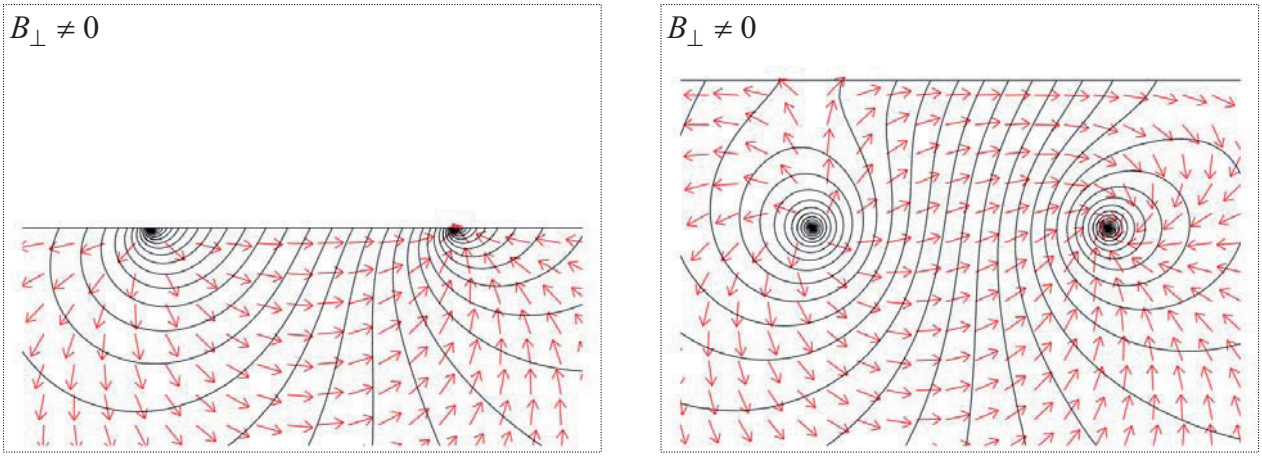

Figure 2.9: Finite element method simulation of the current flow and electric field between two current injection points on a half plane (semi-infinite conductive sheet). (left) For the conventional van der Pauw technique, the electrodes are positioned on the boundary and the current rotation is completely blocked by the insulating boundary. This results in an asymmetric electric field. (right) If the current injection points are positioned in proximity of the boundary, a fraction of the current rotation is obstructed, which also gives rise to an asymmetric electric field.

The MHE is very similar to the conventional van der Pauw technique. However, in van der Pauw measurements only the B configuration (cf. Fig. 2.1) results in a Hall electric field. In MHE both B and C configuration gives rise to an electric field, although the maximum Hall Effect measured in C configuration is much smaller than in B configuration. An additional important difference is that in MHE it is necessary to know the exact positions of the electrodes, which is ideally irrelevant with the van der Pauw technique.

2.3.2 Single insulating boundary

For MHE measurements it is convenient to define the resistance difference $\Delta R_{BB'} \equiv R_B - R_{B'}$ and the resistance average $R_{BB'} \equiv (R_B + R_{B'})/2$ as this partially separates the Hall sheet resistance R_H and sheet resistance R_S. Equivalent resistance difference and resistance average may be defined for the A and C configurations, although $\Delta R_{AA'} = 0$. For a straight insulating boundary parallel to the four contacts of a collinear equidistant four-point probe, the resistance difference and resistance average can be found as a function of the probe pitch s and the distance y between the probe and the boundary [V].

$$\Delta R_{BB'} = \frac{2R_H}{\pi}\left(3\arctan\frac{s}{2y} - \arctan\frac{3s}{2y}\right) \tag{8}$$

$$R_{BB'} = \frac{R_S}{2\pi}\left(1+\frac{R_H^2}{R_S^2}\right)\ln 3 + \frac{R_S}{2\pi}\left(1-\frac{R_H^2}{R_S^2}\right)\ln\sqrt{\frac{9+4\left(\frac{y}{s}\right)^2}{1+4\left(\frac{y}{s}\right)^2}} \tag{9}$$

The geometrical magnetoresistance contribution, $(R_H/R_S)^2 = (\mu_H B_z)^2$, can generally be neglected for USJ characterization. However, it should be included for large magnetic flux density and/or high mobility samples as described in Paper VII. Paper V provides analytical solutions to a quarter-plane, stripe and rectangle, and any polygon may be solved using numerical conformal mapping as we demonstrate in Papers VIII and x.

2.3.3 Sensitivity and spatial frequency transfer function

As described for the M4PP R_S measurements in Sect. 2.2.2, knowing the sensitivity of MHE measurements is equally important for the correct analysis of the measurement results. However, the sensitivities of the properties extracted in MHE measurements to variations in local sheet carrier density N_L and local carrier mobility μ_L are much different from the R_S sensitivity as it relies on the specific choice of method to extract N_{HS}, μ_H and R_S. Describing the sensitivity of the measured quantity $\Delta R_{BB'}$ is also not straightforward as it depends on the positions of the electrodes and boundary.

Figure 2.10 shows an example of the sensitivities of $\Delta R_{BB'}$ to local variations in N_L and μ_L, when four collinear equidistant electrodes are positioned parallel to an insulating boundary at a distance of s/5 [IX]. The sensitivity of $\Delta R_{BB'}$ to variations in N_{HS} is purely negative and the average sensitivity is -1. However, the average sensitivity of $\Delta R_{BB'}$ to variations in μ_H is zero [IX], but still the local sensitivity is not zero as the local mobility, μ_L, affects the current distribution [IX]. The sensitivity sign change seen in Fig. 2.10(right) is important to be aware of, as it may potentially lead to misinterpretation of measurement results.

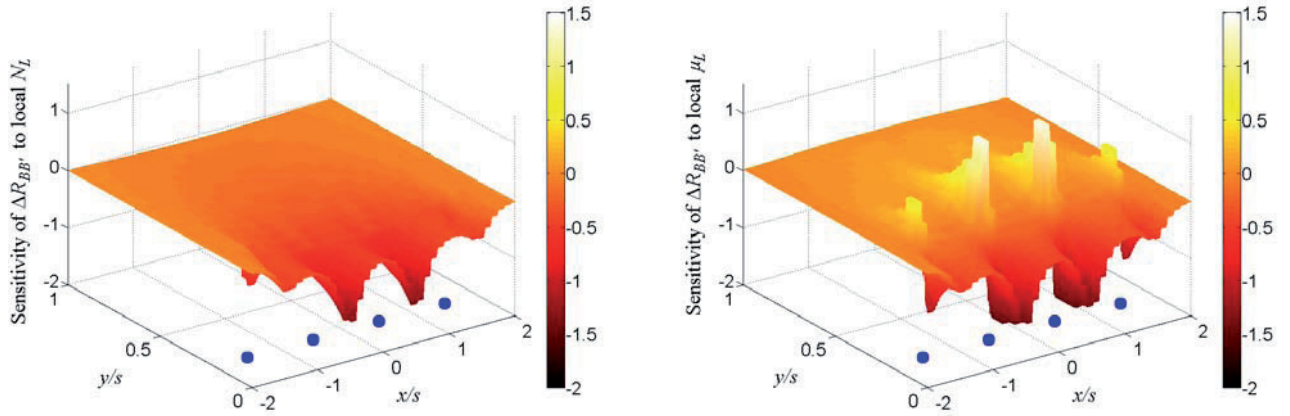

Figure 2.10: Finite element method simulations of the sensitivities of $\Delta R_{BB'}$ to local variations in sheet carrier density N_L (left) and carrier mobility μ_L (right) on a semi-infinite sheet (half-plane) with an insulating barrier at $y/s = 0$. The four electrodes are positioned at $y/s = 0.2$ and $x/s = \{-1.5, -0.5, 0.5, 1.5\}$ as illustrated by blue points. Figures are adapted from Paper IX.

Most importantly, what we may learn from Fig. 2.10 is that the MHE sensitivity does not look similar to the R_S sensitivity. This inconvenient result was also described by D.W. Koon and C.J. Knickerbocker [32] for van der Pauw geometries. As Hall Effect and R_S measurements in general will average over different areas, this can lead to unfortunate measurement errors on non-uniform samples.

In Papers IX and X the 1D and 2D sensitivities are found for MHE measurements using the Fast 3s Separation (F3S) method [VI] which is described in Sect. 4.2.3. Using these sensitivities the spatial frequency transfer functions for 1D periodic variation of N_{HS} and μ_H, respectively, are found to be very similar to the spatial frequency transfer function for R_S measurements with $s/\lambda < 0.3$ (cf. Figs. 2.5 and 2.11). As for R_S measurements we may define the maximum electrode pitch desired to characterize periodic variations of N_{HS} and μ_H. For MHE measurements a desired accuracy of 1 % was defined in Sect. 1.2. Thus, if the variation amplitude is 10 %, then the maximum electrode pitch becomes roughly $s = \lambda/12$. Here, it is important also to notice the cross sensitivity errors, i.e. sensitivity of N_{HS} to μ_L and μ_H to N_L [X]. These errors must also be monitored and minimized.

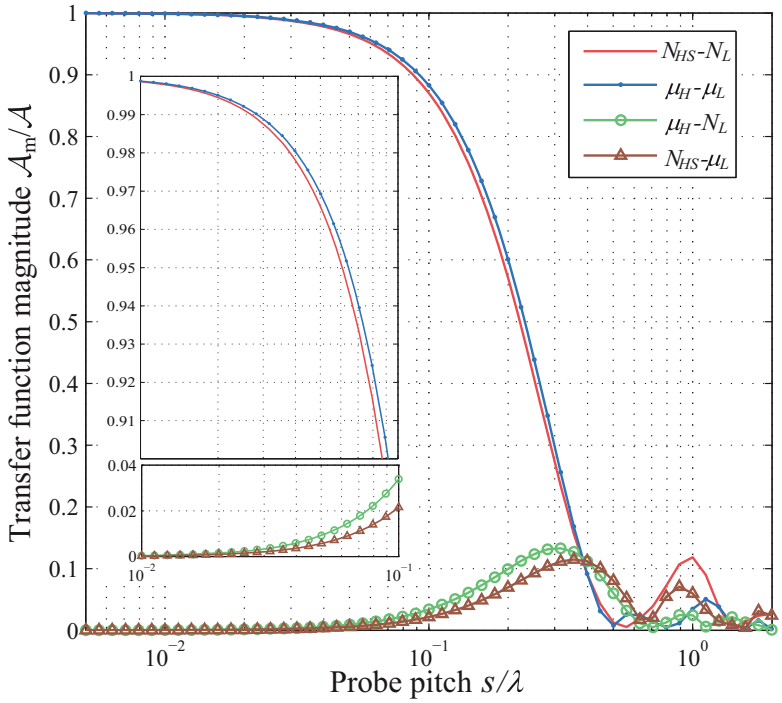

Figure 2.11: Plot of the MHE spatial frequency transfer functions, for measurements performed with the F3S method. Here, the 1D spatial variations in N_L and μ_L are defined parallel to the insulating boundary. In MHE analysis it is also important to keep track of the cross sensitivities, if the electrode pitch becomes large. Adapted from Paper X. Courtesy of Fei Wang.

2.3.4 Position errors

Even more so for the MHE than for R_S measurements, the statistical analysis of position errors is vital for accurate MHE measurements. The statistical analysis is applied directly for optimization of the practical MHE measurement procedure to arrive at a total measurement time of less than a minute. The position errors for MHE measurements near a single straight boundary are illustrated in Fig. 2.12.

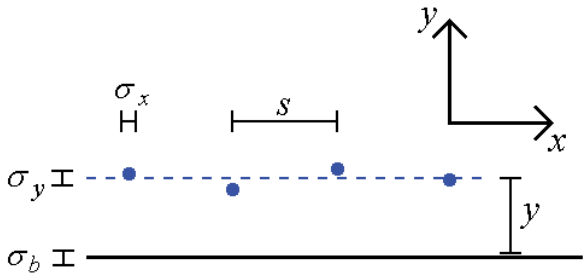

Figure 2.12: Schematic illustration of in-line and off-line position errors, as well as the error on the boundary position.

Similar to position errors in R_S measurements, we may evaluate the effect of dynamic position errors. For this evaluation, a static position error is assumed always between measurements of R_B and $R_{B'}$ (we may simply think of the measurements as performed simultaneously). The relative standard deviation of the resistance average $R_{BB'}$ and the resistance difference $\Delta R_{BB'}$ are found as Eqs. 10 and 11 [VI] for the single straight boundary illustrated in Fig. 2.12.

$$\sigma_{\Delta R_{BB'}}^{rel} = \frac{1}{\Delta R_{BB'}} \sqrt{\sum_{n=1}^{4} \left(\left(\frac{\partial \Delta R_{BB'}}{\partial x_n} \right)^2 \sigma_x^2 + \left(\frac{\partial \Delta R_{BB'}}{\partial y_n} \right)^2 \sigma_y^2 \right) + \left(\sum_{n=1}^{4} \frac{\partial \Delta R_{BB'}}{\partial y_n} \sigma_b \right)^2} \tag{10}$$

$$\sigma_{R_{BB'}}^{rel} = \frac{1}{R_{BB'}} \sqrt{\sum_{n=1}^{4} \left(\left(\frac{\partial R_{BB'}}{\partial x_n} \right)^2 \sigma_x^2 + \left(\frac{\partial R_{BB'}}{\partial y_n} \right)^2 \sigma_y^2 \right) + \left(\sum_{n=1}^{4} \frac{\partial R_{BB'}}{\partial y_n} \sigma_b \right)^2} \tag{11}$$

Here, (x_n, y_n) are the positions of the four electrodes, σ_x and σ_y are the absolute standard deviations of positions errors and σ_b is the absolute standard deviation of the average distance y between the boundary and the probe. The additional two terms of Eq. 11 compared to Eq. 4 result from the current sources mirrored in the boundary, which give rise to a first order off-line measurement error. It is important here to note, that a dynamic position error occurring between the measurement of R_B and $R_{B'}$ will have a huge effect on $\Delta R_{BB'}$ (even possible sign change) and less of an impact on $R_{BB'}$.

The relative position errors between the electrodes may be assumed uncorrelated. However, the distance between the boundary and the probe will result in a correlated position error. On an infinite sheet, the dual configuration method eliminates in-line position errors as discussed in Sect. 2.2. Similarly, the pseudo sheet resistance $R_P = \chi R_S$, calculated from the resistance average values $R_{AA'}$ and $R_{BB'}$ has been found to greatly reduce the uncorrelated position errors in practical measurements [VI].

$$\exp\left(\frac{2\pi R_{AA'}}{R_P} \right) - \exp\left(\frac{2\pi R_{BB'}}{R_P} \right) = 1 \tag{12}$$

Furthermore, the geometrical correction function χ can be actively used to simultaneously eliminate the correlated boundary position error σ_b for $\Delta R_{BB'}$ and R_P. The elimination of uncorrelated and correlated errors is the key to fast and accurate MHE measurements and can be implemented in simple measurement procedures [VI, VIII]. In Sect. 4.2.3, it will be shown how the analysis of position errors in combination with pseudo sheet resistance measurements may be used to almost completely eliminate electrode position errors in MHE measurements.

Chapter 3

3 Micro four-point probes

This section will give a brief description of micro four-point probe (M4PP) fabrication, lifetime and choice of cantilever materials. We will also focus on reliable surface detection and micro-mechanical vibration tolerance, and present two innovative solutions [i, 33*] implemented with M4PP to solve problems related to reliable characterization of USJ.

3.1 Probe fabrication

The M4PP was developed by C. L. Petersen et al. in 1999; originally it consisted of four Au coated SiO_2 cantilevers extending from the edge of a silicon support die and with an electrode pitch ranging from 1.1 μm to 60 μm [34]. Similar M4PP have also been fabricated using SiC [35], Si_3N_4 [36] and SU8 [37] as cantilever material. Also, the electrodes may be placed on a single cantilever [38] or individually movable cantilever electrodes may extend from a larger cantilever [39]. However, most M4PP used in this study have been produced with poly-silicon cantilevers using the high aspect ratio probe (HARP) fabrication process [40*] which also enables fabrication of a wide variety of other microelectromechanical system (MEMS) devices [XV, XVII, i, xii-xix] with a high fabrication yield [xiv] and 3-4 weeks design-to-test lead time.

The HARP fabrication process uses 100 mm polysilicon-on-insulator (poly-SOI) wafers (cf. Fig. 3.1). These Poly-SOI wafers are prepared from standard Si (100) wafers by growth of a 1 μm thick thermal SiO_2, followed by low-pressure chemical vapor deposition (LPCVD) of 5 μm thick

polycrystalline silicon. The poly-Si and oxide is removed from the wafer backside by unmasked SF_6 based reactive ion etching (RIE) and buffered hydrofluoric acid (bHF), respectively.

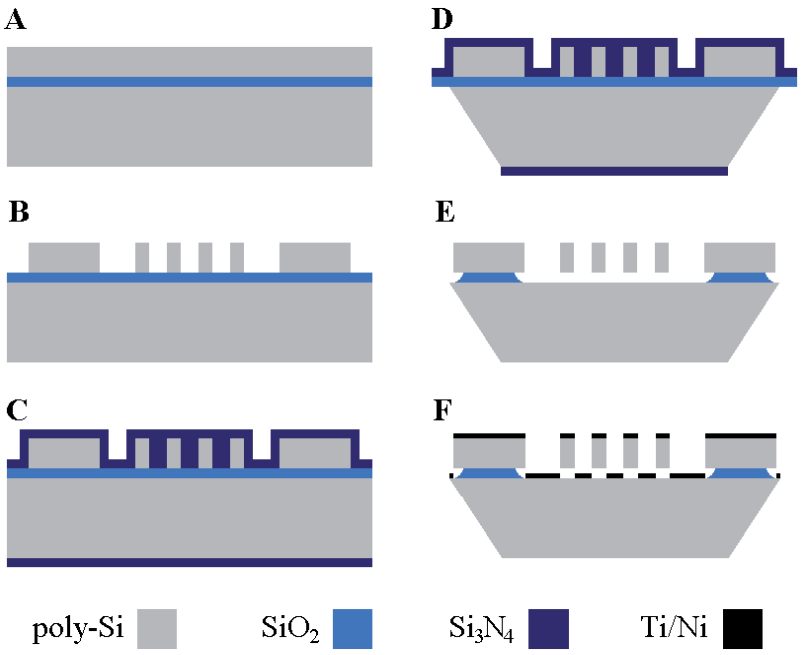

Figure 3.1: Illustration of the HARP process [40*]. Adapted from Paper xiv.

Fig. 3.1 shows the main steps of the HARP process sequence. The polysilicon device layer is etched through lithographically patterned photoresist using an SF_6/C_4F_8 based inductively coupled plasma etch, and the photoresist is removed in an O_2/N_2 plasma clean (cf. Fig. 3.1B). The wafers are then covered by a 300 nm thick LPCVD silicon rich Si_xN_y layer (cf. Fig. 3.1C), and the backside nitride is patterned in a photoresist masked CHF_3/C_2F_6 RIE etch with subsequent O_2/N_2 plasma clean. The wafers are then etched in 80°C potassium hydroxide (KOH) using the patterned nitride as an etch mask (cf. Fig. 3.1D). The nitride is etched in 180°C phosphoric acid and the cantilevers are released by a bHF oxide etch (cf. Fig. 3.1E). Finally, 10 nm Ti and 200 nm Ni is deposited as adhesion and electrode layers using electron beam physical vapor deposition (cf. Fig. 3.1F). After microfabrication, the M4PP are individually glued to a centimeter sized Al_2O_3 substrate and wirebonded to connector leads [41]. The packaging is performed using a high precision automatic die-bonder to avoid excessive probe misalignment. The total misalignment tolerance between the line of the electrode tips and the sample surface is 1° (to be discussed in Sect. 3.3). This cannot be achieved by manual packaging without significant yield loss.

A 5 µm thick device layer is usually used for ≥10 µm pitch M4PP. For smaller electrode pitch the device layer thickness is reduced proportionally. Ti and Ni can easily be replaced with other metal combinations in batch fabrication (300 probes). However, for small scale testing, manual probe packaging is currently required.

A variety of M4PP designs are necessary to characterize different materials and to evaluate different material properties at different length scales. For electrical characterization of USJ, M4PP with electrode pitch ranging from 1.5 µm to 500 µm have been fabricated using the HARP process [I-II].

3.2 Surface detection

Surface detection reliability is critical for automated M4PP measurements in order to minimize damage to the sample surface and the probe tips, and specifically to avoid cantilever fracture and probe crash. This may be done by electrical or force detection [I].

The most commonly used M4PP surface detection method is electrical detection which is commercially available for magnetic tunnel junction characterization [41] and has been used for chip leveling by N. Weiss et al. [42]. Here the two-point resistance is measured continuously between two electrodes until a resistance drop is detected upon contact with a conductive surface. The electrical detection is reasonably reliable on conductive surfaces except if the electrode tips have been significantly damaged. However, we have found it to be highly unreliable on semiconductor surfaces, i.e. it is believed to depend on the semiconductor material, surface resistivity and native oxide thickness.

Unlike electrical detection, force detection is independent on the sample surface conductivity. In atomic force microscopy [43] optical laser detection is the most commonly used with subatomic resolution [44, 45]. This method is applied in Ref. [36], but for small cantilevers extending from a solid probe body it is not easily implemented. Most pioneering work on M4PP have used visual detection methods [34, 46, 47], for which the cantilever deflection is observed manually in optical or electron microscope or via optical pattern recognition as a change in reflection [48]; the latter with a resolution down to 10 nm. Other means of force detection include integrated sensors using strain gauge effect [49, i] or piezoresistive strain [50], the latter with subatomic resolution.

In this work, strain gauge surface detection has been chosen as the primary method, because it is reliable and easily integrated with the M4PP fabrication process and four-point probe electronics [I] of the CAPRES MicroRSP-M150 [41]. Figure 3.2 shows two examples of strain gauge sensors integrated with M4PP. The sensors are designed with a Wheatstone bridge, i.e. passing a current between diagonal contacts and measuring voltage across the second diagonal (cf. Fig. 3.2(left)). Figure 3.3 shows an example of the output voltage V_{out} of an Au coated strain gauge; the offset voltage is device specific (here 4.95 µV). Strain gauge type A (cf. Fig. 3.2(left)) generally has a lower offset than type B (cf. Fig 3.2(right)) due to better symmetry, i.e. longer straight connecting leads.

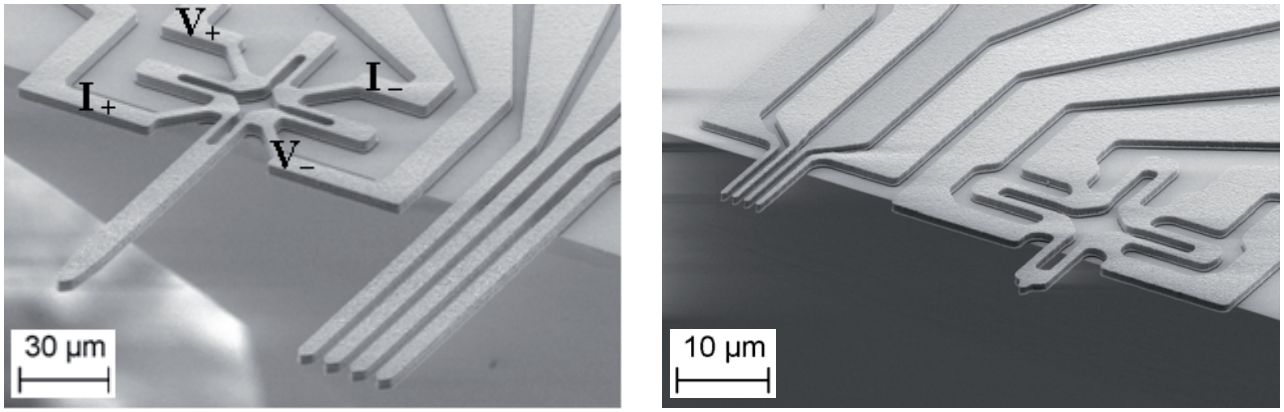

Figure 3.2: Type A (left) and type B (right) strain gauge integrated with a 10 µm and a 1.5 µm pitch M4PP, respectively. Type A is designed with symmetrical leads of length 5×width to reduce Wheatstone bridge off-set, but there is not room for this on the type B design. A typical current and voltage configuration is illustrated (left) by I and V, respectively.

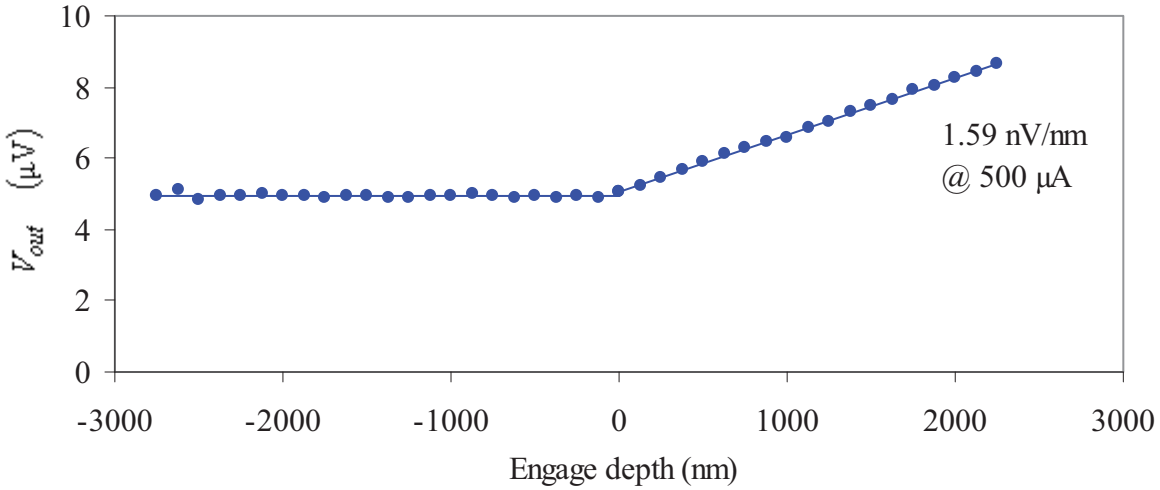

Figure 3.3: Example of Wheatstone bridge output voltage V_{out} for an Au coated strain gauge type B. The measurement is performed with 500 μA at 987 Hz giving a sensitivity of 1.59 nV/nm.

A strain gauge surface detecting algorithm has been integrated in the CAPRES MicroRSP-M150 software, such that it detects a sample surface within one engage increment, which is typically set to 100 nm. It can detect strain gauge malfunction prior to engage and via a build-in calibration scheme, it is largely independent on the conductivity, thickness and geometry of the Wheatstone bridge resistors. A surface detection repeatability better than 100 nm is achievable with Ni coated strain gauges, cf. Fig. 3.4. However, the absolute contact force of the four electrode tips is dominated by probe-to-surface misalignment and the distance between the sensor and the electrodes. In contrast to Au (cf. Fig. 3.3), thin film strain gauges of Ni are highly non-linear [49]. Nevertheless, Ni strain gauges are used for most M4PP measurements today[3].

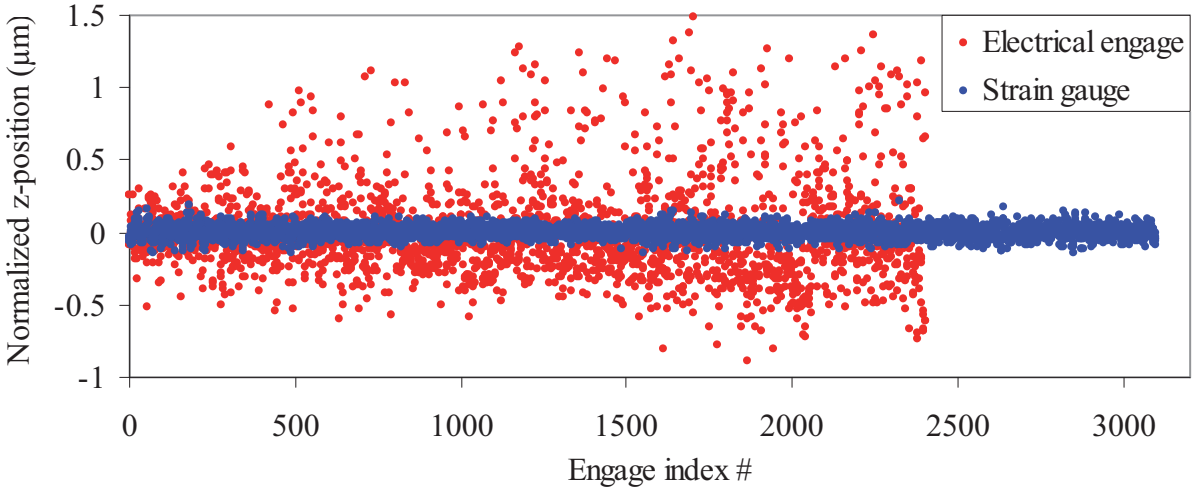

Figure 3.4: Representative measurements of surface detection repeatability for two equivalent M4PP using electrical engage and a Ni coated type A strain gauge, respectively. The *z*-position at engage is extracted from the *z*-stage (a linear motor with ±5 nm resolution), and the position is normalized to account for thermal drift and probe tip deformation. The electrical engage data corresponds to the measurements in Fig. 4.5 and the strain gauge data to the measurements in Fig. 4.6 plus three additional scans performed in sequence.

[3] No systematic study of the non-linear gauge factor of Ni strain gauges has been performed in this project. It just happens to work well, cf. Fig. 3.4.

Strain gauge surface detection has for 2½ years been used continuously as the standard method on two M4PP systems with 100% reliability (six different strain gauge designs), i.e. no events of significant engage overshoot in $>10^6$ engages. In comparison tens of M4PP surface crashes and cantilever fractures have occurred in much less engages when using electrical surface detection for USJ characterization. However, strain gauge failure has occurred during measurements at a few occasions, at which point the measurement is simply terminated, instead of crashing the probe into the surface, which would be completely unacceptable.

3.3 Tip wear and cantilever materials

In conventional scanning probe systems, the probe approaches the sample in a direction normal to the sample surface, and this is also the case for the CAPRES MicroRSP-M150 used for M4PP measurements. When a M4PP with straight cantilevers is brought into contact with a surface at an angle of $\varphi = 30°$, the cantilever tips will slide in the longitudinal direction of the cantilevers for a distance, Δx, which is proportional to the engage depth Δz of each tip individually.

$$\Delta x = \Delta z \tan\varphi \approx \Delta z \cdot 0.577 \tag{13}$$

This sliding may cause frictional wear of the tip as seen in Fig. 3.5 where the M4PP tips with nominal spring constants of 20 N/m have been excessively worn after 2000 engages with an engage depth of more than 1 µm (uncertain as electrical surface detection was used).

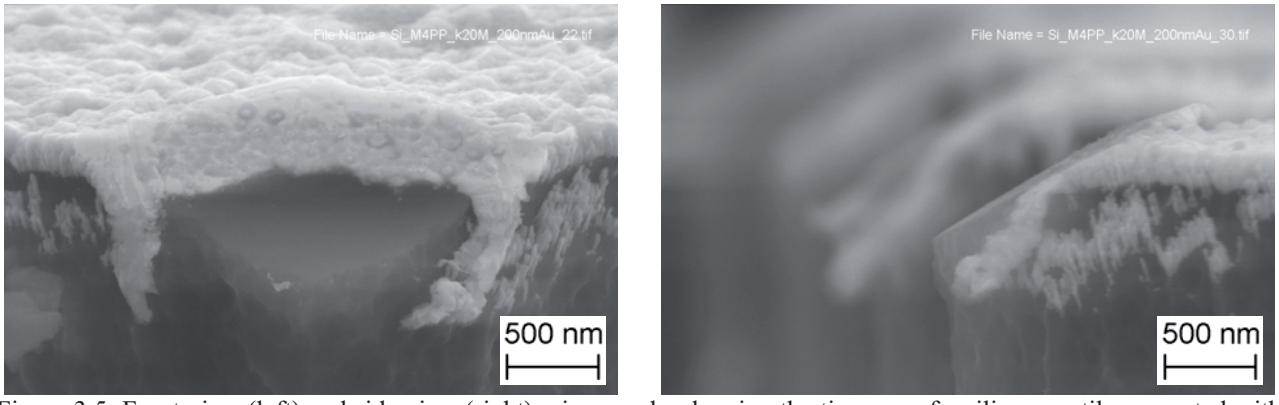

Figure 3.5: Front view (left) and side view (right) micrographs showing the tip wear of a silicon cantilever coated with 200 nm Au. The cantilever has a nominal spring constant of 20 N/m and the tip was engages 2000 times on a Si surface with an engage depth of >1µm. Four-point probe measurements were performed after each engage.

Frictional wear is only part of the tip wear as illustrated in Fig. 3.6. Here, a tip has been exclusively mechanically worn (i.e. no current was intentionally passed through this tip) while electrode tips (i.e. used for electrical measurements) on the same probe show significant morphological degradation as well as a change of the grain structure of the metal. This was attributed as electrical/thermal effects [XVI].

With strain gauge surface detection it is possible to control the engage depth much better and the abrasive wear can be reduced. However, if the probe to sample misalignment exceeds a tolerance of 1°, then the misalignment itself is a cause of uncontrolled engage depth and possible excessive frictional wear. Note that for small electrode pitch, e.g. 1.5 µm the tolerance of 1° results from geometry, as the cantilevers are short and the probe body is comparably huge. N. Weiss et al. [42] report a misalignment of ±0.05° can be achieved using four extra cantilevers and a stage

misalignment correction technique; this is done to avoid excessive contact force as well as cantilever fracture for 10 μm long cantilevers.

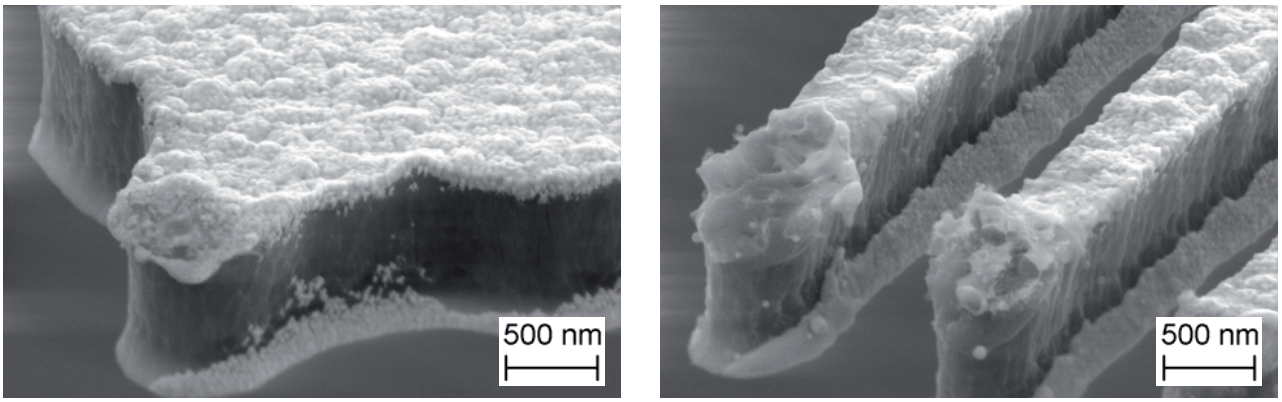

Figure 3.6: Comparison between frictional wear (left) and electrically induced tip degradation (right). All tips are located on the same M4PP of the design shown in Fig. 3.2(right), and the probe has performed 100 engages/measurements. (right) Reproduced from Paper XVI.

The electrical/thermal effects appear less commonly for thick cantilevers than for thin cantilevers (e.g. Figs. 3.6 and 3.7), and probe lifetime is consistently one order of magnitude higher for 5 μm thick cantilevers than for 750 nm thick cantilevers. The most obvious physical parameters affecting the probe lifetime are believed to be metal thickness, wear resilience, specific contact resistivity, thermal conductance, heat capacity and geometry in general; but the list is not exhaustive.

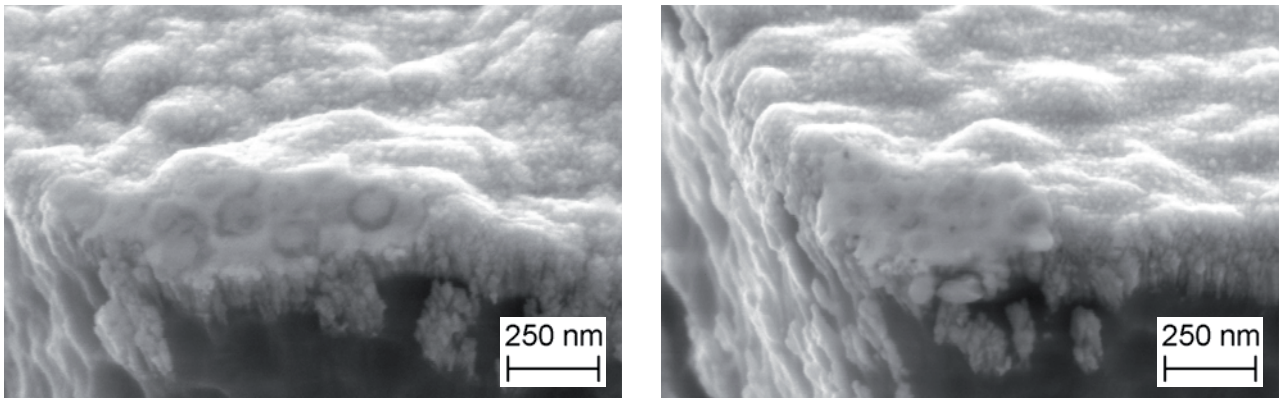

Figure 3.7: Example of reduced probe wear. Again purely mechanical wear (left) is compared to a tip used as electrode (right) to measure the same sample as in Fig. 3.7(right). No electrically induced tip degradation is visible. Both tips are located on the same M4PP of the design shown in Fig. 3.2(left), and the probe was used for the MHE line scan in Fig. 4.14 and has performed 108 engages.

To comply with a demand for a CMOS compatible[4] M4PP, the highest possible probe lifetime and accurate measurements, a number of different electrode materials with different thicknesses have been tested (incl. Al, Au, diamond-like-carbon (p^{++}), Ni, Pt, Ru, Si (p^{++}), Ta, Ti, TiW and W). As a single lifetime experiment may take anywhere from 15 minutes to 5 days, generating solid statistical data is unfeasible with the systems available. Thus, no conclusive studies have been carried out.

A general picture of M4PP lifetime is given here. M4PP with SiO_2 cantilevers and Ta, TiW or W electrodes seems to have extremely short life-time (0-5 engages), whereas Al, Au and Pt perform

[4] CMOS compatible metals may be a matter of belief. Materials already used in CMOS fabrication may not even be CMOS compatible, e.g. Cu is not allowed before interconnect processing.

much better (30-120 engages) and Ni seems the best (100-400 engages). For Au, Ni or Pt coated Si cantilevers a probe lifetime of >1000 engages can be achieved. The best life-time and measurement quality on USJ seems to be achieved with 150-400 nm thick Ni on 5µm thick Si cantilevers. This combination results in an USJ sample dependent probe life-time between 500 and 10,000 measurements per probe, compared to prior state-of-the-art M4PP with 30-120 measurements using Au on 1 µm thick SiO_2 cantilevers[5]. A drastic lifetime reduction is found when reducing the Si cantilever dimensions a factor of ~7 while maintaining the cantilever stiffness and electrode thickness, i.e. the two probes seen in Fig. 3.2 have a typical lifetime of >1000 and ~100 engages for the 10 µm and the 1.5 µm pitch M4PP, respectively.

3.4 Static contact – vibration tolerant design

A key problem of frictional wear is the initial sliding of the electrode tips against the surface during probe engage and retraction. The reason can be attributed to the large difference in spring constants in the *x*, *y* and *z* directions. By matching the stiffness of the cantilever in all directions, a static contact may be formed. In addition, the unbalanced stiffness of straight cantilevers may cause unwanted movements of the contact points during measurements with slight vibrations.

3.4.1 L-shaped cantilevers

To improve vibration tolerance and to reduce sliding and tip wear, a static contact may be formed between the cantilever tips and the sample surface using a high aspect ratio L-shaped cantilever design [XV] as illustrated in Fig. 3.8.

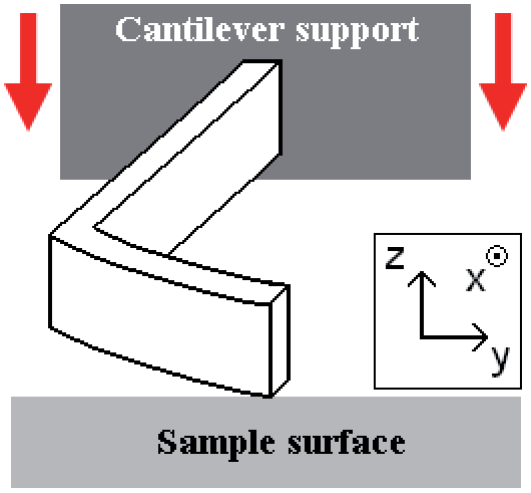

Figure 3.8: Illustration of a three-way flexible L-shaped cantilever engaged on a surface.

When the three-way flexible L-shaped cantilever tip is deflected a distance, Δz, in the z-direction, the force, **F**, acting on the tip is given by Hooke's law.

$$\begin{bmatrix} F_x \\ F_y \\ F_z \end{bmatrix} = -\begin{bmatrix} k_{xx} & k_{xy} & k_{xz} \\ k_{yx} & k_{yy} & k_{yz} \\ k_{zx} & k_{zy} & k_{zz} \end{bmatrix} \begin{bmatrix} 0 \\ 0 \\ \Delta z \end{bmatrix} \tag{14}$$

[5] Ni coated M4PP with Si cantilevers have recently become commercially available [41].

For a static contact to form, the absolute force acting in the *xy*-surface plane must be less than the friction force, which is proportional to the static friction coefficient, μ_S. The static contact criterion is then fulfilled when

$$\mu_S \geq \frac{\sqrt{k_{xz}^2 + k_{yz}^2}}{k_{zz}}. \tag{15}$$

The L-shaped cantilever may also be designed such that zero force is acting in the *xy*-surface plane. The zero force criterion is then given by $k_{xz} = k_{yz} = 0$, at which point the static contact becomes independent on the friction coefficient. The stiffness coefficients k_{ij} can be calculated using the Euler beam equation [51] and the L-shaped beam dimensions h, w_1, w_2, L_1 and L_2 are illustrated in Fig. 3.9, where $\theta = 45°$ and $\varphi = 30°$ are chosen as fixed values due to convenience.

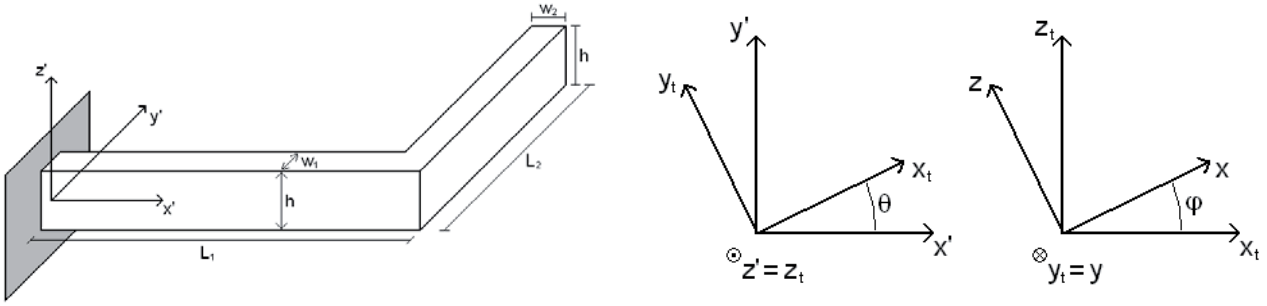

Figure 3.9: Definition of cantilever dimensions and coordinate system rotations from the cantilever reference system (*x'*, *y'*, *z'*) to the sample reference system (*x*, *y*, *z*) which is shown in Fig. 3.8.

In the following numeric calculations of cantilever design space; beam deflection, torsion, compression and elongation are all included. However, in the analytical expressions, compression and elongation are neglected, and an aspect ratio of $h/w_1 = h/w_2 = 4$ is assumed for approximation of the torsion stiffness. For the L-shaped beam shown in Fig. 3.9, it can be shown that to fulfill the zero force criterion, the cantilever dimensions must be given by Eqs. 16 and 17.

$$\frac{w_1}{w_2} = \left(\frac{L_1^3}{L_2^3} - \frac{3L_1}{L_2} \right)^{1/3}, \qquad \left(\frac{L_1}{L_2} \right)^2 > 3 \tag{16}$$

$$\frac{w_1}{h} = \sqrt{\frac{\frac{L_1^2}{L_2^2} - \frac{3}{2}\frac{L_1}{L_2} - \frac{16}{9}(1+\nu)}{\frac{L_1^2}{L_2^2} + \left(1 - \frac{L_2^2}{L_1^2}\right)^{1/3} + \frac{16}{9}(1+\nu)}} \tag{17}$$

Here ν is Poisson's ratio. Figure 3.10 shows the zero force criterion, calculated from Eqs. 16 and 17, and the design space calculated numerically from Eq. 15 for a friction coefficient of $\mu_S = 0.3$. Whereas the zero force criterion requires a minimum height-to-width aspect ratio of 5.8 the static contact criterion is less stringent with a minimum aspect ratio of 4.0. It should be noted that these calculations are preliminary, and finite element method simulations are in progress for final verification.

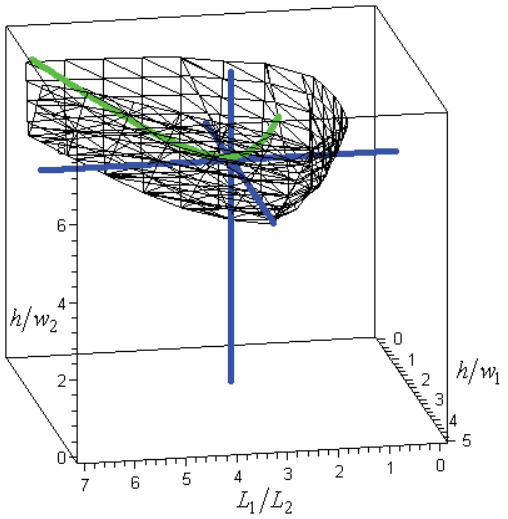

Figure 3.10: Numeric calculation[6] of the design space and zero force line for an L-shaped cantilever. The blue lines intersect at the point of lowest aspect ratio for the zero force criterion. For these calculations, a Poisson's ratio of 0.3 was used.

3.4.2 Micro-mechanical vibration tolerance

The realization of high quality M4PP measurements in a comparably noisy environment, such as a standard cleanroom facility, is challenging. Even for small dynamic position errors of a few nanometers, the R_S measurement requirement of <0.1 % in repeatability cannot be met. Similarly, for MHE measurements, sub-nanometer stability is required for the duration of the measurement in order to obtain <1 % measurement error.

We may evaluate the geometrical design space for vibration tolerance by assuming that the cantilever tips slide to a place of rest, where the resulting force in the *xy*-surface plane is zero. We then systematically apply deflections of $\Delta x = \pm d$ and $\Delta y = \pm d$ in both *x*- and *y*-direction giving 4 permutations. The maximum resulting force must then again be less than the static friction force;

$$\mu_S \geq \max \sqrt{\frac{\left(k_{xx}\Delta x + k_{xy}\Delta y\right)^2 + \left(k_{yx}\Delta x + k_{yy}\Delta y\right)^2}{\left(k_{zx}\Delta x + k_{zy}\Delta y + k_{zz}\Delta z\right)^2}} \,. \tag{18}$$

In Fig. 3.11 we plot the zero force criterion (Eqs. 16 and 17) and the vibration tolerant design space given by Eq. 18, for $d = \Delta z/10$ and $\mu_S = 0.3$. We observe that the design space for vibration tolerance is much larger than that of the static contact criterion, and that even low aspect ratio L-shaped cantilevers may be used with successfully improved vibration tolerance. If both static contact and vibration tolerance must be met, then the static contact design space shrinks accordingly.

For a vibration tolerance of $d = \Delta z/20$ (e.g. 50 nm amplitude vibrations and 1 µm engage depth) the design space becomes huge, i.e. the fabrication process tolerance on the cantilever aspect ratio and morphology are no longer critical in contrast to a previous statement in Paper XV for the static contact cantilevers. Figure 3.11 also illustrate two designs that have been tested for vibration tolerance (red, cf. next section) and static contact (maroon, cf. Paper XV). Again it is noted that these calculations are preliminary and are verification is in progress.

[6] The following constants were used for this calculation: $\mu_S = 0.3$, $\nu = 0.3$, $\theta = 45°$ and $\varphi = 30°$.

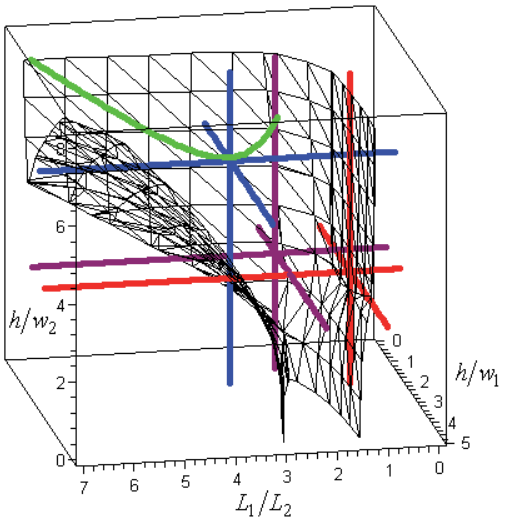

Figure 3.11: Illustration of the vibration tolerant design space for $d = \Delta z/10$. All other constants are the same as Fig. 3.10. The maroon lines illustrate the probe design used in Paper XV and the red lines a probe design used for the results presented in Tab. 3.1.

3.4.3 Results

In order to obtain a measurement repeatability of 0.1 % in M4PP R_S measurements, dynamic position errors must be minimal. To evaluate the effect of a vibration tolerant cantilever design, a direct comparison between M4PP with straight and L-shaped cantilevers has been performed in collaboration with Ane Jensen (Capres A/S). We found that the L-shaped cantilevers perform much better than straight cantilevers in environments with medium and large noise levels cf. Tab. 3.1. That is, the L-shaped cantilevers M4PP measured R_S of an USJ with a relative standard deviation (SD) lower than 0.1 %, while the M4PP with straight cantilevers do not meet the measurement requirements of semiconductor manufactures as described in Sect. 1.2.

Table 3.1: Comparative repeatability test on an USJ with straight and L-shaped cantilevers at two different acoustic noise levels. Each probe test is based on 60 engages and sheet resistance measurements and data treatment are performed using the procedure described in the Sect. 4.1.1. The data is representative of several similar tests performed by Ane Jensen (Capres A/S).

Cantilever design	Straight	L-shaped	Straight	L-shaped
Acoustic noise level[7]	Medium	Medium	High	High
Measurements yield	81 %	100 %	0 %	100 %
Relative SD on R_S	0.17 %	0.05 %	NA	0.09 %
Dynamic position errors[8]				
• SD	49 nm	2.8 nm	NA	5.7 nm
• Median	11 nm	1.7 nm	NA	2.2 nm
• Maximum	404 nm	31 nm	NA	66 nm
• Minimum	0.1 nm	0.0 nm	NA	0.0 nm

From Tab. 3.1, an obvious relationship can be seen between the SD on R_S (dual configuration) and the SD on dynamic position errors, which is calculated from the SD of single configuration four-point resistance measurements using Eq. 4. Due to the low number of measurements (60 engages and 8 four-point resistance measurements per engage), it is convenient to look not only at the SD of

[7] The actual amplitude of vibrations is confidential.
[8] Contact movements are estimated from Eq. 4.

dynamic position errors, but also the median, maximum and minimum. For instance, the median position error shows the most commonly occurring movements whereas the SD is highly affected even by a single large movement. In addition to dynamic position errors and the relative SD on R_S, the measurement yield (i.e. the number of accepted R_S measurements) is equally important; also here the L-shaped cantilever design is clearly better. In all cases, the conclusion is clearly that L-shaped cantilevers do indeed work as a vibration tolerant design.

For USJ characterization in a low noise environment, the lifetime of L-shaped cantilever M4PP has been in the range of 50-2500 engages, depending on the specific cantilever design and sample properties. This is similar to straight cantilever M4PP in a low noise environment, so no significant lifetime improvements have been demonstrated yet. Ongoing work will show, if moving closer to the zero force criterion will improve probe lifetime. Another interesting feature in controlling the individual stiffness coefficients is the ability to force in-line movements rather than off-line movements, such that the measurement precision is not affected by individual contact movements. However, preliminary calculations estimates a quite narrow geometrical design space for forced in-line movements, and thus it may not be feasible for large scale fabrication.

It should be noted, that although contact movements according to the applied theory are real, it may not necessarily be related to physical deflections of the cantilever tip. That is, in calculations we use the mathematical contact point of each tip, whereas the real contact may consist of several smaller contacts. Thus, even for a mechanically stable static contact, small variations in the current flow in the contact region may result in apparent dynamic contact movements of the mathematical contact positions.

Finally, the more stringent criterion of static contact was investigated in Paper XV for a lifetime experiment on a Ru thin film, which is relevant for magnetic tunnel junction characterization [52, 52]. The L-shaped cantilever M4PP outperformed all previous lifetime experiments, by measuring continuously for 115 hours and 15000 engages before we terminated the experiment. Static contact behavior was observed[9] even though the specific design is outside the estimated design space for static contact. This could indicate that the micro-scale friction coefficient between Au and Ru is larger than $\mu_S = 0.3$ or the static contact may be aided by adhesive forces[10] [53].

[9] Small off-line cantilever tip jumps were observed occasionally.
[10] When slowly retracting an L-shaped cantilever probe from a surface, it tends to stick a little before it releases.

Chapter 4

4 High resolution USJ characterization

In this chapter, a summary of the most important experimental results obtained with M4PP is given. The focus will be on the metrology methods and process variability. Further analyses of the laser annealing process are given in Papers XI-XIII.

M4PP measurements of USJ are performed at room temperature (25-30 °C) using a CAPRES MicroRSP-M150 system. The four cantilever electrodes are brought into contact with the sample using a linear motor with a resolution of ±5 nm. Four-point resistance is then measured using lock-in technique with a reference frequency of 11 Hz. The probe is engaged on the sample surface and retracted between each measurement position and the contact force between each tip and the sample is on the order of 5 μN to 50 μN.

In general, the M4PP is considered as a zero probe penetration technique [17*, I]. However, even with the low contact force and the soft and ductile Ni electrodes, junction penetration may occur occasionally. Moreover, the metal-semiconductor contact may be non-ohmic and in some cases the current source may not be able to supply a sinusoidal current. Thus, the measurement data treatment methods for both sheet resistance and MHE measurements are designed to detect such measurement artifacts and exclude measurement errors. In Papers V, VII and XIV, we show that even for softer sample materials such as Ge and InGaAs, USJ may be characterized with effectively zero probe penetration.

4.1 Sheet resistance characterization

4.1.1 Data treatment and accuracy

Paper I summarizes the efforts to determine the accuracy of M4PP sheet resistance measurements. Here, a more elaborate explanation of the data treatment and filtering is given.

A M4PP dual configuration measurement is performed using configuration switching based on *A* and *B* configurations. Tabs. 4.1 and 4.2 illustrate the data treatment principle. It consists of 8 sequentially measured configurations: R_A, R_B, $R_{A'}$, $R_{B'}$, R_A, R_B, $R_{A'}$ and $R_{B'}$ (cf. Fig. 2.1). Unreliable resistance measurements are first excluded using a 1° phase filter to ensure a sinusoidal current. If no resistance values are excluded, seven temporary R_{ST} values are then calculated from adjacent pairs using the dual configuration method, Eq. 2. Using a 2 % median filter to remove outliers, the R_S value is calculated as the arithmetic mean of the remaining temporary R_{ST} values.

The median filter is important because the temporary R_{ST} values are calculated from two resistance measurements acquired sequentially in time. Thus, if the mathematical contact point of one of the electrodes move in the time between measurements of R_A and R_B, then the calculated dual configuration R_{ST} is no longer correct according to theory. That is, the dual configuration method eliminates static position errors but not dynamic position errors as described in Ex. 4.1.

> *Example 4.1*
> *If one of the two inner contacts of a 10 µm pitch M4PP moves by ±3.7 nm in-line between the measurement of R_A and R_B, then the error in R_{ST} is already 0.1 %, which is the target for repeatability. This scales linearly with electrode pitch, so for a M4PP with 1.5 µm pitch, the maximum allowed movement of one of the inner contacts would be just ±0.56 nm.*

As a third precaution, at least five of seven temporary R_{ST} values are required to pass the phase filter and median filter for a measurement to be accepted, and if this criterion is not met, the R_S measurement is completely discarded or remeasured. Discarding measurements based on less than 5 of 7 temporary R_{ST} values is an indirect verification that $R_A = R_{A'}$ and $R_B = R_{B'}$ is true. The criterions $R_A = R_{A'}$ and $R_B = R_{B'}$ may also be applied directly, but using the indirect method allows for one or two contact movements and increases the number of accepted measurements with the target precision.

Table 4.1: Example of a M4PP measurement discarded due to a phase error. A close look at the resistance values shows that $R_B \neq R_{B'}$. One R_{ST} value look acceptable, but the result is discarded.

Index #	Configuration	Phase	Resistance	Dual R_S	Median filter
#		°	Ω	Ω/□	Ω/□
1	*A*	-0.03	147.241		
2	*B*	13.2	122.696	Excluded	Excluded
3	*A'*	-3.87	147.317	Excluded	Excluded
4	*B'*	-0.012	119.156	Excluded	Excluded
5	*A*	-0.108	147.164	645.386	645.386
6	*B*	13.074	122.612	Excluded	Excluded
7	*A'*	-4.188	147.553	Excluded	Excluded
8	*B'*	-1.92	119.118	Excluded	Excluded
Arithmetic mean					Discarded

Table 4.2: Example of an accepted M4PP measurement. A close look at the resistance values show that $R_A \neq R_{A'}$ for index 1 and 3. A contact movement on the order of 60 nm is required between index 1 and 3 which is plausible.

Index	Configuration	Phase	Resistance	Dual R_S	Median filter
#		°	Ω	Ω/□	Ω/□
1	*A*	0.042	150.796		
2	*B*	-0.174	126.054	625.732	Excluded
3	*A'*	-0.012	152.688	648.091	648.091
4	*B'*	-0.042	126.382	645.115	645.115
5	*A*	0	152.604	644.127	644.127
6	*B*	-0.012	126.077	646.898	646.898
7	*A'*	0.012	152.421	644.751	644.751
8	*B'*	-0.036	126.069	644.823	644.823
Arithmetic mean					645.6

The high level acceptance criteria for each sheet resistance value measured with M4PP, does to a large extend insure, that the values reported are reliable, accurate and consistently in agreement with theory. The probability that four-point resistance values are perfectly off-set to pass the 3 filters is extremely low.

Using this measurement procedure, repeatability as well as short term and long term reproducibility better than 0.1% have been demonstrated on uniform USJ samples [III], and this is a representative result of several unpublished reproducibility and repeatability studies on p-type and n-type USJ. Furthermore, M4PP have in several studies been compared to both conventional and exploratory characterization techniques [17*, v, vi, III, VII, XI-XIII]; and in all studies to date, M4PP measurements are in consistent agreement with theory describing leakage current [19*], sensitivity to non-uniformities [IX-X] and sample geometry [23*, I, IV, XI, XIV].

Note that in Monte Carlo simulations (with zero electrical noise) the dual configuration measurements R_S (R_A, R_C) based on R_A and R_C configurations ideally give lower standard deviation than R_S (R_A, R_B). However, the measured voltage in R_C measurements is significantly lower than for R_B, which results in an increased electrical noise. No conclusive experimental study has been performed to verify which method is best, most likely R_S (R_A, R_C) measurements are better for some samples and R_S (R_A, R_B) better for others.

One of the main drawbacks of this elaborate data treatment technique is the increased measurement time, as compared to performing only two four-point resistance measurements. E.g. the average measurement time for the CAPRES MicroRSP-M150 is currently approximately 20 seconds (including probe engage, measurement and remeasurements), but this may be reduced to 10 seconds by optimizing the time spent on probe engage. The current state-of-the-art measurement time is less than 7 seconds for the CAPRES MicroRSP-A300. Thus, a choice must be made, if measurement reliability or measurement time is the most important parameter. As discussed in Sect. 1.2, both parameters are crucially important to a metrology, but one reliable R_S measurement still easily beats ten poor or even wrong R_S measurements.

4.1.2 Non-uniform samples

The small area of sensitivity of the M4PP enables measurements of sub-mm sheet resistance non-uniformities with high accuracy. This is verified by the spatial frequency transfer function for R_S [X] (cf. Fig. 2.5). It was further verified experimentally, by characterization of non-patterned laser

annealed[11] USJ with periodic sheet resistance variations using M4PP with electrode pitch ranging from 1.5 µm to 500 µm [II], cf. Fig. 4.1. As described by the spatial frequency transfer function, only M4PP with small electrode pitch (<20 µm) are able to characterize the main periodic sheet resistance variations, which have spatial wavelengths of 750 µm and 3.65 mm. For larger electrode pitch, the correct variation may be deduced from the spatial frequency transfer function using Fourier series [X].

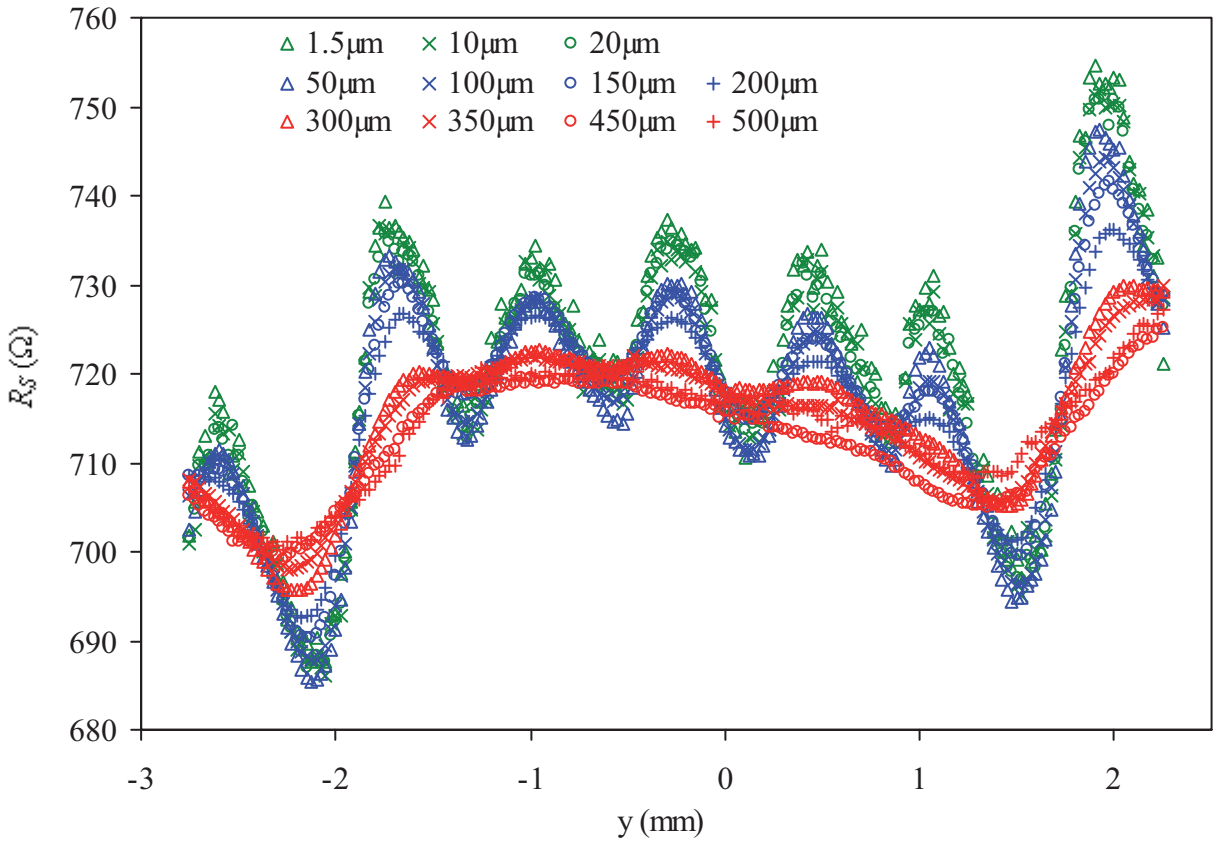

Figure 4.1: M4PP sheet resistance measurements performed at the same location on an USJ formed in n-type Si by low energy B implantation (0.5 keV and 10^{15} cm^{-2}) with subsequent laser anneal. The electrode pitch ranges from 1.5 µm to 500 µm, and the maximal electrode pitch to characterize the full variations is s = 750/40 µm = 18.75 µm.

In Ref. 19* we demonstrated the first micro-scale sheet resistance line scan on laser annealed USJ with a spatial wavelength of approximately 20 µm using a 3 µm pitch M4PP. However, in this case only 75 % of the actual sheet resistance variation was measured according to the spatial frequency transfer function. Furthermore, the non-uniform sheet resistance had an apparent R_S ranging from 50 Ω to 250 Ω which may not be considered a small variation. Thus, the spatial frequency transfer function may in this case not be completely valid but serves as an estimate.

In Paper II, M4PP sheet resistance measurements were extended, via significantly improved probe lifetime, to 2D mapping of non-uniformities. Figure 4.2 shows a 45×101 point sheet resistance map performed with a 10 µm pitch M4PP. Here, periodic sheet resistance variations are observed with spatial wavelengths of 3.65 mm and 750 µm in the y-direction and 500 µm in the x-direction. The variations in y-direction have been traced to stitching of the scanned laser, as illustrated in Figs. 4.3 and 4.4, and spatial variations in laser power density. Also, the variations in x-direction have been traced to arise from 300 Hz noise in the laser scan speed [vii]. The process variations causing sheet

[11] Laser annealing was performed in an Applied Materials DSA chamber.

resistance variations on non-patterned Si wafers have furthermore been linked to variability in transistor threshold voltage by C. Ortolland, et al. [54].

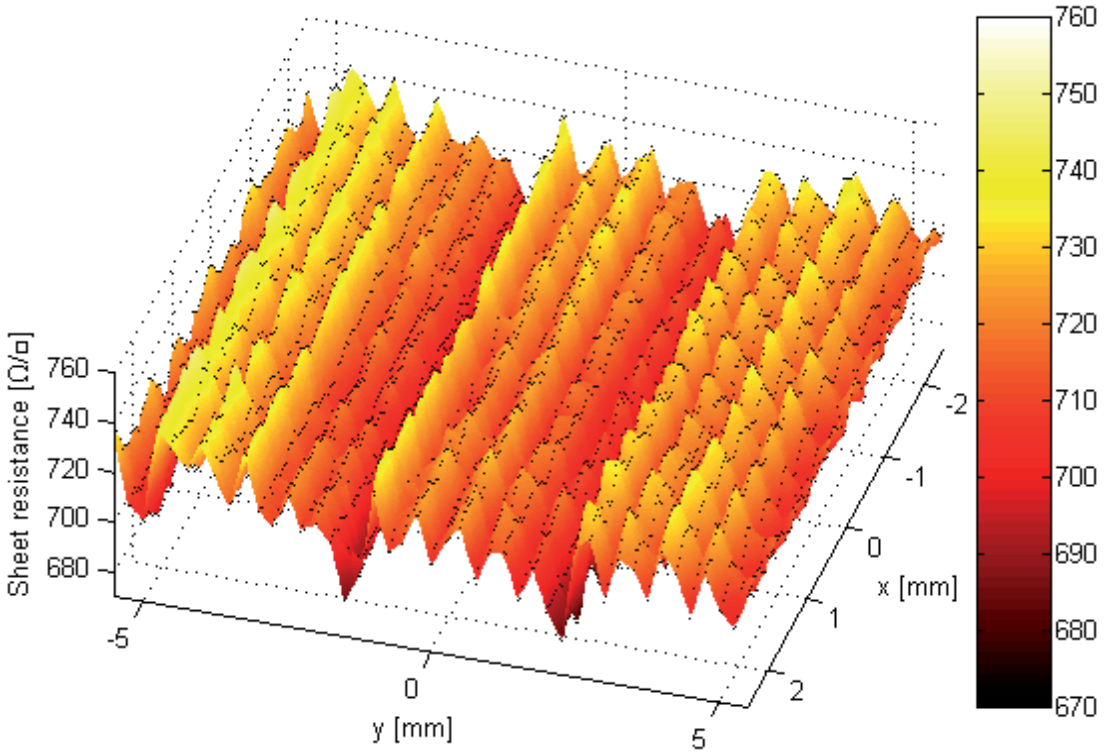

Figure 4.2: 2D R_S map performed with a 10 µm pitch M4PP. Reproduced from Paper II.

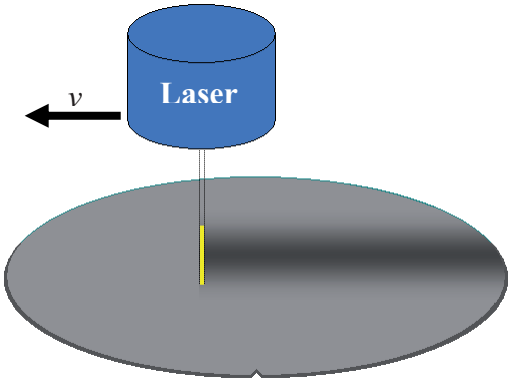

Figure 4.3: Schematic illustration of the laser annealing process. The laser spot is 11 mm wide and extends 75 µm in the scanning direction.

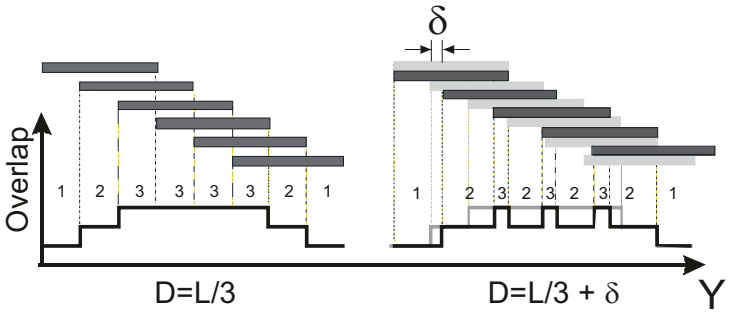

Figure 4.4: Illustration showing the laser stitching overlap for a laser stepping distance $D = L/3$ (left) and $D = L/3+\delta$. (right). Reproduced from Paper vii.

With the ability to map non-uniformities, a study was undertaken to reduce these three sources of process variations [vii]. Figure 4.4 shows the principle of laser stitching overlap and in Fig. 4.5 the sheet resistance line scans corresponding to four different stitching overlaps are shown. Significant changes occur even when changing the overlap by just 2 % as indicated in Fig. 4.5. The process induced sheet resistance variations may be reduced by careful optimization of the stitching overlap, the laser power density uniformity and the scan speed, which we show in Paper [vii].

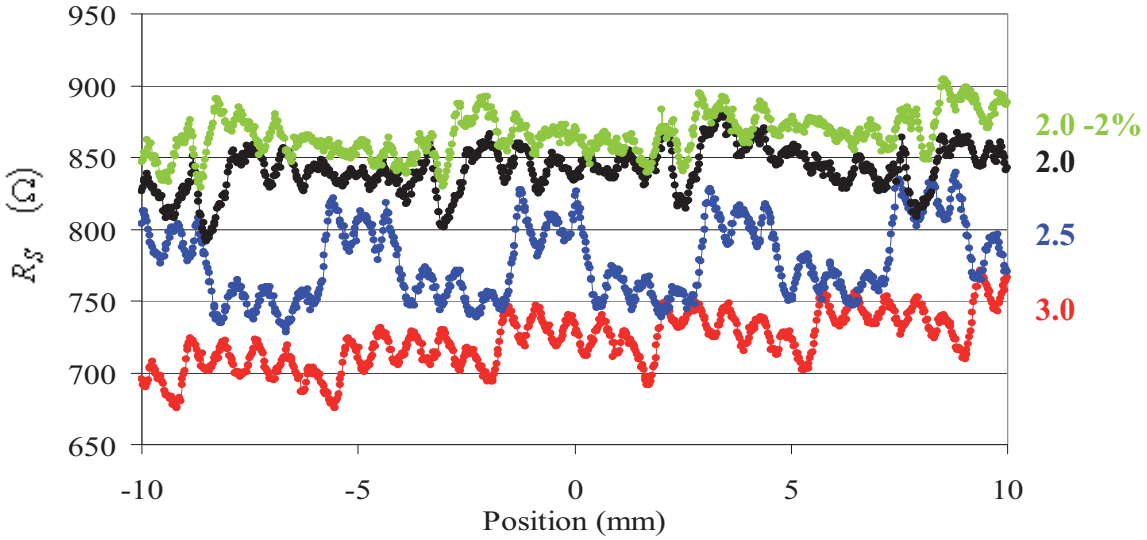

Figure 4.5: R_S line scans for four different stitching overlaps; i.e. 1.96, 2.0, 2.5 and 3.0 overlaps are achieved by stepping the 11 mm wide laser beam 5.60, 5.48, 4.38 and 3.65 mm, respectively.

4.1.3 Small pads

The integration of USJ source/drain extensions in a full CMOS process flow yields new challenges related to process variability. For instance, device wafers are patterned with shallow trench isolation (STI) oxide which may vary in thickness and pattern density. In Paper XI we investigate the STI pattern effect on the sheet resistance uniformity of USJ. Figure 4.6 show an example of R_S variations in a laser annealed 400×430 μm^2 B doped Si test pad surrounded by ~330 nm thick STI. The large sheet resistance variations in proximity of the STI are found to result from variations in the absorbed laser power caused by the difference in reflection coefficient of Si and SiO_2/Si [XI].

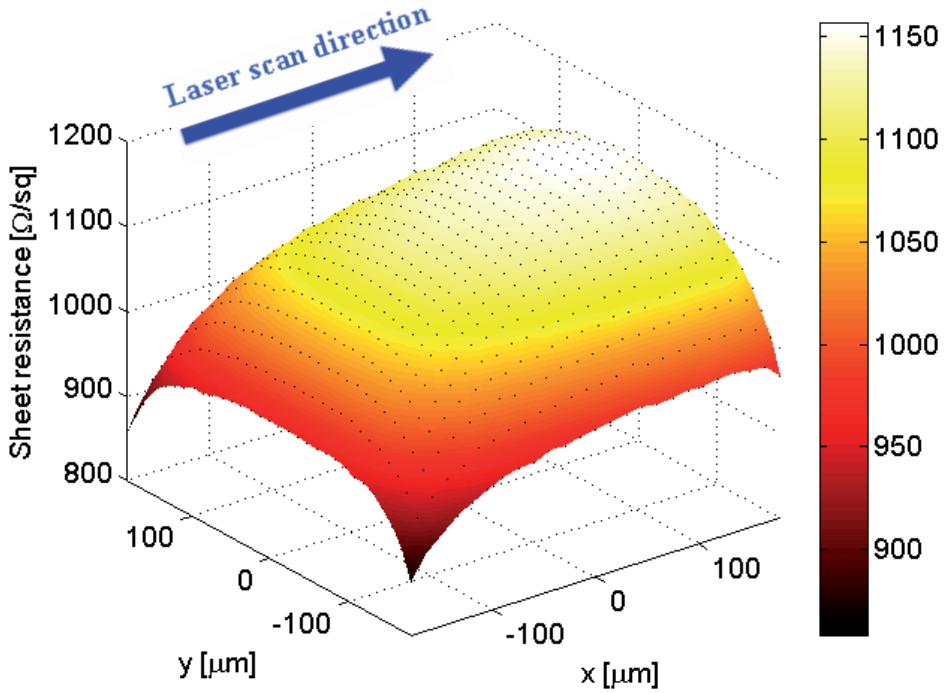

Figure 4.6: 25×31 point R_S map of a laser annealed 400×430 μm^2 B doped (0.5 keV and 10^{15} cm^{-2}) Si test pad surrounded by ~330 nm thick STI oxide. Adapted from Paper XI.

As more silicon is exposed to the laser beam, the macroscopic[12] anneal temperature decreases, thereby increasing the resulting R_S along the laser scan direction (x-direction). Across the laser scan direction (y-direction), the difference in reflectivity causes a microscopic temperature gradient, which is governed by the locally absorbed power and the thermal diffusion length, which in this case is on the order of 140 µm [XI].

To investigate pattern density effects of the laser annealing, a 1.5 µm pitch M4PP was used to measure the R_S sheet resistance for pad sizes down to 10×10 µm^2, cf. Fig. 4.7. R_S was measured in the pad center (on the mirror plane) and an R_S decrease of more than a factor of two was observed for reducing pad size [XI], cf. Fig. 4.8. This huge sheet resistance difference may be explained by a combination of the macroscopic and microscopic temperature effects. In Paper XI, we further show experimentally how R_S variations are greatly reduced when adding an optical absorber layer prior to laser annealing.

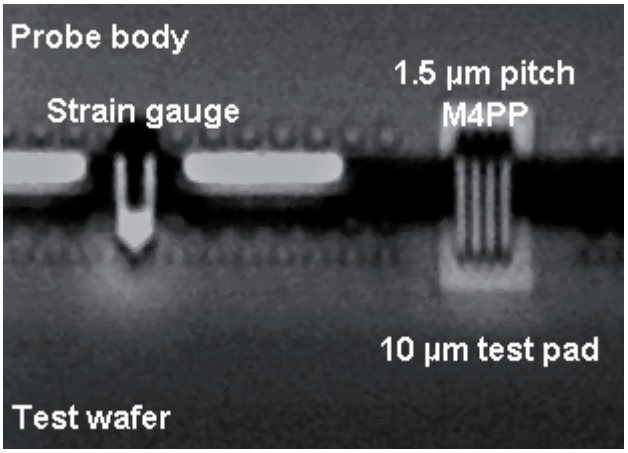

Figure 4.7: Optical microscope image of a M4PP with 1.5 µm pitch measuring in the center of a 10×10 µm^2 pad. Reproduced from Paper XI.

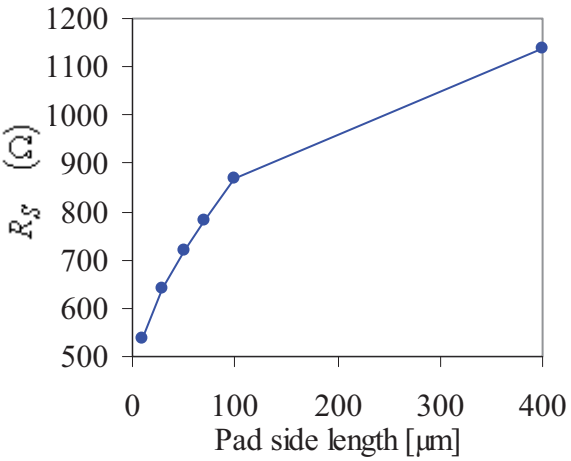

Figure 4.8: Sheet resistance as a function of pad size. The Si test pads are surrounded by 330 nm thick STI. Adapted from Paper XI.

From Fig. 4.8 it is evident, that it is important to be able to characterize R_S in small test structures to monitor process variability. With a 1.5 µm pitch M4PP used in this study and a positioning error of ±2.5 µm, it is possible to perform correction-free R_S measurements with a geometrical error of <5 % [IV]. To reduce the measurement error to <0.1 %, smaller electrode pitch or better alignment is necessary.

In Paper XI, we also show R_S variations as an indirect result of STI thickness variations across the wafer. Thus, it is necessary to characterize pattern effect at more than one location. Here, the measurement time of M4PP is a bottleneck in acquiring enough measurement points to truly monitor pattern induced R_S variations. Alternatively, as we show in Paper XI, faster methods like Therma-Probe could be useful for monitoring these R_S variations on small test structures. The ideal R_S measurement time of Therma-Probe is approximately one second compared to currently 6-7 seconds for M4PP. However, the Therma-Probe method does not provide direct R_S measurements and frequent calibration would be necessary to ensure measurement reliability. Thus, either the measurement time of M4PP should be reduced significantly or M4PP could be used as a calibration tool for a faster method like Therma-Probe. Another possibility is to use M4PP R_S characterization to improve understanding of process variability for a specific process flow and find correlations

[12] The macroscopic temperature is defined as the bulk temperature in proximity of the laser beam. The beam length is 75 µm so the macroscopic temperature change on a similar length scale when the average reflection change.

between R_S and other physical parameters, e.g. STI oxide thickness. Then R_S variations could be monitored indirectly by ellipsometry or similar. Finally, a reevaluation of the data treatment method for M4PP R_S measurements could result in further reduction measurement time, e.g. reduced requirements to measurement precision could allow for an R_S measurement time of less than 2 seconds.

4.2 Micro Hall Effect

In addition to R_S measurements, Micro Hall Effect (MHE) measurements may yield information about the individual contributions of carrier mobility μ and sheet carrier density N_S. Thus, it is possible to investigate in more detail the physics of micro non-uniformities. In Papers V-VIII, XII-XIII and viii-x we use MHE to study a variety of different USJ structures as well as other semiconductor materials. This section, describes in more detail the measurement setup and data treatment methodology, and summarizes some of the most important results in relation to Si USJ.

4.2.1 Magnetic flux density uniformity

For MHE measurements, the sample chuck is fitted with a permanent magnet as illustrated in Fig. 4.9. The permanent magnet has a diameter of 35 mm and the magnetic flux density is B_z = 0.50 T at the position of the sample surface.

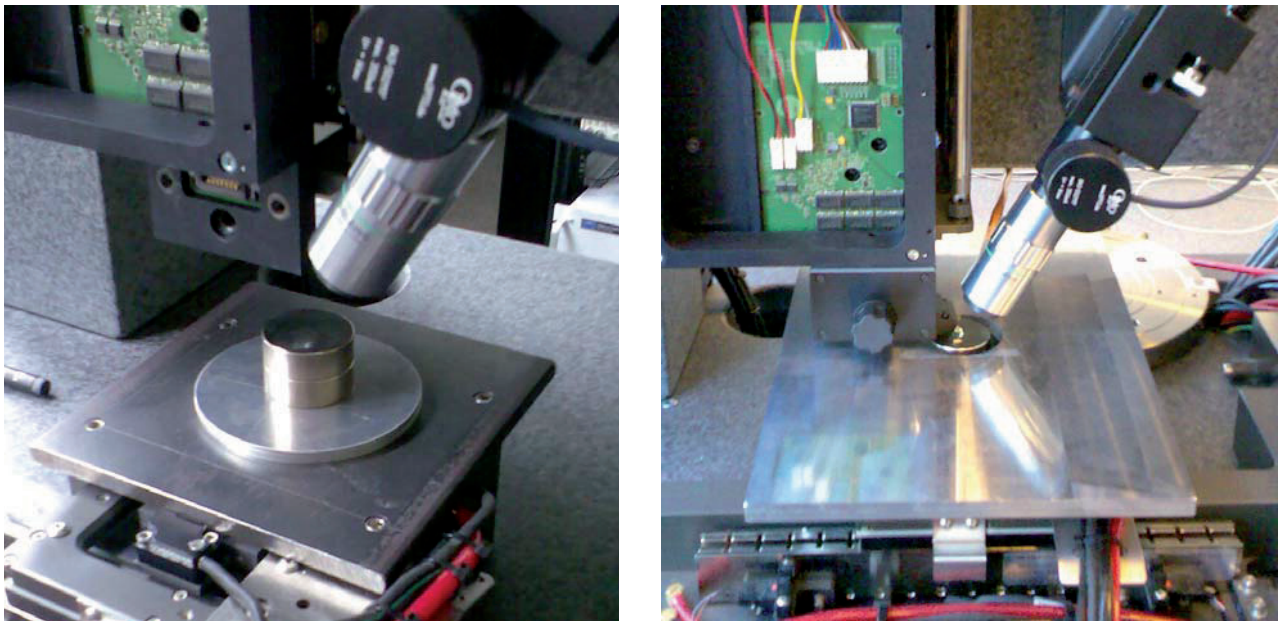

Figure 4.9: Pictures of the CAPRES MicroRSP-M150 fitted with a modified stage for MHE measurements. The cylindrical permanent magnet (left) is mounted on the *xy*-stage an aluminum chuck is placed in level with the magnet (right) such that both millimeter sized samples and full 300 mm wafers may be characterized without system modification.

In practical measurements, the magnetic flux density is measured at each MHE measurement position using a custom made Hall Cross sensor. The Hall Cross sensor has a sensitive volume of roughly $x \times y \times z$ = 50×50×0.35 μm^3 and is calibrated to within 2 % of a LakeShore 460 3-Channel Gaussmeter at 500 mT. Figure 4.10 shows a magnetic flux density B_z map of the permanent magnet at a distance of z = 650 ±25 μm from the magnet surface, as well as a 2D map of the relative deviation of B_z from the calibration value. The 2D map reveals a constant magnetic flux density

with variations on the order of one percent within a diameter of ~25 mm. Similar 2D maps are shown in Fig. 4.11 for the positions z = 550 ±25 µm and z = 850 ±25 µm. At z = 850 µm, the diameter with a nominal deviation of <3 % shrinks to ~20 mm.

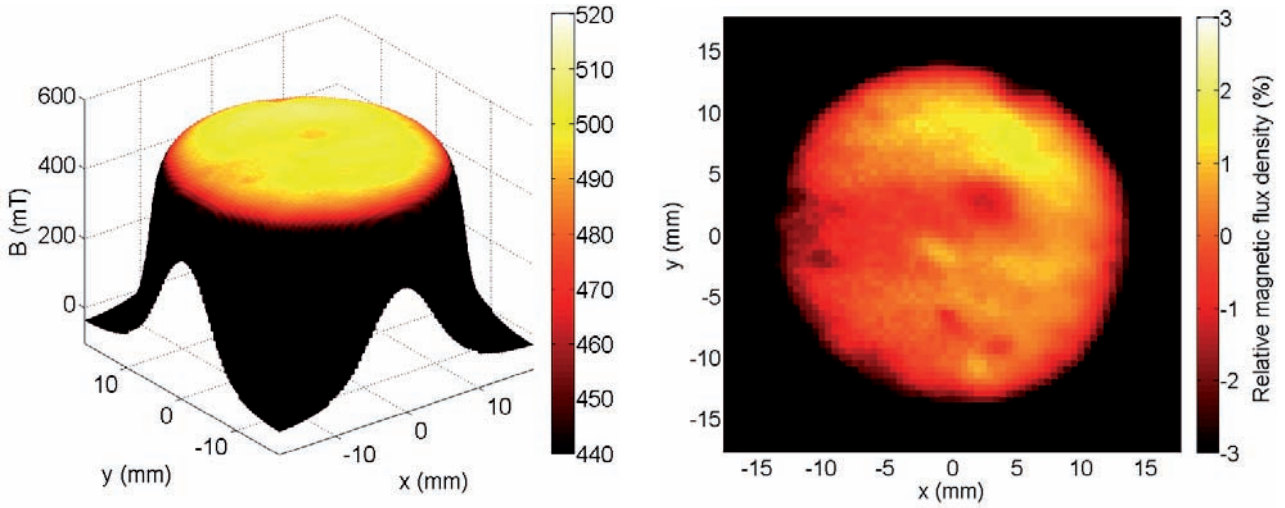

Figure 4.10: (left) A 71×71 points surface plot of the magnetic flux density B_z performed with a custom made Hall Cross sensor in a distance of 650 ±25 µm from the surface of the permanent magnet. (right) The measured magnetic flux density is normalized to the calibration field (500 mT).

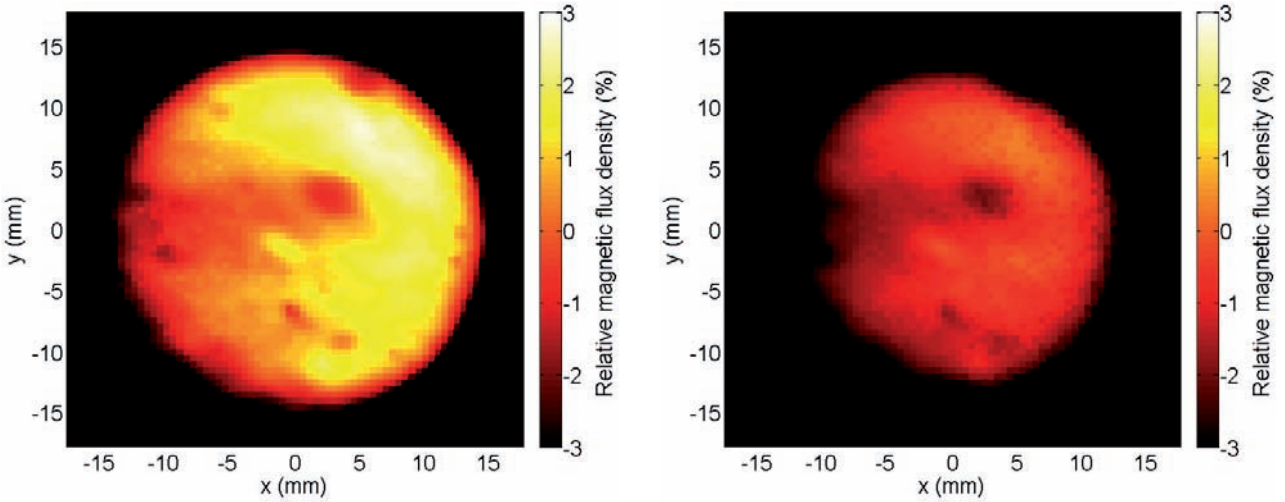

Figure 4.11: As in Fig. 4.10(right) the deviation of the magnetic flux density from the calibration field is shown for a distance of 550 ±25 µm (left) and 850 ±25 µm (right). Each pixel corresponds to a magnetic flux density measurement without value interpolation.

Most USJ samples are either 200 mm or 300 mm wafers with nominal thicknesses of 725 µm and 775 µm, respectively. Thus, the magnetic flux density maps in Figs. 4.10 and 4.11 demonstrate that correction free MHE measurements may be safely performed with an uncertainty in the relative magnetic flux density of <3% within a radius of 10 mm from the magnet center. Also, the sample thickness is not critical. However, for highly accurate MHE measurements as presented in the Fig. 4.14, the magnetic flux density is measured at the (x, y, z) positions of each MHE measurement point.

4.2.2 Data treatment

Similar to M4PP R_S measurements, MHE data treatment relies on sequential measurements of R_A, $R_{A'}$, R_B and $R_{B'}$ to extract the resistance averages ($R_{AA'}$ and $R_{BB'}$) and the resistance difference $\Delta R_{BB'}$. Similar to sheet resistance measurements, phase filter, median filter and minimum pair filter are used to remove unreliable resistance measurements and dynamic position errors. As described in Sect. 2.3.4, the dual configuration method (Eq. 12) is used in order to minimize static position errors. The effect is demonstrated in Figs. 4.12 and 4.13(left) for MHE measurements on laser annealed USJ with a 20 µm pitch M4PP.

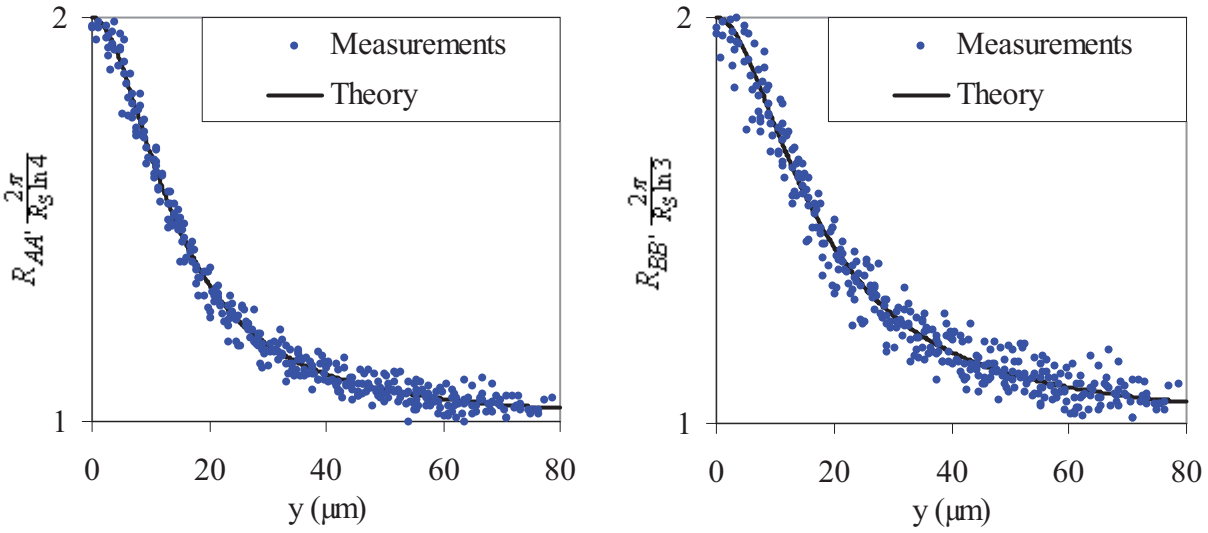

Figure 4.12: Normalized resistance average measurements as a function of the distance y to a parallel insulating boundary. The measurements were performed on a B doped (0.5 keV, 10^{15} cm^{-3}) and laser annealed USJ using a 20 µm pitch M4PP.

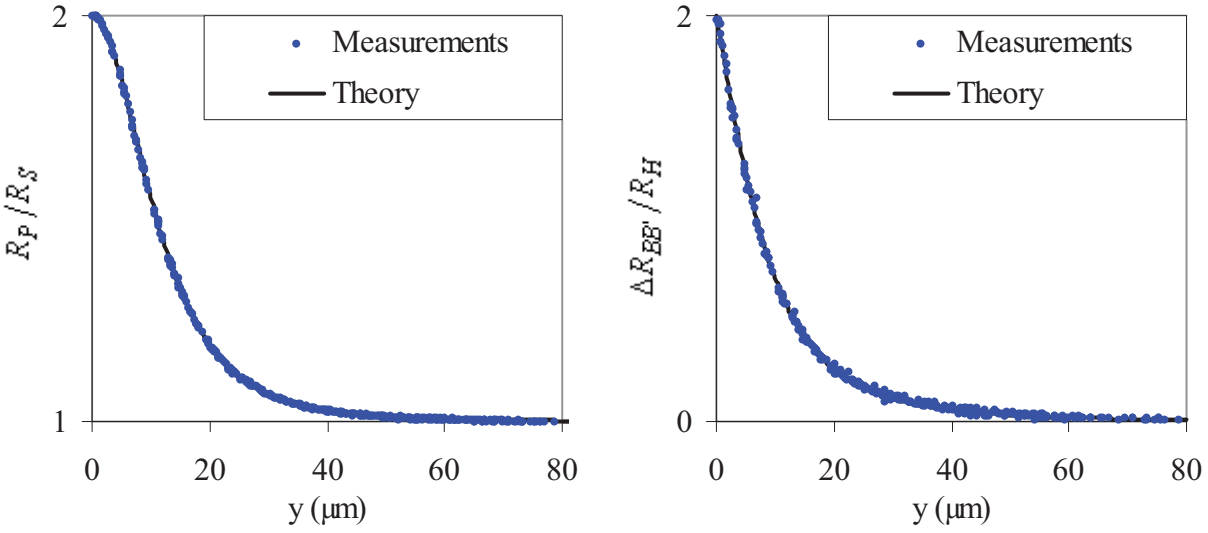

Figure 4.13: Normalized pseudo sheet resistance R_P and resistance difference as a function of the distance y to a parallel insulating boundary. R_P is calculated from the dataset of Fig. 4.12 and $\Delta R_{BB'}$ from the R_B and $R_{B'}$ data used for Fig. 4.12(right).

Figure 4.13(right) shows the theoretical resistance difference function (Eq. 8) fitted to extracted $\Delta R_{BB'}$ data. Note that each measurement point in Figs. 4.12 and 4.13 is filtered without reference to other measurement points, i.e. there is an exceptional good agreement between each measurement

and the proposed theory (Sect. 2.3). Unlike R_P, $\Delta R_{BB'}$ includes static position errors. However, from Fig. 4.13(right) it is obvious that the sensitivity of $\Delta R_{BB'}$ to static position errors is very low. This is because the in-line position error of measured $\Delta R_{BB'}$ to first order is zero for the two inner contacts, while the sensitivity to position errors from the outer two electrodes is low.

Example 4.2
While MHE measurements are relatively insensitive to in-line static position errors, the main source of measurement error is due to dynamic position errors not eliminated by the data filtering. For instance, consider a 20 μm pitch M4PP, positioned at a distance of 4 μm from a parallel straight insulating boundary. If one of the two inner contacts moves by ±0.92 nm (in-line) between the measurement of R_B and $R_{B'}$, then the error in $\Delta R_{BB'}$ is already 1 %, which is the target defined for repeatability. If the movement occurs as an off-line error ±11 nm is allowed.

Another important error is due to a shortcoming of the electronics of the CAPRES MicroRSP-M150, that was not developed specifically for MHE measurements. As the Hall Effect signal is only a small fraction of the much larger resistance signal, bit rounding becomes a serious issue in measurement precision. For instance, the ratio $\Delta R_{BB'}/R_{BB'}$ is for B doped USJ typically less than 0.6 %, and $\Delta R_{BB'}$ must be measured with an accuracy at least better than 1 %. This means that R_B and $R_{B'}$ must measured with an error of <0.006%.

4.2.3 Data treatment 2: Position error suppression

The data treatment should allow for both fast and accurate evaluation of R_S, N_S and μ, and here we present how MHE measurements may be performed in less than a minute with an error of <1 %. For accurate MHE measurements it is necessary to eliminate the static position errors σ_x, σ_y and σ_b, for $R_{BB'}$ and $\Delta R_{BB'}$ (cf. Eqs. 8-11), while all dynamic position errors are sought removed by data filtering. The following is a preliminary description of how position error elimination works.

1. σ_x is effectively eliminated.
    a. Using dual configuration R_P instead of the resistance average $R_{BB'}$ effectively removes the static position errors σ_x on the two inner contacts, while movements of the outer two contacts effectively change the relative distance y/s to the boundary.
    b. $\Delta R_{BB'}$ has, to first order, zero sensitivity to σ_x on the inner two contacts. Also here, the static position errors on the outer two contacts effectively change the relative distance y/s to the boundary.
    c. Thus, we may translate the position errors on σ_x to a correlated boundary position error σ_b, assuming the effective changes in relative boundary distance y/s are equal for R_P and $\Delta R_{BB'}$.
2. σ_y is effectively eliminated.
    a. To first order, we may assume for both R_P and $\Delta R_{BB'}$ that a small movement of one contact Δy in the y-direction is equivalent to moving all four contacts a smaller distance in the same direction.
    b. Thus, for small static position errors, σ_y may be translated to an additional boundary position error σ_b.
3. σ_b is effectively eliminated.
    a. Measuring R_P and $\Delta R_{BB'}$ at two different distances to the boundary, y_1 and y_2, locations yields four equations with four unknown parameters (R_S, R_H, y_1' and y_2'), where y_1' and y_2' may be different from the nominal positions y_1 and y_2. This equation system may be solved for $y_1' \neq y_2'$ using Eqs. 8 and 9.

Two methods have been developed to calculate the distance y between the probe and boundary. We may define the pseudo sheet resistance ratio and resistance difference ratio as [VI, VIII]

$$\frac{R_{P1}}{R_{P2}} = \frac{f\left(\frac{y_1}{s}\right)}{f\left(\frac{y_1+\Delta y}{s}\right)} \tag{19}$$

and

$$\frac{\Delta R_{BB'1}}{\Delta R_{BB'2}} = \frac{g\left(\frac{y_1}{s}\right)}{g\left(\frac{y_1+\Delta y}{s}\right)}. \tag{20}$$

Here the index 1 and 2 refer to a measurement point close to the boundary and further away from the boundary, respectively. We define $\Delta y \equiv y_2 - y_1$, and the known functions f and g are given by Fig. 4.13. The unknown variables y_1 and Δy can be found by solving Eqs. 19 and 20.

Using Monte Carlo simulations, the optimal nominal positioning of the probe was determined in Papers VI and VIII for the F3S (Fast 3s Separation) and FSS (Fast Short Separation) methods. For both methods the best nominal position of y_1 was found to be as close as possible to the boundary; in practical measurements this is approximately 4 µm for a 20 µm pitch M4PP. The F3S method solely uses Eq. 19 and defines $\Delta y \equiv 3s$ (for which the error is minimal), whereas the FSS method makes no assumption on the actual separation Δy with a nominal value of approximately 3 µm for a 20 µm pitch M4PP. Both methods assume uniform sheet carrier density and carrier mobility.

In practical measurements on a uniform As-implanted USJ, the F3S method has performed with a relative standard deviation on μ_H of 0.95 % in a repeatability experiment [VI], which is similar to the result of 0.65 % obtained with Monte Carlo simulations [VI]. According to Monte Carlo simulations the FSS method should give a standard deviation on μ_H of 6 % but be less sensitive even to large 25 % variations in sheet carrier density near the boundary [VIII]. Both methods have a measurement time of less than a minute.

4.2.4 Non-uniform samples

The MHE F3S method was used to investigate the non-uniform sheet resistance resulting from a laser anneal process. Figure 4.14 summarizes the results where an evident correlation was found between the R_S non-uniformities and N_{HS}, whereas μ_H is reasonably constant. The measurements were performed with a 20 µm pitch M4PP and from the spatial frequency transfer function for MHE we see that the 750 µm spatial wavelength of non-uniformities is resolved with ~99% accuracy. The relative standard deviation on μ_H was found to be 1.3%, and this increase relative to a uniform sample may be related to the sheet resistance variations. That is, if the conductive sheet is not perfectly uniform on the length scale of the measurement point separation ($3s$ = 60 µm), the F3S method will introduce a systematic measurement error according to the sensitivity study in Paper IX. However, assuming the variations to be similar for adjacent measurement points, which is supported by 2D sheet resistance characterization (cf. Fig 4.2), it is reasonable to trust the relative variations of the MHE measurement results.

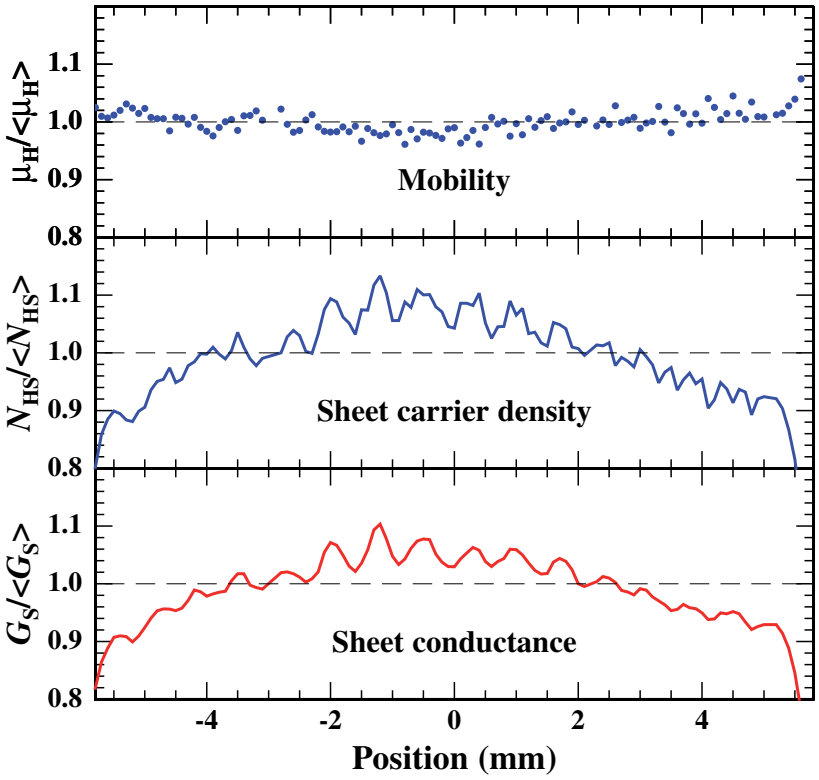

Figure 4.14: Scanned MHE measurement of a B doped USJ annealed by a single pass of an 11 mm wide laser beam. Hall mobility, Hall sheet carrier density and sheet conductance are each normalized by their respective average value. Adapted from Paper VI. Note that SEM micrographs of the tips of the M4PP used for this measurement are shown in Fig. 3.7.

The relative measurement error induced by magnetic flux density variations may obscure the true variations in N_{HS} and μ_H. Thus, for N_{HS} and μ_H calculated in Fig. 4.14, the magnetic flux density has been calibrated at each measurement location along the 11.4 mm scan. Figure 4.15 show the variation in relative magnetic flux density with a peak-to-peak variation of 1.3 %.

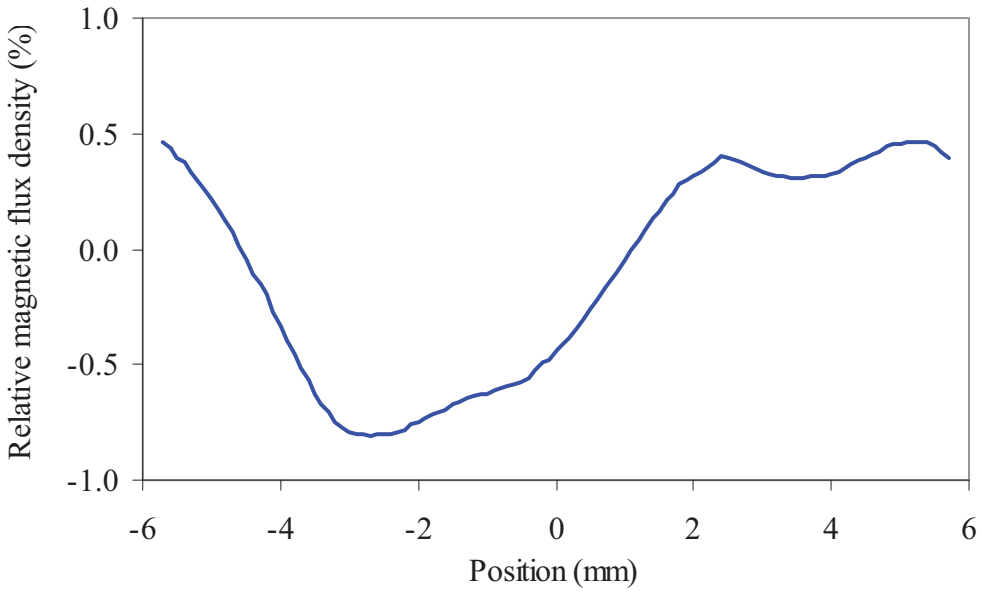

Figure 4.15: Magnetic flux density calibration curve corresponding to the measurements in Fig. 4.14. The average magnetic flux density was 496 mT and the peak-to-peak variation was 1.3 %.

The absolute accuracy of the MHE F3S method was investigated in Papers XII and XIII and the results are reviewed in Paper I. Here we compared different methods to extract R_S, N_S and μ from non-uniform laser annealed USJ with B implants of 10^{14}-10^{15} atoms/cm^2. The only two methods to consistently agree on N_S and μ are the conventional cloverleaf method and MHE (cf. Fig. 4.16). Methods to measure N_S, with a sample preparation time similar to MHE, all gave unreliable results (each deviating by >30% from MHE and cloverleaf for one or more samples); however the carrier mobility was within 23% of the MHE results for all methods tested [XII].

The cloverleaf measurements were performed by Nick S. Bennett, Newcastle University. The reported cloverleaf measurement results were each based on 4-6 samples prepared for each implanted dose. It was found that the arithmetic averages of μ_H obtained by the cloverleaf method did not agree with $R_S = (e\mu_H N_{HS})^{-1}$ due to significant measurement variations (~20 %). However, using the appropriate statistical averaging (geometrical mean[13]) the cloverleaf and MHE methods do agree within a reasonable experimental uncertainty as the samples where not uniform, cf. Fig. 4.16.

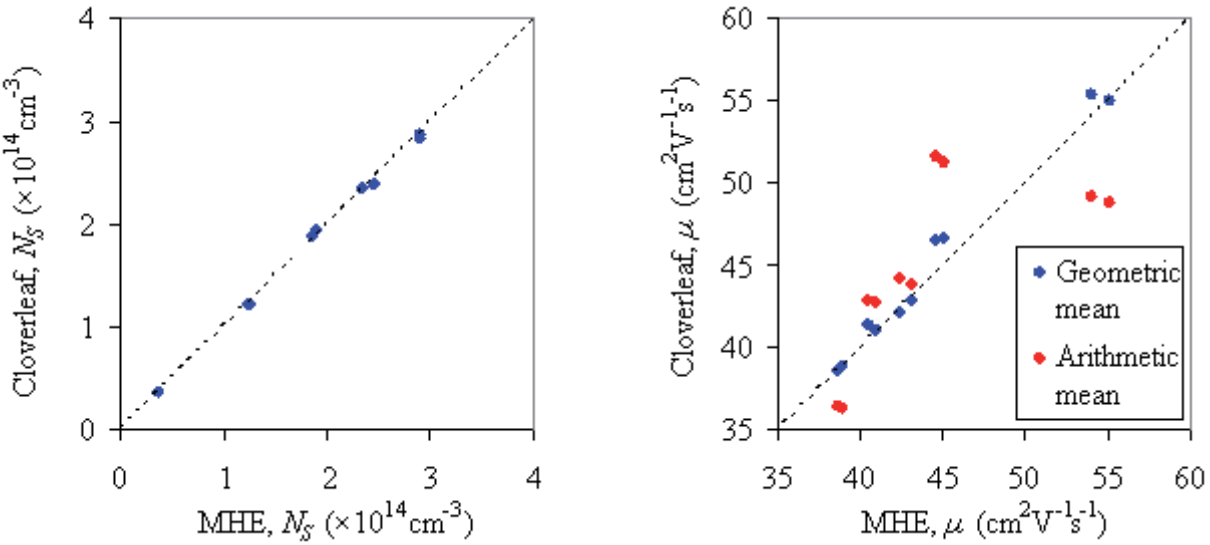

Figure 4.16: Comparison of sheet carrier density (left) and carrier mobility (right) measured with both MHE and cloverleaf method. The method of statistical averaging can be important for calculation of carrier mobility when the measurement uncertainty is high as for cloverleaf measurements. For the highly reproducible MHE measurements it is less important. The ten Si samples were implanted with 1, 3, 5, 7 and 10 ($\times 10^{14}$) atoms/cm^2 0.5keV B and laser annealed with a dwell time of 0.5 ms and 0.3 ms, respectively, and a Hall scattering factor of 0.8 was assumed [XII, XIII].

4.2.5 MHE on small pads

Annealing conditions on patterned wafers may differ much from non-patterned wafers. Thus, it may be interesting to characterize both N_S and μ also on patterned wafers. In Paper VIII we investigate the possibility of performing accurate MHE on small B-implanted laser annealed test pads, cf. Fig. 4.6. Here we employ the F3S and FSS methods for fast characterization with electrode pitch of 20, 30 and 50 µm, and we use an AI (all inclusive) method for reference. The AI method involves: a) R_S line scans with 1.5 µm pitch to determine sample variations, b) Finite Element Method simulations to extract the expected electrostatic potential distribution, c) numeric conformal mapping to determine geometrical effects, and d) scanned MHE measurements with a 20 µm pitch M4PP. For all three methods, we assume a uniform carrier mobility as found in Paper VI (cf. Fig. 4.14). Figure 4.17 combines the theoretical and simulated R_S, R_P and $\Delta R_{BB'}$ fitted to the measurement results.

[13] Using geometrical mean was suggested by Philippe J. Roussel (IMEC) and proved by Frederik W. Østerberg.

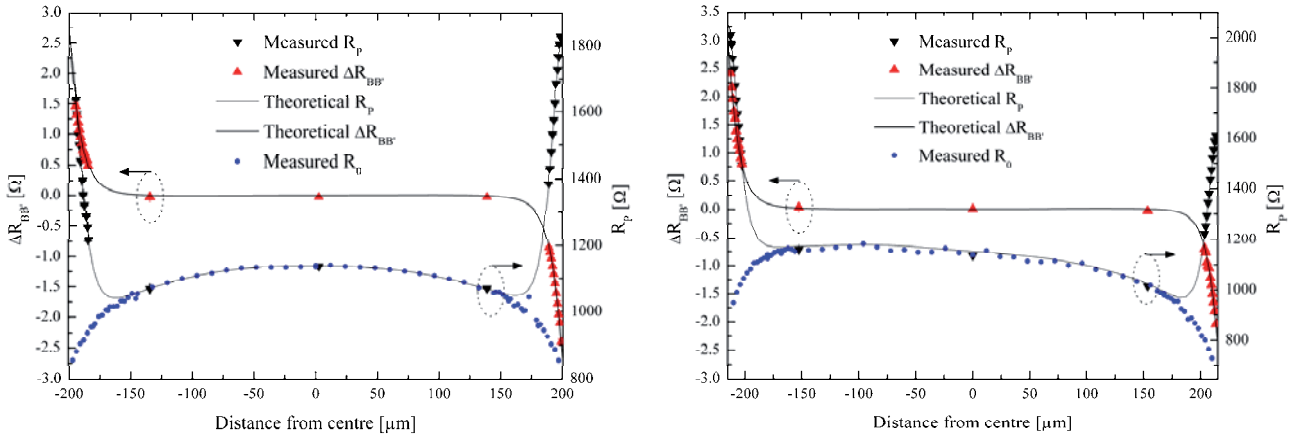

Figure 4.17: MHE (AI method) measurements of a 400×430 µm^2 B doped Si test pad (10^{15} cm^{-2}, 500 eV, laser annealed) surrounded by STI. R_S (blue points) was measured using a 1.5 µm pitch M4PP scanning parallel to the mirror planes of the pad and show a 15-35 % R_S decrease near the pad edges. R_P (black) and $\Delta R_{BB'}$ (red) where measured using 20 µm pitch scanning transverse to the mirror planes. Four Hall mobility values were extracted, one at each boundary of the rectangle giving a mean Hall mobility of μ_H = 32.4 cm^{2}V^{-1}s^{-1} with a relative standard deviation of 1.9%. (left) Reproduced from Paper VIII and (right) courtesy of Frederik W. Østerberg.

Even with huge 15-35 % in R_S variations near the edges of a pad, it is possible with the MHE AI method to perform reproducible extraction of the carrier mobility with a relative standard deviation of <2 % [VIII]. However, in Paper VIII we also show that for these highly inhomogeneous samples, the F3S and FSS methods no longer provide accurate results as shown in Tab. 4.3. For less non-uniform pads (2-5 % variation close to the edges) the F3S and FSS method give reasonable results considering the measurement time of less than a minute.

Table 4.3: Mean Hall mobilities and standard deviations extracted by the AI, F3S and FSS methods. The mean Hall mobilities extracted with the F3S and the FSS methods are averaged from measurements performed with 20, 30 and 50 µm electrode pitch.

R_S near edge	-15 % to -35 % (cm^{2}V^{-1}s^{-1})	2 % to 5 % (cm^{2}V^{-1}s^{-1})
AI	32.4 ±0.6	31.4 ±0.3
F3S	43.2 ±4.5	28.5 ±1.9
FSS	28.3 ±1.6	30.6 ±1.6

The absolute measurement deviation on Hall mobility of the F3S and FSS methods have been verified by a sensitivity study [IX] and FEM assisted Monte Carlo simulations [VIII], respectively. In a contemporary study [iv], another method has been proposed to perform accurate MHE measurements, also on these highly non-uniform small pads and with a measurement time on the order of a minute. However, even with the extensive measurement procedure of the AI method, accurate MHE measurements may be performed in less than 15 minutes, if the method is integrated on a fully automatic system like the CAPRES MicroRSP-A300, which includes pattern recognition and automatic probe changing [41]. It is relevant to realize, that no other technique allows for correct extraction of N_{HS} and μ_H on highly non-uniform small structures with a similar measurement time. Finally, we are currently extending the MHE method to non-uniform pads down to 70×70 µm^2 [x], and a preliminary result is shown in Fig. 4.18. From the preliminary measurements we find an exceptionally good agreement between theory and measurements, with the exception of a couple of outliers of measured $\Delta R_{BB'}$ when approaching zero at the center of the pad. The latter may be a result of the data treatment technique.

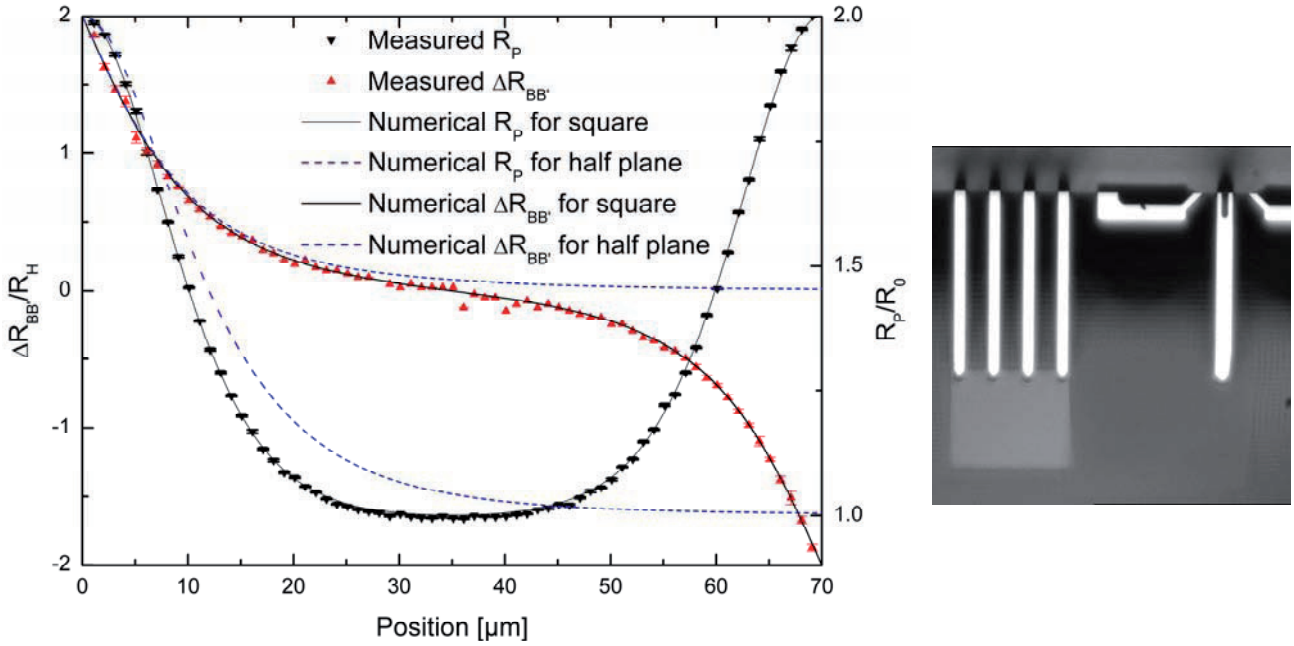

Figure 4.18: (left) First principle MHE measurements of a 70×70 μm^2 pad using the AI method (including 1σ error bars); courtesy of Frederik W. Østerberg. (right) Optical microscope image of a 20 μm pitch M4PP measuring near the edge of the test pad.

Chapter 5

5 Outlook and summary

5.1 Outlook

The focus until now has been solely on USJ characterization and micro-uniformity. However, for future development of CMOS and post-CMOS devices, characterization of materials at smaller length scales may be useful, as well as characterization of different material types such as graphene. This section presents preliminary results from work in progress on prototyping of nano-scale M4PP and electrical characterization of pristine graphene flakes.

5.1.1 M4PP miniaturization

Aggressive M4PP miniaturization may be useful for electrical characterization of bi-layer material properties such as the contact resistivity at silicide/semiconductor interfaces and magnetic tunnel junctions [52, 52], as well as surface conductivity of bulk materials [55]. In Paper XVI we investigated the fundamental size limitations of the M4PP including geometrical, mechanical, thermal and electrical limitations. Here we found, that the minimum electrode pitch of a M4PP is 950 nm, primarily limited by electromigration, probe fracture and sample Joule heating due to contact resistance [XVI]. However, these results are based on the conventional design and materials used for M4PP, as well as requirements to probe lifetime and measurement precision. With the set of equations given in Paper XVI, it may be possible to tune the size limitations by proposing new design methods and using new materials for further miniaturization of M4PP (e.g. Patent iii). That is, the size limitations given in Paper XVI are only fundamental to conventional M4PP design and materials.

Regardless of individual approaches to probe design or choice of materials, a method for rapid prototyping of nanoprobes may be relevant. One possible way to realize nano-scale structures in a variety of different materials is by focused ion beam (FIB) milling [XVII]. For this purpose, a template chip with a membrane extending over the edge of a silicon die has been developed. With a resolution down to approximately 50 nm, it is possible to mill virtually any two dimensional design as illustrated in Fig. 5.1. A FIB prototyping example is given in Fig. 5.2, where a M4PP with 5 µm pitch has been milled. The turn-around time for device prototyping is only 20 minutes, with little or no post processing [XVII, 56]. This must be viewed in relation to several weeks for the design/fabrication process as described in Sect. 3.1 [40*].

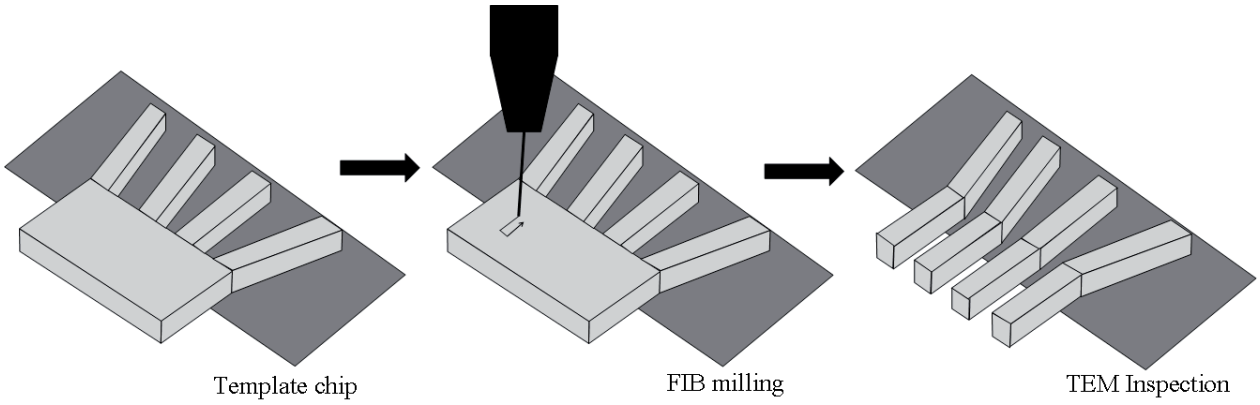

Figure 5.1: Illustration of the FIB assisted nanoprobe prototyping processing. Courtesy of Anders Lei.

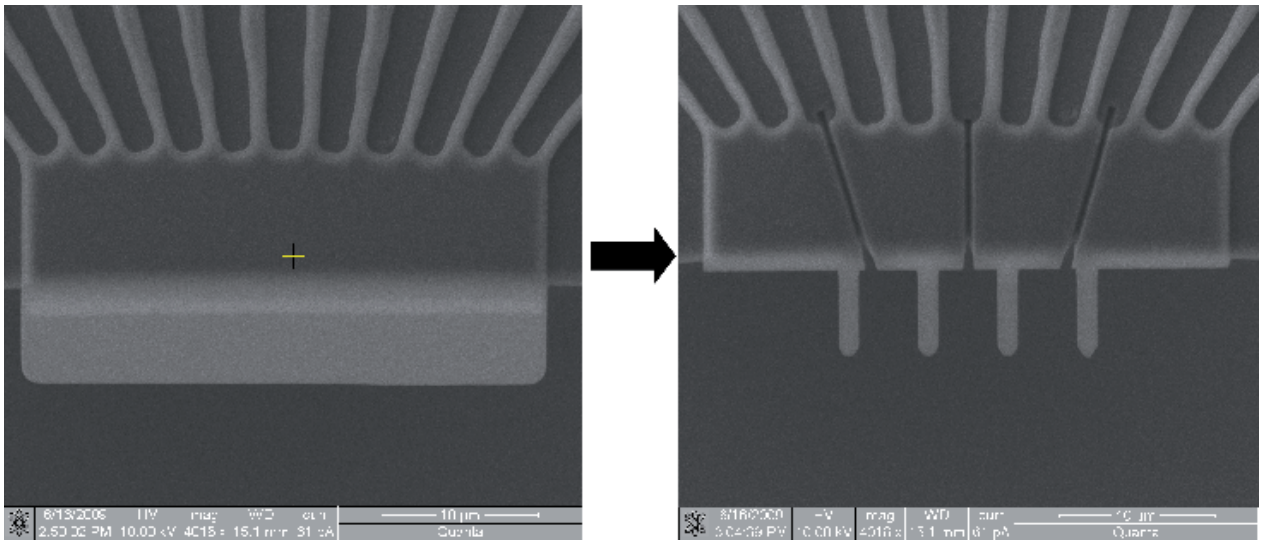

Figure 5.2: Ion beam micrographs of the prototyping of a M4PP with 5µm pitch from a template Si membrane with dimensions 12×35 µm^2. Courtesy of Anders Lei.

5.1.2 Graphene characterization

Graphene have in the recent years attracted much attention for post CMOS devices due to material properties such as a high carrier mobility and thermal conductivity [57]. However, electrical characterization is typically done using lithographically patterned Hall bars. In Paper xi we demonstrate how M4PP can be used for direct characterization of pristine graphene, i.e. no need for e-beam or photo-lithography to define electrode contacts.

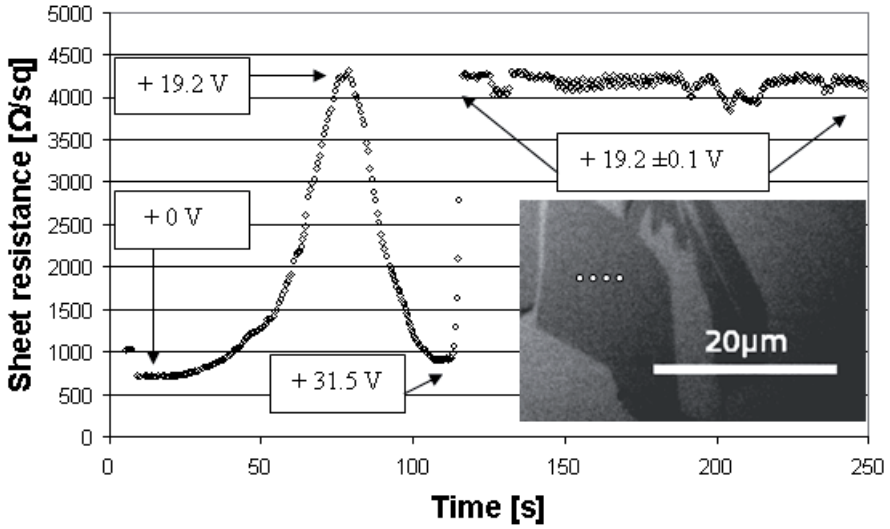

Figure 5.3: Dual configuration sheet resistance measurement of the graphene flake shown in the insert optical microscope image. The graphene flake is positioned on a SiO_2/Si substrate which is used as a gate electrode. The measurement was performed using a M4PP with 1.5 µm pitch and the gate voltage was controlled by a manually adjustable voltage source.

Figure 5.3 shows the first attempt to characterize the Dirac point of graphene using a M4PP. The graphene flake is placed on a low resistivity Si wafer with a 300 nm thick thermal oxide [58]. The Si wafer is used as a gate electrode to change the charge carrier density in the graphene flake [57]. A sheet resistance peak is seen at a Dirac voltage V_D = 19.2 V. The maximum sheet resistance for this measurement is 4314 Ω and the Dirac voltage is stable within ±0.1 V for the four minutes duration of the measurement. Although the first experiment was promising, reproducibility and temporal variations has continued to be a problem in following experiments. For instance, on a different graphene flake (on the same wafer) the maximum resistance was found to be 4122 Ω at V_D = 11.2 V. In principle it should be possible to perform sheet resistance and MHE measurements on virtually any flake geometry by transforming a microscope image into a polygon and applying numerical conformal mapping as for the MHE AI method [VIII, x].

5.2 Summary

The main intension of this work has been to develop and evaluate the M4PP sheet resistance and MHE techniques for characterization of USJ. The work has been focused on development of micro-probes and methods to produce these, new methods for electrical characterization, and data treatment methods to improve reliability and accuracy.

Three major improvements to the M4PP design have been developed. 1) The lifetime of M4PP has been improved by more than one order of magnitude by using Si cantilevers with Ni as electrode material (prior state-of-the-art was SiO_2 and Au). A simple strain gauge surface detection method has been implemented [i], which has shown 100 % reliability in $>10^6$ surface engages. And finally, a vibration tolerant cantilever design [33*, XV] has been shown to significantly improve measurement precision at high acoustic noise levels where conventional straight cantilevers do not perform well.

For sheet resistance measurements, a data treatment method for accurate and reliable characterization of USJ has been presented. The data treatment is based on a careful analysis of the

electrical contacts positions during measurements. Whereas static position errors are eliminated by use of the dual configuration technique [24], dynamic position errors (i.e. contact movements between four-point resistance measurements) and non-reliable resistance measurements are eliminated by phase filter, median filter and minimum number of accepted temporary R_{ST} values filter.

Additionally, a Hall Effect characterization technique has been developed for M4PP [V]. The Micro Hall Effect (MHE) technique differs from conventional Hall Effect measurements as the electrical contacts are deliberately positioned within the sample region and not on the sample edge. A method to eliminate all first order position errors has been proposed, and two position error suppression methods are proposed (F3S and FSS) [VI, VIII], that rely on the use of van der Pauw like corrections in proximity of a barrier for determining the electrode positions within the sample.

Through sensitivity studies, the R_S and MHE measurement techniques are evaluated for characterization of non-uniform samples. For a sample with periodic variations, spatial frequency transfer functions are calculated from one-dimensional sensitivities [X]. The spatial frequency transfer function for R_S is verified by detailed characterization of periodic R_S variations with spatial wavelengths of 0.75 and 3.65 mm using electrode pitch in the range 1.5 μm to 500 μm [II]. For characterization of periodic variations with an amplitude of 10 %, an maximum electrode pitch of $\lambda/40$ of the spatial wavelength λ is found necessary, in order to characterize the amplitude of periodic variations with 99% accuracy, giving a measurement error of 0.1%. For MHE measurements a maximum pitch $s = \lambda/12$ is found to result in a measurement error of 1 %.

In reproducibility and repeatability studies on uniform USJ samples, both measurement reproducibility and repeatability of <0.1% and <1% are found for M4PP sheet resistance [III] and MHE [V, VI], respectively. For a non-uniform sample with periodic sheet resistance variations at spatial wavelengths of 0.5 mm and 0.75 mm with <8% peak-to-peak amplitude, a repeatability of 1.3% on carrier mobility was found for the MHE F3S method [VI]. The latter study also suggests that the source of sheet resistance variations is not variations in carrier mobility, but rather variations in activation degree (i.e. sheet carrier density) [VI].

For small test pads with dimensions similar to the M4PP, the “sweet spot” for square, rectangular and circular geometries is determined, where correction-free dual configuration sheet resistance measurements may be performed with an error of less than 0.1 %. In a study of shallow trench isolation (STI) pattern effects in laser annealing, sheet resistance mapping of 400×430 μm^2 test pads indicates peak temperature variations up to 40°C during the laser anneal [XI]. Furthermore, sheet resistance characterization of square test pads with dimensions down to 10×10 μm^2 indicates pattern density induced peak temperature variations up to 120°C during the laser anneal [XI]. It has been shown that although applying an optical absorber layer prior to laser annealing does reduce pattern effects, they are not completely eliminated.

MHE characterization of square test pads down to 70×70 μm^2 was also successfully performed with a standard deviation of <2% in repeatability; even with within pad sheet resistance variations of 15% to 35% [VIII, x]. This was achieved by application of numeric conformal mapping and finite element method simulations. However, the F3S and FSS methods do not work well for such highly non-uniform samples, where a static measurement error on the order of 33% and -13% was observed for the two methods, respectively. For less non-uniform pads these two methods are much more reliable and both have a measurement time of less than minute [VI, VIII, x].

In comparative studies, M4PP sheet resistance and MHE outperform both conventional four-point probe and van der Pauw measurements as well as optical measurement techniques in terms of reliability on state-of-the-art USJ [I, XII-XIII, v]. Thus, the M4PP sheet resistance and MHE methods currently appear to be the best suited characterization techniques available for evaluation of sheet resistance, sheet carrier density and carrier mobility of USJ.

Supplementary, the high spatial resolution of M4PP has been applied for carrier profiling of USJ, for which it has shown an exceptional potential over the conventional spreading resistance probe [XIV]. And finally, M4PP sheet resistance and MHE characterization of post CMOS materials such as highly doped InGaAs [VII] and Ge [V, XIV] has been demonstrated as well as sheet resistance measurements of gated graphene [xi].

6 Bibliography

6.1 List of papers reprinted as appendices

[I] D.H. Petersen, O. Hansen, T.M. Hansen, P. Bøggild, R. Lin, D. Kjær, P.F. Nielsen, T. Clarysse, W. Vandervorst, E. Rosseel, N.S. Bennett, N.E.B. Cowern, *Review of electrical characterization of ultra-shallow junctions with micro four-point probes*, J. Vac. Sci. Technol. B **28**, C1C27-C1C33 (2010).

[II] D.H. Petersen, R. Lin, T.M. Hansen, E. Rosseel, W. Vandervorst, C. Markvardsen, D. Kjær, P.F. Nielsen, *Comparative study of size dependent four-point probe sheet resistance measurement on laser annealed ultra-shallow junctions*, J. Vac. Sci. Technol. B **26**, 362-367 (2008).

[III] D. Kjaer, R. Lin, D.H. Petersen, P.M. Kopalidis, R. Eddy, D.A. Walker, W.F. Egelhoff, and L. Pickert, *Micro Four-Point Probe with High Spatial Resolution for Ion Implantation and Ultra Shallow Junction Characterization*, AIP Conf. Proc. **1066**, 167-170 (2008). DOI:10.1063/1.3033583

[IV] S. Thorsteinsson, F. Wang, D.H. Petersen, T.M. Hansen, D. Kjær, R. Lin, J.-Y. Kim, P.F. Nielsen, and O. Hansen, *Accurate microfour-point probe sheet resistance measurements on small samples*, Rev. Sci. Instrum. **80**, 053902 (2009).

[V] D.H. Petersen, O. Hansen, R. Lin, and P.F. Nielsen, *Micro-four-point probe Hall effect measurement method*, J. Appl. Phys. **104**, 013710 (2008).

[VI] D.H. Petersen, O. Hansen, R. Lin, P.F. Nielsen, T. Clarysse, J. Goossens, E. Rosseel, and W. Vandervorst, *High precision micro-scale Hall Effect characterization method using in-line micro four point probes*, Proceedings of the 16th IEEE International Conference on Advanced Thermal Processing of Semiconductors, RTP 2008 (IEEE, New York, 2008) pp. 251-256.

[VII] D.H. Petersen, O. Hansen, P. Bøggild, R. Lin, P.F. Nielsen, D. Lin, C. Adelmann, A. Alian, C. Merckling, J. Penaud, G. Brammertz, J. Goossens, W. Vandervorst, T. Clarysse, *Electrical characterization of InGaAs ultra-shallow junctions*, J. Vac. Sci. Technol. B **28**, C1C41-C1C47 (2010).

[VIII] F.W. Osterberg, D.H. Petersen, F. Wang, E. Rosseel, W. Vandervorst, and O. Hansen, *Accurate micro Hall Effect measurements on scribe line pads*, Proceedings of the 17th IEEE International Conference on Advanced Thermal Processing of Semiconductors, RTP 2009 (IEEE, New York, 2009) pp. 157-162.

[IX] F. Wang, D.H. Petersen, T.M. Hansen, T.R. Henriksen, P. Bøggild, O. Hansen, *Sensitivity study of micro four-point probe measurements on small samples*, J. Vac. Sci. Technol. B **28**, C1C34-C1C40 (2010).

[X] F. Wang, D.H. Petersen, F.W. Osterberg, and O. Hansen, *Accuracy of Micro Four-Point Probe Measurements on Inhomogeneous Samples: A Probe Spacing Dependence Study*, Proceedings of the 17th IEEE International Conference on Advanced Thermal Processing of Semiconductors, RTP 2009 (IEEE, New York, 2009) pp.151-156.

[XI] E. Rosseel, D.H. Petersen, F.W. Osterberg, O. Hansen, J. Bogdanowicz, T. Clarysse, W. Vandervorst, C. Ortolland, T. Hoffmann, P. Chan, A. Salnik, and L. Nicolaides, *Monitoring of local and global temperature non-uniformities by means of Therma-Probe and Micro Four-Point Probe metrology*, Proceedings of the 17th IEEE International Conference on Advanced Thermal Processing of Semiconductors, RTP 2009 (IEEE, New York, 2009) pp. 129-134.

[XII] T. Clarysse, J. Bogdanowicz, J. Goossens, A. Moussa, E. Rosseel, W. Vandervorst, D.H. Petersen, R. Lin, P.F. Nielsen, O. Hansen, G. Merklin, N.S. Bennett, and N.E.B. Cowern, *On the analysis of the activation mechanisms of sub-melt laser anneals*, Mater. Sci. and Eng. B **154**, 24 (2008).

[XIII] E. Rosseel, W. Vandervorst, T. Clarysse, J. Goossens, A. Moussa, R. Lin, D.H. Petersen, P.F. Nielsen, O. Hansen, N.S. Bennett, and N.E.B. Cowern, *Impact of multiple sub-melt laser scans on the activation and diffusion of shallow Boron junctions*, Proceedings of the 16th IEEE International Conference on Advanced Thermal Processing of Semiconductors, RTP 2008 (IEEE, New York, 2008) pp.135-140.

[XIV] T. Clarysse, P. Eyben, B. Parmentier, B. Van Daele, A. Satta, W. Vandervorst, R. Lin, D.H. Petersen, and P.F. Nielsen, *Advanced carrier depth profiling on Si and Ge with micro four-point probe*, J. Vac. Sci. Technol. B **26**, 317-321 (2008).

[XV] D.H. Petersen, O. Hansen, T.M. Hansen, P.R.E. Petersen, and P. Bøggild, Static contact micro four-point probes with <11 nm positioning repeatability, Microelectron. Eng. **85**, 1092-1095 (2008).

[XVI] T. Ansbæk, D.H. Petersen, O. Hansen, J.B. Larsen, T.M. Hansen, and P. Bøggild, *Fundamental size limitations of micro four-point probes*, Microelectron. Eng. **86**, 987–990 (2009).

[XVII] A. Lei, D.H. Petersen, T. Booth, A.N. MacDonald, Ö.S. Sukas, Y. Gyrsting, C. Kallesøe, P. Bøggild, *Customizable in situ TEM devices fabricated in freestanding membranes by focused ion beam milling*, Nanotechnology **21** (40), 405304 (2010).

6.2 Publications not reprinted in this thesis[14]

[i] D.H. Petersen and R. Lin, *Device including a contact detector*, WIPO Patent Application WO/2008/110174-A1, 12/3-2007. Description: A four-point probe with integrated strain gauge sensor for fast and accurate surface detection. http://www.freepatentsonline.com/WO2008110174A1.html

[ii] D.H. Petersen and O. Hansen, *A method of determining an electrical property of a test sample*, WIPO Patent Application WO/2009/030230-A1, 3/9-2008. Description: The patent includes a theoretical model for performing accurate Hall Effect measurements with electrode contacts placed inside a test area.
http://www.freepatentsonline.com/WO2009030230A1.html

[iii] D.H. Petersen, *A multi-point probe for testing electrical properties and a method of producing a multi-point probe*, European Patent Application EP08388023, 30/6-2009. Description: An asymmetric four-point probe design and a method for improving surface sensitivity of sub-micrometer pitch four-point probes.
http://www.freepatentsonline.com/EP2141503.html

[iv] F. Wang, D.H. Petersen and O. Hansen, *A Method for Measurement of Electrical Transport Properties of Thin Samples*, European Patent Application EP10196137, 21/12-2010. Description: Invention regarding error suppression in micro Hall effect measurements.

[v] T. Clarysse, A. Moussa, B. Parmentier, J. Bogdanowicz, W. Vandervorst, H. Bender, M. Pfeffer, M. Schellenberger, P.F. Nielsen, S. Thorsteinsson, R. Lin, D.H. Petersen, *Photo-voltage versus micro-probe sheet resistance measurements on ultra-shallow structures*, J. Vac. Sci. Technol. B **28**, C1C8-C1C14 (2010).

[vi] E. Rosseel, J. Bogdanowicz, T. Clarysse, W. Vandervorst, C. Ortolland and T. Hoffmann, A. Salnik, L. Nicolaides, S.-H. Han, D.H. Petersen, R. Lin and O. Hansen, *Study of submelt laser induced junction nonuniformities by means of Therma-Probe*, J. Vac. Sci. Technol. B. **28**, C1C21-C1C26 (2010).

[vii] W. Vandervorst, E. Rosseel, R. Lin, D.H. Petersen, T. Clarysse, J. Goossens, P.F. Nielsen, and K. Churton, *Micro-uniformity during laser anneal : metrology and physics*, Mater. Res. Soc. Symp. Proc. **1070**, 1070-E01-10 (Warrendale, PA, 2008).

[viii] L. Vanamurthy, M. Huang, H. Bakrhu, T. Furukawa, N. Berliner, J. Herman, Z. Zhu, P. Ronsheim, B. Doris, M. Li, P. Banks, D.H. Petersen, J.K. Christensen, and P.F. Nielsen, *Measurement of dopant activation and defects in sub 1 keV B dopes samples using Ion beam channeling*, INSIGHT 2009, San-Francisco, US, 251 (2009).

[ix] K. Huet, R. Lin, C. Boniface, F. Desse, D.H. Petersen, O. Hansen, N. Variam, A. La Magna, M. Schuhmacher, A. Jensen, P.F. Nielsen, H. Besaucele, and J. Venturini, *Activation of ion implanted Si for backside processing by Ultra-fast Laser Thermal Annealing: Energy homogeneity and micro-scale sheet resistance*, Proceedings of the 17th IEEE International Conference on Advanced Thermal Processing of Semiconductors, RTP 2009 (IEEE, New York, 2009) pp. 105-108.

[14] Patents, peer-reviewed papers and conference proceedings. Conference abstracts without proceeding are not included.

[x] F.W. Osterberg, D.H. Petersen, P.F. Nielsen, E. Rosseel, W. Vandervorst, and O. Hansen, *Fast micro Hall effect measurements on small pads*, J. Appl. Phys. **110**, 033707 (2011).

[xi] M.B. Klarskov, H.F. Dam, D.H. Petersen, T.M. Hansen, A. Löwenborg, T.J. Booth., M.S. Schmidt, R. Lin, P.F. Nielsen, and P. Bøggild, *Fast and direct measurements of the electrical properties of graphene using micro four-point probes*, Nanotechnology **22** (44), 445702 (2011).

[xii] K. Carlson, K.N. Andersen, V. Eichhorn, D.H. Petersen, K. Mølhave, I.Y.Y. Bu, K.B.K. Teo, W.I. Milne, S. Fatikow, and P. Bøggild, *A carbon nanofibre scanning probe assembled using an electrothermal microgripper*, Nanotechnology **18**, 345501 (2007).

[xiii] K.N. Andersen, K. Carlson, D.H. Petersen, K. Mølhave, V. Eichhorn, S. Fatikow, and P. Bøggild, *Electrothermal microgrippers for pick-and-place operations*, Microelectron. Eng. **85**, 1128-1130 (2008).

[xiv] K.N. Andersen, D.H. Petersen, K. Carlson, K. Mølhave, O. Sardan, A. Horsewell, V. Eichhorn, S. Fatikow, and P. Bøggild, *Multimodal Electrothermal Silicon Microgrippers for Nanotube Manipulation*, IEEE Transactions on Nanotechnology **8** (1), 76-85 (2009).

[xv] O. Sardan, D.H. Petersen, O. Sigmund and P. Bøggild, *Simulation of Topology Optimized Electrothermal Microgrippers*, Proceedings of 2008 Comsol Conference, (Hannover, Germany, 2008).

[xvi] O. Sardan, D.H. Petersen, K. Mølhave, O. Sigmund and P. Bøggild, *Topology optimized electrothermal polysilicon microgrippers*, Microelectron. Eng. **85**, 1096-1099 (2008).

[xvii] O. Sardan, V. Eichhorn, D.H. Petersen, S. Fatikow, O. Sigmund and P. Bøggild, *Topology optimized microgrippers for nanomanipulation of carbon nanotubes*, ASME Conf. Proc. 2008, pp. 799-801 (2008). DOI:10.1115/DETC2008-49540

[xviii] O. Sardan, V. Eichhorn, D.H. Petersen, S. Fatikow, O. Sigmund and P. Bøggild, *Rapid prototyping of nanotube-based devices using topology-optimized microgrippers*, Nanotechnology **19** (49), 495503 (2008).

[xix] A. Cagliani, R. Wierzbicki, L. Occhipinti, D.H. Petersen, K.N. Dyvelkov, Ö.S. Sukas, B.G. Herstrøm, T. Booth and P. Bøggild, *Manipulation and in-situ transmission electron microscope characterisation of sub-100 nm nanostructures using microfabricated nanogripper*, J. Micromech. Microeng., in review.

[xx] Z. Davis, J. Hales, D.H. Petersen, and R.H. Pedersen, Nanofabrikationens værktøjskasse, Nanoteknologiske Horisonter (in Danish), 112-127 (2008).

[xxi] K. Mølhave, B.A. Wacaser, D.H. Petersen, J.B. Wagner, L. Samuelson, and P. Bøggild, *Epitaxial integration of nanowires in microsystems by local micrometer-scale vapor-phase epitaxy*, Small **4** (10), 1741-1746 (2008).

6.3 List of references

[1] A. Uhlir, Jr., Bell Syst. Tech. J. **34**, 105 (1955).

[2] F.M. Smits, Bell Syst. Tech. J. **37**, 711 (1958).

[3] L.J. van der Pauw, Philips Res. Rep. **13**, 1 (1958).

[4] L.J. van der Pauw, Philips Tech. Rev. **20**, 220 (1958).

[5] E.H. Hall, Am. J. Math. **2**, 287 (1879).

[6] R.S. Popović, *Hall Effect Devices, Magnetic Sensors and Characterization of Semiconductors*, The Adam Hilger Series on Sensors (Adam Hilger, Bristol, 1991).

[7] D.S. Perloff, J. Electrochem. Soc. **123**, 1745 (1976).

[8] D.S. Perloff, J. Electrochem. Soc. **124**, 582 (1977).

[9] J. Opsal, *"Modulated Interference Effects and Thermal Wave Monitoring of high-dose Implantation in Semiconductors" in Review of Progress in Quantitative Non-destructive Evaluation*, edited by D.O. Thompson and D.E. Chimenti (New York: Plenum 1989, 8B), pp. 1241-1245.

[10] M.I. Current and J.O. Borland, *Proceedings of the 16th IEEE International Conference on Advanced Thermal Processing of Semiconductors, RTP 2008* (IEEE, New York, 2008), pp. 43-55.

[11] L. J. Swartzendruber, Solid-State Electron. **7**, 413 (1964).

[12] M.I. Current, N. Ohno, K. Hurley, W.A. Keenan, T.L. Guitner, and C. Jeynes, Solid State Technol. **36**, 111 (1993).

[13] M.I. Current, T. Guitner, N. Ohno, K. Hurley, W.A. Keenan, W. Johnson, R.J. Hillard, and C. Jeynes, Nucl. Instr. and Meth. in Phys. Res. B **55**, 173 (1991).

[14] A.C. Diebold, *In-Line Metrology, Handbook of Semiconductor Manufacturing Technology, Second Edition*, edited by R. Doering and Y. Nishi (CRC Press, Boca Raton, FL, 2007).

[15] T. Sugii, Solid-State Electron. **50**, 2 (2006).

[16] T. Clarysse, P. Eyben, T. Hantschel, and W. Vandervorst, Mater. Sci. Semicond. Process. **4**, 61 (2001).

[17*] T. Clarysse, A. Moussa, F. Leys, R. Loo, W. Vandervorst, M.C. Benjamin, R.J. Hillard, V.N. Faifer, M.I. Current, R. Lin, and D.H. Petersen, Mater. Res. Soc. Symp. Proc. **912**, 197 (2006).

[18] R.J. Hillard, R.G. Mazur, C.W. Ye, M.C. Benjamin, and J.O. Borland, Solid State Technol. **47**, 47 (2004).

[19*] C.L. Petersen, R. Lin, D.H. Petersen, and P.F. Nielsen, Proceedings of the 14th IEEE International Conference on Advanced Thermal Processing of Semiconductors, RTP 2006 (IEEE, New York, 2006) pp. 153-158.

[20] A. Salnik, D. Shaughnessy, and L. Nicolaides, IEEE/SEMI Advanced semiconductor manufacturing conference (Cambridge, MA-USA, 2008), pp. 404.

[21] V.N. Faifer, M.I. Current, T.M.H. Wong, and V. V. Souchkov, J. Vac. Sci. Technol. B **24**, 414 (2006).

[22] W. Vandervorst, AIP Conf. Proc. **931**, 233 (2007)

[23*] T. Clarysse, W. Vandervorst, R. Lin, D.H. Petersen, and P.F. Nielsen, Nucl. Instr. and Meth. in Phys. Res. B **253**, 136 (2006).

[24] R. Rymaszewski, J. Phys. E: J. Sci. Instrum. **2**, 170 (1969).

[25] L.B. Valdes, Proc. IRE **42**, 420 (1954).

[26] D.W. Koon and C.J. Knickerbocker, Rev. Sci. Instrum. **63**, 207 (1992).

[27] D.W. Koon and Winston K. Chan, Rev. Sci. Instrum. **69**, 4218 (1998).

[28] L.K.J. Vandamme and W.M.G. van Bokhoven, Appl. Phys. **14**, 205 (1977).

[29] L.K.J. Vandamme and G. Leroy, Fluct. Noise Lett. **6**, L161 (2006).

[30] D.W. Koon, Rev. Sci. Instrum. **77**, 094703 (2006).

[31] K. Seeger, *Semiconductor Physics, An Introduction, Solid-State Sciences* No. 40, 5th ed. (Springer, Berlin, 1991)

[32] D.W. Koon and C.J. Knickerbocker, Rev. Sci. Instrum. **64**, 510 (1993).

[33*] D.H. Petersen, T.M. Hansen, and P.R.E. Petersen, A probe for testing electrical properties of a test sample, WIPO Patent Application WO/2007/051471-A1, 31/10-2005. http://www.freepatentsonline.com/WO2007051471A1.html

[34] C.L. Petersen, T.M. Hansen, P. Bøggild, A. Boisen, O. Hansen, T. Hassenkam, and F. Grey, Sens. Actuators A **96**, 53 (2002).

[35] A. Choudhury, and P.J. Hesketh, *2003 Nanotechnology Conference and Trade Show - Nanotech 2003*, pp. 542-545.

[36] B.-F. Ju, Y. Ju and M. Saka, J. Micromech. Microeng. **15**, 2277 (2005).

[37] S. Keller, S. Mouaziz, G. Boero, and J. Brugger, Rev. Sci. Instrum. **76**, 125102 (2005).

[38] L. Gammelgaard, P. Bøggild, J.W. Wells, K. Handrup, P. Hofmann, M.B. Balslev, J.E. Hansen, and P.R.E. Petersen, Appl. Phys. Lett. **93**, 093104 (2008).

[39] J.-K. Kim, Y. Zhang, and D.-W. Lee, *2009 IEEE 22nd International Conference on Micro Electro Mechanical Systems - MEMS 2009*, pp. 84-87.

[40*] D. H. Petersen, *High aspect ratio silicon beam fabrication and large scale nanowire integration*, in Proc. MIC, Technical University of Denmark (2006).

[41] Capres A/S, URL: http://www.capres.com.

[42] N. Weiss, U. Drechsler, M. Despont, and S.S.P. Parkin, Rev. Sci. Instrum. **79**, 123902 (2008).

[43] G. Binnig, C.F. Quate and C. Gerber, Phys. Rev. Lett. **56**, 930 (1986).

[44] R. Erlandsson, G.M. McClelland, C.M. Mate, and S. Chiang, J. Vac. Sci. Technol. A **6**, 266 (1988).

[45] G. Meyer, and N.M. Amer, Appl. Phys. Lett. **53**, 1045 (1988).

[46] J.W. Wells, K. Handrup, J.F. Kallehauge, L. Gammelgaard, P. Bøggild, M.B. Balslev, J.E. Hansen, P.R.E. Petersen, and P. Hofmann, J. Appl. Phys. **104**, 053717 (2008).

[47] T.M. Hansen, K. Stokbro, O. Hansen, T. Hassenkam, I. Shiraki, S. Hasegawa, and P. Bøggild, Rev. Sci. Instrum. **74**, 3701 (2003).

[48] P. Bøggild, T.M. Hansen, O. Kuhn, F. Grey, T. Junno, L. Montelius, Rev. Sci. Instrum., **71**, 2781-2783 (2000).

[49] R.L. Parker and A. Krinsky, J. Appl. Phys. **34**, 2700 (1963).

[50] M. Tortonese, R.C. Barrett, and C.F. Quate, Appl. Phys. Lett. **62**, 834-836 (1993).

[51] S.P Timoshenko, *Theory of Elasticity*, Third Edition (McGraw-Hill, 1970).

[52] D.C. Worledge, P.L. Trouilloud, Appl. Phys. Lett. **83**, 84 (2003).

[52] D.W. Abraham, P.L. Trouilloud, and D.C. Worledge, IBM J. Res. Dev. **50**, 55 (2006).

[53] B. Bhushan, *Springer Handbook of Nanotechnology* (Springer-Verlag, Berlin Heidelberg, 2004).

[54] C. Ortolland, T. Noda, T. Chiarella, S. Kubicek, C. Kerner, W. Vandervorst, A. Opdebeeck, C. Vrancken, N. Horiguchi, M. De Potter, M. Aoulaiche, E. Rosseel, S.B. Felch, P. Absil, R. Schreutelkamp, S. Biesemans, and T. Hoffmann, *2008 IEEE Symposium on VLSI Technology*, pp. 186.

[55] P. Hofmann and J.W. Wells, J. Phys.: Condens. Matter **21** 013003 (2009).

[56] *Focused Ion Beam Shaped Nanotools*, in Proc. DTU Nanotech, Technical University of Denmark (2009).

[57] A.K. Geim and K.S. Novoselov, Nat. Mat. **6**, 183 (2007).

[58] Graphene Industries, URL: http://grapheneindustries.com.

Paper I

J. Vac. Sci. Technol. B **28**, C1C27-C1C33 (2010).

PhD students contribution:

Idea and manuscript writing with only minor revision from co-authors except O. Hansen who prepared Figs. 2 and 7.

Co-authors contribution:

Co-authors contributed with supporting discussions; especially on material limitations, comparison between cloverleaf and MHE, and carrier profiling.

Review of electrical characterization of ultra-shallow junctions with micro four-point probes

Dirch H. Petersen[a)]
Department of Micro- and Nanotechnology, Technical University of Denmark, DTU Nanotech, Building 345 East, DK-2800 Kgs. Lyngby, Denmark; CAPRES A/S, Scion-DTU, Building 373, DK-2800 Kgs. Lyngby, Denmark; and IMEC, Kapeldreef 75, B-3001 Leuven, Belgium

Ole Hansen
Department of Micro- and Nanotechnology, Technical University of Denmark, DTU Nanotech, Building 345 East, DK-2800 Kgs. Lyngby, Denmark and Centre for Individual Nanoparticle Functionality (CINF), Technical University of Denmark, Building 345 East, DK-2800 Kgs. Lyngby, Denmark

Torben M. Hansen and Peter Bøggild
Department of Micro- and Nanotechnology, Technical University of Denmark, DTU Nanotech, Building 345 East, DK-2800 Kgs. Lyngby, Denmark

Rong Lin, Daniel Kjær, and Peter F. Nielsen
CAPRES A/S, Scion-DTU, Building 373, DK-2800 Kgs. Lyngby, Denmark

Trudo Clarysse
IMEC, Kapeldreef 75, B-3001 Leuven, Belgium

Wilfried Vandervorst
IMEC, Kapeldreef 75, B-3001 Leuven, Belgium and Institute of voor Kern-en Stralingsfysica, K. U. Leuven, Celestijnenlaan 200D B-3001 Leuven, Belgium

Erik Rosseel
IMEC, Kapeldreef 75, B-3001 Leuven, Belgium

Nick S. Bennett and Nick E. B. Cowern
School of Electrical, Electronic and Computer Engineering, Newcastle University, Newcastle upon Tyne NE1 7RU, United Kingdom

(Received 11 June 2009; accepted 10 August 2009; published 1 March 2010)

Electrical characterization of ultra-shallow junctions, relying on advanced implant and anneal processes, has received much attention in the past few years since conventional characterization methods fail. With continued scaling of semiconductor devices, the problems associated with conventional techniques will become even more evident. In several recent studies micro four-point probe (M4PP) has been demonstrated as a reliable high precision metrology method for both sheet resistance and Hall effect measurements of ultra-shallow implants and has revealed a promising potential for carrier profiling. © *2010 American Vacuum Society.* [DOI: 10.1116/1.3224898]

I. INTRODUCTION

Accurate electrical characterization of surface materials such as ultra-shallow junctions (USJs) is critical for continued process development, qualification, and monitoring. Conventional four-point probes,[1,2] van der Pauw measurements,[3,4] and spreading resistance probe[5] (SRP) have for several decades been the metrologies of choice for characterization of sheet resistance, mobility, carrier density, and carrier profiling. However, these techniques lack the necessary spatial resolution, accuracy, and reliability on USJ,[6–12] thus providing inadequate or even false results when used with advanced nanoscale structures.

Since the development of the micro four-point probe (M4PP) by C. L. Petersen *et al.* in 1999,[13] it has mainly been used for characterization of magnetic tunnel junctions (MTJs) via the current-in-plane tunneling method,[14] and is now an important metrology tool for development of MTJ devices such as hard disk read heads and magnetic random access memory.[15] In 2005, a measurement technique was developed at CAPRES[16] allowing for characterization of USJ with unsurpassed combination of resolution and accuracy.[6,17] The method was in 2006 extended to carrier profiling by Clarysse *et al.*[18] and in 2007 a new Hall effect method was developed by D. H. Petersen and Hansen allowing for high precision and very fast characterization of sheet carrier density and mobility with minimal sample preparation.[19,20]

In this review, we present the advances of three measurement techniques utilizing M4PP as the primary tool for USJ characterization. We address both measurement accuracy and limitations of the different measurement techniques and present state-of-art M4PP with integrated strain gauge sensor for reliable surface detection.

II. MICRO FOUR-POINT PROBES

M4PP measurements on ultra-shallow junctions are performed using a CAPRES microRSP-M150 system.[16] The

[a)]Electronic mail: dhpe@nanotech.dtu.dk

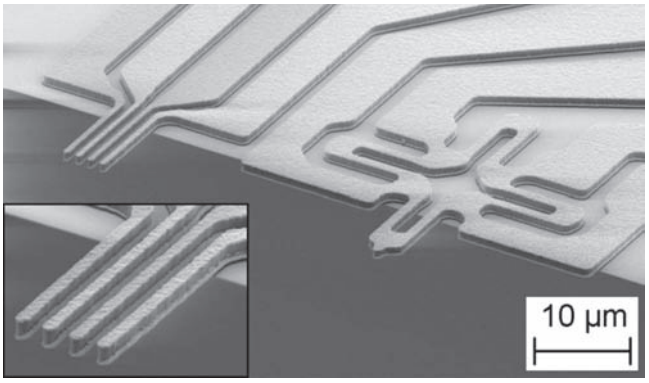

FIG. 1. Micrograph of a M4PP with integrated strain gauge sensor. The insert shows a magnified image of the four cantilevers with an electrode pitch of 1.5 μm.

M4PP consists of metal coated cantilevers extending from the edge of a support die. The four cantilever electrodes are brought into contact with the sample using a linear motor with a resolution of ± 5 nm. The M4PP is engaged on the surface and retracted between each measurement position, and four-point resistance is measured using lock-in technique.

A. Surface detection

Surface detection is an important issue for automated M4PP measurements and can be done by electrical or force detection. In electrical detection, the two-point resistance between two electrodes is measured continuously until a resistance drop is detected upon surface contact. The electrical detection is only reliable on highly conductive surfaces and does not work consistently on semiconductor surfaces. Whereas optical detection is difficult because of the small cantilever dimensions, an integrated strain gauge sensor allows for reliable surface detection on both conductive and nonconductive materials and is easily integrated with the electronics necessary for four-point measurements.

Figure 1 shows a M4PP with an electrode pitch of 1.5 μm, used for carrier profiling. The strain gauge sensor is integrated in a Wheatstone bridge configuration and surface detection repeatability better than 50 nm is achievable. However, the absolute contact force is dominated by probe-to-surface misalignment and the distance between the sensor and the four cantilever electrodes.

B. Probe dimensions

The cantilever dimensions are designed for a vertical spring constant of 1–100 N/m depending on the required contact force. For measurement on silicon USJ, a contact force of 10–100 μN has been found empirically to be desirable when using Ni as the electrode material. For comparison, conventional four-point probes use a contact force on the order of 1 N. The choice of electrode pitch depends on the specific measurement purpose; the pitch achieved with cantilever electrodes ranges from 0.9 μm (Ref. 21) to 500 μm,[6] for which the latter is obtained using high aspect ratio L-shaped cantilever geometry[22] as opposed to the straight cantilevers. The minimum achievable electrode pitch is dependent on measurement requirements and is discussed in detail by Ansbæk.[21]

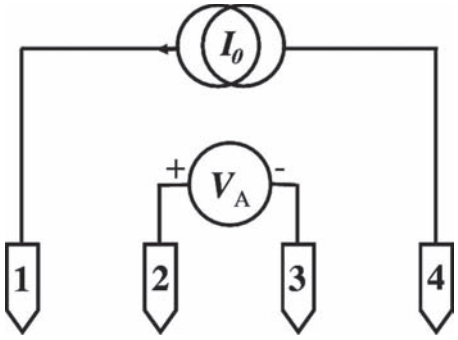

FIG. 2. *A* configuration. The four probe pins (Nos. 1–4) have position vectors $\mathbf{r}_1$, $\mathbf{r}_2$, $\mathbf{r}_3$, and $\mathbf{r}_4$.

C. Theory

A four-point measurement is performed using four electrodes in contact with a conducting sample.[2] A current I_0 is driven through the sample between two current injection electrodes and the potential difference V is then measured between two remaining electrodes as illustrated in Fig. 2. The current flowing in the sample results in an electrostatic potential distribution $\mathbf{\Phi}(\mathbf{r})=\mathbf{\Phi}(\mathbf{r},\mathbf{r}_+,\mathbf{r}_-)$ which is a function of the position $\mathbf{r}$, the position of the current injection electrodes, $\mathbf{r}_+$ and $\mathbf{r}_-$, the sample geometry, and the sample resistivity. There are six possible nontrivial electrode combinations of current and potential electrodes, cf. Table I, excluding polarity changes which only result in sign change of the measured potential. In the absence of a magnetic field $V_A=V_{A'}$, $V_B=V_{B'}$, and $V_C=V_{C'}$,[23] and $V_A=V_B+V_C$. We also define the four-point resistance $R_A=V_A/I_0$, where the subscript denotes the electrode configuration.

D. Sheet resistance–infinite sheet

For a conductive filamentary sheet, we may define the sheet resistance as $R_S=\rho/d=cV/I_0$.[2] ρ is the sample resistivity, d is the sample thickness, and c is a geometrical correction factor which depends on the position of the electrodes and the sample geometry. In the absence of any lateral insu-

TABLE I. Six possible four-point probe configurations and the geometrical correction factors used to obtain the sheet resistance from a single four-point resistance measurement on an infinite, thin sample.

Configuration	Electrode combination	Infinite sheet
A	$V_A=\mathbf{\Phi}(\mathbf{r}_2,\mathbf{r}_1,\mathbf{r}_4)-\mathbf{\Phi}(\mathbf{r}_3,\mathbf{r}_1,\mathbf{r}_4)$	$c=\frac{\pi}{\ln 2}$
A'	$V_{A'}=\mathbf{\Phi}(\mathbf{r}_1,\mathbf{r}_2,\mathbf{r}_3)-\mathbf{\Phi}(\mathbf{r}_4,\mathbf{r}_2,\mathbf{r}_3)$	
B	$V_B=\mathbf{\Phi}(\mathbf{r}_2,\mathbf{r}_1,\mathbf{r}_3)-\mathbf{\Phi}(\mathbf{r}_4,\mathbf{r}_1,\mathbf{r}_3)$	$c=\frac{2\pi}{\ln 3}$
B'	$V_{B'}=\mathbf{\Phi}(\mathbf{r}_1,\mathbf{r}_2,\mathbf{r}_4)-\mathbf{\Phi}(\mathbf{r}_3,\mathbf{r}_2,\mathbf{r}_4)$	
C	$V_C=\mathbf{\Phi}(\mathbf{r}_4,\mathbf{r}_1,\mathbf{r}_2)-\mathbf{\Phi}(\mathbf{r}_3,\mathbf{r}_1,\mathbf{r}_2)$	$c=\frac{2\pi}{\ln \frac{4}{3}}$
C'	$V_{C'}=\mathbf{\Phi}(\mathbf{r}_2,\mathbf{r}_3,\mathbf{r}_4)-\mathbf{\Phi}(\mathbf{r}_1,\mathbf{r}_3,\mathbf{r}_4)$	

lating barriers the correction factors for an equidistant collinear four-point probe with electrode pitch s is given in Table I. If the four electrodes are collinear but not equidistant, the exact sheet resistance may be extracted numerically with the dual configuration method based on conformal mapping,[4,23]

$$\exp\left(\frac{2\pi R_A}{R_S}\right) - \exp\left(\frac{2\pi R_B}{R_S}\right) = 1$$

$$\text{or} \quad \exp\left(-\frac{2\pi R_A}{R_S}\right) + \exp\left(-\frac{2\pi R_C}{R_S}\right) = 1. \tag{1}$$

That is, even with large in-line position errors relative to the electrode pitch, the exact sheet resistance may be calculated. Note that off-line position errors only change the distance between the electrodes to second order, and such errors only become of relevance for submicrometer pitch M4PP.

E. Material limitations

A general requirement for sheet resistance measurements is that the conductive sheet is continuous with no significant flaws or defects. This sets a fundamental requirement to the electrical junction thickness for any given carrier concentration. The minimum number of charge carriers (or ionized dopants outside the depletion region), $N_{\min}$, within a cube of dimensions d^3, where d is defined by the electrical junction depth, must at least be of order of 1 for statistical reasons. That is, the standard deviation on the number of carriers in the box will be $\sqrt{N_{\min}}$ and thus a high probability of carrierless boxes results if $N_{\min}$ is too small. In terms of the carrier concentration n and the sheet carrier density n_s, the number of charge carriers in a box may be expressed as $N=nd^3=n_sd^2 \geqslant N_{\min}$. If N is less than $N_{\min}$, the conductive sheet will disappear from a large fraction of the area of the semiconductor surface, and at some point a continuous conductive sheet can no longer be assumed as the charges become electrically insulated from one another, i.e., one must include the possibility of three dimensional depletion regions (both parallel and normal to the surface). Note that the electrical junction position depends on both USJ and substrate doping concentration; thus $N_{\min}$ may not be a unique number for all structures but only serves as a rough estimate.

F. Sensitivity

The assumption of a homogenous sheet resistance is not always true, and thus it is important to know the sensitivity to sheet resistance variations. It was previously shown that the sensitivity S to local sheet resistance variations $R_{S,L}$ can be defined as $S=s^2\partial^2 R_S/(\partial R_{S,L}\partial A)$,[6] where s is the electrode pitch and A is the area. It was found that whereas single configuration four-point measurements exhibit both positive and negative sensitivities, the dual configuration has purely positive sensitivity (cf. Fig. 3); i.e., for dual configuration, a local increase in sheet resistance will always result in an increased measured sheet resistance. In a single configuration measurement both positive and negative sensitivities exist, and this can give rise to unreliable measurement results.[6]

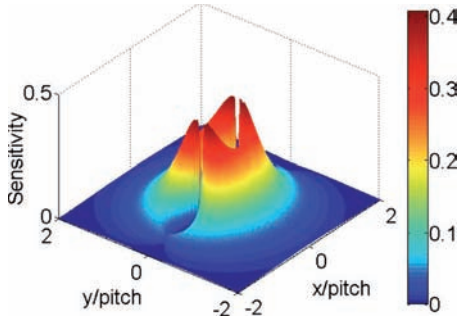

FIG. 3. (Color online) Sensitivity of the dual configuration sheet resistance measurement to local sheet resistance variations; adapted from Ref. 6. The four electrodes are positioned at (−1.5,0), (−0.5,0), (0.5, 0), and (1.5, 0).

In Fig. 3 it may be seen that the sensitivity at the electrode contact points is virtually zero (although not exact[24]). Furthermore, it is evident that the four-point probe is mostly sensitivity to a circularlike area with a radius roughly corresponding to the electrode pitch. The sensitivity in proximity of laterally isolating barriers such as a small test pad has been investigated by Wang *et al.*;[24] and although the sensitivity changes slightly a similar shape is maintained.

III. SHEET RESISTANCE

A. Zero probe penetration

For correct electrical characterization of USJ, one must avoid junction penetration, such that all of the current is injected into the surface layer and not into the substrate. Note that the electrical junction depth of an ultra-shallow implant is highly dependent on the substrate doping, i.e., for a highly doped substrate (e.g., a halo implant), the electrical junction depth is much shallower than for a lightly doped substrate. In a study by Clarysse *et al.*[7] the sheet resistance of ultra-shallow junctions formed by epitaxial layer growth was measured by M4PP and several other techniques. Silicon layers with a nominal boron concentration of 2×10^{19} cm^{-3} were grown on medium doped substrates (7×10^{17} cm^{-3}) and the layer thickness ranged from 1.1 to 132 nm. M4PP failed to measure on all sub-5 nm structures, which is in good agreement with the fundamental limitation (~4 nm at 2×10^{19} cm^{-3}) set by the minimum number of charge carriers in a box as described in Sec. II E. Of course inactive dopants and dopant loss due to native oxide growth will significantly reduce the sheet carrier density, and thus play an important role for accurate electrical characterization of such extremely shallow junctions. M4PP was able to measure all other samples and the thinnest layer was 7.7 nm. In a similar contemporary study on electrical characterization, a variety of advanced USJ were all measured successfully.[8]

Although the M4PP utilizes an electrode material much softer than silicon, it does not necessarily prevent surface penetration in every single measurement. However, the combination of contact force and contact area of the M4PP, which is much smaller than that of conventional four-point probes, reduces the probability of probe penetration significantly. Furthermore, the measurement scheme is designed to

detect leakage current as well as to validate the measured resistance values. Measurements are only accepted if the measured voltage is in phase with the current; this effectively eliminates measurements affected by substrate leakage current, which is highly nonlinear. In addition, the resistance values are validated by the relations given in Sec. II C. An invalid measurement result is either remeasured or discarded. Thus, sheet resistance results are readily obtained only from measurements with zero probe penetration, i.e., all of the current is confined in the USJ giving accurate measurement results. Even for much softer semiconductor materials such as InGaAs, zero probe penetration can be achieved for USJ (i.e., sub-20 nm junction depth).[25]

B. Accuracy

The absolute accuracy of M4PP measurements on USJ is difficult to prove since no silicon USJ standards exist. However, in a study performed by Kjær *et al.*,[26] M4PP was compared to conventional four-point probe measurements on low energy implants (10^{15} cm^{-2}, 2 keV, B and As, respectively) in lightly doped silicon annealed by rapid thermal annealing. On all samples the conventional four-point probe measured a few percent lower sheet resistances than M4PP. This could be due to junction leakage when using large electrode pitch as described by C. L. Petersen *et al.*,[17] but overall the agreement was good. In the study by Kjær *et al.*,[26] the sheet resistance repeatability as well as short term and long term reproducibilities was investigated. The short term reproducibility test was performed with both new and used probes, and the long term reproducibility test was performed over 7 days. In all cases the standard deviation on the measured sheet resistance was less than 0.1%.

One of the possibilities with M4PP is, due to the small probe dimension, to measure sheet resistance directly on product wafers to reduce test wafer consumption. Thorsteinsson *et al.*[27] demonstrated that accurate correction free sheet resistance measurements may be performed at any mirror plane of a small sample or test pad. In the same study we found that for a probe-to-sample alignment accuracy of ± 2.5 μm, the smallest test area which can be measured with a measurement error of less than 0.1% is 50×50 μm^2 when using an electrode pitch of 10 μm.

C. Micro non-uniformity

Accurate sheet resistance measurements on nonuniform samples is more challenging as one must take into account the probe dimensions relative to the sample variations. In a comparative study by D. H. Petersen *et al.*,[6] we showed how a probe pitch much smaller than the spatial variations is necessary for accurate sheet resistance characterization. Whereas a conventional probe pitch of 500 μm completely averages out the sheet resistance variations and thus characterize a test sample as being homogeneous, a smaller electrode pitch ($\leqslant 20$ μm) reveals the true sheet resistance, cf. Fig. 4. This is in good agreement with the area of sensitivity shown in Fig. 3. We also demonstrated the advantage of high

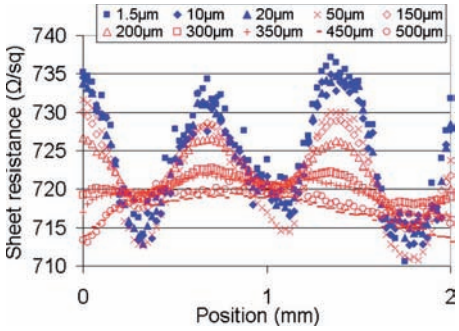

FIG. 4. (Color online) Sheet resistance non-uniformity measured with electrode pitch ranging from 1.5 to 500 μm. The characteristic length scale of sheet resistance variations is 750 μm. Data adapted from Ref. 6.

spatial resolution, by high resolution area mapping of laser annealed USJ, cf. Fig. 5. Since the sheet resistance resulting from the laser anneal process can be characterized with high precision, the sources of non-uniformity may be easily discovered and the process optimized as described by Vandervorst *et al.*[28]

IV. MICRO HALL EFFECT

The high precision in four-point resistance enables measurement of the much smaller Hall effect signal (e.g., $\Delta R/R \approx 0.2\%$ for p-type silicon USJ at 500 mT). Micro Hall effect measurements are performed with a moderate magnetic flux density B_z normal to the sample surface and in close proximity to an insulating barrier (e.g., a cleaved edge) parallel to the line of four electrodes. In a known distance from the insulating barrier, the four-point resistance is measured in configurations B and B', cf. Fig. 2. The resistance difference, $\Delta R_{BB'} = R_B - R_{B'}$, is simply related to the Hall carrier mobility μ_H and Hall sheet carrier density N_{HS} through a geometrical correction factor[19] which can be determined with very high precision.[20]

The repeatability and reproducibility of micro Hall effect measurements on USJ have been studied and found to be better than 1% and 1.5%, respectively, on USJ structures in Si and Ge.[19,20] To verify the measurement accuracy, comparative studies with cloverleaf patterned Hall effect measurements have been carried out with excellent agreement on

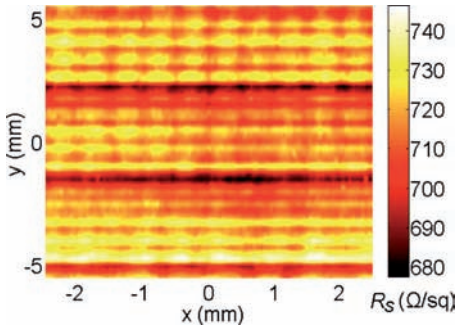

FIG. 5. (Color online) 45×101 point area scan measured with a 10 μm pitch M4PP. Periodic variations due to the laser anneal process are clearly visible in both the x and y directions. Adapted from Ref. 6.

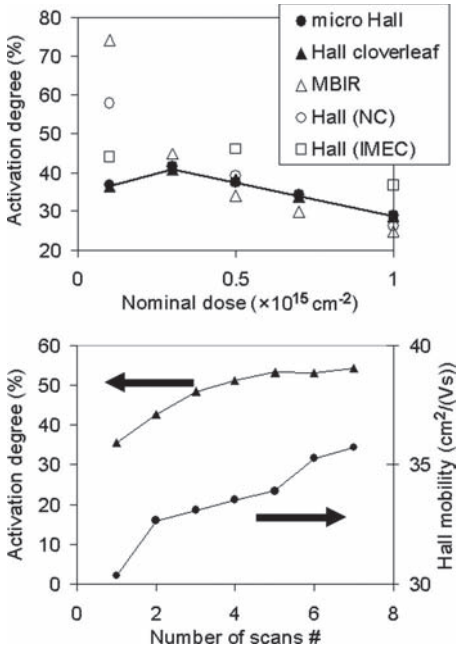

FIG. 6. Laser annealed 0.5 keV B implant in Si. (a) Collected results comparing the micro Hall effect method to other techniques (Refs. 9 and 29). (b) Activation degree and mobility as a function of the number of laser anneals for an implanted dose of 10^{15} cm^{-2} (adapted from Ref. 29).

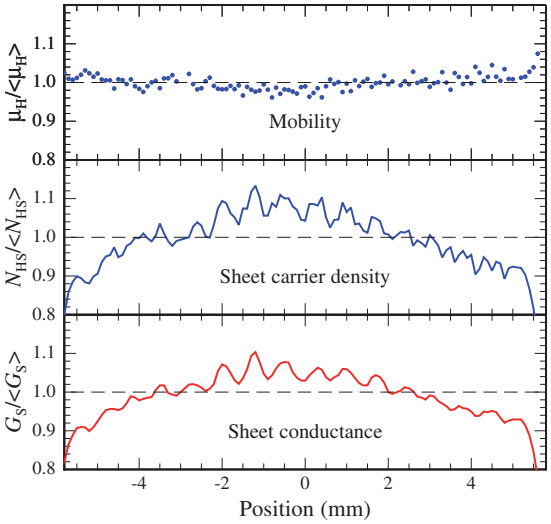

FIG. 7. (Color online) Scanning micro Hall effect of a silicon sample with a 0.5 keV, 10^{15} cm^{-2} B implant annealed in a single pass by an 11 mm wide laser beam. Values are each normalized by their respective average. The variations in sheet conductance and dopant activation correlate while carrier mobility is almost constant with a slight increase at the outer boundaries of the scanned area (adapted from Ref. 20).

USJ with different boron implant doses ranging from 10^{14} to 10^{15} cm^{-2},[29] and it has been demonstrated that techniques with similar measurement and sample preparation time, i.e., Hall effect measurements on nonpatterned square samples [Hall (NC) and Hall (IMEC)], as well as model based infrared spectroscopy, are much less reliable on USJ,[9] cf. Fig. 6(a). In recent work by Rosseel *et al.*[29] the activation mechanism of ultra-shallow dopant profiles was investigated, and micro Hall effect measurements were used to determine the activation degree and the carrier mobility resulting from multiple submelt laser anneals [cf. Fig. 6(b)]. Finally, we demonstrated the unique capability of micro Hall effect to investigate the reason behind the variations in sheet resistance described in Sec. III C. By scanning across a wafer annealed by a single laser pass, it was possible to directly correlate the sheet resistance variations to variations in dopant activation (cf. Fig. 7).

V. CARRIER PROFILING

Traditionally, carrier profiling has been performed using spreading resistance probes (SRPs) on beveled samples but this conventional technique is not reliable for sub-30 nm junctions.[7] An important difference between M4PP and SRP is that M4PP is an absolute technique while SRP is comparative (i.e., calibration samples and a contact model are needed). Another important difference between SRP and M4PP measurements is the volume to which the measurement techniques are sensitive. In SRP the measurement result is dominated both by the resistivity directly below the probe contact and the sheet resistance in proximity of the probe contact. The high sensitivity at the contact points in combination with the large contact force necessary in SRP is a significant drawback which limits the accuracy on USJ. However, the M4PP uses four orders of magnitude lower contact force and is sensitive only to the area surrounding the contacts, cf. Fig. 3. These advantages can potentially lead to more reliable carrier profiling and a complementary technique to differential Hall effect measurements.[30,31]

The potential for M4PP to perform carrier profiling on beveled samples of USJ in both Si and Ge was recently investigated in comparative studies with conventional SRP profiling.[18,32] It was found that M4PP is significantly less susceptible to carrier spilling (cf. Fig. 8) and there is no need for probe calibration as is the case for SRP. With both SRP and M4PP the preparation of high quality, high magnification bevel sample structures remains an inherent difficulty as well as carrier spilling due to junction displacements caused by the material removal. Figure 9 shows a surface plot of the measured sheet conductance, $G_{S,m}=1/R_{S,m}$, of a shallow Ge bevel structure. The effect of surface roughness on the measured result is evident as a clear deviation from the average profile which relates to surface scratches caused by the bevel preparation. Because of the finite size of the M4PP sensitivity and the assumption of a homogeneous infinite sheet, the measured sheet conductance may not be identical to the true sheet conductance profile, but must be related to the detailed geometry of the bevel, e.g., scratches and three-dimensional current flow.[10] Furthermore, the sheet conductance measured near the junction is significantly affected by geometrical errors as the sheet conductance becomes zero, and a deconvolution method[33] must be applied to extract the true sheet conductance profile. What is encouraging is the fact that the measurement noise observed relates to the sample geometry,

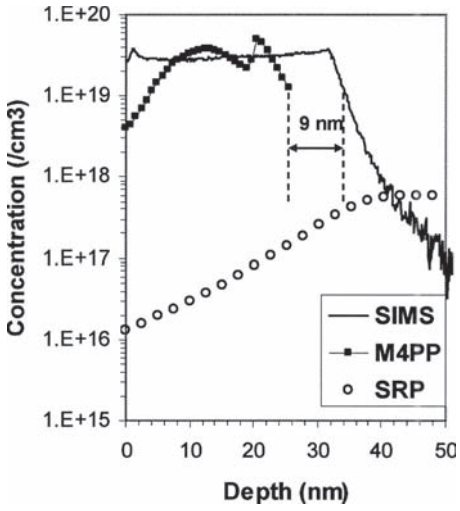

FIG. 8. Carrier concentration of a $p{+}{+}/n{+}$ structure extracted from M4PP and SRP carrier profiling is compared to the dopant concentration measured by secondary ion mass spectrometry. Reprinted from Ref. 32. Copyright (2008), American Vacuum Society.

which may eventually be corrected for using geometrical information from atomic force microscopy and improved models.

VI. CONCLUSION

Accurate and reliable sheet resistance measurements of ultra-shallow junctions with micro four-point probes (M4PPs) have been demonstrated in several studies. Because of zero probe penetration and the small probe dimensions, it is possible to avoid leakage currents which result in huge measurement errors with conventional four-point probe metrology. The high precision resistance measurements further allow for micro Hall effect measurements using the same M4PP by adding a moderate magnetic field and one or more lateral barriers. The reproducibility and repeatability are for sheet resistance measurements of USJ typically better than 0.1%, and for sheet carrier concentration and carrier mobility 1% can be achieved.

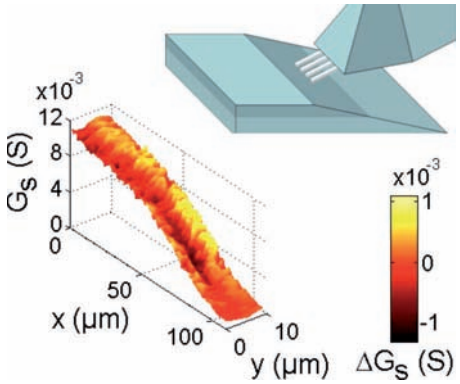

FIG. 9. (Color online) 110×10 point sheet conductance scan of a beveled 150 nm junction Ge sample. The color scale show deviations from the average profile which are related to the surface roughness. The insert shows a schematic illustration of a M4PP measuring on a bevel sample.

The high spatial resolution allows for uniformity studies that may be used for optimization of advanced processes such as laser annealing. Furthermore, the small probe pitch enables accurate sheet resistance measurement virtually at the edge of a wafer and allow for accurate characterization of both sheet resistance and Hall effect on small test pads (e.g., 50×50 μm^2). Finally, the M4PP technique has been extended to include carrier profiling, and although this technique is not fully developed, it shows an exceptional potential over conventional spreading resistance probe.

ACKNOWLEDGMENTS

The authors are grateful for the financial support from Copenhagen Graduate School for Nanoscience and Nanotechnology (C:O:N:T), the Danish Research Agency (FTP). Center for Individual Nanoparticle Functionality (CINF) is sponsored by The Danish National Research Foundation.

[1]L. B. Valdes, Proc. IRE **42**, 420 (1954).
[2]F. M. Smits, Bell Syst. Tech. J. **37**, 711 (1958).
[3]L. J. van der Pauw, Philips Res. Rep. **13**, 1 (1958a).
[4]L. J. van der Pauw, Philips Tech. Rev. **20**, 220 (1958b).
[5]R. G. Mazur and D. H. Dickey, J. Electrochem. Soc. **113**, 255 (1966).
[6]D. H. Petersen, R. Lin, T. M. Hansen, E. Rosseel, W. Vandervorst, C. Markvardsen, D. Kjær, and P. F. Nielsen, J. Vac. Sci. Technol. B **26**, 362 (2008).
[7]T. Clarysse *et al.*, Mater. Res. Soc. Symp. Proc. **912**, 197 (2006).
[8]T. Clarysse *et al.*, J. Vac. Sci. Technol. B **28**, C1C8 (2010).
[9]T. Clarysse *et al.*, Mater. Sci. Eng., B **154–155**, 24 (2008).
[10]T. Clarysse, P. Eyben, T. Hantschel, and W. Vandervorst, Mater. Sci. Semicond. Process. **4**, 61 (2001).
[11]W. Vandervorst, AIP Conf. Proc. **931**, 233 (2007).
[12]M. I. Current and J. O. Borland, *Proceedings of the 16th IEEE International Conference on Advanced Thermal Processing of Semiconductors, RTP 2008* (IEEE, New York, 2008), pp. 43–55.
[13]C. L. Petersen, T. M. Hansen, P. Bøggild, A. Boisen, O. Hansen, T. Hassenkam, and F. Grey, Sens. Actuators, A **96**, 53 (2002).
[14]D. C. Worledge and P. L. Trouilloud, Appl. Phys. Lett. **83**, 84 (2003).
[15]D. W. Abraham, P. L. Trouilloud, and D. C. Worledge, IBM J. Res. Dev. **50**, 55 (2006).
[16]Capres A/S, http://www.capres.com.
[17]C. L. Petersen, R. Lin, D. H. Petersen, and P. F. Nielsen, *Proceedings of the 14th IEEE International Conference on Advanced Thermal Processing of Semiconductors, RTP 2006* (IEEE, New York, 2006), pp. 153–158.
[18]T. Clarysse, W. Vandervorst, R. Lin, D. H. Petersen, and P. F. Nielsen, Nucl. Instrum. Methods Phys. Res. B **253**, 136 (2006b).
[19]D. H. Petersen, O. Hansen, R. Lin, and P. F. Nielsen, J. Appl. Phys. **104**, 013710 (2008).
[20]D. H. Petersen, O. Hansen, R. Lin, P. F. Nielsen, T. Clarysse, J. Goossens, E. Rosseel, and W. Vandervorst, *Proceedings of the 16th IEEE International Conference on Advanced Thermal Processing of Semiconductors, RTP 2008* (IEEE, New York, 2008), pp. 251–256.
[21]T. Ansbæk, D. H. Petersen, O. Hansen, J. B. Larsen, T. M. Hansen, and P. Bøggild, Microelectron. Eng. **86**, 987 (2009).
[22]D. H. Petersen, O. Hansen, T. M. Hansen, P. R. E. Petersen, and P. Bøggild, Microelectron. Eng. **85**, 1092 (2008).
[23]R. Rymaszewski, J. Phys. E **2**, 170 (1969).
[24]F. Wang, D. H. Petersen, T. M. Hansen, T. R. Henriksen, P. Bøggild, and O. Hansen, J. Vac. Sci. Technol. B **28**, C1C34 (2010).
[25]D. H. Petersen *et al.*, J. Vac. Sci. Technol. B **28**, C1C41 (2010).
[26]D. Kjaer, R. Lin, D. H. Petersen, P. M. Kopalidis, R. Eddy, D. A. Walker, W. F. Egelhoff, and L. Pickert, AIP Conf. Proc. **1066**, 167 (2008).
[27]S. Thorsteinsson, F. Wang, D. H. Petersen, T. M. Hansen, D. Kjær, R. Lin, J.-Y. Kim, P. F. Nielsen, and O. Hansen, Rev. Sci. Instrum. **80**, 053902 (2009).
[28]W. Vandervorst, E. Rosseel, R. Lin, D. H. Petersen, T. Clarysse, J. Goossens, P. F. Nielsen, and K. Churton, Mater. Res. Soc. Symp. Proc.

1070, 41 (2008).
[29]E. Rosseel *et al.*, *Proceedings of the 16th IEEE International Conference on Advanced Thermal Processing of Semiconductors, RTP 2008* (IEEE, New York, 2008), pp. 135–140.
[30]T. Alzanki, R. Gwilliam, N. Emerson, and B. J. Sealy, Appl. Phys. Lett. **85**, 1979 (2004).
[31]N. S. Bennett *et al.*, Mater. Sci. Eng., B **154–155**, 229 (2008).
[32]T. Clarysse *et al.*, J. Vac. Sci. Technol. B **26**, 317 (2008).
[33]T. M. Hansen, K. Stokbro, O. Hansen, T. Hassenkam, I. Shiraki, S. Hasegawa, and P. Bøggild, Rev. Sci. Instrum. **74**, 3701 (2003).

Paper II

J. Vac. Sci. Technol. B **26**, 362-367 (2008).

PhD students contribution:

Idea for study. Probe designs and fabrication. FEM simulations, experimental M4PP measurements and draft manuscript.

Co-authors contribution:

W. Vandervorst and T.M. Hansen assisted with major manuscript revisions. R. Lin assisted with experimental M4PP measurements. T.M. Hansen did the numerical sensitivity calculations. E. Rosseel did the sample fabrication. C. Markvardsen and D. Kjær assisted with FFT data treatment and figure with 2D surface map. Experimental support and discussions with P.F. Nielsen.

Comparative study of size dependent four-point probe sheet resistance measurement on laser annealed ultra-shallow junctions

Dirch Hjorth Petersen[a)]
MIC–Department of Micro and Nanotechnology, Nano·DTU, Technical University of Denmark (DTU), Building 345 East, DK-2800 Kongens Lyngby, Denmark and Capres A/S, Scion-DTU, Building 373, DK-2800 Kongens Lyngby, Denmark

Rong Lin
Capres A/S, Scion-DTU, Building 373, DK-2800 Kongens Lyngby, Denmark

Torben Mikael Hansen
MIC–Department of Micro and Nanotechnology, Nano·DTU, Technical University of Denmark (DTU), Building 345 East, DK-2800 Kongens Lyngby, Denmark and Capres A/S, Scion-DTU, Building 373, DK-2800 Kongens Lyngby, Denmark

Erik Rosseel
IMEC, Kapeldreef 75, B-3001 Leuven, Belgium

Wilfried Vandervorst
IMEC, Kapeldreef 75, B-3001 Leuven, Belgium and K.U. Leuven, Electrical Engineering Department, INSYS, Kasteelpark Arenberg 10, B-3001 Leuven, Belgium

Christian Markvardsen, Daniel Kjær, and Peter Folmer Nielsen
Capres A/S, Scion-DTU, Building 373, DK-2800 Kongens Lyngby, Denmark

(Received 31 May 2007; accepted 14 September 2007; published 31 January 2008)

In this comparative study, the authors demonstrate the relationship/correlation between macroscopic and microscopic four-point sheet resistance measurements on laser annealed ultra-shallow junctions (USJs). Microfabricated cantilever four-point probes with probe pitch ranging from 1.5 to 500 μm have been used to characterize the sheet resistance uniformity of millisecond laser annealed USJs. They verify, both experimentally and theoretically, that the probe pitch of a four-point probe can strongly affect the measured sheet resistance. Such effect arises from the sensitivity (or "spot size") of an in-line four-point probe. Their study shows the benefit of the spatial resolution of the micro four-point probe technique to characterize stitching effects resulting from the laser annealing process. © *2008 American Vacuum Society.* [DOI: 10.1116/1.2794743]

I. INTRODUCTION

Maintaining adequate device performance within the continued miniaturization of semiconductor devices necessitates the development of extremely shallow (<20 nm) source/drain extensions with very high dopant concentration and electrical activation level.[1] As the millisecond annealing process used for ultra-shallow junction (USJ) formation today only leads to partial (metastable) activation, one can no longer assume 100% activation. Thus, the dopant profile is no longer a good measure for the electrically active carrier profile, and secondary ion mass spectroscopy profiles cannot accurately predict the sheet resistance, which is of utmost importance. Sheet resistance measured with conventional four-point probes has for many decades been used to characterize the doped region. However, conventional four-point probe measurements are seriously hampered by probe penetration, leading to excessive sampling of the underlying substrate.[2] Hence, alternative approaches for characterization of sheet resistance are presently being investigated based on optical tools, noncontact measurements, or four-point probe systems with drastically reduced probe penetration. The micro four-point probe (M4PP) technology developed at MIC (Ref. 3) and Capres A/S (Ref. 4) has proved to be a possible candidate to measure the sheet resistance of USJ as it provides an evaluation of the sheet resistance without the artifacts of probe penetration. Moreover, its drastically reduced electrode separation enables the analysis of sheet resistance variations on a much finer scale than feasible previously.

In this work, the M4PP was used to probe the lateral sheet resistance uniformity of laser annealed junctions. Periodic features related to the stitching overlays of the laser beams as well as nonuniformities within the laser beam itself can be clearly resolved. Using probes with various dimensions, the probe pitch effects on these measurements could be clearly resolved. A theoretical interpretation of its smoothening effect and the role of the actual measurement configuration are presented.

II. EXPERIMENT

In this study, an ultra-shallow junction was formed by low energy ^{11}B implantation (0.5 keV and 1×15 cm^{-2}) into a lowly doped 300 mm *n*-type Si wafer followed by laser an-

a)Electronic mail: dhp@mic.dtu.dk

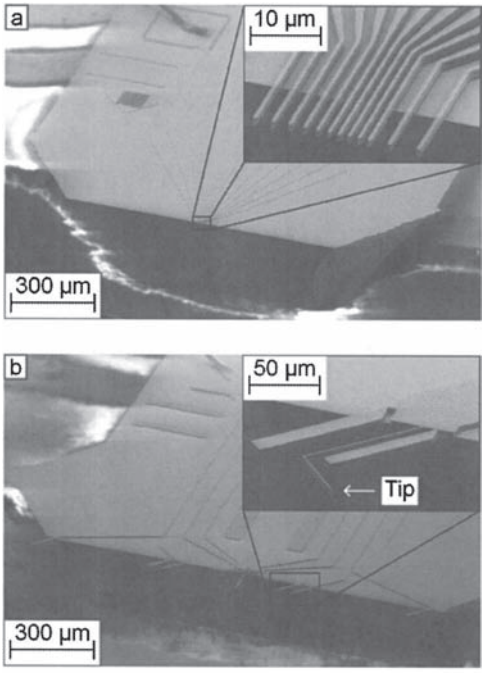

FIG. 1. Scanning electron micrographs of (a) a multicantilever probe with minimum electrode pitch of 1.5 μm and (b) a 500 μm pitch four-point probe with L-shaped static contact cantilevers.

nealing. The laser anneal aimed at a nominal anneal temperature of 1300 °C, resulting in a junction depth of 20 nm at 1×18 cm^{-3}. The laser beam was scanned in straight lines across the sample surface with a step size of 3.65 mm, whereas its spot size is significantly larger ($\sim$11 mm) such that the scanned lines overlap and each region is irradiated several times.

To avoid a contribution from probe penetration, conventional four-point probes were not used for comparison in this work and all results were obtained with M4PP (Capres) and similar cantilever four-point probes. These four-point probes consist of micromachined cantilever electrodes extending from the edge of a silicon support. The cantilevers consist of silicon oxide or silicon coated with a metal thin film and provide extremely low contact forces ($\sim10^{-5}$ N).[3] Probes were fabricated with an electrode pitch ranging from 1.5 to 500 μm (cf. Fig. 1) and their specifications are summarized in Table I.

For the large pitch four-point probes ($\geqslant$50 μm), the alignment between probe and sample is critical as all four cantilevers should contact the surface at the same time. Any misalignment will necessitate the use of excessive contact force which could possibly result in surface scratching and extreme probe wear. For this reason static contact cantilevers were designed with an L-shaped high aspect ratio geometry to eliminate/minimize surface movements.[5]

TABLE I. Specifications of four-point probes used in this work.

Electrode pitch (μm)	Cantilever material	Electrode material	Cantilever geometry	Spring constant (N/m)
1.5	SiO_2	Ti/Ni	Straight beam	$\sim$20
7–20	Polysilicon	Ti/Ni or Ti/Au	Straight beam	$\sim$50
50–500	Polysilicon	Ti/Ni or Ti/Au	L shaped	$\sim$1–10

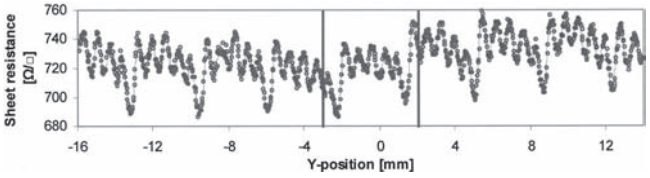

FIG. 2. 30 mm sheet resistance line scan perpendicular to the laser scan direction using a 10 μm pitch four-point probe and a step size of 25 μm. The vertical lines define the area which was consecutively probed with different probe pitches (cf. Fig. 3). A continuous function of the sheet resistance was approximated (thin line) for finite element method (FEM) simulations (cf. Fig. 9).

The choice of Ni or Au as electrode material does not impact the measurement precision but can affect probe lifetime/wear and of course acceptability in a complementary metal-oxide semiconductor–production environment. All the scans presented in this work have been measured in a random mode (meaning that the sheet resistance data are measured in random order) to rule out any periodic variations in the measurement condition, and no deterioration of the sheet resistance precision over the probe life span has been observed. The four-point measurements were performed with the four electrodes being placed on a line orthogonal to the laser annealing scan direction and in a dual configuration mode based on the A and C configurations [cf. Fig. 7 and Eq. (2)].

III. UNIFORMITY OF LASER ANNEALING

To study the (local) inhomogeneities following laser annealing, a 30 mm line scan was measured with a 10 μm pitch M4PP and a step size of 25 μm in a direction perpendicular to the laser scan direction. The result is shown in Fig. 2 and indicates significant periodic sheet resistance variations.

In order to study the periodic variations in more detail and the impact of electrode pitch on these results, a 5 mm line scan was measured repeatedly with 11 different electrode pitches. All these measurements were performed in the same region, as indicated by the vertical lines in Fig. 2.

In Fig. 3, we selectively plot six characteristic 5 mm long line scans obtained using different electrode pitches. The measurement results demonstrate the electrode pitch effect on the measured sheet resistance. The largest probe pitch (500 μm) significantly smoothens out the resistance values and "characterizes" the sheet resistance as being more homogeneous than the smaller pitch probes ($\leqslant$20 μm).

To quantify the smoothening effect of the large pitched probes, the relative standard deviation and peak-to-peak variation of the sheet resistance are calculated and plotted as a function of probe pitch in Fig. 4. In these plots, we restrict the calculations to the oscillations within one period (i.e.,

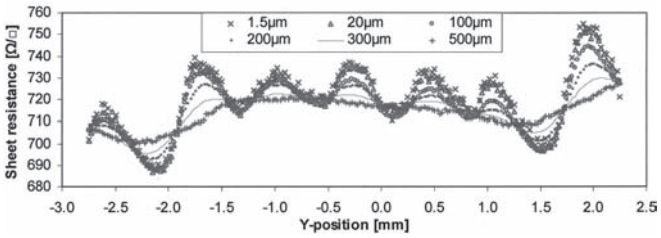

FIG. 3. Raw data of a 5 mm line scan with 25 μm step size repeated at the same location with various pitched four-point probes to compare macro and micro sheet resistances. Only selected electrode pitch results are shown for easy comparison.

3.65 mm and 750 μm for the two main periods observed in Fig. 2—the corresponding line segments are illustrated in Fig. 5). It is clear that the sheet resistance standard deviation and peak-to-peak variation obtained with the large pitched four-point probes are much less than those obtained using M4PP with 1.5–20 μm pitch for both periods. A small increase in sheet resistance variation is seen with the 500 μm pitch probe relative to the 300–450 μm pitch probes for the 750 μm period [cf. Fig. 4(b)]. However, this is likely an artifact caused by other variations such as the 3.65 mm period, i.e., the 500 μm pitch probe is larger than the line scan itself.

Figure 5 illustrates the two line segments used for the calculations of the sheet resistance variation. The vertical

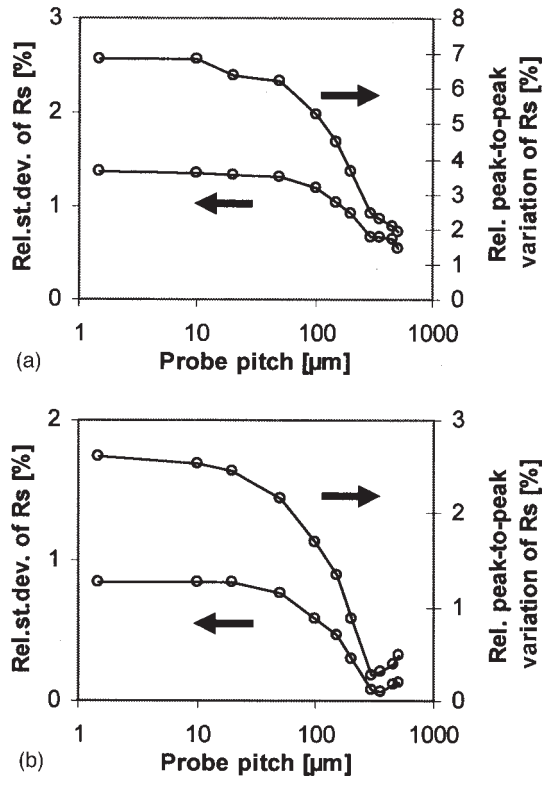

FIG. 4. Comparison of the relative standard deviation and relative peak-to-peak variation of the sheet resistance measured with different electrode pitches for (a) $Y=(-1.825,1.825)$ mm [cf. Fig. 5(a)] and (b) $Y=(0.10,0.85)$ mm [cf. Fig. 5(b)].

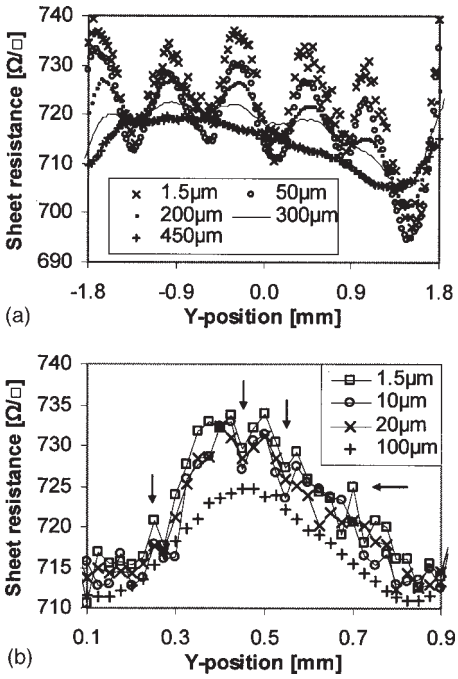

FIG. 5. Selected electrode pitch and line segment of the 5 mm line scan in Fig. 3. A line segment was chosen to represent the two main periodic variations of (a) 3.65 mm and (b) ~750 μm.

arrows [on Fig. 5(b)] point to unexpected coincident sheet resistance peaks and valleys obtained with the small pitched probes ($\leqslant$20 μm). The horizontal arrow on the same figure points to a resistance peak obtained with the 1.5 μm pitch probe. This peak is not resolved by the 10 and the 20 μm pitch probe, and it remains to be proved if these variations are true or accidental measurement error.

In order to probe nonhomogeneities in the laser scan direction, a full two dimensional (2D) map was made using a 10 μm pitch M4PP and scan step sizes of 50 and 250 μm in the *X* and *Y* directions, respectively. The result shown in Fig. 6 indicates not only the periodic pattern in the *Y* direction but

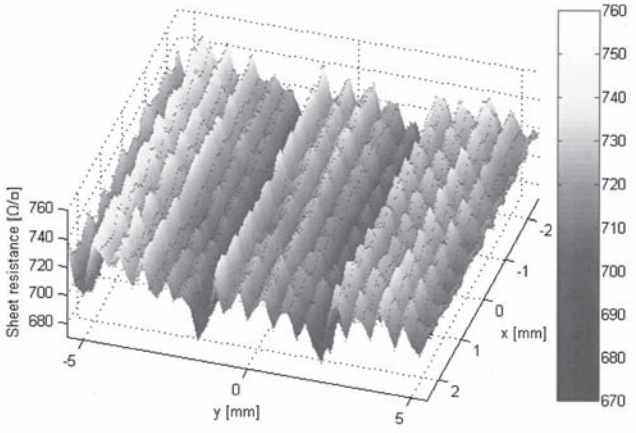

FIG. 6. 45×101 point area scan measured with a 10 μm pitch M4PP. The scan step sizes are 50 and 250 μm in the *X* and *Y* directions, respectively. Raw data are represented by dots.

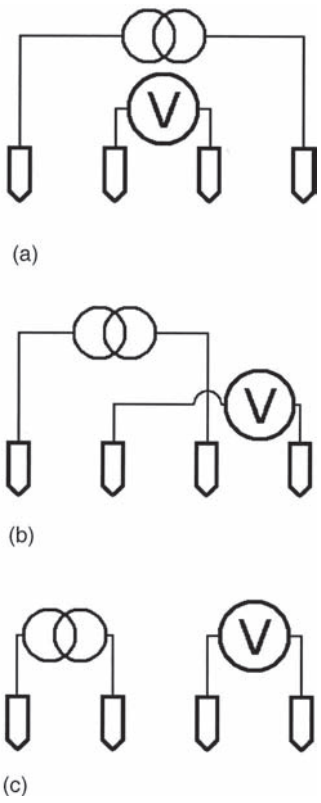

FIG. 7. Illustration of three independent four-point configurations, (a) A, (b), B and (c) C configurations.

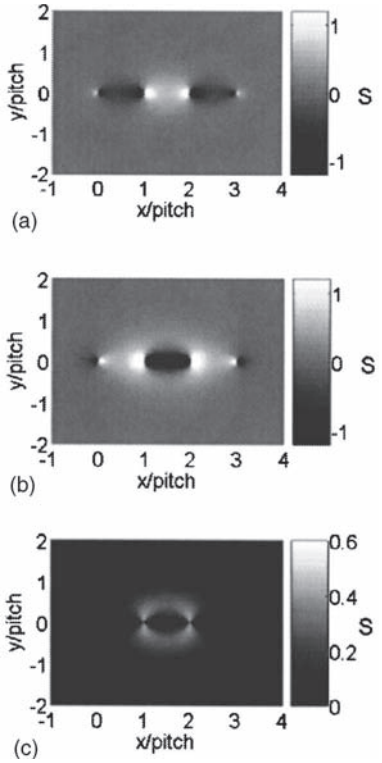

FIG. 8. Contour plots of the sensitivity to resistance variations for an in-line four-point probe in the A, C, and dual configuration modes, (a), (b), and (c), respectively. The four contacts are positioned at $(x,y)=(0,0)$, (1,0), (2,0), and (3,0). The sensitivity goes to $\pm$infinity at the contact points for the A and C configurations; however, the color scale has been cut off (at $S = \pm 1.2$) to see the surrounding contour. The color scale has not been cut off for the dual configuration contour plot.

also an apparent sheet resistance variation in the X direction with a period of roughly 500 μm. The peak-to-peak variation in the X direction is roughly 30 $\Omega/\square$ (or 4%). The cause of these variations could be time dependent fluctuations in temperature, laser movement, laser power, etc., and is the subject of further investigation.

IV. DISCUSSION

Prior to the discussion of the origin of the electrode pitch effect, it is important to address the issue of the probe configuration itself. Basically, there exist three independent probe configurations (Fig. 7) for an in-line four-point probe which can be used to extract the sheet resistance of a conductive infinite sheet.

Generally, the sheet resistance R_S is calculated from[6]

$$R_S = \frac{V}{I} c, \tag{1}$$

where I is the applied current, V is the measured voltage, and c is a geometrical correction factor that depends on the sample shape and the contact positions. The in-line four-point measurement can be shown to be a special case of a van der Pauw measurement,[7] and Rymaszew has used the ideas of van der Pauw to perform position correction valid for an infinite sheet.[8] In the dual configuration mode, the resistance is measured in two of the independent probe configurations, e.g., A and C, and the sheet resistance is calculated based on these two measurements,

$$\exp\left(\frac{-2\pi R_A}{R_S}\right) + \exp\left(\frac{-2\pi R_C}{R_S}\right) = 1, \tag{2}$$

where R_A and R_C are the four-point voltage-to-current ratios measured with the A and C configurations, respectively. If the contact points are located along a straight line, positional error along the line is eliminated[8,9] and off-line positional errors influence the measurement only as a second order effect.[9] If the infinite sheet has an otherwise homogeneous sheet resistance, the sensitivity S to local resistance variations $R_{S,L}$ may be calculated using the adjoint system method[10,11] adapted to the dual configuration mode.[9] The normalized four-point probe sensitivity is defined as

$$S = \frac{\partial^2 R_S}{\partial R_{S,L} \partial A} p^2, \tag{3}$$

where A is the area and p is the electrode pitch. To get the change in measured sheet resistance, the sensitivity must be integrated over the affected area; e.g., when measuring with an electrode pitch of 500 μm if an area of 50×50 μm^2 with a constant sensitivity of 1 changes by 100 $\Omega/\square$, then the measured sheet resistance will change by only 1 $\Omega/\square$. It follows that a smaller probe pitch must be used to correctly characterize such an area.

In Fig. 8, the sensitivity S, as defined by Eq. (3), is plotted

for an equidistant electrode pitch. Shown are sensitivities for A, C, and dual configuration modes. Configuration B shows a similar sensitivity characteristic as configuration A. For the correct interpretation of the following results, it is important to notice that an in-line four-point probe measuring in the A and C configurations has an opposite sign of sensitivity to sheet resistance variations. This means that if a thin film with otherwise homogeneous sheet resistance has an increased resistance at some point, the sheet resistance measured with a four-point probe centered at this point will be higher for the A configuration and lower for the C configuration. Negative sensitivity has previously been reported by Koon and Knickerbocker for the A configuration and dual configuration.[12] They do not find the negative sensitivity to be eliminated as in the case of the dual mode applied here. However, this may be due to an error in normalization of the sensitivity.[13]

In order to verify the experimental results of the electrode pitch size effect, theoretical simulations using a finite element method (FEM) were performed. In these simulations, we used a two dimensional sheet with a spatial variation in sheet resistance based on the 30 mm line scan of Fig. 2 (the sheet resistance is defined by an approximated continuous (wave) function of Y and with no variation in the X direction). The FEM simulations were performed with COMSOL 3.3 using a 2D model (Conductive Media DC). An electrode pitch of 500 μm was used, and it was verified that the simulations were insensitive to further mesh refinements and did not suffer from edge effects.

The results are compared in Fig. 9 to the assumed sheet resistance variation and the experimental data for the corresponding electrode pitch. Whereas the pattern can clearly reproduce, the absolute differ slightly, probably due to the approximations used to describe the sample. It is also interesting to see the impact of the measurement mode. For instance, it appears that the A configuration gives the most "correct" sheet resistance variation, whereas the C configuration gives a completely out-of-phase sheet resistance pattern, turning peaks into valleys. The apparent good result of the A configuration mode is due to an interferencelike behavior of the positive and negative sensitivities for single configuration measurements. If the sheet resistance was not periodic but rather spikelike (only half-period on an otherwise homogeneous sample), the A configuration would not give a trustworthy representation of the sheet resistance.[14] For the same reason the dual configuration 500 μm pitch probe smoothens the sheet resistance because it only has positive sensitivity. In either case, the conclusion is clear that the 500 μm pitch probe leads to unreliable results and cannot be used to assess these small scale variations.

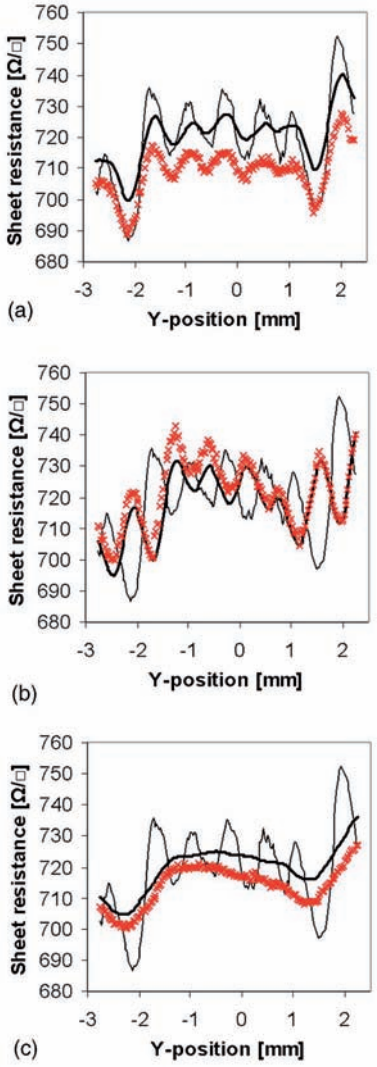

FIG. 9. Comparison of A, C, and dual configurations, (a), (b), and (c), respectively, for a 500 μm pitch four-point probe on a nonhomogeneous USJ. The thin line represents the surface sheet resistance as defined for the FEM simulations (which corresponds to the sheet resistance measured with a 10 μm pitch M4PP). The thick line is the FEM simulated result and the cross represents the experimentally measured result (raw data).

V. CONCLUSION

Accurate sheet resistance characterization of ultra-shallow implants is crucial for further development of CMOS transistors. From this study, it is evident that due to their smaller sampling volume, micro four-point probes can resolve sheet resistance variations more precisely than conventional sized four-point probes.

This is illustrated in detail by analyzing the (local) nonuniformities of laser annealed junctions. Periodic patterns related to the laser scan overlay pattern and laser beam nonuniformities are observed. These can be characterized in much more detail when using a fine electrode pitch, whereas the regular 500 μm pitch leads to an excessive smoothening, thereby obscuring the finer details of the laser anneal process.

A theoretical analysis of the four-point measurements has been performed, assessing the sensitivity of the various configuration modes to small local sheet resistance variations. Whereas in a dual configuration mode, the sensitivity is purely positive, a single configuration four-point measurement may exhibit both positive and negative sensitivities to resistance variations leading to an unexpected correlation to local inhomogeneities. Based on this formalism also, the ef-

fect of electrode pitch on the measurements has been simulated. These simulations confirm the experimental observations that the 500 μm pitch four-point probe significantly underestimates the sheet resistance variations present on a laser annealed ultra-shallow junction (20 nm).

ACKNOWLEDGMENTS

The authors are grateful for the financial support from Copenhagen Graduate School for Nanoscience and Nanotechnology (C:O:N:T) and the Danish Research Agency (FTP), and acknowledge valuable discussions with Ole Hansen and Peter Bøggild.

[1]International Technology Roadmap for Semiconductors (ITRS), Front End Processes (http://www.itrs.net).
[2]T. Clarysse *et al.*, *MRS Spring Meeting, San Francisco, US, 2006* (Materials Research Society, Warrendale, 2006), p. 197.
[3]C. L. Petersen, T. M. Hansen, P. Boggild, A. Boisen, O. Hansen, T. Hassenkam, and F. Grey, Sens. Actuators, A **96**, 53 (2002).
[4]http://www.capres.com
[5]D. H. Petersen, O. Hansen, T. M. Hansen, P. R. E. Petersen, and P. Boggild, 33rd International Conference on Micro- and Nano-Engineering 2007, Copenhagen, Denmark, p. 409.
[6]F. M. Smits, Bell Syst. Tech. J. **37**, 711 (1958).
[7]L. J. van der Pauw, Philips Res. Rep. **13**, 1 (1958).
[8]R. Rymaszew, J. Phys. E: J. Sci. Instrum. **2**, 170 (1969).
[9]T. M. Hansen, D. H. Petersen, R. Lin, D. Kjær, and P. F. Nilsen (unpublished).
[10]L. K. J. Vandamme and W. M. G. van Bokhoven, Appl. Phys. **14**, 205 (1977).
[11]L. K. J. Vandamme and G. Leroy, Fluct. Noise Lett. **6**, L161 (2006).
[12]D. W. Koon and C. J. Knickerbocker, Rev. Sci. Instrum. **63**, 207 (1992).
[13]D. W. Koon (private communication).
[14]T. M. Hansen, K. Stokbro, O. Hansen, T. Hassenkam, I. Shiraki, S. Hasegawa, and P. Boggild, Rev. Sci. Instrum. **74**, 3701 (2003).

Paper III

AIP Conf. Proc. **1066**, 167-170 (2008).

PhD students contribution:

Significant discussions on experimental work with M4PP, figures and comparison between M4PP and CDE. Idea and data treatment for measurements on curved wafer edge. Minor manuscript and references revisions.

Micro Four-Point Probe with High Spatial Resolution for Ion Implantation and Ultra Shallow Junction Characterization

Daniel Kjaer[1], Rong Lin[1], Dirch Hjorth Petersen[1, 2], Petros M. Kopalidis[3*], Ronald Eddy[4], David A. Walker[4], William F. Egelhoff, Jr.[5], Larry Pickert[6]

[1]*CAPRES A/S, Scion-DTU, Building 373, DK-2800 Kgs., Lyngby, Denmark*
[2]*DTU Nanotech - Dept. of Micro and Nanotechnology, Technical University of Denmark, B-345 East DK-2800 Kgs. Lyngby, Denmark*
[3]*Technological Educational Institute of Thessaloniki, Sindos 57400, Greece*
[4]*Innovion Corporation, Chandler, AZ 85226, USA*
[5]*National Institute of Standards & Technology, Gaithersburg, MD 20899, USA*
[6]*Microchip Technology Inc., Chandler, AZ 85224, USA*

* kopalidis@urgrad.rochester.edu

Abstract. The application of micro four-point probe technique in ion implantation non-uniformity mapping and analysis is demonstrated in this work. The technique uses micron-size probes with electrode pitch of 10 μm to achieve greatly enhanced spatial resolution of sheet resistance (Rs) measurements. Rs non-uniformities due to uneven dopant distribution or activation can be mapped with improved accuracy, making it easier to detect implanter scanning problems, dose and charge control malfunctions and annealer related non-uniformities. The technique's superior performance in spatial resolution over conventional four-point probe measurements is demonstrated by zero edge exclusion sheet resistance measurements at the wafer edge. In addition, the technique is used to investigate potential Rs variations between equivalent As+ and As_2+ implants with the same effective energy. Finally, repeatability and reproducibility are investigated by making multiple measurements on a selected ULE implanted and annealed wafer.

Keywords: Sheet resistance, four-point probe, ion implantation, process control, diagnostics
PACS: 07.10.Cm; 84.37.+q; 85.85.+j

INTRODUCTION

A major concern in ion implantation process qualification and control is to ensure consistent uniformity of dopant distribution over large numbers of processed wafers. Modern ion implanter design involves complex mechanisms of ion beam and/or wafer scanning as well as dose and charge control that, when deviating even slightly from their normal operation can result in unacceptable non-uniformities and seriously affect implanter uptime and availability. Sheet resistance (Rs) measurements by conventional four-point probe (FPP) have long been used as a principal way of detecting and analyzing such wafer non-uniformities [1], however recent work has demonstrated that the technique sometimes becomes limited in its usefulness to characterize ultra shallow implants, due to probe penetration [2] and leakage current [3], as well as non-uniformities, due to limited spatial resolution [4]. The micro four–point probe (M4PP) technique, utilizing micron sized and non-destructive probes, provides a straightforward solution to these difficulties.

In this work the main focus for Innovion is to determine the usefulness of the M4PP system, manufactured at Capres for process monitoring, process diagnostics and for wafer detail correlation to die problems.

EXPERIMENTAL

n- and p-type 200 mm wafers were implanted in a batch, high current ion implanter (Axcelis GSD-200E2) with energies and doses as shown in Table 1. The wafers were annealed in a rapid thermal annealer at either of two locations – Innovion and Microchip – using an Axcelis-Reliance 850 and a Mattson-AST SHS2800 respectively. The anneal recipe used with the Axcelis Reliance 850 rapid thermal annealer is 35 sec, 1100°C with 50% N_2 in air. A different anneal recipe is used with the Mattson-AST SHS2800, as follows: 18 sec, 1050°C with 10% O_2 in N_2 gas.

Test #	Species	Energy, keV	Dose, ions/cm^2	Rs, Ohm/sq. Capres (M4PP)	Rs, Ohm/sq. CDE (B-type FPP)	M4PP-FPP Diff., %	Notes
1	As+	2	1E15	163.64	146.87	10.80	Flood on
2	As+	2	1E15	149.25	141.82	5.11	Flood off for comparison
3	As_2+	2	1E15	152.85	148.94	2.59	Dimer; Particle energy and dose are same as in Run 1
4	B+	2	1E15	155.78	153.17	1.69	
5	BF_2+	3	1E15	273.52	268.94	1.69	Effective B energy = 0.67 KeV
6	As+	2	1.2E15	132.08	126.25	4.51	Dose Sensitivity vs. Test #1
7	As+	2	8E14	203.57	191.32	6.20	Dose Sensitivity vs. Test #1

TABLE 1. Experimental matrix of implanted species, energies and doses.

The FPP used at Innovion is a CDE ResMap Model 178 with a 1 mm pitch probe. The M4PP consists of an array of micro-machined, metal coated silicon cantilevers providing an extremely low contact force (~ 10^{-5} N) [4]. In this work M4PPs with 10 μm probe pitch were utilized.

RESULTS AND DISCUSSION

The average sheet resistances (Rs) measured with the CDE and the M4PP (see Table 1) indicate generally quite good agreement between the two instruments for all implanted wafers, with the differences in average Rs within 6.2 % with the exception of the first implant for which the difference is 10.8 %. It is not clear at the time of publication what caused the large difference in this implant. For all implants, the Capres M4PP gives slightly higher Rs values than the CDE. This is partially due to a difference in lab temperature, 19.5 °C for the CDE and 26.5 °C for the M4PP, and most likely partially due to leakage current on the CDE part [2,3]. The higher roughness of the CDE contour maps origins from unintended rotations of the sample during measurements as the wafer is not fixed in the tool.

Rs Comparison for Flood Off, Dimer and BF_2 Implants

The first three implants, cf. Table 1, involve a comparison of sheet resistance between FPP and M4PP for a baseline 2 keV, 1e15 As^+ implant, the same implant with the charge neutralization device of the implanter turned off and an equivalent As dimer implant. The Rs values for the baseline implant are 146.87 and 163.64 Ω/sq respectively for the 4PP and M4PP, a 10.80 % difference. Both probes show a drop in Rs and worsening uniformity when the charge neutralization is turned off, an expected consequence of the ion beam blowing up as it traverses the Si wafer from the aluminum disk. The Rs maps for the flood-off implants are shown in Figure 1.

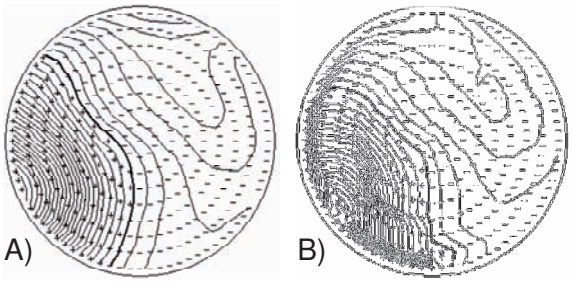

FIGURE 1. Rs contour maps from a) the M4PP and b) the CDE for a flood-off implanted wafer (notch down, 2 % contour intervals).

Compared to the baseline the Rs values from the As_2^+ implanted wafer differ by -1.4 % and 6.6 % for the FPP and the M4PP probes respectively. These variations are up to 3 times higher than previously published results [5], which could be due to the different type of implanter used in this study.

The next comparison involves a 3 keV, 1e15 BF_2 implant (annealed in the SHS2800) with an effective B energy of 0.67 keV. The Rs maps from the BF_2 implant are shown in Figure 2.

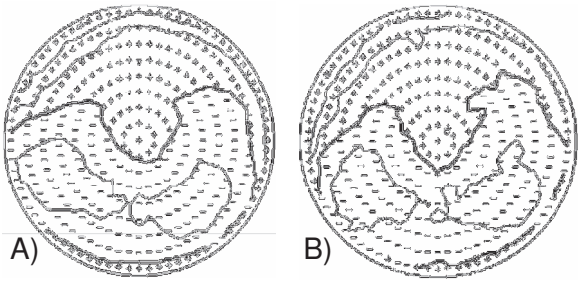

FIGURE 2. Rs contour maps from a) the M4PP and b) the CDE for a 3 keV, 1e15 BF_2 implanted wafer (notch down, 1 % contour intervals).

Reproducibility, Repeatability and Dose Sensitivity

Repeatability and reproducibility studies of the M4PP were performed on the BF_2 implant. The repeatability of the instrument was tested at five points on a 2×2 mm square. The sheet resistance at each position was measured repeatedly 20 times in a random manner. The mean Rs, the standard deviation (SD), and the relative SD calculated for the five points are given in Table 2.

X / µm	Y / µm	<Rs> / Ω/sq	SD / Ω/sq	SD / %
-1000	-1000	275.2	0.25	0.09%
-1000	1000	275.41	0.39	0.14%
0	0	275.24	0.24	0.09%
1000	-1000	275.15	0.25	0.09%
1000	1000	275.42	0.16	0.06%

TABLE 2. Repeability data for 5 locations measured 20 times each in a random manner.

The reproducibility of the M4PP was checked for four different probes: one used probe with more than 1000 touches and three new probes. A 2.5 mm line scan with 100 µm step size was repeatedly measured by these probes at the same locations. Table 3 summarizes the measurement results.

	Probe 1 (old)	Probe 2 (new)	Probe 3 (new)	Probe 4 (new)
<Rs> / Ω/sq	274.64	274.52	274.66	274.55
SD / Ω/sq	0.23	0.24	0.18	0.20
SD / %	0.08	0.09	0.06	0.07

TABLE 3. Reproducibility on a 2.5 mm line scan repeatedly measured by four M4PPs.

An additional long term reproducibility test was performed in a scan area of 5x5 points each separated by 10 mm. The scan was measured 3 times a day (with a time span of 4 hours) for 5 days over a period of 7 days and the wafer was transferred to and from the measurement system during the test. In Figure 3 the mean Rs values as well as the temperature for each measurement time are plotted.

The relative SD of the 15 scans was calculated to be 0.08 %. It is evident that the measurement deviations are correlated to and can be explained by the variation in lab temperature.

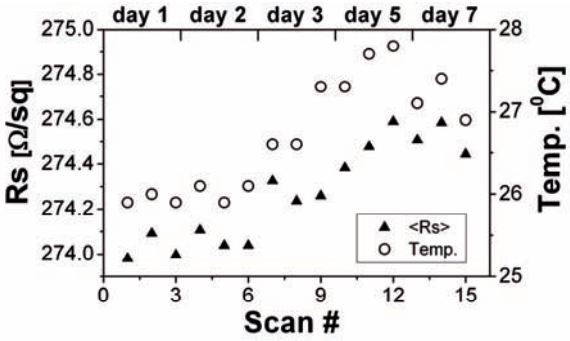

FIGURE 3. Rs and temperature for long term test.

The 2 keV, 1e15 As^+ implant (test # 1) was analyzed for dose sensitivity by running two additional implants with +/-20% dose difference (tests # 6 and 7). The dose sensitivity as described in reference [6] was 1.1 and 1.0 for the M4PP and the conventional 4PP respectively. This is in good agreement with the theoretical dose sensitivity which is 1.04 for the choice of doses while assuming constant mobility and 100% dose activation.

Edge Measurements

The Capres M4PP has due to the microscopic tip separation virtually no edge exclusion. This has been shown by performing a line scan all the way to the wafer edge and beyond (see Figure 4). The step size of the line scan was lowered to 5 µm as the probe approached the edge. For each measurement point an Rs value was read out together with the z-position of the probe thus effectively mapping the topology of the wafer edge. These results are plotted in Figure 5 and 6 together with information of the wafer slope, α and the measured sheet conductance, Gs. Beyond the wafer edge a significant increase in Rs is observed mainly due to the smaller projected area of this region with respect to the direction of the ion beam. The estimated sheet conductance based on the expression: $Gs \propto dose \times \cos(\arctan(\alpha))$, was found to deviate less than 2 % from the measured values for a slope angle up to 20° and the result was reproducible on different wafers.

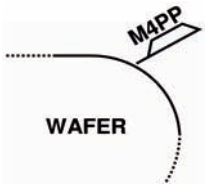

FIGURE 4. M4PP measuring beyond the wafer edge.

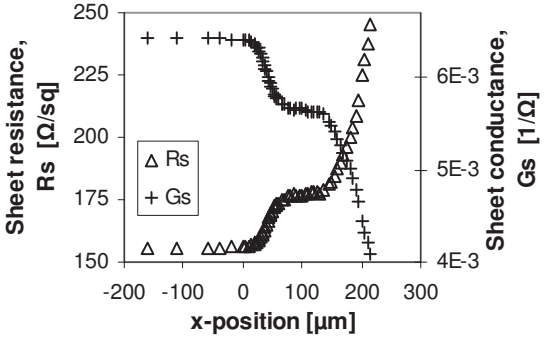

FIGURE 5. Rs and Gs as a function of x-pos.

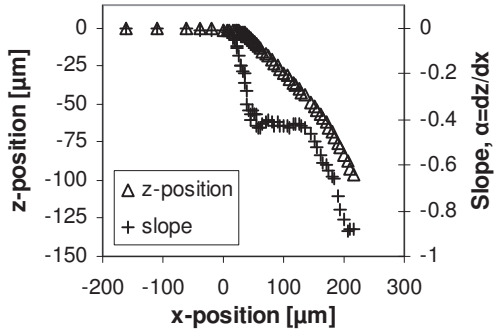

FIGURE 6. z-pos. and slope as a function of x-pos.

The M4PP can perform similar high resolution line/area scans anywhere on a wafer and thus the tool allows the user to map even very confined areas such as test pads in scribe lines, which can not be measured using a conventional FPP. With its micron-size probes and nanoscale positioning the M4PP is a natural choice for the assessment of the "critical diameter" that coincides with the corrected scan plane of all implanter types. This can be used to assess new recipe setups as well as to verify possible drift in that setup after longer wafer runs.

CONCLUSIONS

In this work we investigate the advantages of using M4PP technique for dose and uniformity control in comparison with the conventional FPP. In general we find that conventional FPP measures lower Rs values than M4PP which has previously been reported to be related to probe and substrate leakage current present for conventional FPP measurements. The M4PP technique utilizes micron-size probes and spacing between them, thus allowing for very localized measurements. This can give high resolution Rs information in tight areas of the wafer and can help to identify and trouble-shoot process problems related to implant and/or anneal. The zero probe penetration and micron-size probe pitch ensure more accurate and reliable measurements and overcome the shortcomings of a conventional FPP. Furthermore we demonstrate the repeatability and reproducibility of the Capres M4PP system to be below 0.1 %.

The identification of commercial instruments is to specify the experimental conditions and does not imply any NIST endorsement or recommendation that it is necessarily the best instrument for the purpose.

REFERENCES

1. C. Yarling, M. I. Current, *Ion Implantation Process Measurement, Characterization and Control*, in Ion Implantation Science and Technology, J.F. Ziegler editor, Yorktown, NY, 692, 1996.
2. T. Clarysse, A. Moussa, F. Leys, R. Loo, W. Vandervorst, M. C. Benjamin, R. J. Hillard, V. N. Faifer, M. I. Current, R. Lin, and D. H. Petersen, Materials Research Society Symposium Proceedings 912, 197 (2006).
3. C. L. Petersen, R. Lin, D. H. Petersen, P. F. Nielsen, *Micro-Scale Sheet Resistance Measurements on Ultra Shallow Junction* 14th IEEE Conference on Advanced Thermal Processing of Semiconductors Proceedings, IEEE, Piscataway, NJ, 153, 2006.
4. D. H. Petersen, R. Lin, T. M. Hansen, E. Rosseel, W. Vandervorst, C. Markvardsen, D. Kjær, and P. F. Nielsen, Journal of Vacuum Science and Technology B: Microelectronics and Nanometer Structures 26, 362 (2008).
5. P. M. Kopalidis, B. S. Freer, M. Rathmell, *Low Energy Ion Implantation Using the Arsenic Dimer Ion: Process Characterization and Throughput Improvement*, Journal of the Electrochemical Society 152, G623, 2005.
6. S. Falk, R. Callahan, P. Lunquist, *Accurate Dose Matching Measurements Between Different Ion Implanters*, 11th International Conference on Ion Implantation Technology Proceedings, E. Ishida, S. Banerjee, S. Mehta, T. C. Smith, M. Current, A. Tasch editors, IEEE, Piscataway, NJ, 268, 1997.

Paper IV

Rev. Sci. Instrum. **80**, 053902 (2009).

PhD students contribution:

Identification of interesting structures for which to perform calculations. Input related to experimental procedure and representation of geometrical errors. Significant contributions to manuscript; especially abstract, introduction, experiment, discussion, conclusion and figures. Supporting calculations and discussions.

Accurate microfour-point probe sheet resistance measurements on small samples

Sune Thorsteinsson,[1] Fei Wang,[2] Dirch H. Petersen,[1,2] Torben Mikael Hansen,[2] Daniel Kjær,[1] Rong Lin,[1] Jang-Yong Kim,[2] Peter F. Nielsen,[1] and Ole Hansen[2,3,a)]
[1]*Capres A/S, Scion-DTU, Building 373, DK-2800, Kgs. Lyngby, Denmark*
[2]*Department of Micro- and Nanotechnology, Technical University of Denmark, DTU Nanotech Building 345 East, DK-2800, Kgs. Lyngby, Denmark*
[3]*Danish National Research Foundation's Center for Individual Nanoparticle Functionality (CINF), Technical University of Denmark, DK-2800, Kgs. Lyngby, Denmark*

(Received 23 February 2009; accepted 6 April 2009; published online 1 May 2009)

We show that accurate sheet resistance measurements on small samples may be performed using microfour-point probes without applying correction factors. Using dual configuration measurements, the sheet resistance may be extracted with high accuracy when the microfour-point probes are in proximity of a mirror plane on small samples with dimensions of a few times the probe pitch. We calculate theoretically the size of the "sweet spot," where sufficiently accurate sheet resistances result and show that even for very small samples it is feasible to do correction free extraction of the sheet resistance with sufficient accuracy. As an example, the sheet resistance of a 40 μm (50 μm) square sample may be characterized with an accuracy of 0.3% (0.1%) using a 10 μm pitch microfour-point probe and assuming a probe alignment accuracy of ± 2.5 μm. [DOI: 10.1063/1.3125050]

I. INTRODUCTION

In a wide range of semiconductor applications sheet resistance of the thin films used is of prime importance for the final device performance. It follows that experimental characterization of thin film sheet resistance is essential. For decades four-point probe measurements have been the preferred metrology technique[1,2] due to the low requirements on sample preparation and the high accuracy. The measurements are mostly done on large samples—test-wafers—with dimensions much larger than the pitch of the four-point probes. With the increasing wafer size and processing costs, considerable savings may be realized if accurate sheet resistance characterization could be done on small dedicated areas on device wafers instead.

Recently microfabricated four-point probes[3] have become commercially available.[4] Microfour-point probes (M4PPs) have been proven to be a very useful tool for characterizing ultrashallow junctions without junction penetration,[5] and resolving stitching phenomena on laser annealed junctions.[6,7] Recently even scanning Hall mobility measurements have been demonstrated[8,9] using M4PPs. The available M4PPs have a small pitch that allows for measurements on scribe line test pads of production wafers.[6]

Four-point probe measurements on samples with dimensions of the same scale as the probe pitch, however, are strongly affected by the proximity of insulating sample boundaries, thus interpretation of the measurement results is nontrivial. Geometric correction factors for the proximity of sample boundaries have been calculated for a variety of different sample geometries[10–17] including single boundaries, corners, squares, rectangles, and circles; even finite thickness samples[18] have been treated. In some cases analytical correction factors exist, however, in the presence of boundary effects, from two or more boundaries, the analytical expressions are complicated and require accurate knowledge about sample geometry and probe position; this detailed knowledge is rarely available.

Measurements using dual configurations, in which two of three different, nontrivial permutations of voltage and current pins are used to extract the sheet resistance of a sample, have been proven to correct in-line positional errors,[15,19–21] and to extract the correct sheet resistance regardless of sample shape when certain symmetries exist.[15,19] The dual configuration method is known to significantly decrease the effect of the boundary for circular samples, provided that the probe is located more than a few times the electrode pitch from the edge.[15,20] Further, it is expected to have a similar effect on other samples.[21] Even though the method is based on a thin sample assumption, it has been shown to give accurate sheet resistances even on samples with a thickness of the order of the electrode pitch.[22]

Here we explore the use of dual configuration M4PP measurements for correction free, accurate characterization of small samples with dimensions on the order of a few times the probe pin pitch. We analyze the requirements on probe positioning to achieve this goal on several simple sample geometries: single boundary, double boundary, circular disks, squares, and rectangles. We show that with dual configuration M4PP measurements even significantly smaller samples than those suggested in Ref. 6 may be accurately characterized without applying correction factors. Finally, we demonstrate practical measurements on small square samples.

a)Electronic mail: ole.hansen@nanotech.dtu.dk.

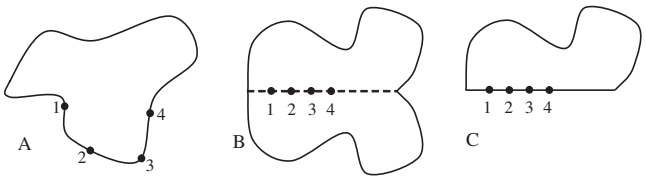

FIG. 1. Schematic of four-point probe measurement cases. In (A) the case discussed by van der Pauw is shown. In (B) a collinear four-point probe measurement on the trace of the sample mirror plane is shown. In (C) a van der Pauw measurement on half of the symmetric sample in (B) is shown.

II. THEORY

Accurate measurement of the sheet resistance $R_\square$ of a small sample may in theory be achieved by dual configuration four-point probe measurements on the perimeter of any small sample, since van der Pauw[23,24] has shown that for any filamentary sample

$$\exp\left(-\frac{\pi R_a}{R_\square}\right)+\exp\left(-\frac{\pi R_c}{R_\square}\right)=1$$

or

$$\exp\left(\frac{\pi R_a}{R_\square}\right)-\exp\left(\frac{\pi R_b}{R_\square}\right)=1, \tag{1}$$

where $R_a=V_{23}/I_{14}$, $R_b=V_{24}/I_{13}$, and $R_c=V_{43}/I_{12}$, respectively are the measured resistances with the four probe pins (1–4) at an arbitrary but fixed position on the perimeter of the sample as illustrated in Fig. 1(a). Here I_{ij} is the current forced through the sample from probe pin i to probe pin j while $V_{k\ell}$ is the voltage measured between probes k and ℓ. However, in real measurements it is not convenient or possible to position the probe pins on the perimeter, due to alignment problems, possible damage to the probes, curved sample perimeter, or ill defined sample perimeter.

For a small sample with one or more mirror planes, however, four-point resistance measurements on the trace of a mirror plane using a collinear four-point probe [see Fig. 1(b)] lead to a vanishing current density $\mathbf{J}$ normal to the mirror plane, $\mathbf{J}\cdot\mathbf{n}=0$, where $\mathbf{n}$ is a unit vector normal to the mirror plane. Thus the potential is unaffected if the mirror plane is replaced by an insulating boundary in this case, and the measured resistances $R_A=V_{23}/I_{14}$, $R_B=V_{24}/I_{13}$, and $R_C=V_{43}/I_{12}$ are exactly half of the resistances one would measure on the perimeter of half the sample with the probes in the same position on the boundary [see Fig. 1(c)], that is $R_A=R_a/2$, $R_B=R_b/2$, and $R_C=R_c/2$, and thus the resistances fulfill

$$\exp\left(-\frac{2\pi R_A}{R_\square}\right)+\exp\left(-\frac{2\pi R_C}{R_\square}\right)=1$$

or

$$\exp\left(\frac{2\pi R_A}{R_\square}\right)-\exp\left(\frac{2\pi R_B}{R_\square}\right)=1, \tag{2}$$

for an arbitrary but fixed probe arrangement on the trace of the mirror plane. Extraction of the sheet resistance from a pair of resistance measurements would thus also simultaneously correct for unintended errors in probe pin spacing.[19]

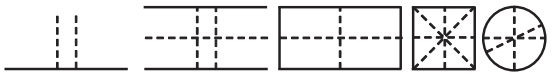

FIG. 2. Schematic of some simple sample geometries with mirror planes (dashed lines).

In practical measurements it may not be possible to place the probes exactly on the trace of the mirror plane thus the conditions for use of Eq. (2) are violated. The resistances, however, will fulfill

$$\exp\left(-\frac{2\pi R_A}{\chi R_\square}\right)+\exp\left(-\frac{2\pi R_C}{\chi R_\square}\right)=1$$

or

$$\exp\left(\frac{2\pi R_A}{\chi R_\square}\right)-\exp\left(\frac{2\pi R_B}{\chi R_\square}\right)=1, \tag{3}$$

where χ is a parameter $0<\chi\leq 2$. In a rather wide region near the mirror plane, however, $\chi\simeq 1$ and thus quite accurate sheet resistance estimates $R_{\square\mathrm{est}}=\chi R_\square$ may be extracted from measured dual configuration four-point resistances using Eq. (2). The resulting relative error on the extracted sheet resistance is

$$(R_{\square\mathrm{est}}-R_\square)/R_\square=\chi-1, \tag{4}$$

thus χ serves as an error parameter for this approach.

III. ANALYTIC, NUMERIC, AND EXPERIMENTAL METHODS

For the simple geometries, as illustrated in Fig. 2, with a few boundaries: the single straight boundary, the corner, the narrow stripe, and the circular disk, analytic expressions for the four-point resistances R_A and R_B are evaluated for varying probe position and orientation, and subsequently Eq. (3) is solved numerically for χ with each pair of four-point resistances. These analytic expressions are all based on a point current source model for the single straight boundary,[9] which by use of conformal mapping[25] may also be applied to other geometries such as the corner, the narrow stripe, and the circular disk (see Appendix).

For rectangles and squares, both analytic expressions (double infinite sums of point source solutions[9]) and finite element modeling using COMSOL MULTIPHYSICS 3.3 are used for evaluation of the four-point resistances, whereafter Eq. (3) is solved numerically for χ with each pair of four-point resistances. A comparison of the results from the two techniques is used to validate convergence and accuracy.

The M4PP measurements were performed using a CAPRES microRSP-M150 system.[4] The M4PP used in these experiments consists of Ni coated silicon cantilever electrodes extending from the edge of a silicon die; in the experiments probes with a probe pin pitch of 10 μm were used. The sample used was a patterned shallow (80 nm) p-type junction formed in Ge using Rapid Thermal Annealing (RTA) of a boron implant (10 keV, 2×10^{15} cm^{-2}) following a preamorphization implant.

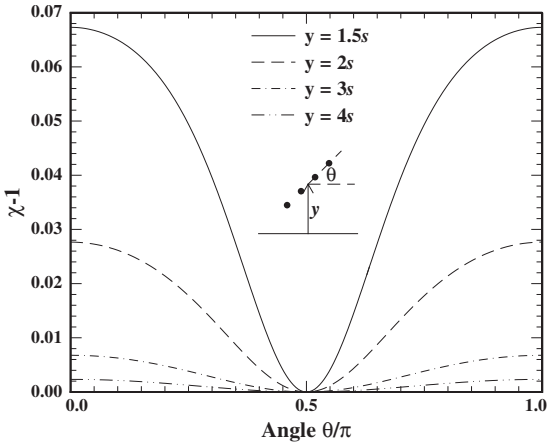

FIG. 3. The error $\chi-1$ as a function of angle θ between the line of the probe and a single insulating boundary with the distance between the boundary and the probe center y as parameter. Calculations for $y/s \in [3/2,\ 2,\ 3,\ 4]$ are shown.

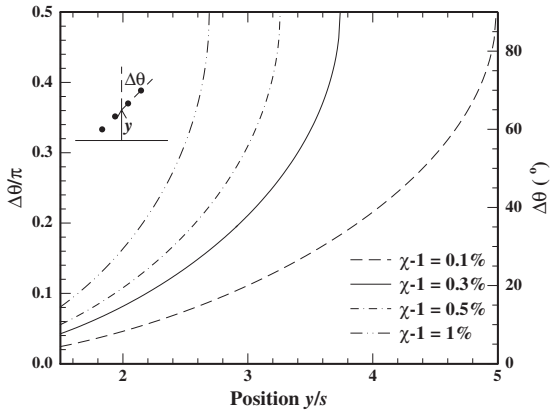

FIG. 4. Allowable misalignment angle $\Delta\theta$ as a function of the probe to boundary distance y, with the error $\chi-1$ as parameter for measurements on a sample with a single straight insulating boundary. Calculations for $\chi-1 \in [0.1\%,\ 0.3\%,\ 0.5\%,\ 1\%]$ are shown.

IV. RESULTS AND DISCUSSION

Dual configuration sheet resistance measurements on infinitely large homogenous samples may be performed with a repeatability better than 0.1% (Ref. 26) using M4PPs since Eq. (2) corrects for in-line position errors and only small off-line position errors contribute. It would be desirable if measurements on small samples could be performed with approximately the same accuracy, such that the presence of the sample boundaries contributes with an error less than 0.1% to make the total error less than ~0.15%. In many practical applications, however, an accuracy of 0.3% is sufficient, thus $|\chi-1| \leq 0.3\%$ may be allowed; this condition is therefore used in the discussion below while graphs also illustrate the effect of enforcing the condition $|\chi-1| \leq 0.1\%$. The proper length scale for the structures investigated here is the probe pin pitch s, therefore all dimensions are stated in units of s.

A. Single insulating boundary sample

A thin semi-infinite sample with a single insulating straight boundary has mirror planes with traces normal to the boundary, and even though it does not qualify as a small sample an analysis may be helpful in interpreting the behavior of more complicated structures. From the presence of a mirror plane it follows that any dual configuration four-point probe measurement with the line of the probe normal to the boundary will fulfill Eq. (2), thus $\chi \equiv 1$ and accurate sheet resistance extraction results. Now, in real measurements the probe may be rotated some small angle $\Delta\theta$ away from the ideal angle $\theta=\pi/2$ between probe and boundary and a small error in the extracted sheet resistance results.

For this sample comparatively simple analytic expressions for the resistances R_A, R_B, and R_C as a function of probe position and orientation are easily obtained using mirror images. Even in this simple sample, however, χ can only be calculated numerically by solving Eq. (3) for χ. In Fig. 3 such calculations are shown for probe center distances $y \in [3s/2,\ 2s,\ 3s,\ 4s]$ from the insulating boundary as a function of the angle θ between the line of the probe and the boundary. Here $y/s=3/2$ is the minimum relevant probe center to boundary distance since in the ideal configuration $\theta=\pi/2$ one probe is exactly on the boundary.

In Fig. 4 the allowable angle alignment error $\Delta\theta$ from the ideal probe angle $\theta=\pi/2$ is shown as a function of probe to boundary separation with the resulting error contribution $\chi-1$ as parameter. Calculations for $\chi-1 \in [0.1\%,\ 0.3\%,\ 0.5\%,\ 1\%]$ are shown. In particular, the full line shows the allowable angle alignment error $\Delta\theta$ at $\chi-1=0.3\%$; obviously, for probe-boundary distances larger than $\sim 3.75s$ the probe-boundary angle is unimportant for the resulting error in this case, and thus at a distance of approximately $3.75s$ the measurement is almost unaffected by the presence of the boundary. Further, it can be seen that even in closer proximity of the edge, $y \geq 3s/2$, angle alignment errors as large as approximately $\pm 7°$ may be allowed.

B. Corner with top angle φ

A semi-infinite region with two straight insulating boundaries intersecting at an angle φ to form a corner has a mirror plane, with the bisector as the trace of the mirror plane. This problem may be solved using the method of images, however, part of the behavior may be analyzed easily by recognizing that the conformal mapping $z=w^{\pi/\varphi}$ maps the corner on a single straight boundary. A radially aligned equispaced collinear probe at the angle θ is mapped on a radially aligned collinear probe at the angle $\pi\theta/\varphi$, which however is not equispaced. In particular the bisector is mapped on the straight boundary mirror plane. Since the mapped probes are not equispaced the length scale of the problem is modified, but Eq. (3) may still be used and with the probes on the mirror plane, Eq. (2) is still exact. We can however conclude that for a radially aligned probe the allowable angular misalignment is in worst case approximately $\pm(\varphi/\pi) \times 7°$ by a direct comparison to the single straight boundary analysis in the previous subsection.

Probes that are not radially aligned, however, is a more difficult problem since they are not mapped on a collinear probe. We shall not pursue that issue further.

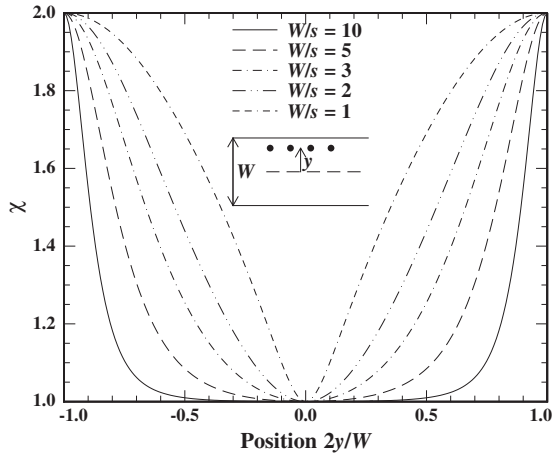

FIG. 5. Error parameter χ for a stripe of width W with the probe parallel to the stripe as a function of probe displacement y from the mirror plane. Calculations for normalized stripe widths $W/s \in [1, 2, 3, 5, 10]$ are shown.

C. Narrow stripe sample

An infinitely long narrow stripe of width W has two types of mirror planes, one parallel to the insulating boundaries and an infinite number of mirror planes normal to the insulating boundaries. Analytic expressions for the four-point resistances R_A, R_B, and R_C may be obtained using conformal mapping and the solution for a single straight boundary, as shown in the Appendix.

Figure 5 shows the error parameter χ for a stripe of width W with the probe parallel to the stripe as a function of probe displacement y from the mirror plane. Calculations for normalized stripe widths $W/s \in [1, 2, 3, 5, 10]$ are shown. From Fig. 5 it may be seen that for small widths of the stripe, the probe is allowed to move closer to the parallel boundary than in the single boundary case for a given allowed error, since the two boundaries tend to quench each other. We shall elaborate further on this behavior below.

In Fig. 6 the error parameter χ is shown as a function of the angle θ between the probe and the stripe boundary when the probe center is in the middle of the stripe. Calculations for $W/s \in [3, 3.5, 5, 10]$ are shown. In all cases $\chi \leq 1$ and

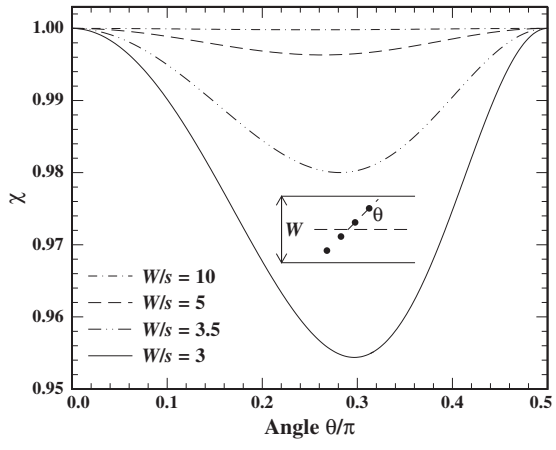

FIG. 6. Error parameter χ for a stripe of width W with the probe center at $W/2$ as a function of the angle θ between the probe and the insulating boundaries. Calculations for $W/s \in [3, 3.5, 5, 10]$ are shown.

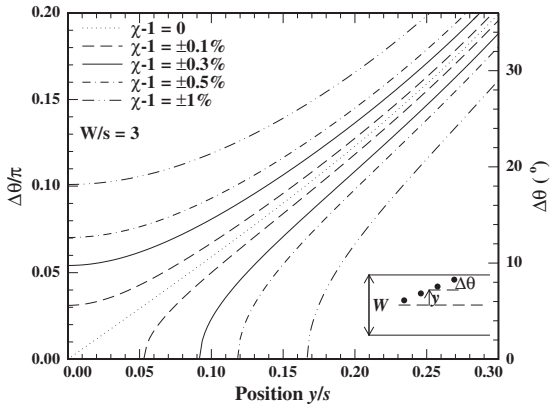

FIG. 7. Relation between allowable angular ($\Delta\theta$) and lateral (y) misalignments for a probe parallel to the boundaries of a stripe of width $W=3s$. The dotted curve shows the trajectory where $\chi \equiv 1.00$. Calculations for $\chi-1 \in [\pm 0.1\%, \pm 0.3\%, \pm 0.5\%, \pm 1.0\%]$ are shown.

the two mirror planes are easily recognized. Only for the narrow stripes $W=3s$, where a full rotation is just possible, and $W=3.5s$ a significant error due to rotation results. The allowable angular misalignment is significantly larger for a probe parallel to the boundaries than for a probe orthogonal to the boundaries.

In Fig. 7 constant error curves relating angular ($\Delta\theta$) and lateral (y) misalignment for a probe with an ideal position in the middle of the stripe parallel to the boundaries. The dotted curve shows the trajectory where $\chi=1.00$. Obviously, the effects of angular and lateral misalignments on the resulting error show a tendency to cancel each other. It follows, that evaluation of the individual allowable misalignments represents a worst case scenario.

In Fig. 8 the allowable angular misalignment $\Delta\theta$ as a function of stripe width W is shown. The allowable angular misalignment increases rapidly with increasing sample width and with $W \geq 3s$ it becomes larger than approximately $\pm 10°$.

In Fig. 9 the allowable lateral misalignment y is shown as a function of stripe width W when the probe is parallel to the boundaries of the stripe. Calculations for $\chi-1 \in [0.1\%, 0.3\%, 0.5\%, 1\%]$ are shown. The allowable misalignment initially increases rapidly with increasing sample width and for large sample widths $W \geq 8s$ it increases

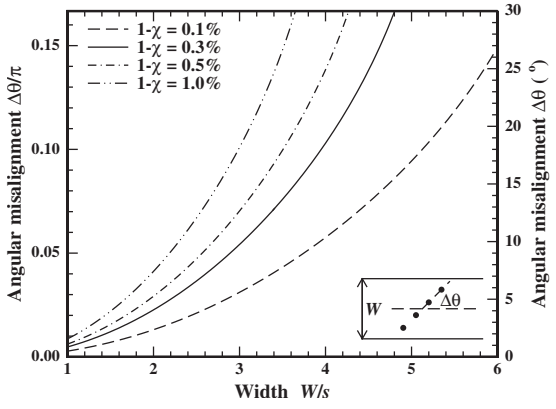

FIG. 8. Allowable angular misalignment $\Delta\theta$ as a function of stripe width W. Probe initially parallel to the boundaries and in the middle of the stripe. Calculations for $1-\chi \in [0.1\%, 0.3\%, 0.5\%, 1\%]$ are shown.

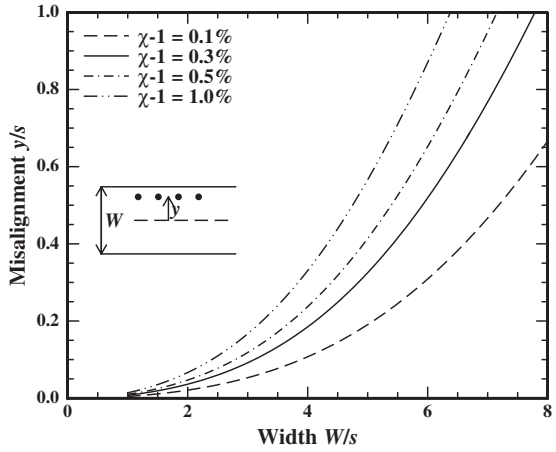

FIG. 9. Allowable lateral misalignment y as a function of stripe width. Probe parallel to the boundary. Calculations for $\chi-1 \in [0.1\%, 0.3\%, 0.5\%, 1\%]$ are shown.

nearly linearly with sample width, such that a minimum distance ($\sim 3.75s$) from a parallel boundary is required. In this regime the behavior is similar to that of two noninteracting boundaries, where a probe displaced more than $\sim 3.75s$ from any of the boundaries remains unaffected by these. At small sample widths a smaller distance from the boundary is allowed.

D. Circular disk samples

The circular disk is comparatively simple to analyze since any diameter is a trace of a mirror plane. It follows that only a misalignment normal to the intended diagonal needs to be characterized.

Figure 10 shows isoerror contours (dashed and full black lines) for a circular disk of radius $R=5s$ along with the trace (full blue line) of the probe center with one probe pin on the disk boundary. Isoerror contours for $\chi-1 \in [0.1\%, 0.3\%, 1\%, 3\%, 10\%, 30\%]$ are shown. To indicate the scale a probe positioned exactly at the center of the disk is shown.

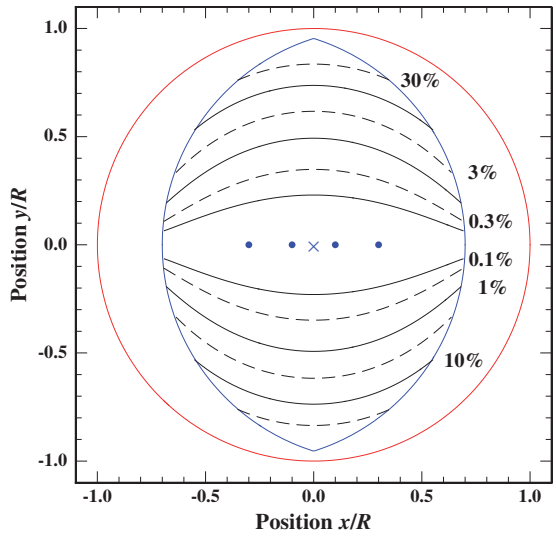

FIG. 10. (Color online) Isoerror contours on a circular disk with radius $R=5s$. The full red curve indicates the sample perimeter, while the full blue curve is the trajectory of the center of the probe with one pin on the perimeter of the disk. Isoerror contours for $\chi-1 \in [0.1\%, 0.3\%, 1\%, 3\%, 10\%, 30\%]$ are shown. To indicate the scale a probe positioned exactly at the center of the disk is shown.

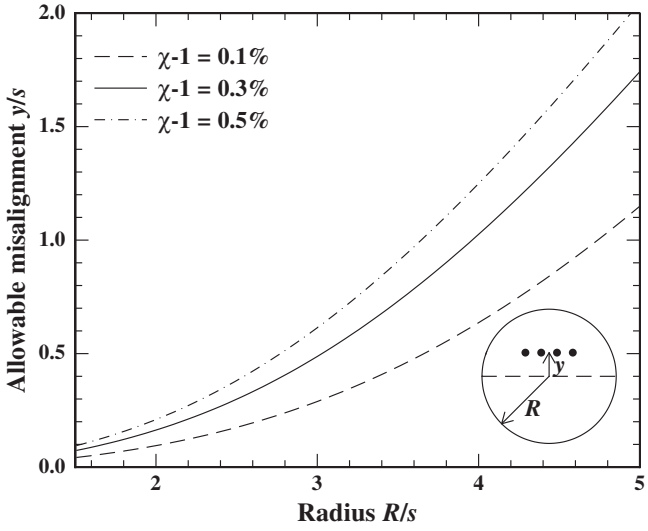

FIG. 11. Allowable misalignment y/s of the four-point probe from the center of a circular disk sample of radius R. Calculations are shown for $\chi-1 \in [0.1\%, 0.3\%, 0.5\%]$.

Figure 11 shows the width of the sweet spot as the allowable misalignment y normal to the disk diagonal from the center as a function of the radius R of the circular disk sample. Calculations for allowable errors $\chi-1 \in [0.1\%, 0.3\%, 0.5\%]$ are shown. At radii larger than approximately $5s$ the allowable misalignment y increases approximately linearly with radius, in agreement with the expectation that a certain distance ($\sim 3.75s$) from the boundary is required. At smaller radius ($R \leq 5s$) a closer relative proximity to the boundary is seen to be allowed.

Figure 12 shows calculated contours relating the intended relative radial position x/R on a diagonal to the relative displacement y/R normal to the diagonal for constant

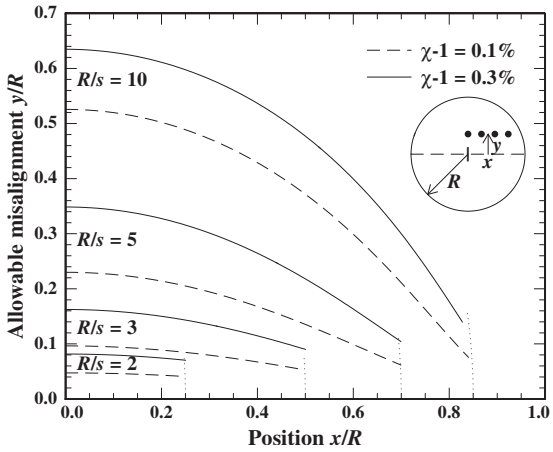

FIG. 12. Relation between relative radial probe position x/R and relative off diagonal position y/R for constant χ in four-point probe measurements on a circular disk of radius R. Calculations for $\chi-1 \in [0.1\%, 0.3\%]$ and $R \in [2s, 3s, 5s, 10s]$ are shown.

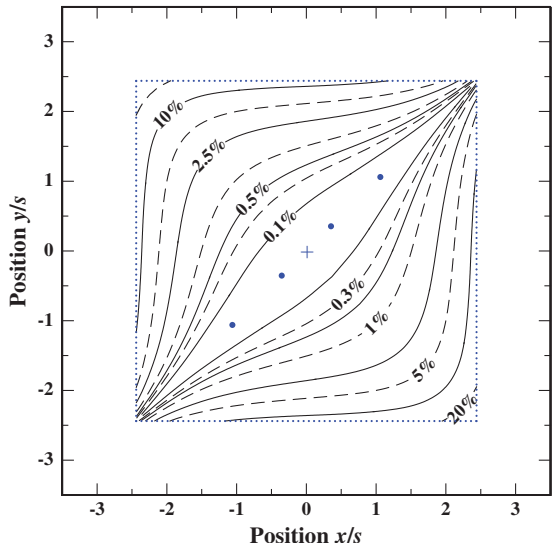

FIG. 13. (Color online) Contour plot showing isoerror curves for the M4PP parallel to the diagonal of a square with the side-width $W=7s$. The dotted square indicates the position of the probe center in the extreme position with one probe pin on the boundary of the square, while the boundary of the square sample coincides with the boundary of the plot. Contour-lines corresponding to $\chi-1\in[0.1\%,\ 0.3\%,\ 0.5\%,\ 1\%,\ 2.5\%,\ 5\%,\ 10\%,\ 20\%]$ are shown. To assist visual interpretation of the graph the four-point probe is shown in its ideal position.

error $\chi-1\in[0.1\%,\ 0.3\%]$ calculated using four different values of the disk radius $R\in[2s,\ 3s,\ 5s,\ 10s]$. The full lines show contours corresponding to $\chi-1=0.3\%$ while the short dotted curves show the relation between the x/R and y/R in the most extreme position with the outermost probe pin on the boundary of the disk. Figure 12 clearly demonstrates the comparatively large sweet spot on the circular disk, which makes probe alignment very easy experimentally.

E. Square samples

A square sample has four mirror planes, two along the diagonals and two parallel to the sides. Figure 13 shows isoerror contours (positions of the center of the probe) for a M4PP parallel to the diagonal of a square with the side-width $W=7s$. Calculated contour-lines corresponding to $\chi-1\in[0.1\%,\ 0.3\%,\ 0.5\%,\ 1\%,\ 2.5\%,\ 5\%,\ 10\%,\ \times 20\%]$ are shown as full and dashed lines. The dotted line indicates the trace of the probe center with one probe pin on the edge of the square sample, while the boundary of the sample coincides with the boundary of the plot. The sweet spot is seen to have a considerable width, but it becomes narrower as the probe is moved toward the corner.

Figure 14 shows the allowable transversal misalignment δ from the ideal position on the middle of the diagonal of a square as a function of the edge length W for three different values of the allowable error $\chi-1\in[0.1\%,\ 0.3\%,\ 0.5\%]$.

Figure 15 shows isoerror contours for a M4PP parallel to an edge of a square sample of width $W=6s$. Contour-lines corresponding to $\chi-1\in[0.1\%,\ 0.3\%,\ 0.5\%,\ 1\%,\ 5\%,\ \times 10\%,\ 20\%,\ 40\%,\ 60\%,\ 80\%]$ are shown as full and dashed lines. The dotted lines are the trajectory of the probe center with one probe pin on the boundary of the sample.

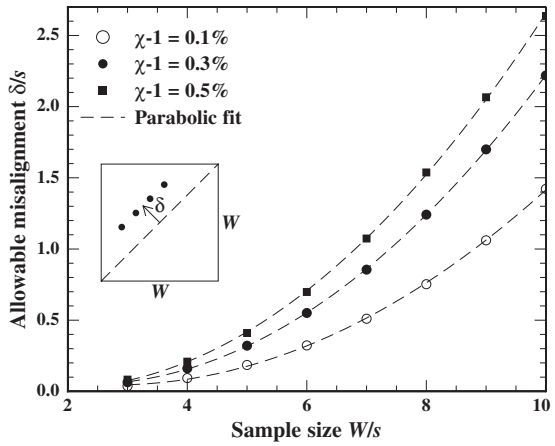

FIG. 14. Allowable misalignment δ from the ideal diagonal center position on a square sample for the errors $\chi-1\in[0.1\%,\ 0.3\%,\ 0.5\%]$. Calculations are shown for a sample width W in the range from $3s$ to $10s$.

The boundary of the plot coincides with the boundary of the sample. The width of the sweet spot is quite large and increases when the probe is moved laterally toward the orthogonal edges. This screening effect is always seen with probes orthogonal to a boundary and is easily understood since images in that boundary contribute significantly to the measured resistance values when the probe is in close proximity to the boundary, and thereby the relative contributions from other boundaries are suppressed.

Figure 16 shows the allowable misalignment y for a probe aligned parallel to one edge of a square sample as a function of the sample size. For square samples larger than $\sim 8s$ the allowable misalignment increases approximately linearly with sample size in agreement with the expectation that a certain distance ($\sim 3.75s$) from a parallel boundary is

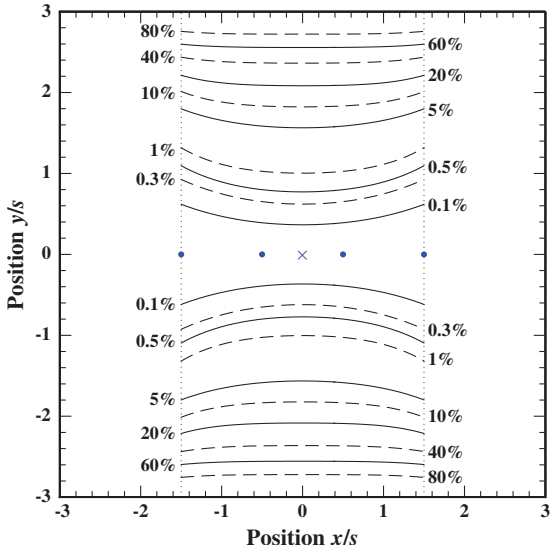

FIG. 15. (Color online) Contour plot showing isoerror curves for the M4PP parallel to an edge of a square sample of width $W=6s$. Contour-lines corresponding to $\chi-1\in[0.1\%,\ 0.3\%,\ 0.5\%,\ 1\%,\ 5\%,\ 10\%,\ 20\%,\ 40\%,\ \times 60\%,\ 80\%]$ are shown as full and dashed lines. The dotted lines show the trace of the probe center with one probe pin on the edge of the sample, while the sample boundary coincides with boundary of the plot. To assist visual interpretation of the graph the M4PP is shown in its ideal position in the center.

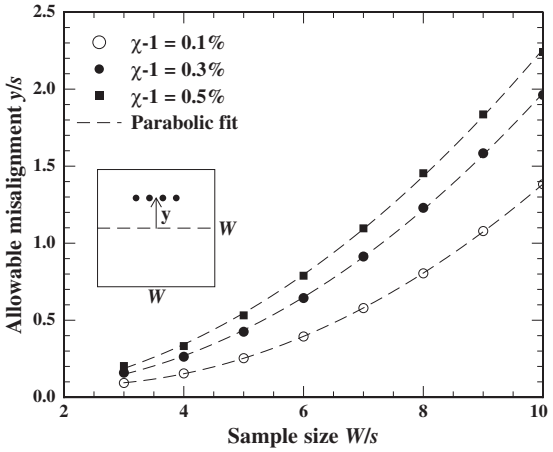

FIG. 16. Allowable misalignment y/s from the ideal position at the center with the probe parallel to the edge of a square sample as a function of the sample size W/s. Calculations for $\chi-1 \in [0.1\%,\ 0.3\%,\ 0.5\%]$ are shown.

required. For smaller samples a closer relative proximity to the parallel boundary is allowed.

Figure 17 shows error parameter χ as a function of the probe angle θ when the probe is placed in the center of a square or rectangular sample; initially, the probe is parallel to the longer edge of the sample. Calculations are shown for squares with $W/s \in [3,\ 3.2,\ 3.5,\ 5]$ and rectangles with $H/W \in [3s/3.2s,\ 3s/3.5s,\ 3s/5s,\ 3s/8s]$. In all cases $\chi \leq 1$ results; it follows that errors due to simultaneous lateral and angular misalignments tend to cancel in the same manner as seen in the case of a narrow stripe sample. For square samples the two types of mirror planes are easily recognized, and the errors due to angular misalignment are small. For instance, the smallest square ($W=3s$) where the probe just fits in has $1-\chi \leq 1\%$, and the error diminishes rapidly with increasing sample size and has almost vanished at $W=5s$. For rectangular samples the two mirror planes are recognized, and the allowable angular misalignment near these two planes differs in the same manner as seen with a narrow stripe; in fact the curve shown for $H/W=3s/8s$ may hardly

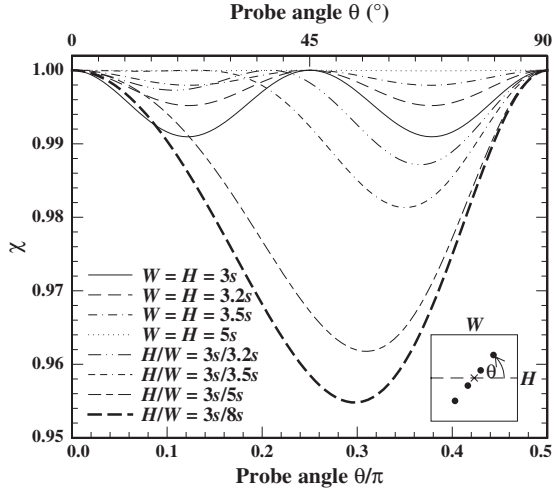

FIG. 17. Error parameter χ as a function of probe angle θ with the M4PP positioned at the center of a square or a rectangle. Calculations for squares with $W/s \in [3,\ 3.2,\ 3.5,\ 5]$ and rectangles with $H/W \in [3s/3.2s,\ 3s/3.5s,\ 3s/5s,\ 3s/8s]$ are shown.

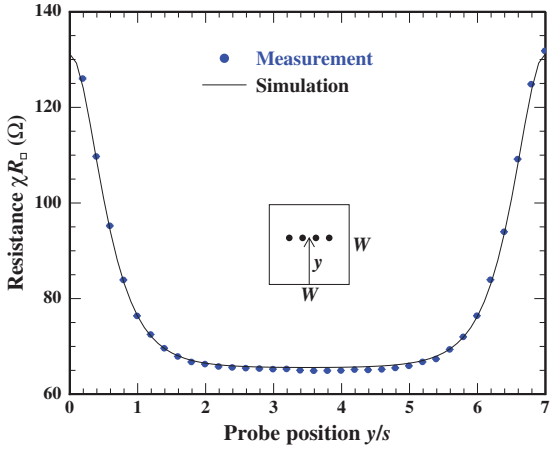

FIG. 18. (Color online) A series of M4PP measurements (•) on an approximately 70×70 μm^2 sample using a 10 μm pitch probe arranged parallel to a sample edge; between each measurement the probe position is incremented by 2 μm normal to the line of the probe. The full curve shows model calculations. Excellent agreement between measurement data and model is seen. Note, error bars on the experimental resistance data are drawn, but are not visible.

be distinguished from the corresponding curve for the stripe $W=3s$ in Fig. 6.

A comparison of the calculations for the probe aligned parallel to a diagonal and parallel to a side of a square sample, Figs. 14 and 16, respectively, shows that for squares smaller than approximately $8s$, the allowable misalignment at 0.3% error is larger for the probe aligned parallel to a side (Fig. 16), thus this represents the preferable measurement configuration on small squares; moreover in this configuration a displacement of the probe in the orthogonal direction increases the allowable misalignment, as seen in Fig. 15. A comparison with the circular disk sample in Fig. 11 reveals that measurements on a square sample parallel to the sides are more favorable than measurements on the inscribed circular disk sample.

1. Square samples: Experiments

Figure 18 shows a series of M4PP measurements (•) on a shallow p-type Ge junction square pad (approximately 70×70 μm^2) using a 10 μm pitch probe, while Fig. 19 illus-

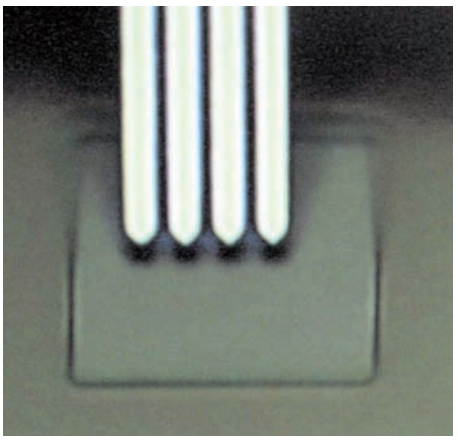

FIG. 19. (Color online) Micrograph showing the 10 μm pitch M4PP above a 70×70 μm^2 pad as seen on the screen of the measurement system.

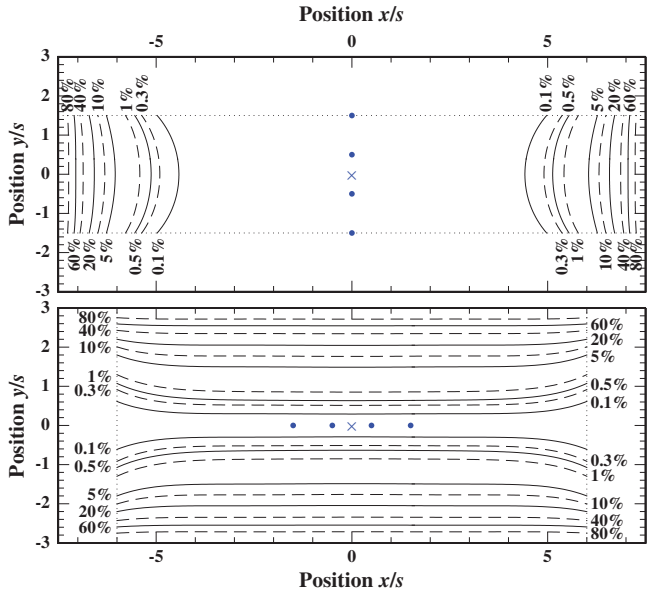

FIG. 20. (Color online) Contour plots showing isoerror curves for a probe arranged parallel to the short (top panel) and long (bottom panel) edge of a rectangle of width $W=15s$ and height $H=6s$, respectively. The boundary of the plots coincides with the sample boundary. The dotted lines show the trajectory of the probe center with one probe pin on the boundary of the sample. To ease visual interpretation of the plots the four-point probes are shown in their ideal positions in the center of the sample. Calculations for $\chi-1 \in [0.1\%,\ 0.3\%,\ 0.5\%,\ 1\%,\ 5\%,\ 10\%,\ 20\%,\ 40\%,\ 60\%,\ 80\%]$ are shown.

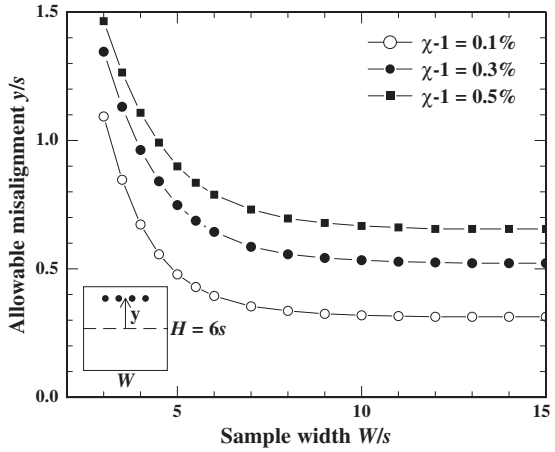

FIG. 21. Allowable misalignment for a M4PP arranged parallel to the edge of width W for a rectangle of height $H=6s$. Calculations are shown for $\chi-1 \in [0.1\%,\ 0.3\%,\ 0.5\%]$ and sample width W in the range from $3s$ to $15s$.

trates the probe positioned above the sample prior to measurements. The measurements in Fig. 18 were obtained with the probe aligned parallel to one edge of the sample while it was scanned in steps of 2 μm in a direction normal to that edge between each measurement. The full curve shows a model fit to the experimental data and excellent agreement between measurement and model is seen; the small discrepancy in the central part of the scan is most likely due to sample inhomogeneity. The error bars on the measured resistance data are invisible since the relative error is $\leq 0.1\%$. Error bars on the position are not drawn, but the absolute error on the 2 μm step length is less than 50 nm, while the error on the absolute position of the first point relative to the sample edge is significantly larger.

F. Rectangular samples

A rectangular sample has two mirror planes through the center, one parallel to the short and one parallel to the long edge. Figure 20 show a contour plot for the probe aligned parallel to the short (top panel) and the long (bottom panel) edge of a rectangle of width $W=15s$ and height $H=6s$, respectively. The boundaries of the plots coincide with the sample boundaries and the dotted lines show the traces of the probe center with one probe pin on the sample boundary, while the full and dashed lines are the isoerror contours. Calculations for $\chi-1 \in [0.1\%,\ 0.3\%,\ 0.5\%,\ 1\%,\ 5\%,\ \times 10\%,\ 20\%,\ 40\%,\ 60\%,\ 80\%]$ are shown. A significantly larger sweet spot is observed for the probe aligned parallel to the short edge, since again a certain minimum distance from a parallel boundary is required. The larger sweet spot is, however, accompanied by a smaller allowable angular misalignment as seen in Fig. 17, but still this is the better configuration in practical measurements.

Figure 21 shows the allowable misalignment y/s from the center as a function of sample width W for a rectangle of height $H=6s$ in the case where the probe is parallel to the edge of length W. Calculations for $\chi-1 \in [0.1\%,\ 0.3\%,\ 0.5\%]$ are shown. Interestingly, the allowable misalignment increases as the sample width decreases due to screening from the boundary orthogonal to the probe. The sample width becomes unimportant when the sample width increases above $W \sim 10s$, i.e., to the probe the sample seems infinitely wide. It follows that on rectangular samples measurements may advantageously be performed with the probe parallel to the shorter edge.

G. Practical measurement issues

Currently, M4PPs are available with an electrode pitch in the range of 0.75–20 μm, while the commonly used probes have an electrode pitch of 10 μm. How accurately these probes may be positioned depends on the measurement system parameters. Currently, with the CAPRES microRSP-M150 system the positioning accuracy is limited primarily by the built-in imaging system, which is inclined at an angle of 60° to the surface. Therefore a practical, conservatively estimated, positioning accuracy better than ± 2.5 μm results, while the angular error to some extent depends on the structure of the sample, however, often an error less than $\pm 2°$ apply. Figure 19 shows a 10 μm pitch probe imaged above a 70×70 μm^2 square sample as seen on the screen of the measurement system. Both misalignment values may be improved if an imaging system with an axis normal to the sample is added. With these practical limitations we shall discuss the implications for practical measurements on the different simple samples.

In the case of a single insulating boundary a measurement with the probe parallel to the boundary may be performed with the probe ~ 40 μm ($3.75s+2.5$ μm) from the boundary using a 10 μm probe, while a measurement with

the probe normal to the boundary is easily performed with the probe at any distance from the boundary since the angular accuracy is always sufficient.

For a stripe, a measurement with the probe normal to the boundaries may be performed on a sample with a width slightly larger than $3s$, i.e., $W \geq 35$ μm for a 10 μm probe, to allow for lateral misalignment. In this case the angular alignment accuracy is sufficient in all cases. With the probe parallel to the boundaries a width of $W \geq 45$ μm ($W \geq 55$ μm) is sufficient at an accuracy of 0.3% (0.1%) for a 10 μm probe. Also here, the angular alignment accuracy is more than sufficient in all cases.

The circular disk sample has a fairly large area where dual configuration measurements are almost unaffected by the proximity of the boundary, from Figs. 11 and 12 it is seen that for a disk of radius $R \geq 23$ μm ($R \geq 29$ μm) an accuracy better than 0.3% (0.1%) is achieved independent on the angular misalignment.

Dual configuration measurements on a square pad are best performed with the probe aligned parallel to a boundary. Considering a 10 μm probe and Fig. 16, measurements using dual configuration are feasible on a square with a side length of 40 μm (50 μm) or more, and here our calculations (Fig. 17) show that an angular misalignment is without importance.

Measurements on rectangles are best performed with the probe parallel to the shorter edge where the allowable misalignment increases significantly. To allow for lateral misalignment the short edge should be longer than 35 μm as in the stripe case.

V. CONCLUSION

We have shown that correction free, accurate sheet resistance measurements may be performed using dual configuration measurements on small samples if the measurement is performed close to mirror planes of the sample. In practical measurements samples with characteristic dimensions $\sim 3s + 5$ μm may be characterized with sufficient care assuming an alignment accuracy of ± 2.5 μm. The preferred sample for accurate measurements is a rectangle or a stripe with the probe aligned normal to the long edges; for such samples a 10 μm pitch M4PP may be used to accurately (0.1%) characterize a sample with a short edge longer than 35 μm. If it is essential that the area of the sample surface is minimized a square sample should be chosen; in this case the 10 μm pitch M4PP may be used to characterize squares with a side length of 40 μm (50 μm) with a resulting accuracy of 0.3% (0.1%).

ACKNOWLEDGMENTS

The authors would like to thank Alessandra Satta and Antoine Brugere for preparation of the Ge sample. We are grateful for the financial support from Copenhagen Graduate School for Nanoscience and Nanotechnology (C:O:N:T), the Danish Research Agency (FTP), and Danish National Advanced Technology Foundation. Center for Individual Nanoparticle Functionality (CINF) is sponsored by The Danish National Research Foundation. We thank Peter Bøggild for continuous support, encouragement and fruitful discussions.

APPENDIX: FOUR-POINT RESISTANCE SOLUTIONS

The potential and the four-point resistance in the single straight boundary case is easily calculated using point current sources and mirrors of these current sources.[9] It is useful to use complex numbers, $z=x+iy$ with $i=\sqrt{-1}$, to represent the coordinates as illustrated in Fig. 22, since that allows use of conformal mapping techniques[25] for more complicated geometries.

In the single straight boundary case, the z-plane in Fig. 22, the potential due to point current sources I at z_p and $-I$ at z_n is

$$\Phi(z,z_p,z_n) = \frac{IR_\square}{2\pi} \ln \left| \frac{(z-z_n)(z-z_n^*)}{(z-z_p)(z-z_p^*)} \right|, \tag{A1}$$

where z^* is the complex conjugate of z. The four-point resistance is $R_A=[\Phi(z_2,z_1,z_4)-\Phi(z_3,z_1,z_4)]/I$, where z_j with $j \in [1,\ 2,\ 3,\ 4]$ are the probe pin positions, thus

$$\frac{2\pi R_A}{R_\square} = \ln \left| \frac{(z_2-z_4)(z_2-z_4^*)}{(z_2-z_1)(z_2-z_1^*)} \frac{(z_3-z_1)(z_3-z_1^*)}{(z_3-z_4)(z_3-z_4^*)} \right|, \tag{A2}$$

and since $R_B=[\Phi(z_2,z_1,z_3)-\Phi(z_4,z_1,z_3)]/I$ the similar relation for R_B is

$$\frac{2\pi R_B}{R_\square} = \ln \left| \frac{(z_2-z_3)(z_2-z_3^*)}{(z_2-z_1)(z_2-z_1^*)} \frac{(z_4-z_1)(z_4-z_1^*)}{(z_4-z_3)(z_4-z_3^*)} \right|. \tag{A3}$$

1. Narrow stripe

The conformal mapping pair $z=\exp(\pi w/W)$ and $w=W/\pi \ln z$ maps the stripe $0 \leq \mathrm{Im}\, w \leq W$ on the upper half-plane $\mathrm{Im}\, z \geq 0$, as illustrated in Fig. 22. In particular the probe pin positions w_j with $j \in [1,\ 2,\ 3,\ 4]$ are mapped into the half plane positions

$$z_j = \exp\left(\pi \frac{w_j}{W}\right). \tag{A4}$$

With these positions the four-point resistances may be calculated using Eqs. (A2) and (A3).

2. Circular disk

The conformal Möbius mapping pair $w=R(z-i)/(z+i)$ and $z=i(R+w)/(R-w)$ maps the circular disk $|w| \leq R$ on the

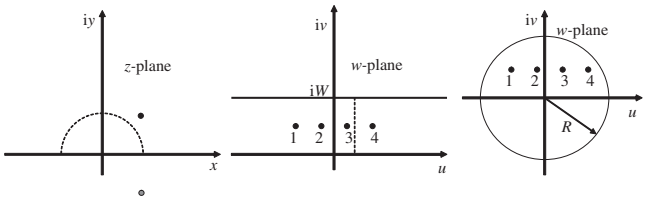

FIG. 22. Left, the upper half plane $\mathrm{Im}\, z \geq 0$ with an insulating boundary at $\mathrm{Im}\, z=0$. In the middle, the narrow stripe $0 \leq \mathrm{Im}\, w \leq W$ with a collinear four-point probe. Right, the circular disk $|w| \leq R$ with a collinear four-point probe.

upper half-plane $\mathrm{Im}\, z \geq 0$. In particular the probe pin positions w_j with $j \in [1, 2, 3, 4]$ are mapped into the half plane positions

$$z_j = i\frac{(R + w_j)}{(R - w_j)}. \tag{A5}$$

With these positions the four-point resistances may be calculated using Eqs. (A2) and (A3).

3. Corner

The conformal mapping pair $z = w^{\pi/\varphi}$ and $w = z^{\varphi/\pi}$ maps the corner $0 \leq \mathrm{Arg}(w) \leq \varphi$ on the upper half-plane $\mathrm{Im}\, z \geq 0$; and in particular the mapping pair $z = w^2$ and $w = \sqrt{z}$ maps the right angle corner $0 \leq \mathrm{Arg}(w) \leq \pi/2$ on the upper half-plane $\mathrm{Im}\, z \geq 0$. The probe pin positions w_j are mapped onto $z_j = w_j^2$.

4. Square

The conformal mapping $w = \int \frac{dz}{\sqrt{z}\sqrt{z^2-1}}$ maps the upper half-plane $\mathrm{Im}\, z \geq 0$ on a square. The integral, however cannot be solved analytically and thus cannot be inverted analytically; it follows that conformal mapping is not as straightforward to apply for evaluation of four-point probing on a square.

[1] D. K. Schroder, *Semiconductor Material and Device Characterization*, 3rd ed. (Wiley, New York, 2006).
[2] P. Blood and J. W. Orton, *The Electrical Characterization of Semiconductors: Majority Carriers and Electron States, Techniques of Physics* (Academic, London, 1992), Vol. 14.
[3] C. L. Petersen, T. M. Hansen, P. Bøggild, A. Boisen, O. Hansen, T. Hassenkam, and F. Grey, Sens. Actuators, A **96**, 53 (2002).
[4] Capres A/S, http://www.capres.com.
[5] T. Clarysse, A. Moussa, F. Leys, R. Loo, W. Vandervorst, M. C. Benjamin, R. J. Hillard, V. N. Faifer, M. I. Current, R. Lin, and D. H. Petersen, Mater. Res. Soc. Symp. Proc. **912**, 197 (2006).
[6] C. L. Petersen, R. Lin, D. H. Petersen, and P. F. Nielsen, *Proceedings of the 14th IEEE International Conference on Advanced Thermal Processing of Semiconductors, RTP 2006* (IEEE, New York, 2006), pp. 153–158.
[7] D. H. Petersen, R. Lin, T. M. Hansen, E. Rosseel, W. Vandervorst, C. Markvardsen, D. Kjær, and P. F. Nielsen, J. Vac. Sci. Technol. B **26**, 362 (2008).
[8] D. H. Petersen, O. Hansen, R. Lin, P. F. Nielsen, T. Clarysse, J. Goossens, E. Rosseel, and W. Vandervorst, *Proceedings of the 16th IEEE International Conference on Advanced Thermal Processing of Semiconductors, RTP 2008* (IEEE, New York, 2008), pp. 251–256.
[9] D. H. Petersen, O. Hansen, R. Lin, and P. F. Nielsen, J. Appl. Phys. **104**, 013710 (2008).
[10] F. M. Smits, Bell Syst. Tech. J. **37**, 711 (1958).
[11] A. Uhlir, Jr., Bell Syst. Tech. J. **34**, 105 (1955).
[12] D. Vaughan, Br. J. Appl. Phys. **12**, 414 (1961).
[13] A. Mircea, J. Sci. Instrum. **41**, 679 (1964).
[14] M. Albert and J. Combs, IEEE Trans. Electron Devices **11**, 148 (1964).
[15] D. Perloff, J. Electrochem. Soc. **123**, 1745 (1976).
[16] M. Buehler and W. Thurber, Solid-State Electron. **20**, 403 (1977).
[17] L. J. Swartzendruber, Solid-State Electron. **7**, 413 (1964).
[18] M. Yamashita and M. Agu, Jpn. J. Appl. Phys., Part 1 **23**, 1499 (1984).
[19] R. Rymaszewski, J. Phys. E: J. Sci. Instrum. **2**, 170 (1969).
[20] D. S. Perloff, J. N. Gan, and F. E. Wahl, Solid State Technol. **24**, 112 (1981).
[21] ASTM Standard F1529, (1997).
[22] M. Yamashita, T. Nishi, and H. Mizutani, Jpn. J. Appl. Phys., Part 1 **42**, 695 (2003).
[23] L. J. van der Pauw, Philips Res. Rep. **13**, 1 (1958).
[24] L. J. van der Pauw, Philips Tech. Rev. **20**, 220 (1958).
[25] W. Kaplan, *Introduction to Analytic Functions* (Addison-Wesley, Reading, MA, 1966).
[26] D. Kjaer, R. Lin, D. H. Petersen, P. M. Kopalidis, R. Eddy, D. A. Walker, W. F. Egelhoff, and L. Pickert, AIP Conf. Proc. **1066**, 167 (2008).

Paper V

J. Appl. Phys. **104**, 013710 (2008).

PhD students contribution:

Conceptual idea and main inventor of method. FEM simulations, experimental work and data treatment for initial proof of concept. Supporting theoretical calculations. Manuscript writing was shared equally with O. Hansen.

Co-authors contribution:

O. Hansen (co-inventor) was the main contributer to the theoretical part of the manuscript and did the final data treatment implementation. Experimental support by R. Lin and P.F. Nielsen.

The paper is based on patent application by D.H. Petersen and O. Hansen.

Micro-four-point probe Hall effect measurement method

Dirch H. Petersen,[1,2] Ole Hansen,[1,3,a)] Rong Lin,[2] and Peter F. Nielsen[2]
[1]*Department of Micro- and Nanotechnology, Technical University of Denmark, DTU Nanotech Building 345 East, DK-2800 Kgs. Lyngby, Denmark*
[2]*CAPRES A/S, Scion-DTU, Building 373, DK-2800 Kgs. Lyngby, Denmark*
[3]*Danish National Research Foundation's Center for Individual Nanoparticle Functionality (CINF), Technical University of Denmark, Building 312, DK-2800 Kgs. Lyngby, Denmark*

(Received 18 February 2008; accepted 23 May 2008; published online 11 July 2008)

We report a new microscale Hall effect measurement method for characterization of semiconductor thin films without need for conventional Hall effect geometries and metal contact pads. We derive the electrostatic potential resulting from current flow in a conductive filamentary sheet with insulating barriers and with a magnetic field applied normal to the plane of the sheet. Based on this potential, analytical expressions for the measured four-point resistance in presence of a magnetic field are derived for several simple sample geometries. We show how the sheet resistance and Hall effect contributions may be separated using dual configuration measurements. The method differs from conventional van der Pauw measurements since the probe pins are placed in the interior of the sample region, not just on the perimeter. We experimentally verify the method by micro-four-point probe measurements on ultrashallow junctions in silicon and germanium. On a cleaved silicon ultrashallow junction sample we determine carrier mobility, sheet carrier density, and sheet resistance from micro-four-point probe measurements under various experimental conditions, and show with these conditions reproducibility within less than 1.5%. © *2008 American Institute of Physics*. [DOI: 10.1063/1.2949401]

I. INTRODUCTION

In processing of semiconductor devices a wide range of analytical techniques are applied for process control and characterization,[1] which is essential due to the very high complexity of the full process flow and due to the high costs involved. Process control and characterization will become even more important and difficult in the future due to the continued scaling of, e.g., complementary metal–oxide–semiconductor (CMOS) processes. In these CMOS processes extremely shallow (<20 nm) source/drain extensions with very high carrier concentration and high carrier mobility are required.[2] Several techniques are applied for characterization of activated ion-implanted shallow junctions; some of these require specialized sample preparation others are destructive or require delicate calibration.[1] Among the parameters that must be characterized are sheet resistance, sheet carrier density, and carrier mobility. Four-point probes are widely used for sheet resistance characterization since essentially no additional sample preparation is necessary.[1] It has recently been shown that micro-four-point probes[3] are able to accurately measure sheet resistance of ultrashallow junctions with high spatial resolution[4] and without artifacts due to probe penetration[5] and leakage current;[6] moreover carrier profiling on beveled ultrashallow junctions has been demonstrated.[7,8]

The implantation and annealing processes used in semiconductor fabrication today cannot guarantee 100% activation of the implanted dose, and defects not removed by annealing may lead to reduced carrier mobility.[9] While standard four-point probe measurements characterize the sheet resistance only, a combination with Hall effect[10] or van der Pauw[11,12] measurements allow separation of the carrier sheet density and mobility contributions to the sheet resistance. The Hall effect characterization, however, usually requires some level of sample preparation, which might even be destructive, e.g., machining of a Greek cross from the sample.[1]

In this work we show analytically and experimentally that standard micro-four-point probes can be applied to Hall effect measurements on thin films in addition to the conventional sheet resistance measurement application. The only additional requirements are that at least one lateral insulating boundary must be present on the sample and that a strong magnetic field can be applied normal to the sample surface. The theoretical findings are verified experimentally by electrical characterization of highly doped ultrashallow junctions in Si and Ge where sheet resistance, sheet carrier concentration, and Hall mobility are determined.

II. THEORY

In a four-point probe measurement a current I_0 is forced through the sample surface using two of the four probe pins, while the resulting potential difference is measured between the two remaining probe pins. The current flow in the sample results in an electrostatic potential distribution at the sample surface, $\Phi(\mathbf{r})=\Phi(\mathbf{r},\mathbf{r}_+,\mathbf{r}_-)$, which is a function of the position of interest, $\mathbf{r}$, the positions of the current injection points, $\mathbf{r}_+$ and $\mathbf{r}_-$, and the sample geometry and resistivity.

We shall consider primarily the colinear probe pin configurations B and B′, as shown in Fig. 1. In configuration B, the current is forced through the sample from pin No. 1 to pin No. 3, $\mathbf{r}_+=\mathbf{r}_1$ and $\mathbf{r}_-=\mathbf{r}_3$, while the potential difference

a)Electronic mail: ohan@nanotech.dtu.dk.

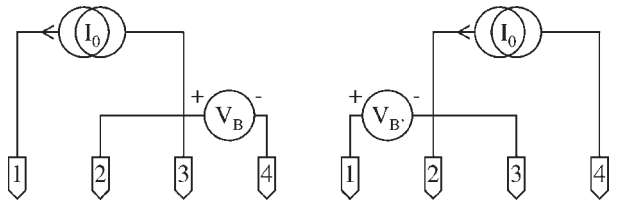

FIG. 1. The four-point probe configurations B and B′. The four probe pins (Nos. 1–4) have position vectors $\mathbf{r}_1$, $\mathbf{r}_2$, $\mathbf{r}_3$, and $\mathbf{r}_4$, respectively. In configuration B probe pins Nos. 1 and 3 are used for current injection, while probe pins Nos. 2 and 4 are used for potential measurements. In configuration B′ the role of the probe pins is reversed.

between pins Nos. 2 and 4 is measured. In configuration B′ the role of the pins is reversed. It follows, that the measured voltages in configurations B and B′ are

$$V_B = \Phi(\mathbf{r}_2,\mathbf{r}_1,\mathbf{r}_3) - \Phi(\mathbf{r}_4,\mathbf{r}_1,\mathbf{r}_3), \tag{1}$$

$$V_{B'} = \Phi(\mathbf{r}_1,\mathbf{r}_2,\mathbf{r}_4) - \Phi(\mathbf{r}_3,\mathbf{r}_2,\mathbf{r}_4), \tag{2}$$

respectively, where $\mathbf{r}_i$ is the in-plane position vector of pin No. i. In micro-four-point probe Hall effect measurements the difference, $\underline{\Delta V_{BB'}} \equiv V_B - V_{B'}$, between these voltages and their average, $\overline{V_{BB'}} \equiv (V_B + V_{B'})/2$, turns out to be particularly useful. In any case, the essential problem is to find the electrostatic potential $\Phi(\mathbf{r},\mathbf{r}_+,\mathbf{r}_-)$ at the surface of the sample in presence of an applied magnetic flux density.

We shall restrict the analysis to thin, laterally homogenous filamentary samples with insulating boundaries. The sample thickness h is assumed small compared to the lateral sample dimensions and to the probe pitch. We shall use Cartesian coordinates with base vectors $\mathbf{e}_x$, $\mathbf{e}_y$, and $\mathbf{e}_z$. Moreover, the magnetic flux density $\mathbf{B}$ is assumed constant and normal to the sample $\mathbf{B} = B_z\mathbf{e}_z$. As a result, the current density, $\mathbf{J}$, the electric field, $\mathbf{E}$, and the Lorentz force, $\mathbf{F} = Ze(\mathbf{E} + \mathbf{v}_d \times \mathbf{B})$, are normal to the magnetic flux density except in a small region in close proximity of the current injection points; we shall ignore this region since its effect is insignificant on a length scale set by the probe pitch. It follows that the problem of solving for the potential and the electric field is reduced to two dimensions. Here Ze is the carrier charge ($Z = \pm 1$), e the unit charge, and $\mathbf{v}_d$ is the carrier drift velocity. With these simplifications the current density becomes[13,14]

$$\mathbf{J} = \sigma_d(\mathbf{E} - Z\mu_H\mathbf{B} \times \mathbf{E}), \tag{3}$$

where we have explicitly used the condition $\mathbf{B}\cdot\mathbf{E} = 0$. σ_d is the direct conductivity and μ_H the Hall mobility, both of these parameters might be dependent on the magnetic flux density magnitude. It follows that a tensorial two-dimensional (2D) conductivity $\boldsymbol{\sigma}$ and a corresponding 2D resistivity tensor $\boldsymbol{\varrho} = \boldsymbol{\sigma}^{-1}$ can be defined[15]

$$\boldsymbol{\sigma} = \begin{pmatrix} \sigma_d & \sigma_H \\ -\sigma_H & \sigma_d \end{pmatrix},$$

$$\boldsymbol{\varrho} = \begin{pmatrix} \varrho_0 & -\varrho_H \\ \varrho_H & \varrho_0 \end{pmatrix}, \tag{4}$$

where the resistivity $\varrho_0 = [\sigma_d(1 + \mu_H^2 B_z^2)]^{-1}$, and the Hall conductivity $\sigma_H = \sigma_d Z\mu_H B_z$, while the Hall resistivity $\varrho_H = \varrho_0 Z\mu_H B_z$.

Conventionally, the Hall coefficient $\mathcal{R}_H$ is used as the primary measured entity in Hall effect measurements. The Hall coefficient $\mathcal{R}_H \equiv \mathbf{E}\cdot(\mathbf{B}\times\mathbf{J})/|\mathbf{B}\times\mathbf{J}|^2 = Z\mu_H\varrho_0 = \varrho_H/B_z$ with the conditions given here.[14] The Hall coefficient has the same sign as the carrier charge and is inversely proportional to the carrier density. Unfortunately the Hall mobility is different from the carrier conductivity mobility μ, $\mu_H = r_H\mu$, where r_H is the Hall scattering factor. The Hall scattering factor is of the order 1 and accounts for the different statistical averaging needed for the two mobilities,[14] $r_H = \langle\tau_m^2\rangle/\langle\tau_m\rangle^2$, where τ_m is the momentum relaxation time.

If the thin sample is nonhomogenous in the z direction, such that $\sigma_d = \sigma_d(z)$ and $\mu_H = \mu_H(z)$, the potential remains two dimensional, $\Phi = \Phi(x,y)$, except in the small region in close proximity of the current injection points. The current density, however, varies in the z-direction $\mathbf{J} = \mathbf{J}(x,y,z)$, while $J_z = 0$. Integration of Eq. (3) across the thickness of the sample yields the sheet current density $\mathbf{J}_S = \mathbf{J}_S(x,y)$,

$$\mathbf{J}_S \equiv \int_0^h \mathbf{J}\mathrm{d}z = \mathbf{E}\int_0^h \sigma_d\mathrm{d}z - \mathbf{e}_z \times \mathbf{E}\int_0^h \sigma_H\mathrm{d}z, \tag{5}$$

where the direct sheet conductance G_d and the Hall sheet conductance G_H can be defined as follows:

$$G_d \equiv \int_0^h \sigma_d\mathrm{d}z \quad \text{and} \quad G_H \equiv \int_0^h \sigma_H\mathrm{d}z. \tag{6}$$

With this definition Eq. (5) becomes

$$\mathbf{J}_S = G_d\mathbf{E} - G_H\mathbf{e}_z \times \mathbf{E}. \tag{7}$$

It follows that sheet conductance, $\boldsymbol{G}_S$, and sheet resistance, $\boldsymbol{R}_S = \boldsymbol{G}_S^{-1}$, tensors,

$$\boldsymbol{G}_S = \begin{pmatrix} G_d & G_H \\ -G_H & G_d \end{pmatrix},$$

$$\boldsymbol{R}_S = \begin{pmatrix} R_0 & -R_H \\ R_H & R_0 \end{pmatrix}, \tag{8}$$

may be defined, where the direct sheet resistance is $R_0 = [G_d(1 + G_H^2/G_d^2)]^{-1}$, while the relative Hall sheet resistance equals the relative Hall sheet conductance, $R_H/R_0 = G_H/G_d$. In analogy to the Hall coefficient a sheet Hall coefficient may be defined as $\mathcal{R}_{\mathrm{HS}} \equiv \mathbf{E}\cdot(\mathbf{B}\times\mathbf{J}_S)/|\mathbf{B}\times\mathbf{J}_S|^2 = R_H/B_z$.[1]

In the homogenous region of interest, Ω, the sheet current density must be divergence free, $\nabla\cdot\mathbf{J}_S = 0$, except at the current injection points, furthermore, the sheet current density normal to the insulating boundary $\delta\Omega$ must vanish. It follows from Eq. (7) that the electrostatic potential, Φ, must fulfill

$$\nabla\cdot\mathbf{J}_S = -G_d\nabla_{2\mathrm{D}}^2\Phi = I_0[\delta(\mathbf{r}-\mathbf{r}_+) - \delta(\mathbf{r}-\mathbf{r}_-)] \text{ in } \Omega,$$

$$\mathbf{J}_S \cdot \mathbf{n} = (G_d \mathbf{E} - G_H \mathbf{e}_z \times \mathbf{E}) \cdot \mathbf{n} = 0 \text{ on } \delta\Omega, \tag{9}$$

since $\mathbf{E}=-\nabla\Phi$, and $\nabla\cdot(\mathbf{B}\times\mathbf{E})=\mathbf{E}\cdot(\nabla\times\mathbf{B})-\mathbf{B}\cdot(\nabla\times\mathbf{E})=0$ for a constant position- and time-independent magnetic flux density. Here $\mathbf{r}=(x,y)$ is the in-plane position vector, $\mathbf{r}_+$ and $\mathbf{r}_-$ are the points where the currents $\pm I_0$ are injected, while $\mathbf{n}$ is the unit vector normal to the lateral insulating boundary $\delta\Omega$, and $\delta(\mathbf{r})$ is Dirac's delta function. Note the magnetic flux density affects the potential only through the boundary conditions.

In Secs. II A–II C and in the Appendix, we shall solve Eq. (9) for a number of sample geometries relevant to four-point probe measurements; these solutions differ from the solutions given by van der Pauw[12] since the probe pins are assumed to be in the interior of the region Ω, and not restricted to the perimeter $\delta\Omega$ as assumed by van der Pauw.

A. Infinite sheet

If the lateral boundaries of the sample are infinitely far from the current injection points the potential which solves Eq. (9) is particularly simple, a superposition of two logarithmic potentials

$$\Phi(\mathbf{r}) = \frac{I_0}{2\pi G_d}\ln\frac{|\mathbf{r}-\mathbf{r}_-|}{|\mathbf{r}-\mathbf{r}_+|} = \frac{I_0 R_0}{2\pi}\left(1+\frac{R_H^2}{R_0^2}\right)\ln\frac{|\mathbf{r}-\mathbf{r}_-|}{|\mathbf{r}-\mathbf{r}_+|}, \tag{10}$$

which is formally identical to the solution[16] for zero magnetic flux density except for the effect of the magnetic flux density on the direct conductivity, $\sigma_d=\sigma_d(B)$. The current density, however, is different since it is not only a sum of two purely radial current density contributions, two additional tangential current density contributions around each current injection point are also needed.

Using the colinear probe configurations B and B′, as shown in Fig. 1, we find from the potential in Eq. (10) that the measured voltages V_B and $V_{B'}$ are equal

$$V_B = V_{B'} = \frac{I_0 R_0}{2\pi}\left(1+\frac{R_H^2}{R_0^2}\right)\ln\frac{|\mathbf{r}_2-\mathbf{r}_3|}{|\mathbf{r}_2-\mathbf{r}_1|}\frac{|\mathbf{r}_4-\mathbf{r}_1|}{|\mathbf{r}_4-\mathbf{r}_3|}, \tag{11}$$

a result that is valid for an arbitrary two-dimensional spatial arrangement of the four probe pins. If the probe pins are equidistant with the pitch s, the measured voltages in the two configurations are

$$V_B = V_{B'} = \frac{I_0 R_0}{2\pi}\left(1+\frac{R_H^2}{R_0^2}\right)\ln 3, \tag{12}$$

a result that except for the factor $(1+R_H^2/R_0^2)=(1+\bar{\mu}_H^2 B_z^2)$ is identical to the result at zero magnetic flux density. This factor accounts for part of the magnetoresistance, which at ordinary magnetic flux densities is a quite small effect, except in very high mobility samples. The average Hall mobility $\bar{\mu}_H$ is defined in Eq. (24).

B. Semi-infinite sheet—Upper half-plane

In the case of the semi-infinite sheet, $y\geq 0$, the solution to Eq. (9) can be obtained using the method of images;[17] the arrangement of current injection sources and images is shown in Fig. 2. The images, however, must be modified in order to fulfill the boundary condition $J_{Sy}(x,0)=0$, since the usual image method would ensure $E_y(x,0)=0$, while $J_{Sy}(x,0)=0$ requires $G_d E_y(x,0)-G_H E_x(x,0)=0$ and thus $E_y(x,0)=(G_H/G_d)E_x(x,0)$.

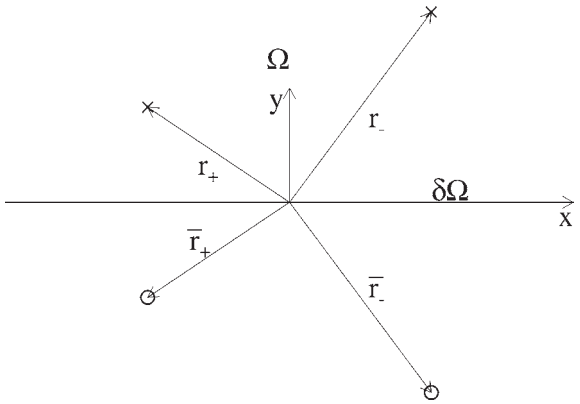

FIG. 2. The arrangement of current injection sources (×) and modified images (◯) in the case of an insulating boundary at $y=0$.

The potential that solves Eq. (9) in Ω is

$$\Phi(\mathbf{r}) = \mathcal{A}_+ \ln\frac{|\mathbf{r}-\mathbf{r}_-|}{|\mathbf{r}-\mathbf{r}_+|} + \mathcal{A}_- \ln\frac{|\mathbf{r}-\bar{\mathbf{r}}_-|}{|\mathbf{r}-\bar{\mathbf{r}}_+|} + \frac{I_0 R_H}{\pi}\left(\arctan\frac{x-x_+}{y+y_+} - \arctan\frac{x-x_-}{y+y_-}\right), \tag{13}$$

where $\bar{\mathbf{r}}_\pm=(\bar{x}_\pm,\bar{y}_\pm)=(x_\pm,-y_\pm)$ are the positions of the modified images of the sources at positions $\mathbf{r}_\pm$. The first term is the source term, while the two remaining terms originate from the images, they are thus due to the boundary conditions at $y=0$. For each of the current sources the boundary conditions are fulfilled by combining a source term representing a purely radial electric field with image terms representing a purely radial current density. For later convenience the coefficients $\mathcal{A}_+$ and $\mathcal{A}_-$ have been defined as follows:

$$\mathcal{A}_+ \equiv \frac{I_0 R_0}{2\pi}\left(1+\frac{R_H^2}{R_0^2}\right),$$

$$\mathcal{A}_- \equiv \frac{I_0 R_0}{2\pi}\left(1-\frac{R_H^2}{R_0^2}\right). \tag{14}$$

Using Eqs. (1) and (2) the measured voltages in probe configurations B and B′ are calculated (the overbar in, e.g., $\bar{\mathbf{r}}_+$ is used as an operator). From these the voltage difference $\Delta V_{BB'}$ results

$$\Delta V_{BB'} = \frac{2 I_0 R_H}{\pi}\left(\arctan\frac{x_2-x_1}{y_2+y_1} + \arctan\frac{x_3-x_2}{y_3+y_2} + \arctan\frac{x_4-x_3}{y_4+y_3} - \arctan\frac{x_4-x_1}{y_1+y_4}\right), \tag{15}$$

while the average voltage $\overline{V_{BB'}}$ becomes

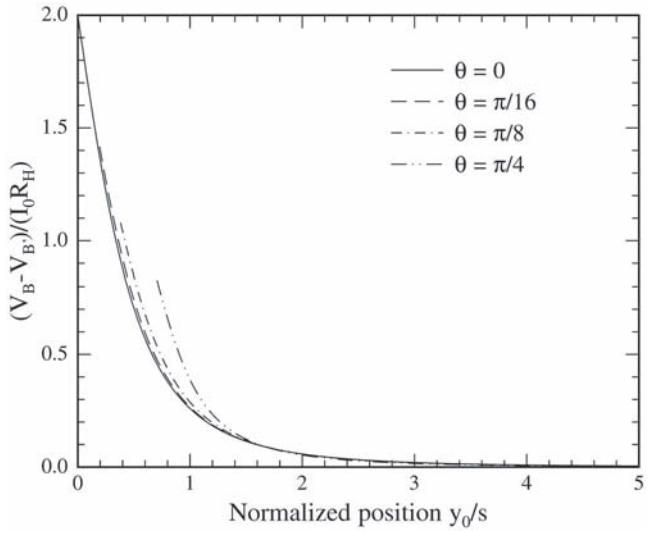

FIG. 3. The difference between measured voltages in configurations B and B′, when the region of interest is the upper half-plane, as a function of normalized position y_0/s, where y_0 is the distance from the boundary to the probe center. Calculations [Eqs. (15) and (17)] are shown for four different angles, $\theta \in [0, \pi/16, \pi/8, \pi/4]$, between the line of the probe pins and the insulating boundary; the line of the probe pins and the boundary are parallel at $\theta=0$.

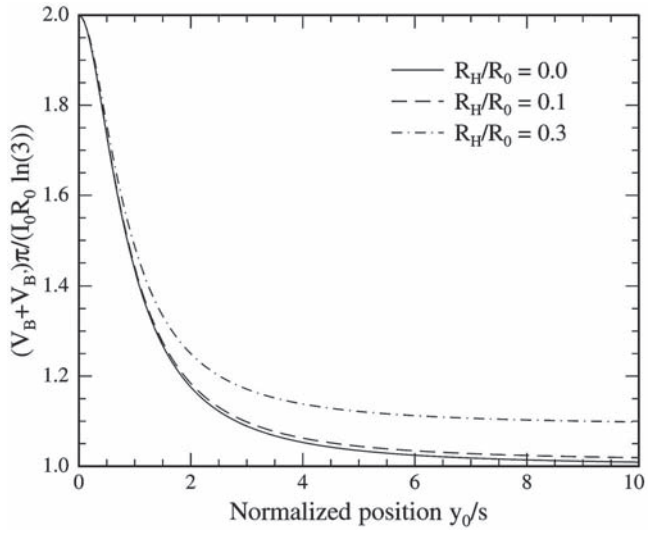

FIG. 4. Position dependence of the average of the measured voltages in configurations B and B′ when the region of interest is the upper half-plane. Voltages calculated from Eq. (18) for three different values of the relative Hall sheet resistance R_H/R_0=0.0, 0.1, and 0.3, respectively, are shown. In silicon or germanium $R_H/R_0<0.1$ at ordinary magnetic flux densities.

$$\overline{V_{BB'}} = \frac{I_0 R_0}{2\pi}\left(1+\frac{R_H^2}{R_0^2}\right)\ln\frac{|\mathbf{r}_2-\mathbf{r}_3|}{|\mathbf{r}_2-\mathbf{r}_1|}\frac{|\mathbf{r}_4-\mathbf{r}_1|}{|\mathbf{r}_4-\mathbf{r}_3|} + \frac{I_0 R_0}{2\pi}\left(1-\frac{R_H^2}{R_0^2}\right)\ln\frac{|\mathbf{r}_2-\bar{\mathbf{r}}_3|}{|\mathbf{r}_2-\bar{\mathbf{r}}_1|}\frac{|\mathbf{r}_4-\bar{\mathbf{r}}_1|}{|\mathbf{r}_4-\bar{\mathbf{r}}_3|}. \quad (16)$$

These equations are valid for any arbitrary spatial probe pin arrangement.

In a practical measurement, with equidistant, colinear four-point probe pins aligned parallel to the y axis such that the four probe pins are positioned at (is, y_0), $i \in \{0,1,2,3\}$, arranged in configurations B and B′, the measured voltages V_B and $V_{B'}$ can be combined as follows:

$$\Delta V_{BB'} = \frac{2I_0 R_H}{\pi}\left(3\arctan\frac{s}{2y_0} - \arctan\frac{3s}{2y_0}\right) \quad (17)$$

and

$$\overline{V_{BB'}} = \mathcal{A}_+ \ln 3 + \mathcal{A}_- \ln\sqrt{\frac{9+4\left(\frac{y_0}{s}\right)^2}{1+4\left(\frac{y_0}{s}\right)^2}}. \quad (18)$$

From Eq. (17) the Hall sheet resistance R_H can be extracted using measured data as a function of distance to the boundary, thereafter the direct sheet resistance R_0 can be determined using Eq. (18).

In Fig. 3, $(V_B-V_{B'})/(I_0R_H)$, calculated from Eqs. (17) and (15), is shown as a function of the normalized distance y_0/s of the probe center to the boundary at $y=0$, where $V_B-V_{B'}=2I_0R_H$. Calculations for four different angles, $\theta \in [0, \pi/16, \pi/8, \pi/4]$, between the line of probe pins and the boundary are shown; at the angle $\theta=\pi/2$ the Hall voltage contribution vanishes, $\Delta V_{BB'}=0$. The measured voltage difference is seen to be significant only very close to the boundary and vanish if the distance is more than a few times the probe pitch. The effect of a small angular misalignment between the probe and the boundary is seen to be very small in the case where parallel probe and boundary is wanted.

In Fig. 4, $(V_B+V_{B'})\pi/(I_0R_0 \ln 3)$, calculated from Eq. (18) is shown as a function of the normalized distance y_0/s from the boundary $y=0$ at three values of the relative Hall resistance, R_H/R_0. The sum of the measured voltages is independent on the relative Hall resistance close to the boundary, where the measured value, $V_B+V_{B'}=(R_0I_0 \ln 3)/\pi$, is twice the value measured very far from the edge at zero magnetic flux density. Far from the edge the full effect of the magnetoresistance affects the sum of the measured voltages. Equation (18) is reminiscent of the usual single insulating boundary proximity correction for four-point probe sheet resistance measurements on thin films.[18,19]

C. Narrow stripe

The potential in the stripe $0 \le y \le w$ with insulating boundaries at $y=0$ and $y=w$ can be found from an infinite sum of alternating modified and ordinary images. The sources and ordinary images are positioned at $\mathbf{r}_\pm + 2n\mathbf{w}$, where the vector $\mathbf{w}=w\mathbf{e}_y$ and n is an arbitrary integer, while the modified images are positioned at $\bar{\mathbf{r}}_\pm + 2n\mathbf{w}$, as illustrated in Fig. 5.

The potential that solves Eq. (9) in Ω is

$$\Phi(\mathbf{r}) = \mathcal{A}_+\sum_{n=-\infty}^{\infty}\ln\frac{|\mathbf{r}-\mathbf{r}_- - 2n\mathbf{w}|}{|\mathbf{r}-\mathbf{r}_+ - 2n\mathbf{w}|} + \mathcal{A}_-\sum_{n=-\infty}^{\infty}\ln\frac{|\mathbf{r}-\bar{\mathbf{r}}_- - 2n\mathbf{w}|}{|\mathbf{r}-\bar{\mathbf{r}}_+ - 2n\mathbf{w}|} + \frac{I_0R_H}{\pi}\sum_{n=-\infty}^{\infty}\left(\arctan\frac{x-x_+}{y+y_+-2nw} - \arctan\frac{x-x_-}{y+y_--2nw}\right). \quad (19)$$

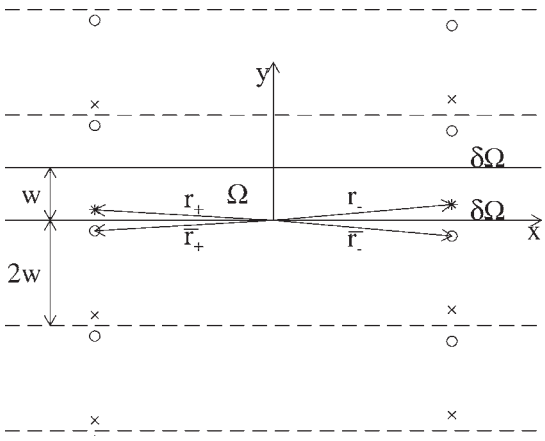

FIG. 5. Arrangement of sources (*), ordinary images (×), and modified images (◯) in the narrow stripe $0 \le y \le w$.

From this potential, the measured voltages, V_B and $V_{B'}$, in configuration B and B′ can be calculated using Eqs. (1) and (2); these voltages can be subtracted or added to yield

$$\Delta V_{BB'} = \frac{2I_0R_H}{\pi}\sum_{n=-\infty}^{\infty}\left(\arctan\frac{x_2-x_1}{y_2+y_1-2nw} + \arctan\frac{x_3-x_2}{y_3+y_2-2nw} + \arctan\frac{x_4-x_3}{y_4+y_3-2nw} - \arctan\frac{x_4-x_1}{y_4+y_1-2nw}\right), \tag{20}$$

and

$$\overline{V_{BB'}} = \mathcal{A}_+\sum_{n=-\infty}^{\infty}\ln\frac{|\mathbf{r}_2-\mathbf{r}_3-2n\mathbf{w}|}{|\mathbf{r}_2-\mathbf{r}_1-2n\mathbf{w}|}\frac{|\mathbf{r}_4-\mathbf{r}_1-2n\mathbf{w}|}{|\mathbf{r}_4-\mathbf{r}_3-2n\mathbf{w}|} + \mathcal{A}_-\sum_{n=-\infty}^{\infty}\ln\frac{|\mathbf{r}_2-\bar{\mathbf{r}}_3-2n\mathbf{w}|}{|\mathbf{r}_2-\bar{\mathbf{r}}_1-2n\mathbf{w}|}\frac{|\mathbf{r}_4-\bar{\mathbf{r}}_1-2n\mathbf{w}|}{|\mathbf{r}_4-\bar{\mathbf{r}}_3-2n\mathbf{w}|}. \tag{21}$$

In a practical measurement, with an equidistant, colinear four-point probe aligned parallel to the y axis such that the four probe pins are positioned at (is, y_0), $i \in \{0,1,2,3\}$, arranged in configurations B and B′, the measured voltages, V_B and $V_{B'}$, can be combined as follows:

$$\Delta V_{BB'} = \frac{2I_0R_H}{\pi}\sum_{n=-\infty}^{\infty}\left(3\arctan\frac{s}{2y_0-2nw} - \arctan\frac{3s}{2y_0-2nw}\right), \tag{22}$$

and

$$\overline{V_{BB'}} = \mathcal{A}_+\sum_{n=-\infty}^{\infty}\ln\sqrt{\frac{9s^2+4n^2w^2}{s^2+4n^2w^2}} + \mathcal{A}_-\sum_{n=-\infty}^{\infty}\ln\sqrt{\frac{9s^2+4(y_0-nw)^2}{s^2+4(y_0-nw)^2}}. \tag{23}$$

In Fig. 6, $(V_B - V_{B'})/(I_0R_H)$, calculated from Eq. (22) is shown as a function of the normalized distance y_0/s from the boundary $y=0$ for a stripe of width $w=5s$; the measured voltage difference is seen to be significant only very close to the boundaries and vanish if the distance from each boundary is more than a few times the probe pitch. In Fig. 6, the result for a half-plane, Eq. (17), is also shown for comparison; this simple result is quite similar to the result for the stripe close to the left boundary. Finally, the approximation resulting from the first two terms in Eq. (22) is shown, but cannot be distinguished from the exact solution; it follows that the sum in Eq. (22) converges very rapidly.

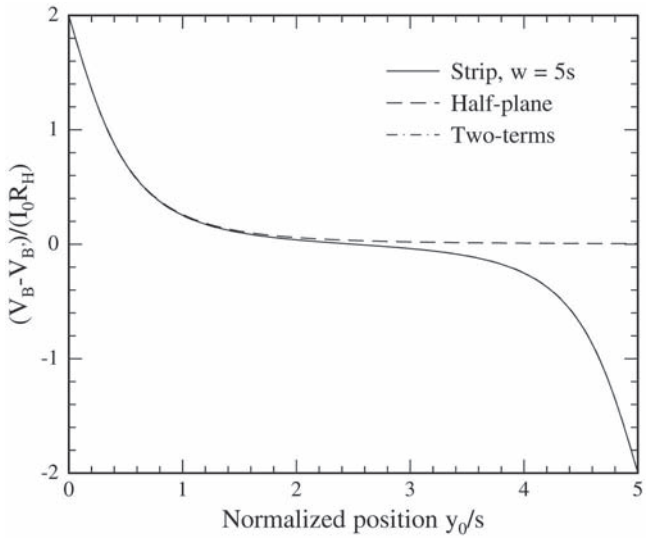

FIG. 6. Position dependence of the difference between measured voltages in configuration B and B′ when the region of interest is the stripe $0 \le y \le w$ [Eq. (22); full line]. The width of the region is assumed to be $w=5s$, where s is the probe pitch. For comparison the result for the upper half-plane region [Eq. (17); dashed line] is also shown. Finally, the approximate result from using only the first two terms in the infinite sum of Eq. (22) is shown, but cannot be distinguished from the full solution.

In Fig. 7, $(V_B+V_{B'})\pi/(I_0R_0 \ln 3)$, calculated from Eq. (23), is shown as a function of the normalized distance y_0/s

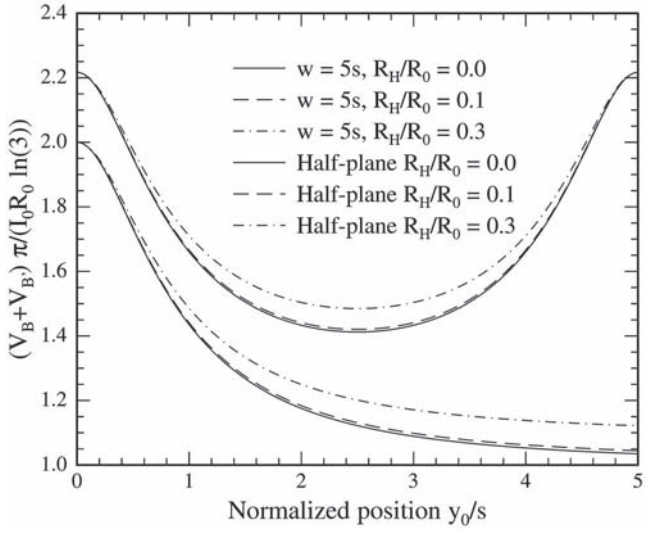

FIG. 7. Position dependence of the average measured voltages in configuration B and B′ when the region of interest is the stripe $0 \le y \le w$ [Eq. (23); upper set of curves]. The width of the region is assumed to be $w=5s$, where s is the probe pitch. For comparison results for the upper half-plane region are also shown [Eq. (18); lower set of curves]. Results for three different values of the relative Hall sheet resistance R_H/R_0 are shown.

from the boundary $y=0$ for a stripe of width $w=5s$ at three values of the relative Hall sheet resistance R_H/R_0. The sum of the measured voltages is independent on the relative Hall sheet resistance close to the boundary. Far from the edge the full effect of the magnetoresistance affects the sum of the measured voltages. The finite width of the stripe affects the sum of the measured voltages at all positions as seen from a comparison with the result for a half-plane, Eq. (18), which is also shown in Fig. 7 for convenience.

D. Interpretation of Hall effect measurements

The primary applications of Hall effect measurements on semiconductor samples are experimental characterization of Hall mobility and carrier concentration. For a homogenous sample, the Hall mobility can be calculated from the measured quantities, the Hall conductivity σ_H, the direct conductivity σ_d (or the respective resistivities), and the magnetic flux density, since $\mu_H=\sigma_H/(\sigma_d Z B_z)=\varrho_H/(\varrho_0 Z B_z)$. The Hall mobility can also be calculated from the Hall coefficient $\mu_H=\mathcal{R}_H/(\varrho_0 Z)$. For a sample with carrier density, $n=n(z)$, and thus mobility variations in the z direction a mean Hall mobility, $\bar{\mu}_H$, can be calculated from the measured Hall sheet conductance, G_H, and direct sheet conductance, G_d, according to[20]

$$\bar{\mu}_H=\frac{G_H}{G_d Z B_z}=\frac{\int_0^h n\mu\mu_H \mathrm{d}z}{\int_0^h n\mu \mathrm{d}z}=\frac{R_H}{R_0 Z B_z}, \tag{24}$$

where Eq. (6) and $\sigma_d=e\mu n$ have been used. The equation $\sigma_d=e\mu n$ is valid at sufficiently low magnetic flux densities.

For a homogenous sample the carrier density is then $n=\sigma_d/e\mu=r_H\sigma_d/(e\mu_H)=r_H Z B_z \sigma_d^2/(e\sigma_H)$. Using relations between resistivities and conductivities the carrier density becomes $n=r_H Z B_z \sigma_d \varrho_0/(e\varrho_H)\simeq r_H Z B_z/(e\varrho_H)=r_H Z/(e\mathcal{R}_H)$ and is thus easily calculated from the measured Hall resistivity if the Hall scattering factor is known. The approximation is valid at sufficiently low magnetic flux densities, where $\varrho_0 \simeq 1/\sigma_d$. For a sample that is nonhomogenous in the z direction the sheet carrier density, $N_S\equiv\int_0^h n\mathrm{d}z$, may be calculated from the measured Hall sheet resistance,[20]

$$N_S=\bar{r}_H\frac{Z B_z G_d^2}{e G_H}=\bar{r}_\mathrm{H}\frac{\left(\int_0^h n\mu\,\mathrm{d}z\right)^2}{\int_0^h n\mu\mu_H\,\mathrm{d}z}\simeq\frac{\bar{r}_H Z B_z}{e R_H}, \tag{25}$$

where the average Hall scattering factor, $\bar{r}_H$, is defined as follows:

$$\bar{r}_H=\frac{\left(\int_0^h n\mu^2 r_H \mathrm{d}z\right)\left(\int_0^h n\mathrm{d}z\right)}{\left(\int_0^h n\mu\mathrm{d}z\right)^2}. \tag{26}$$

Since much of the difficulty in interpretation of Hall measurements is related to the average Hall scattering factor, it is often conveniently assumed to equal 1 in practical Hall effect experiments. In such cases, the measured Hall mobility is still correct, but the sheet carrier density should really be stated as a Hall sheet carrier density $N_\mathrm{HS}\equiv N_S/\bar{r}_H$.

The treatment given here only apply to samples that are homogenous in the $x-y$ plane; a nonhomogenous sample is a far more difficult problem.[21]

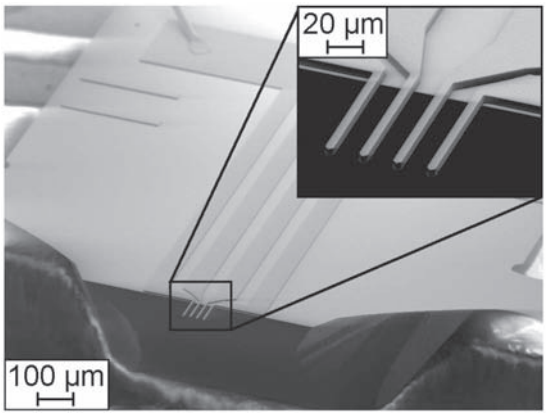

FIG. 8. SEM image of a 20 μm pitch M4PP. The 5 μm thick polysilicon cantilevers are coated with a 200 nm Ni thin film on a 10 nm Ti adhesion layer. The inset shows a close up SEM image of the cantilevers.

III. EXPERIMENTS

Microscale Hall effect measurements were performed with a micro-four-point probe (M4PP) using a CAPRES microRSP-M150 (Ref. 22) system. The M4PP used in these experiments consists of metal coated silicon cantilever electrodes extending from the edge of a silicon die; Fig. 8 shows a scanning electron microscope (SEM) image of a M4PP die with a close up image of the probe cantilevers shown in the inset. In the experiments Ni coated as well as Au coated M4PP's were used. For the microscale Hall measurements, the sample chuck of the microRSP-M150 was fitted with a permanent magnet. The resulting magnetic flux density at the position of the sample was $B_z=0.5$ T as measured using a calibrated Hall sensor.

To explore the potential of the new microscale Hall effect method, highly doped p-type silicon and p-type germanium samples with single and double insulating barrier geometry, respectively, were characterized. These samples are particularly challenging to characterize due to the rather low mobilities and therefore small relative Hall sheet resistances.

First, the sheet resistance is measured far from the insulating barrier (more than three times the electrode pitch) using dual configuration position correction.[4] This is done to determine the sheet resistance more accurately; dual configuration measurements typically allow for sheet resistance repeatability with a standard deviation on the order of 0.1%, whereas the relative standard deviation of a single configuration measurement is an order of magnitude higher depending on the electrode pitch.[23]

Then the M4PP is aligned parallel to an insulating boundary, i.e., the tips of the electrodes are positioned at (is, y_0), $i\in\{0,1,2,3\}$, while the insulating boundary is situated at $y=y_{00}$. After optical alignment, the probe is repeat-

edly engaged with the surface and moved to a new position in a direction perpendicular to the insulating boundary. During each engage, a series of four-point resistance measurements in configurations B and B′ are performed using a measurement current set-point of $I_0=100\ \mu$A. The measurement noise on $\Delta V_{BB'}=\langle V_B-V_{B'}\rangle$ is reduced by averaging the measurements during each engage.

Finally, the Hall sheet resistance R_H and the exact boundary position y_{00} in the probe coordinate system are estimated by fitting to the measured data the appropriate analytical model for the specific geometry, Eqs. (17) or (22), using a nonlinear fitting algorithm.[24] Thereafter, the Hall sheet resistance R_H and standard deviation ΔR_H is calculated using a linear regression where the positions y_0 and y_{00} are used with the analytical model to calculate a nonlinear position axis where a linear relation to $\Delta V_{BB'}$ is expected.

IV. RESULTS AND DISCUSSION

In the Secs. IV A and IV B, where measurements on ultrashallow junctions in silicon and germanium are reported, we experimentally verify the the microscale Hall effect method. A comparative experimental study of this method and alternative characterization methods on ultrashallow junctions is in progress.

A. Silicon—Single barrier

An ultrashallow junction was formed in an *n*-type (100) silicon wafer by low energy boron implantation (3 keV, 1×10^{15} cm^{-2}) followed by rapid thermal annealing (RTA). The nonpatterned wafer was cleaved to provide a well-defined straight insulating boundary. The dual configuration sheet resistance measured on the sample was $267.1\pm0.8\ \Omega$, where the uncertainty is mainly due to sample nonhomogeneity.

On this sample microscale Hall effect measurements were performed under various experimental conditions. For this sample the Hall resistance measurement data were filtered through a simple 40% median filter to eliminate severe measurement outliers (each probe position treated separately) prior to averaging. This was necessary due to measurement noise, probably related to the electrode-sample contact properties.

Figure 9 shows Hall effect measurement data (●) using a 30 μm pitch Au coated M4PP; the full line shows the model fit to the measured data, corresponding to a Hall sheet resistance, $R_H=0.562\pm0.005\ \Omega$, and the estimated boundary position, $y_{00}=0.22\ \mu$m. Hall effect measurements were done using both Au and Ni coated M4PP's in order to investigate if application of a ferromagnetic electrode metal would affect the measurement. Likewise, the effect of electrode pitch and measurement frequency was investigated by performing measurements also using a 10 μm pitch M4PP and by measurements at 11 Hz as well as 987 Hz. The Hall sheet resistances and the corresponding standard deviations extracted from model fits to measurement data are summarized in Table I, where no significant effect of the various experimental conditions is seen. The repeatability even with significant alterations of the experimental conditions is very good, the relative standard deviation on the average of the measurements in Table I is less than 1.5%. The minimum number of measurement points necessary for an accurate extraction of the Hall sheet resistance has not been investigated, but a trade-off between precision and measurement time exists; the total data acquisition time used to produce the data in Fig. 9 was 5 min.

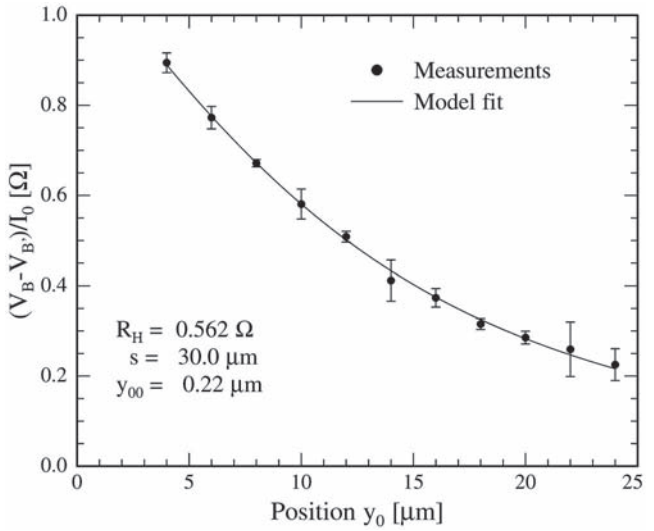

FIG. 9. Microscale Hall effect measurements on a boron doped ultrashallow junction in silicon. The silicon sample has been cleaved to form a semi-infinite sheet and a measurement scan from this edge was performed. The measurement data (●) and a fit (full line) using Eq. (17) with the Hall resistance R_H and the position of the sample edge y_{00} as fitting parameters are shown. The estimated position of the edge is $y_{00}=0.22\ \mu$m.

From the measured Hall sheet resistance and sheet resistance of the sample both active Hall sheet carrier density, N_{HS}, and average Hall mobility, $\bar{\mu}_H$, were calculated using Eqs. (24) and (25), however, since the effective Hall scattering factor is not known $\bar{r}_H=1$ is assumed. The results are summarized in Table I. The calculated active dose is approximately half of the implanted dose; this is in agreement with the expected value since the boron concentration is above the solid solubility and partial dose activation therefore expected. Finally, the Hall mobility is within 10% of the Hall mobility reported by Sasaki for highly boron doped silicon.[25]

B. Germanium—Double barrier

Microscale Hall effect measurements were also performed on a patterned shallow *p*-type junction (80 nm) formed in Ge using RTA of a boron implant (10 keV, 2×10^{15} cm^{-2}) following a preamorphization implant. The pattern used for the measurements was a double insulating barrier with a nominal distance between barriers of 100 μm. Figure 10 illustrates the measurement setup. In the measurements a 20 μm pitch M4PP probe was used at a measurement frequency of 11 Hz. For this sample data were not filtered. Figure 11 shows the measured Hall resistance data (●) resulting from a line scan across the *p*-type stripe; the full line shows a model fit—using Eq. (22)—to measured data with the Hall sheet resistance, R_H, the position of the left boundary, y_{00}, and the width of the stripe, w, as fitting parameters.

TABLE I. Hall sheet resistance R_H and standard deviation extracted from M4PP Hall effect measurements on an ultrashallow boron doped junction in silicon. The active Hall sheet carrier density N_{HS} and Hall mobility $\bar{\mu}_H$ are calculated from M4PP Hall effect and sheet resistance measurements using Eqs. (25) and (24). Four different experimental conditions with variation of electrode material (Au or Ni), probe pitch, s, and measurement frequency, f, were used.

	s (μm)	f (Hz)	$R_H \pm \Delta R_H$ (Ω)	$N_{\mathrm{HS}} \pm \Delta N_{\mathrm{HS}}$ ($\times 10^{14}$ cm^{-2})	$\bar{\mu}_H \pm \Delta\bar{\mu}_H$ (cm^2 V^{-1} s^{-1})
Au	30	11	0.562 ± 0.005	5.55 ± 0.05	42.1 ± 0.4
Ni	10	11	0.570 ± 0.015	5.48 ± 0.14	42.7 ± 1.1
Ni	30	11	0.556 ± 0.008	5.61 ± 0.08	41.6 ± 0.6
Ni	30	987	0.551 ± 0.003	5.66 ± 0.03	41.3 ± 0.3

The experimental results are summarized in Table II. The high precision obtained for the direct sheet resistance ($R_0 = 63.63 \pm 0.02\ \Omega$) does not include sample variations since the measurements were performed at a single position. The low standard deviation on the Hall sheet resistance ($R_H = 0.264 \pm 0.002\ \Omega$) demonstrates the high reproducibility of M4PP measurements on p-type Ge. The calculated active Hall sheet carrier density [$N_{\mathrm{HS}} = (1.18 \pm 0.01) \times 10^{15}$ cm^{-2}] is in good agreement with the expected value considering the implanted dose. The calculated Hall mobility ($\bar{\mu}_H = 83.0 \pm 0.6$ cm^2 V^{-1} s^{-1}) is in agreement with values reported by Golikova *et al.*[26]

V. CONCLUSION

Carrier sheet concentration and mobility are key parameters with a strong effect on semiconductor device performance. Conventional measurements of these parameters become increasingly difficult with the continued miniaturization of CMOS devices, in particular for the ultrashallow junctions required; these parameters nevertheless needs to be characterized for process development and control purposes. In this work we demonstrate for the first time that M4PP's can be used to measure Hall mobility and sheet carrier concentration with little or no additional sample preparation.

The electrostatic potential due to the injected current and applied magnetic flux density is derived for an infinite sheet, a semi-infinite sheet, a narrow stripe, a quarter-plane, and a rectangle. With one or more insulating lateral boundaries present Hall effect affects the potential; without the insulating boundary only magnetoresistance is seen.

The voltage measured with a colinear, equidistant four-point probe is derived for the semi-infinite sheet and the narrow stripe sample geometries. The Hall effect contribution is separated from magnetoresistance and sheet resistance by dual configuration difference and sum methods, respectively. Finally, the sensitivity of the Hall effect signal to small angular misalignment between a four-point probe and an insulating boundary is shown to be virtually zero, which is ideal for experiments.

The theory is verified by experiments on ultrashallow implanted junctions in Si and Ge. The measured sheet carrier concentration and Hall mobility are shown to be reproducible and virtually unaffected by changes in electrode material (diamagnetic versus ferromagnetic), electrode pitch, and measurement frequency.

The microscale Hall effect measurement method has several interesting potential applications since Hall mobility and sheet carrier density may be measured (i) with high spatial resolution, (ii) without the need for lithographically defined metal contacts, (iii) on fragile samples where postpro-

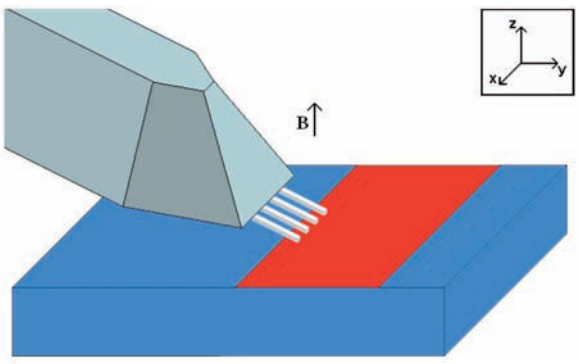

FIG. 10. (Color online) Illustration of a M4PP Hall effect measurement on a narrow stripe of highly doped Ge.

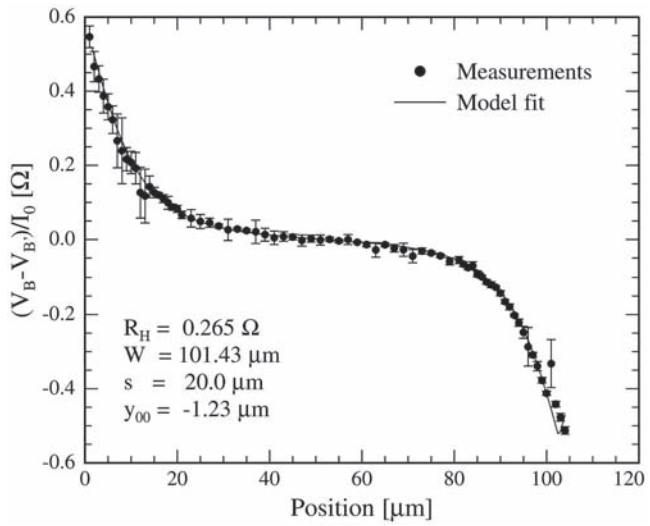

FIG. 11. Microscale Hall effect measurements on a 100 μm wide p-type Ge stripe, doped using a shallow boron implant. A line scan has been performed with a 20 μm pitch probe between the two barriers. The measurement data (●) and a fit (full line) using Eq. (22) with the Hall sheet resistance, R_H, first barrier position, y_{00}, and stripe width, w, as fitting parameters are shown.

TABLE II. Summary of measurements on the shallow *p*-type germanium junction. The sheet resistance, R_0 and the Hall sheet resistance, R_H, were measured using a 20 μm pitch M4PP, and Hall sheet carrier density, N_{HS}, and Hall mobility, $\bar{\mu}_H$, calculated using Eqs. (25) and (24).

$R_0 \pm \Delta R_0$ (Ω)	$R_H \pm \Delta R_H$ (Ω)	$N_{\mathrm{HS}} \pm \Delta N_{\mathrm{HS}}$ ($\times 10^{15}$ cm^{-2})	$\bar{\mu}_H \pm \Delta \bar{\mu}_H$ (cm^2 V^{-1} s^{-1})
63.63 ± 0.02	0.264 ± 0.002	1.18 ± 0.01	83.0 ± 0.6

cessing may alter sample properties, (iv) on micrometer sized samples, and (v) on scribe-line test structures on CMOS device wafers.

ACKNOWLEDGMENTS

The authors would like to thank Alessandra Satta and Antoine Brugere for preparation of the Ge sample. We are grateful for the financial support from Copenhagen Graduate School for Nanoscience and Nanotechnology (C:O:N:T), the Danish Research Agency (FTP). Center for Individual Nanoparticle Functionality (CINF) is sponsored by The Danish National Research Foundation. We thank Peter Bøggild for continuous support, encouragement, and fruitful discussions.

APPENDIX: QUARTER-PLANE AND RECTANGLE

Consider now the upper right quarter plane $x \geq 0$ and $y \geq 0$, see Fig. 12. The sources at $\mathbf{r}_\pm$ must be combined with ordinary images at $-\mathbf{r}_\pm$ and modified images at $\pm\bar{\mathbf{r}}_\pm$, where $\bar{\mathbf{r}}_\pm = (\bar{x}_\pm, \bar{y}_\pm) = (x_\pm, -y_\pm)$ again are the *y*-axis mirrored modified image positions. The potential that solves Eq. (9) in Ω is thus

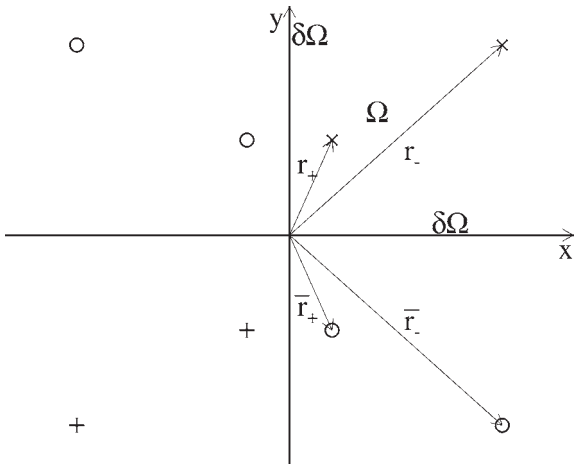

FIG. 12. Arrangement of sources ($\times$), modified images ($\bigcirc$), and ordinary images ($+$) in the upper right quarter plane case.

$$\Phi(\mathbf{r}) = \mathcal{A}_+ \ln\frac{|\mathbf{r}-\mathbf{r}_-|}{|\mathbf{r}-\mathbf{r}_+|}\frac{|\mathbf{r}+\mathbf{r}_-|}{|\mathbf{r}+\mathbf{r}_+|} + \mathcal{A}_- \ln\frac{|\mathbf{r}-\bar{\mathbf{r}}_-|}{|\mathbf{r}-\bar{\mathbf{r}}_+|}\frac{|\mathbf{r}+\bar{\mathbf{r}}_-|}{|\mathbf{r}+\bar{\mathbf{r}}_+|} + \frac{I_0 R_H}{\pi}\left(\arctan\frac{x-x_+}{y+y_+} - \arctan\frac{x-x_-}{y+y_-}\right) - \frac{I_0 R_H}{\pi}\left(\arctan\frac{y-y_+}{x+x_+} - \arctan\frac{y-y_-}{x+x_-}\right). \tag{A1}$$

Here the first term is due to the sources at $\mathbf{r}_\pm$ and the ordinary images at $-\mathbf{r}_\pm$, while the remaining three terms are due to the modified images at $\pm\bar{\mathbf{r}}_\pm$.

The potential in the rectangle, $0 \leq y \leq w$, $0 \leq x \leq \ell$, with insulating boundaries at $y=0$, $y=w$, $x=0$, and $x=\ell$ can be found from a double infinite sum of alternating modified and ordinary images. The sources and ordinary images are positioned at $\pm\mathbf{r}_\pm + 2(n\mathbf{w}+m\boldsymbol{\ell})$, while the modified images are positioned at $\pm\bar{\mathbf{r}}_\pm + 2(n\mathbf{w}+m\boldsymbol{\ell})$, where n and m are arbitrary integers and the vectors $\mathbf{w}=w\mathbf{e}_y$ and $\boldsymbol{\ell}=\ell\mathbf{e}_x$. The potential that solves Eq. (9) in Ω is thus

$$\Phi(\mathbf{r}) = \mathcal{A}_+ \sum_{n=-\infty}^{\infty}\sum_{m=-\infty}^{\infty} \ln\frac{|\mathbf{r}-\mathbf{r}_- - 2(n\mathbf{w}+m\boldsymbol{\ell})|}{|\mathbf{r}-\mathbf{r}_+ - 2(n\mathbf{w}+m\boldsymbol{\ell})|}\frac{|\mathbf{r}+\mathbf{r}_- - 2(n\mathbf{w}+m\boldsymbol{\ell})|}{|\mathbf{r}+\mathbf{r}_+ - 2(n\mathbf{w}+m\boldsymbol{\ell})|} + \mathcal{A}_- \sum_{n=-\infty}^{\infty}\sum_{m=-\infty}^{\infty} \ln\frac{|\mathbf{r}-\bar{\mathbf{r}}_- - 2(n\mathbf{w}+m\boldsymbol{\ell})|}{|\mathbf{r}-\bar{\mathbf{r}}_+ - 2(n\mathbf{w}+m\boldsymbol{\ell})|}\frac{|\mathbf{r}+\bar{\mathbf{r}}_- - 2(n\mathbf{w}+m\boldsymbol{\ell})|}{|\mathbf{r}+\bar{\mathbf{r}}_+ - 2(n\mathbf{w}+m\boldsymbol{\ell})|} + \frac{I_0 R_{\mathrm{H}}}{\pi}\sum_{n=-\infty}^{\infty}\sum_{m=-\infty}^{\infty}\left(\arctan\frac{x-x_+-2m\ell}{y+y_+-2nw} - \arctan\frac{x-x_--2m\ell}{y+y_--2nw}\right) - \frac{I_0 R_{\mathrm{H}}}{\pi}\sum_{n=-\infty}^{\infty}\sum_{m=-\infty}^{\infty}\left(\arctan\frac{y-y_+-2nw}{x+x_+-2m\ell} - \arctan\frac{y-y_--2nw}{x+x_--2m\ell}\right). \tag{A2}$$

Here the first term is due to the sources and ordinary images, while the remaining terms are due to the modified images.

From Eqs. (A1) or (A2) the measured voltages in configurations B and B′ and thus $\Delta V_{BB'}$ and $\overline{V_{BB'}}$ may be calculated; due to the limited space, however, we do not report these equations.

[1] D. K. Schroder, *Semiconductor Material and Device Characterization*, 3rd ed. (Wiley, Hoboken, NJ, 2006).
[2] International Technology Roadmap for Semiconductors, http://www.itrs.net.
[3] C. L. Petersen, T. M. Hansen, P. Bøggild, A. Boisen, O. Hansen, T. Hassenkam, and F. Grey, Sens. Actuators, A **96**, 53 (2002).
[4] D. H. Petersen, R. Lin, T. M. Hansen, E. Rosseel, W. Vandervorst, C. Markvardsen, D. Kjær, and P. F. Nielsen, J. Vac. Sci. Technol. B **26**, 362

(2008).
[5]T. Clarysse, A. Moussa, F. Leys, R. Loo, W. Vandervorst, M. C. Benjamin, R. J. Hillard, V. N. Faifer, M. I. Current, R. Lin, and D. H. Petersen, Mater. Res. Soc. Symp. Proc. **912**, 197 (2006).
[6]C. L. Petersen, R. Lin, D. H. Petersen, and P. F. Nielsen, 14th IEEE International Conference on Advanced Thermal Processing of Semiconductors, RTP '06, pp. 153–158 (IEEE, Danvers, 2006).
[7]T. Clarysse, W. Vandervorst, R. Lin, D. H. Petersen, and P. F. Nielsen, Nucl. Instrum. Methods Phys. Res. B **253**, 136 (2006b).
[8]T. Clarysse, P. Eyben, B. Parmentier, B. V. Daele, A. Satta, W. Vandervorst, R. Lin, D. H. Petersen, and P. F. Nielsen, International Workshop on Insight in Semiconductor Device Fabrication, Metrology and Modeling, Insight 2007, 2008, Vol. 26, p. 317.
[9]H. Ryssel and I. Ruge, *Ion Implantation* (Wiley, Chichester, 1986).
[10]E. H. Hall, Am. J. Math. **2**, 287 (1879).
[11]L. J. van der Pauw, Philips Res. Rep. **13**, 1 (1958a).
[12]L. J. van der Pauw, Philips Res. Rep. **20**, 220 (1958b).
[13]R. S. Popović, *Hall Effect Devices, Magnetic Sensors and Characterization of Semiconductors*, The Adam Hilger Series on Sensors (Adam Hilger, Bristol, 1991).
[14]K. Seeger, *Semiconductor Physics, An Introduction*, Solid-State Sciences No. 40, 5th ed. (Springer, Berlin, 1991).
[15]C. Herring, J. Appl. Phys. **31**, 1939 (1960).
[16]F. M. Smits, Bell Syst. Tech. J. **37**, 711 (1958).
[17]S. Ramo, T. V. Duzer, and J. R. Whinnery, *Fields and Waves in Communication Electronics* (Wiley, New York, 1984).
[18]P. Blood and J. W. Orton, *The Electrical Characterization of Semiconductors: Majority Carriers and Electron States*, Techniques of Physics Vol. 14 (Academic, London, 1992).
[19]L. B. Valdes, Proc. IRE **42**, 420 (1954).
[20]R. Baron, G. A. Shifrin, O. J. Marsh, and J. W. Mayer, J. Appl. Phys. **40**, 3702 (1969).
[21]D. W. Koon and C. J. Knickerbocker, Rev. Sci. Instrum. **64**, 510 (1993).
[22]http://www.capres.com.
[23]C. L. Petersen, D. Worledge, and P. R. E. Petersen, Mater. Res. Soc. Symp. Proc. **738**, 157 (2003).
[24]P. R. Bevington, *Data Reduction and Error Analysis for the Physical Sciences* (McGraw-Hill, New York, 1969).
[25]Y. Sasaki, K. Itoh, E. Inoue, S. Kishi, and T. Mitsuishi, Solid-State Electron. **31**, 5 (1988).
[26]O. A. Golikova, B. Y. Moizhes, and L. S. Stilbans, Sov. Phys. Solid State **3**, 2259 (1962).

Paper VI

in Proc. RTP 2008 (IEEE, New York, 2008) pp. 251-256.

PhD students contribution:

Idea for position error suppression method. Extensive Monte Carlo simulations to define optimal method. All experimental work. Manuscript writing was assisted by O. Hansen.

Co-authors contribution:

Theoretical formulation of Eqs. 4, 5 and 6 was done by O. Hansen. Sample definition and fabrication by T. Clarysse, E. Rosseel, and W. Vandervorst. Supporting SIMS characterization by J. Goossens. Experimental support by R. Lin and P.F. Nielsen.

High precision micro-scale Hall Effect characterization method using in-line micro four-point probes

D.H. Petersen[a,b], O. Hansen[a,c], R. Lin[b], P.F. Nielsen[b], T. Clarysse[d], J. Goossens[d], E. Rosseel[d], W. Vandervorst[d,e]
[a]DTU Nanotech - Dept. of Micro and Nanotechnology, Technical University of Denmark,
B-345 East, DK-2800 Kgs. Lyngby, Denmark,
[b]CAPRES A/S, Scion-DTU, B-373, DK-2800 Kgs. Lyngby, Denmark,
[c]CINF - Centre for Individual Nanoparticle Functionality, Technical University of Denmark,
B-312, DK-2800 Kgs. Lyngby, Denmark,
[d]IMEC, Kapeldreef 75, B-3001 Leuven, Belgium,
[e]KU Leuven, Dept. of Physics-IKS, Celestijnenlaan 200D, B-3001 Leuven, Belgium
E-mail: dhpe@nanotech.dtu.dk, ohan@nanotech.dtu.dk

***Abstract*— Accurate characterization of ultra shallow junctions (USJ) is important in order to understand the principles of junction formation and to develop the appropriate implant and annealing technologies. We investigate the capabilities of a new micro-scale Hall effect measurement method where Hall effect is measured with collinear micro four-point probes (M4PP). We derive the sensitivity to electrode position errors and describe a position error suppression method to enable rapid reliable Hall effect measurements with just two measurement points. We show with both Monte Carlo simulations and experimental measurements, that the repeatability of a micro-scale Hall effect measurement is better than 1 %. We demonstrate the ability to spatially resolve Hall effect on micro-scale by characterization of an USJ with a single laser stripe anneal. The micro sheet resistance variations resulting from a spatially inhomogeneous anneal temperature are found to be directly correlated to the degree of dopant activation.**

Keywords- four-point probe, Hall effect, sheet resistance, dose, mobility, USJ, laser anneal.

I. INTRODUCTION

One of the major challenges for the 32 nm CMOS technology node and beyond is formation of ultra shallow source/drain extensions with very high active dopant concentration and high carrier mobility [1]. In the past, one could safely assume crystalline mobility in many cases when converting sheet resistance to active dopant levels. With more sophisticated processes and structures being developed today (e.g. millisecond anneal, strained Si and SOI), monitoring sheet resistance as well as the degree of dopant activation and carrier mobility in a fast and reliable way is crucial for the understanding of these advanced processes.

Prior experimental work has revealed the need for characterization techniques like the micro four-point probe (M4PP) to accurately characterize sheet resistance of ultra shallow junctions (USJ) [2] with high spatial resolution [3]. Recently, we demonstrated the ability to perform reproducible micro Hall effect measurements to characterize sheet carrier density and mobility of shallow implants in both Si and Ge using M4PP [4]. In a recent comparison between conventional Hall effect methods, Model Based Infra-red spectroscopic Reflectrometry (MBIR) and micro Hall effect measurements, it was found that micro Hall effect measurements seems to give the most reliable results of both sheet resistance, sheet carrier density and carrier mobility when measuring USJ [5].

In this work we demonstrate a new strategy to perform Hall effect measurements with improved measurement precision in less than a minute on unpatterned cleaved wafers with ultra shallow implants. We perform Monte Carlo simulations to investigate the measurement precision and compare this to a repeatability experiment. We then for the first time demonstrate the ability to perform scanning Hall effect measurements with high spatial resolution.

II. THEORY

A. Hall effect measurement

A four-point resistance measurement on a sample is performed by forcing a current, I_0, through two electrodes and simultaneously measuring the potential difference, V, between two other electrodes. In the following we shall consider four-point measurements on a conductive filamentary sheet sample with insulating barriers. Previously, it has been shown that in a moderate magnetic flux density, Hall effect measurements may be performed with a collinear four-point probe in proximity of an insulating barrier, cf. Fig. 1, using two electrode configurations, B and B', where the role of the probe pins are interchanged as illustrated in Figs. 2a and 2b [4].

Two simple definitions become very useful in Hall effect measurements; for resistances measured in configurations B and B', we define the resistance difference, $\Delta R_{BB'} \equiv R_B - R_{B'}$, and the resistance average, $\overline{R_{BB'}} \equiv \left(R_B + R_{B'}\right)/2$. For an equidistant four-point probe placed parallel to a barrier such as a cleaved edge, the resistance difference is [4]

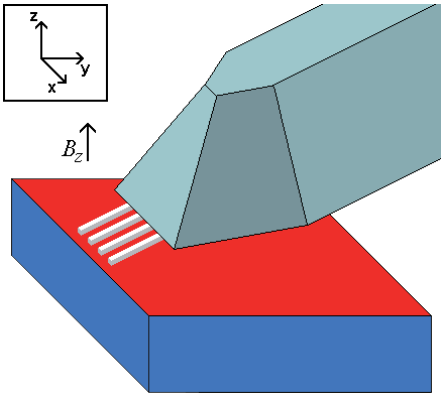

Figure 1. A micro Hall effect measurement is performed with a micro four-point probe (M4PP) positioned in close proximity to an insulating barrier like a cleaved edge.

$$\Delta R_{BB'} = \frac{2R_H}{\pi}\left(3\arctan\left(\frac{s}{2y_0}\right) - \arctan\left(\frac{3s}{2y_0}\right)\right) \quad (1)$$

where R_H is the Hall sheet resistance, s is the electrode pitch and y_0 is the distance between the electrodes and the barrier. The resistance average becomes [4]

$$\overline{R_{BB'}} = \frac{R_0}{2\pi}\left(1+\frac{R_H^2}{R_0^2}\right)\ln(3) + \frac{R_0}{2\pi}\left(1-\frac{R_H^2}{R_0^2}\right)\ln\sqrt{\frac{9+4\left(\frac{y_0}{s}\right)^2}{1+4\left(\frac{y_0}{s}\right)^2}} \quad (2)$$

where R_0 is the direct sheet resistance. Due to symmetry the A and A' configurations, cf. Figs. 2c and 2d, are also interesting since the resistance difference is zero, whereas the resistance average becomes

$$\overline{R_{AA'}} = \frac{R_0}{2\pi}\left(1+\frac{R_H^2}{R_0^2}\right)\ln(4) + \frac{R_0}{2\pi}\left(1-\frac{R_H^2}{R_0^2}\right)\ln\frac{4+4\left(\frac{y_0}{s}\right)^2}{1+4\left(\frac{y_0}{s}\right)^2} \quad (3)$$

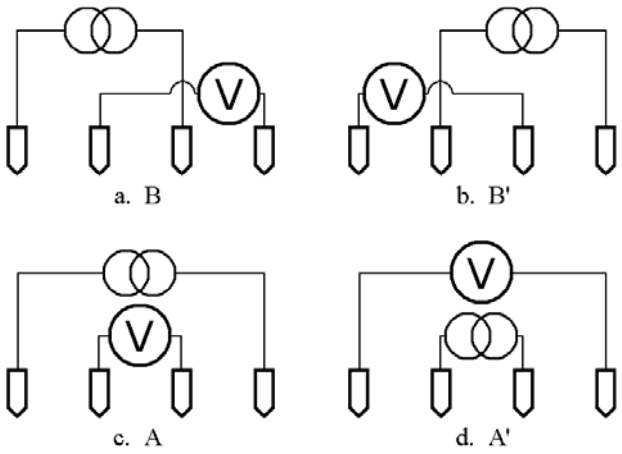

Figure 2. Pin configurations used for Hall sheet resistance and sheet resistance measurements.

The resistance difference, $\Delta R_{BB'}$, can be used to determine the Hall sheet resistance, R_H, while the resistance average can be used to determine the direct sheet resistance, R_0.

B. *Sensitivity to positional errors*

In practical experiments the real positions of the electrodes differ from the ideal positions, and this will affect the measurement precision. Whereas relative position errors between the electrodes may be assumed uncorrelated, the distance between the barrier and the electrodes will result in a correlated position error. Assuming the standard deviations, σ_x and σ_y, of each electrode position are identical for all electrodes, and that the standard deviation on the position of the barrier is σ_b, then the relative standard deviation of $\Delta R_{BB'}$ is [6]

$$\sigma^{rel}_{\Delta R_{BB'}} = \frac{1}{\Delta R_{BB'}}\sqrt{\sum_{N=1}^{4}\left(\left(\frac{\partial \Delta R_{BB'}}{\partial x_N}\right)^2\sigma_x^2 + \left(\frac{\partial \Delta R_{BB'}}{\partial y_N}\right)^2\sigma_y^2\right) + \left(\sum_{N=1}^{4}\frac{\partial \Delta R_{BB'}}{\partial y_N}\sigma_b\right)^2} \quad (4)$$

Based on experience and considerations such as probe positioning accuracy, sample drift and probe tip wear, we assume the magnitude of each position error for a 20 µm pitch M4PP to be σ_x = 500 nm, σ_y = 100 nm and σ_b = 100 nm. The relative standard deviation of the measured resistance difference, $\Delta R_{BB'}$, calculated according to Eq. 4 is then plotted in Fig. 3. The lowest measurement error is found for measurements close to the barrier where the resistance difference is high. Note that for a conventional van der Pauw measurement, the four electrodes are placed on the edge (0 µm from the edge) and the measurement error resulting from the position error σ_x is ideally zero. If the exact position of the probe relative to the barrier can be determined, i.e. σ_b = 0, then the uncertainty of the resistance difference can be reduced to about 0.6 % for a single measurement close to the barrier.

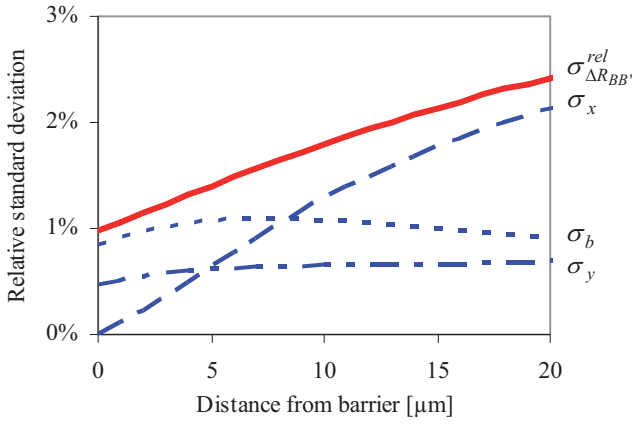

Figure 3. The relative standard deviation of $\Delta R_{BB'}$ measured with a 20 µm pitch M4PP. The relative standard deviation is found by assuming electrode position errors σ_x = 500 nm, σ_y = 100 nm and barrier error σ_b = 100 nm.

C. Position error suppression

The correlated position error, σ_b, can be suppressed if the distance between the probe and the barrier can be determined accurately. To find the average position of the electrodes relative to the barrier and simultaneously extract the sheet resistance, we utilize a dual configuration position correction that is generally used to greatly reduce the effect of electrode position errors on infinite sheets without barriers [7].

$$\exp\left(\frac{2\pi\overline{R_{AA'}}}{R_P}\right)-\exp\left(\frac{2\pi\overline{R_{BB'}}}{R_P}\right)=1 \tag{5}$$

However, due to the presence of the barrier we find a pseudo sheet resistance, R_P, instead of the true sheet resistance. Two pseudo sheet resistance measurements, R_{P1} and R_{P2}, performed with a known distance, Δy, between the measurement positions, may be described as

$$R_{P1}=R_0 f\left(\frac{y_0}{s}\right) \tag{6}$$

$$R_{P2}=R_0 f\left(\frac{y_0+\Delta y}{s}\right) \tag{7}$$

Where R_0 is the direct sheet resistance, y_0 is the position of the barrier, s is the electrode pitch, and the function, f, is implicitly described by Eq. 5. R_0 is eliminated by combining Eqs. 6 and 7.

$$f\left(\frac{y_0}{s}\right)=\frac{R_{P1}}{R_{P2}} f\left(\frac{y_0+\Delta y}{s}\right) \tag{8}$$

Eq. 8 may be solved for y_0 and finally the sheet resistance can be determined by application of Eq. 7. With y_0 determined, the Hall sheet resistance, R_H, is determined by application of Eq. 1. The solution to Eq. 8 is unique if Δy is large enough depending on the value of y_0; if $\Delta y > 1.5s$ the solution is unconditionally unique.

D. Hall carrier mobility and Hall sheet carrier density

The primary parameters measured in a Hall effect measurement are sheet carrier density and carrier mobility. A detailed description of the interpretation of Hall effect measurements may be found elsewhere [4]. The sheet carrier density is determined from

$$N_S=N_{HS}\bar{r}_H=\frac{\bar{r}_H B_z}{ZeR_H} \tag{9}$$

where N_{HS} is the Hall sheet carrier density, Ze is the carrier charge ($Z = \pm 1$), B_z is the magnetic flux density normal to the sample surface and $\bar{r}_H$ is the mean Hall scattering factor. The mean carrier mobility is obtained from

$$\bar{\mu}=\frac{\bar{\mu}_H}{\bar{r}_H}=\frac{ZR_H}{\bar{r}_H R_0 B_z} \tag{10}$$

Here $\bar{\mu}_H$ is the mean Hall carrier mobility. The Hall scattering factor is of order 1 and is dependent on the microscopic details of the carrier momentum relaxation and the carrier distribution function [8].

III. Simulated measurement error

In order to assess the potential accuracy of the position error suppression method described above, a Monte Carlo simulation was performed. From Fig. 3 it was found that the uncertainty of the resistance difference was smaller when the four-point probe is placed in close proximity to the barrier. In practical experiments it is difficult to position the electrodes closer than y_0 = 4 µm from the barrier because this is done optically. Thus, we choose this position for the measurement of R_{P1}. The position of measurement R_{P2} is then varied to find the best relationship of distance between the measurement positions, Δy, and the measurement uncertainty. For the simulation we apply normal distributed position errors for each electrode position (σ_x = 500 nm and σ_y = 100 nm), a normal distributed position error on the barrier position (σ_b = 100 nm) and a normal distributed resistance measurement error ($\sigma_R = R_0/1.5\times10^5$ Ω). For each Δy, 500 independent simulations were performed for a 20 µm pitch four-point probe.

In Fig. 4 the relative standard deviations of extracted R_0 and R_H are shown as a function of the spatial distance, Δy, between measurements R_{P1} and R_{P2}. From the Monte Carlo simulations it is found that the method for extracting R_0 and R_H eliminates the barrier position uncertainty, σ_b, since the relative standard deviation of R_H is reduced from 1.3 %, cf. Fig. 3, to 0.65 % for Δy > 50 µm. Furthermore, the relative standard deviation of direct sheet resistance is <0.05 % for Δy > 50 µm.

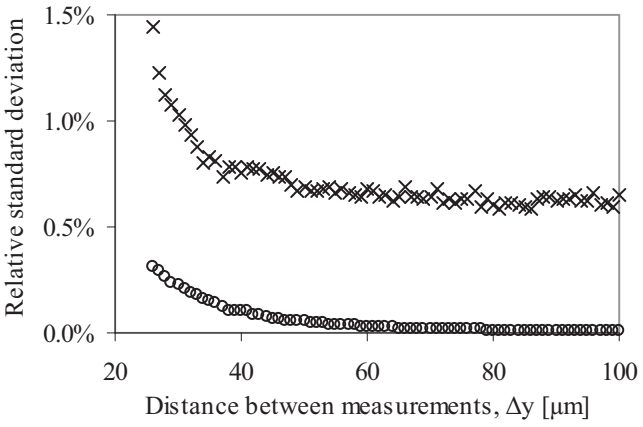

Figure 4. The relative standard deviation of extracted sheet resistance, R_0 (○), and Hall sheet resistance, R_H (×), found from Monte Carlo simulations for a 20 µm pitch four-point probe. Each point is the average of 500 simulations.

The average Hall sheet resistance is found to be underestimated in extracted data from the Monte Carlo simulations by 0.1 % to 0.3 % for $\Delta y > 50$ µm, while the direct sheet resistance is underestimated by <0.01 %. The slightly underestimated direct sheet resistance is expected and is due to the position error in the y-direction, cf. Fig. 1, but the reason for the underestimation of R_H has not been found at this point in time.

IV. Experiments

Micro-scale Hall effect measurements were performed with a micro four-point probe (M4PP) using a CAPRES microRSP-M150 system. The M4PP used in these experiments consists of nickel coated silicon cantilever electrodes extending from the edge of a silicon die. An electrode pitch of 20 µm was chosen for all experiments and the M4PP was equipped with a strain gauge for accurate surface detection. The sample chuck of the microRSP-M150 was fitted with a permanent magnet with a diameter of 35 mm. The resulting magnetic flux density at the position of the samples was on average B_z = 0.5 T, but as the magnetic flux density varies slightly across the distances used in the experiments; a custom made Hall sensor, calibrated to within 5 %, was used to determine the field at the exact measurement location (±20 µm). The temperature during measurements was 30.0 ± 0.5 °C.

Prior to measurements, the M4PP is aligned parallel to the cleaved wafer edge, i.e. each tip of the electrodes is positioned at equal distances from the edge. After optical alignment, two pseudo sheet resistance measurements are performed and the exact distance between the edge and the electrodes is calculated. This is done twice at different positions along the edge to account for sample misalignment.

For comparison to the Monte Carlo simulations the position error suppression method is applied by measuring first at a nominal distance of 4 µm to the cleaved edge of a silicon sample and then second at a nominal distance of either 104 µm or 60 µm from the barrier for repeatability measurements and scanning Hall effect experiments, respectively. At both locations the pseudo sheet resistance and resistance difference is measured.

To avoid making assumptions of the Hall scattering factor, the Hall mobility and Hall sheet carrier density will be used instead of drift mobility and sheet carrier density.

V. Results and Discussion

Previously reported micro Hall effect measurements have been performed using a non-linear fitting algorithm to fit multiple measurement points to Eq. 1 [4, 5]. In Figs. 5 and 6, an example is given of 300 pseudo sheet resistance measurements, R_P, and 300 resistance difference measurements, $\Delta R_{BB'}$, which have been measured on a silicon wafer with a sub-melt laser annealed B implant (0.5 keV, 5×10^{14} cm^{-2}). An excellent agreement between experimental results and theory is seen.

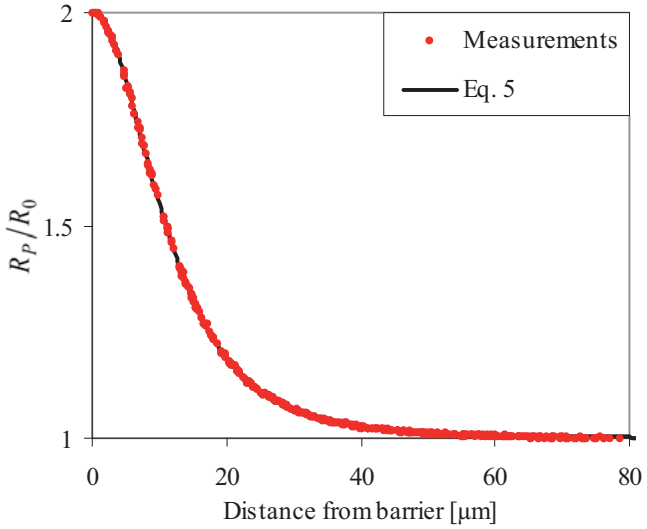

Figure 5. 300 pseudo sheet resistance measurements, R_P, normalized to the direct sheet resistance, R_0. The measurements were performed on a laser annealed USJ with a 20 µm pitch M4PP. The theoretical calculation, Eq. 5, and the experimental results coincide perfectly.

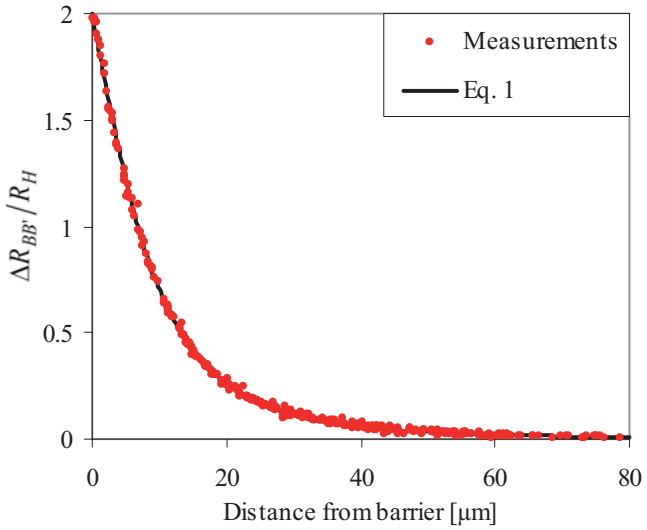

Figure 6. 300 resistance difference measurements, $\Delta R_{BB'}$, normalized to the Hall sheet resistance, R_H. The measurements were performed on a laser annealed USJ with a 20 µm pitch M4PP. The theoretical calculation, Eq. 1, and the experimental results coincide perfectly.

However, such measurements as demonstrated in Figs. 5 and 6 are very time consuming. Thus, the new position error suppression method, that significantly reduces the measurement time needed, is very welcome.

A. Measurement repeatability

To verify the position suppression method experimentally, a repeatability measurement was performed on an RTA annealed silicon wafer with a nominal As dose of 10^{15} cm^{-2} implanted at 2 keV. The wafer was scanned with a 20 µm pitch M4PP along the cleaved edge of the wafer using a step size of 50 µm and performing 50 Hall effect measurements. The measurement results of direct sheet resistance, Hall sheet carrier density and Hall mobility are summarized in Table 1.

TABLE I. VALUES EXTRACTED FROM REPEATABILITY EXPERIMENT.

$R_0 \pm \Delta R_0$	$N_{HS} \pm \Delta N_{HS}$	$\overline{\mu}_H \pm \Delta\overline{\mu}_H$
[Ω]	[$\times 10^{14}$ cm^{-2}]	[cm^{2}V^{-1}s^{-1}]
151.89 ±0.18	6.080 ±0.057	67.60 ±0.58

The relative standard deviation of the measured direct sheet resistance, R_0, and Hall sheet resistance, R_H, is 0.12 % and 0.94 %, respectively. This is higher than predicted in the Monte Carlo simulations, i.e. 0.05 % and 0.65 %, respectively. These differences could be the result of the position of first measurement being different from the nominal 4 µm, cf. the sensitivity plot Fig. 3. However, since the average and standard deviation of the calculated position of the first measurement point, R_{P1}, from the barrier was y_0 = 4.30 ±0.45 µm, it is more likely due to an under estimated position error in the y-direction, i.e. σ_y > 100 nm. Nevertheless, the relative standard deviations are lower than those we have reported earlier [4, 5] and the agreement between Monte Carlo simulation and experiment is reasonably good.

To further reduce the error arising from uncorrelated position errors, static contact M4PP with high aspect ratio L-shaped cantilevers may be useful since position repeatability better than 11 nm has previously been reported [6]. Also, since the sensitivity of both R_0 and R_H to position errors depends on the choice of probe pitch, a slightly larger probe pitch may be used in order improve accuracy, but that will reduce the spatial resolution to resistance variations [3].

B. Scanning Hall effect

In addition to the improved measurement accuracy the position error suppression method significantly reduces the measurement time to less than a minute, i.e. 10-30 times faster than the results reported in previous publications [4, 5]. The reduced measurement time allows for scanning Hall effect measurements to investigate the cause of spatial sheet resistance variations seen for laser annealed USJ. To explore the scanning capability, a silicon wafer with a nominal B dose of 10^{15} cm^{-2} was exposed to a scanning sub-melt laser anneal by performing a single pass of an 11 mm wide laser spot. For convenience we define the direct sheet conductivity, G_0, as

$$G_0 = R_0^{-1} = e\overline{\mu}N_S = e\overline{\mu}_H N_{HS} \qquad (11)$$

The annealed region of the wafer was then characterized and the result is summarized in Fig. 7, where the relative Hall carrier mobility, the relative Hall sheet carrier density and the relative sheet conductivity is plotted. For this scan the average and standard deviation of the calculated position of the first measurement point, R_{P1}, was y_0 = 4.22 ±0.76µm. The slightly higher standard deviation of the position of the first measurement point as compared to ±0.45 µm for the RTA annealed sample may be an indication that the position error suppression is less accurate for samples with micro-scale inhomogeneous sheet resistance.

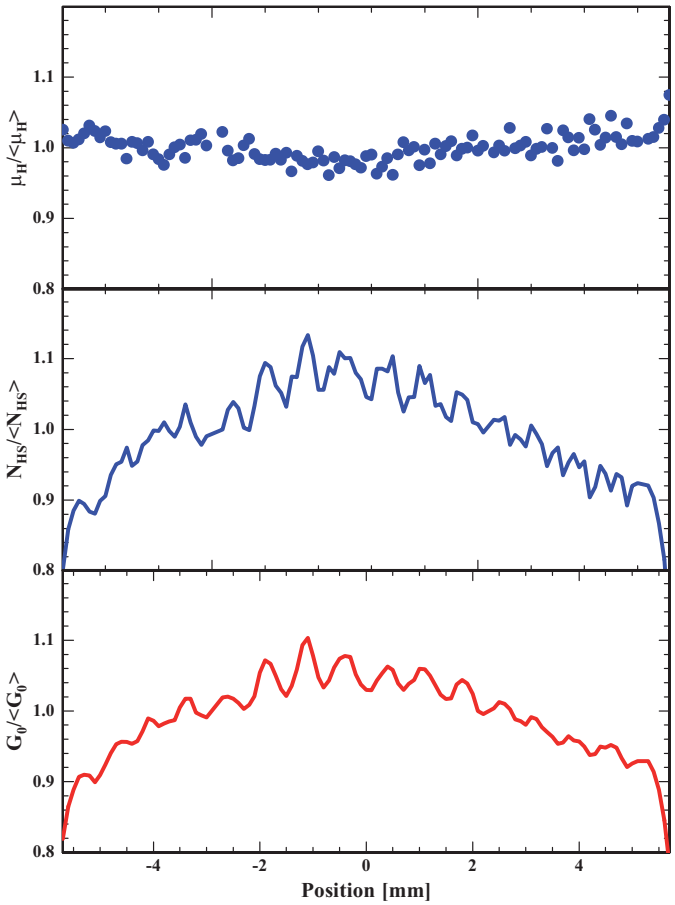

Figure 7. Scanning Hall effect measurement of a silicon sample with an ultra shallow boron implant. The sample was laser annealed in a single pass of an 11 mm wide laser beam. Hall mobility and Hall sheet carrier dose and sheet conductance are each normalized by their respective average value. The measurement time was less than a minute per point.

The result is, as one would expect, an almost perfect correlation between active dose and sheet conductance, since the carrier mobility only has a weak dependence on the active dopant concentration in highly doped material. The slight decrease in Hall mobility seen at higher activation degree could be an indication of increased carrier scattering from ionized impurities, i.e. substitutional B atoms rather than interstitial defects.

To evaluate the micro Hall effect measurement precision on this inhomogeneous sample, we calculate the standard deviation of Hall carrier mobility which according to both theory and Fig. 7 should be the parameter with the smaller dependency on sample variations. For this evaluation we restrict the calculation to the period [-2 ; 2] mm with stable mobility and find the relative standard deviation to be 1.3 %. It may then be reasonable to assume that the relative uncertainty of the measured Hall carrier mobility and Hall sheet carrier density is equal to or better than 1.3 % on this inhomogenous sample while excluding the absolute uncertainty (<5 %) of the magnetic flux density.

VI. Conclusion

We have investigated the precision of a new micro Hall effect measurement method based on measurements with a collinear M4PP near an edge. We calculated the relative standard deviation of the resistance difference, $\Delta R_{BB'}$, and found that the measurement error on $\Delta R_{BB'}$ is lower when performed close to an edge and mainly determined by the uncertainty on the distance, y_0, between the M4PP and the edge. We described a position error suppression method based on measurements at just two positions to reduce the uncertainty on y_0. The position error suppression method was applied first in a Monte Carlo simulation and then in a repeatability experiment; and we find the relative standard deviation of measurement repeatability to be less than 1 % for both simulations and measurements.

Furthermore, we demonstrated spatially resolved scanning micro Hall effect measurements on laser annealed USJ with spatial sheet resistance variations. We find an almost perfect correlation between the active dose and the sheet conductance (inverse sheet resistance), while in regions with low sheet resistance variations the carrier mobility is almost constant. Finally, we find that even for a sample with significant spatial variations in sheet resistance on the order of 5 % a relative standard deviation of less than 1.3 % in micro Hall effect measurements may be expected excluding the absolute uncertainty of the magnetic flux density.

Acknowledgment

We are grateful for the financial support from Copenhagen Graduate School for Nanoscience and Nanotechnology C:O:N:T, the Danish Research Agency FTP. Center for Individual Nanoparticle Functionality (CINF) is sponsored by The Danish National Research Foundation. We thank Peter Bøggild for continuous support, encouragement, and fruitful discussions.

References

[1] International Technology Roadmap for Semiconductors, http://www.itrs.net.

[2] T. Clarysse, A. Moussa, F. Leys, R. Loo, W. Vandervorst, M. C. Benjamin, R. J. Hillard, V. N. Faifer, M. I. Current, R. Lin, and D. H. Petersen, Mater. Res. Soc. Symp. Proc. 912, 197 (2006).

[3] D. H. Petersen, R. Lin, T. M. Hansen, E. Rosseel, W. Vandervorst, C. Markvardsen, D. Kjær, and P. F. Nielsen, J. Vac. Sci. Technol. B 26, 362 (2008).

[4] D. H. Petersen, O. Hansen, R. Lin, and P. F. Nielsen, J. Appl. Phys. 104, 013710 (2008).

[5] T. Clarysse, J. Bogdanowicz, J. Goossens, A. Moussa, E. Rosseel, W. Vandervorst, D.H. Petersen, R. Lin, P.F. Nielsen, O. Hansen, G. Merklin, N.S. Bennett and N.E.B. Cowern, "On the analysis of the activation mechanisms of sub-melt laser anneals", European Material Research Society Spring meeting, Strasbourg, 26-30 May 2008, Symposium I, (to be published in Materials Science and Engineering B).

[6] D. H. Petersen, O. Hansen, T. M. Hansen, P. R. E. Petersen and P. Bøggild, Microelectron. Eng. 85, 1092 (2008).

[7] R. Rymaszew, J. Phys. E: J. Sci. Instrum. 2, 170 (1969).

[8] K. Seeger, Semiconductor Physics, An Introduction, Solid-State Sciences No. 40, 5th ed. (Springer, Berlin, 1991).

Paper VII

J. Vac. Sci. Technol. B **28**, C1C41-C1C47 (2010).

PhD students contribution:

Discovered possibility for magnetoresistance simplification for dual configuration (theoretical formulation by O. Hansen). Responsible for probe designs and fabrication. Experimental M4PP and MHE measurements and data treatment (main experimental M4PP work by R. Lin for Fig. 7). Manuscript writing assisted mainly by D. Lin, G. Brammertz and O. Hansen.

Co-authors contribution:

van der Pauw measurements were performed by A. Alain and G. Brammertz. SIMS and supporting discussions by J. Goossens and W. Vandervorst. Supporting calculations by O. Hansen for thin film mobility. Sample definition and fabrication by C. Adelmann, C. Merckling, J. Penaud and G. Brammertz. Supporting discussions with P. Bøggild, P.F. Nielsen and T. Clarysse.

Electrical characterization of InGaAs ultra-shallow junctions

Dirch H. Petersen[a)]
Department of Micro- and Nanotechnology, Technical University of Denmark, DTU Nanotech, Building 345 East, DK-2800 Kgs. Lyngby, Denmark; CAPRES A/S, Scion-DTU, Building 373, DK-2800 Kgs. Lyngby, Denmark; and IMEC, Kapeldreef 75, B-3001 Leuven, Belgium

Ole Hansen
Department of Micro- and Nanotechnology, Technical University of Denmark, DTU Nanotech, Building 345 East, DK-2800 Kgs. Lyngby, Denmark and Centre for Individual Nanoparticle Functionality (CINF), Technical University of Denmark, Building 345 East, DK-2800 Kgs. Lyngby, Denmark

Peter Bøggild
Department of Micro- and Nanotechnology, Technical University of Denmark, DTU Nanotech, Building 345 East, DK-2800 Kgs. Lyngby Denmark

Rong Lin and Peter F. Nielsen
CAPRES A/S, Scion-DTU, Building 373, DK-2800 Kgs. Lyngby, Denmark

Dennis Lin, Christoph Adelmann, Alireza Alian, and Clement Merckling
IMEC, Kapeldreef 75, B-3001 Leuven, Belgium

Julien Penaud
Riber, rue Casimir Perier 31, 95870 Bezons Cedex, France

Guy Brammertz and Jozefien Goossens
IMEC, Kapeldreef 75, B-3001 Leuven, Belgium

Wilfried Vandervorst
IMEC, Kapeldreef 75, B-3001 Leuven, Belgium and Inst. voor Kern-en Stralingsfysica, K. U. Leuven, Celestijnenlaan 200D, B-3001 Leuven, Belgium

Trudo Clarysse
IMEC, Kapeldreef 75, B-3001 Leuven, Belgium

(Received 11 June 2009; accepted 24 August 2009; published 1 March 2010)

In this study, we investigate the limitations to sheet resistance and Hall effect characterization of ultra-shallow junctions (USJs) in $In_{0.53}Ga_{0.47}As$. We compare conventional van der Pauw and Hall effect measurements with micro four-point probe (M4PP) and micro Hall effect methods. Due to the high carrier mobility of InGaAs, we extend the micro-Hall effect position error suppression method to also take geometrical magnetoresistance into account. We find that the conventional techniques fail to measure accurately on n^{++}/p^{+} USJ due to a significant leakage current, whereas the M4PP and micro Hall effect methods are able to give accurate results. Finally, we observe a significant reduction in the carrier mobility for InGaAs USJ. © *2009 American Vacuum Society.*
[DOI: 10.1116/1.3231492]

I. INTRODUCTION

High mobility substrate materials, such as InGaAs and Ge, have attracted much attention in recent post Si-CMOS device research device. In order to continue device scaling beyond the 22 nm technology node, it is crucial to obtain heavily doped source/drain regions and abrupt junctions in these high mobility semiconductor materials. The study of ultra-shallow implants in InGaAs could ultimately answer questions of scalability associated with such devices, and thus indicate the potential for the development of high performance electronics. Conventional semiconductor metrology methods are, however, often inadequate in characterizing nanoscale materials as these are not specifically designed for structures with extreme dimensions.

It has previously been demonstrated that sheet resistance characterization of ultra-shallow junctions (USJs) in Si with conventional four-point probes is highly unreliable.[1] In contrast, micro four-point probes (M4PPs) are able to accurately characterize sub-10-nm junctions with zero probe penetration, which both reduce sample damage and provide more reliable measurements. Since InGaAs is much softer than Si, one would expect probe penetration to be more pronounced and sheet resistance measurements on ultra-shallow junctions become even more difficult. In addition to sheet resistance characterization, it was recently demonstrated that micro Hall effect measurements can be performed with M4PP in proximity of an insulating barrier.[2] By using a position error suppression technique, in combination with the micro Hall effect method, the measurement accuracy could be improved, while the measurement time was reduced to less than a minute.[3] However, a combination of a very high

a)Electronic mail: dhpe@nanotech.dtu.dk

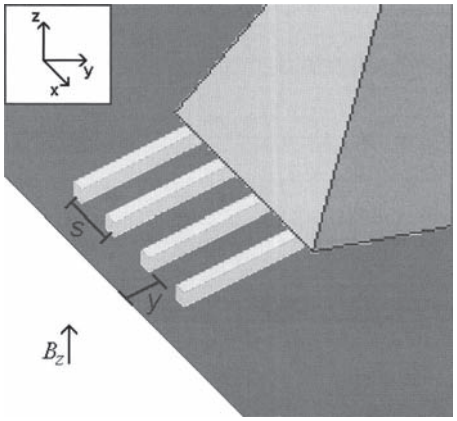

FIG. 1. Schematic illustration of a M4PP measuring close to the edge of a cleaved wafer.

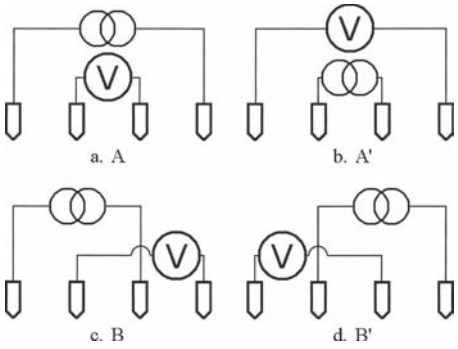

FIG. 2. Illustration of the four electrode combinations A, A′, B, and B′, which are used in micro Hall effect measurements. Adapted from Ref. 3.

carrier mobility and a moderate magnetic flux density may affect the result of micro Hall effect measurement with position error suppression because of a geometrical magnetoresistive contribution.[4]

In this article, we extend the position error suppression method to allow for micro Hall effect measurements in the presence of a geometrical magnetoresistance contribution. We then study sheet resistance and Hall effect characterization of highly doped $In_{0.53}Ga_{0.47}As$ by conventional van der Pauw (VDP) and Hall effect measurements on square test samples and compare to M4PP and micro Hall effect measurements. Finally, we investigate both ion implanted InGaAs and *in-situ* doped epitaxially grown layers with layer thicknesses down to 19 nm.

II. MICRO HALL EFFECT THEORY

Hall effect measurements may be performed on a thin conductive sheet with a four-point probe placed in proximity of at least one laterally insulating boundary.[2] We will describe only the situation where a collinear equidistant four-point probe with electrode pitch s is placed on a conductive sheet at a distance y from an insulating boundary, which is parallel to the four electrode contacts (cf. Fig. 1).

The four-point resistance, $R=V/I_0$, is measured by passing a current, I_0, between two of the electrodes while the voltage difference, V, is measured between the two remaining electrodes. For the analysis of Hall effect measurements, four different electrode combinations defined as configurations A, A′, B and B′ will be used (cf. Fig. 2). With the subscript denoting the electrode configuration, we define the resistance averages, $\overline{R_{AA'}} \equiv (R_A + R_{A'})/2$ and $\overline{R_{BB'}} \equiv (R_B + R_{B'})/2$, and the resistance difference, $\Delta R_{BB'} \equiv R_B - R_{B'}$. The basic equations describing such measurements are summarized in Table I.[2,3]

For the equations in Table I, the Hall sheet resistance, $R_H = Z\mu_H B_z R_0$, is a function of the direct sheet resistance R_0, the magnetic flux density B_z, the Hall carrier mobility μ_H, and the carrier type, $Z = \pm 1$. The Hall sheet resistance may also yield the Hall sheet carrier density as $N_{HS} = ZB_z/(eR_H)$, where e is the unit charge. The pseudo sheet resistance R_P extracted from the dual configuration equation is a function of R_0, R_H, and y; this will be described more detailed in the next section. The subscripts 1 and 2 refer to measurements at two different locations separated by the known distance Δy. The term $R_H^2/R_0^2 = \mu_H^2 B_z^2$ is due to the geometrical magnetoresistance.[4]

A. Position error suppression with magnetoresistance

We previously showed how a micro Hall effect measurement can be performed with high precision in less than a minute using a position error suppression method[3] based on four-point measurements at two locations. In this study, one measurement combining data from all four configurations is performed at a location y_1 close to the insulating boundary (the exact position is unknown). At another location, y_2, far from the boundary a second measurement is performed (e.g., for a 20 μm pitch probe, $y_1 \approx 4$ μm, $y_2 = y_1 + \Delta y$, and $\Delta y = 56$ μm). However, the basic equations described previously[3] do not include the geometrical magnetoresistive contribution, which can become relevant for characterization of high mobility materials. Thus, here we show how the position error suppression method can be extended to take this contribution into account.

The solution to the pseudo sheet resistance function R_P can be found for a known magnetoresistance contribution by numeric calculation using the dual configuration equation (cf. Table I). In Fig. 3 we show the pseudo sheet resistance normalized to the direct sheet resistance R_0 for different magnetoresistance contributions. As it was previously shown for single configuration measurements,[2] it is seen that there is no geometrical magnetoresistance when the four-point probe is placed exactly at the boundary. However, since the carrier mobility is not known prior to measurement, it could be of value to have an analytical approximation to simplify the data treatment. We now demonstrate how such an approximation may be obtained.

The resistance average functions (cf. Table I) can be rewritten as dependent on two geometrical functions $f_i(y/s)$ and $g_i(y/s)$, where i denotes the configurations AA′ and BB′.

TABLE I. Basic equations describing four-point measurements on a conductive sheet with one insulating boundary parallel to the line of the four contacts (Refs. 2 and 3).

Resistance average for configuration A and A′	$\overline{R_{AA'}} = \frac{R_0}{2\pi}\left(1+\frac{R_H^2}{R_0^2}\right)\ln(4) + \frac{R_0}{2\pi}\left(1-\frac{R_H^2}{R_0^2}\right)\ln\frac{4+4\left(\frac{y}{s}\right)^2}{1+4\left(\frac{y}{s}\right)^2}$
Resistance average for configuration B and B′	$\overline{R_{BB'}} = \frac{R_0}{2\pi}\left(1+\frac{R_H^2}{R_0^2}\right)\ln(3) + \frac{R_0}{2\pi}\left(1-\frac{R_H^2}{R_0^2}\right)\ln\sqrt{\frac{9+4\left(\frac{y}{s}\right)^2}{1+4\left(\frac{y}{s}\right)^2}}$
Resistance difference for configuration B and B′	$\Delta R_{BB'} = \frac{2R_H}{\pi}\left(3\arctan\left(\frac{s}{2y}\right) - \arctan\left(\frac{3s}{2y}\right)\right)$
Dual configuration equation	$\exp\left(\frac{2\pi\overline{R_{AA'}}}{R_P}\right) - \exp\left(\frac{2\pi\overline{R_{BB'}}}{R_P}\right) = 1$
Position error suppression	$f\left(\frac{y_1}{s}\right) = \frac{R_{P1}}{R_{P2}} f\left(\frac{y_1+\Delta y}{s}\right)$

$$\overline{R_{AA'}} = R_0\left(f_{AA'}(y/s) + \frac{R_H^2}{R_0^2} g_{AA'}(y/s)\right), \tag{1}$$

$$\overline{R_{BB'}} = R_0\left(f_{BB'}(y/s) + \frac{R_H^2}{R_0^2} g_{BB'}(y/s)\right). \tag{2}$$

Furthermore, it can be shown that the geometrical functions are not independent,

$$g_i(y/s) = f_i(0) - f_i(y/s). \tag{3}$$

We may expect that the pseudo sheet resistance can also be expressed in a similar manner as Eqs. (1) and (2) to a good approximation,

$$R_{P,\mathrm{appr}} \approx R_0\left(f_P(y/s) + \frac{R_H^2}{R_0^2} g_P(y/s)\right). \tag{4}$$

In analogy to Eq. (3), we guess that $g_P(y/s) \approx f_P(0) - f_P(y/s) = 2 - f_P(y/s)$. Thus, the pseudo sheet resistance is, by this approximation, a simple function of the already known numerically determined function, $f_P(y/s)$,[3] and the magnetoresistive contribution. The error of the approximated pseudo sheet resistance function is shown in Fig. 4 where the relative error is calculated as $(R_{P,\mathrm{appr}} - R_P)/R_P$ for different magnetoresistance contributions. The error initially increases with increasing magnetoresistance and returns to zero again at $\mu_H^2 B_z^2 = 1$. However, the position error suppression method relies on measurements at two locations, e.g., at $y_1 = 0.2s$ and $y_2 = 3s$, and at these locations the relative error is quite small and acceptable.

III. EXPERIMENT

Three types of Si doped $In_{0.53}Ga_{0.47}As$ samples have been investigated. For all samples, a 1 μm thick $In_{0.53}Ga_{0.47}As$ thin film was grown epitaxially on lattice matched InP semi-insulating substrates by molecular beam epitaxy. Type IA and IB samples were doped by ion implantation (Si, 50 keV)

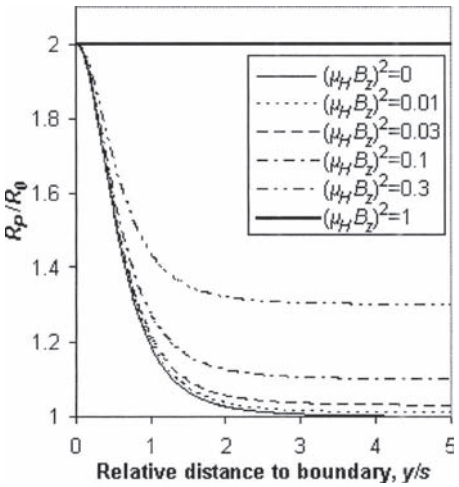

FIG. 3. Pseudo sheet resistance normalized to the direct sheet resistance with different contributions to the geometrical magnetoresistance.

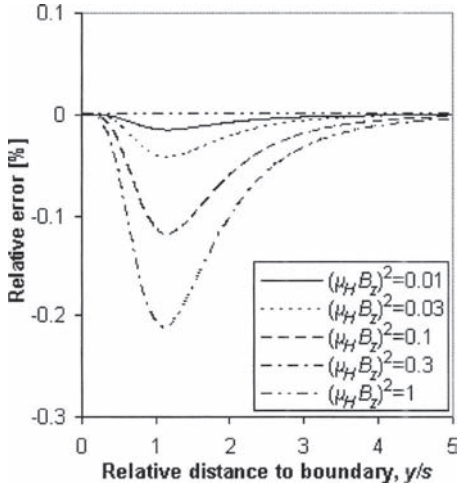

FIG. 4. Relative error of the pseudo sheet resistance approximation for different contributions to the geometrical magnetoresistance.

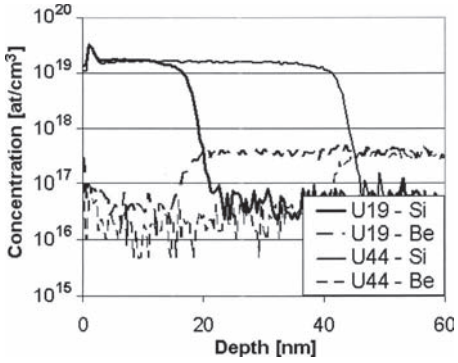

FIG. 5. Dopant concentration of the U19 and U44 samples measured using SIMS.

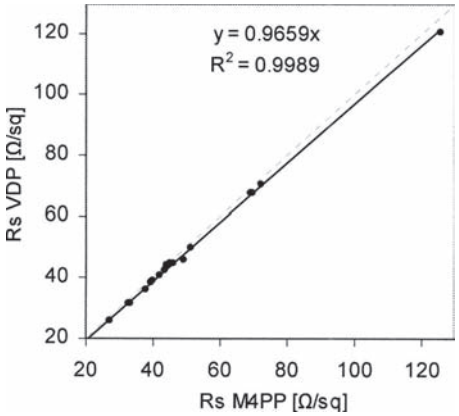

FIG. 7. Comparison of sheet resistance measured using VDP and M4PP, respectively. The samples measured were $In_{0.53}Ga_{0.47}As$ doped with 10^{14} and 10^{15} atoms/cm^2 Si implanted at 50 keV.

with nominal doses of 10^{14} and 10^{15} cm^{-2}, respectively, followed by annealing at different temperatures (550–700 °C) and annealing times (5–600 s). Type U samples were doped in situ during growth with Si and Be to yield an $n^{++}/p^{+}/p^{++}$ structure with nominal thicknesses of the p^{+} and p^{++} layers of 700 and 300 nm, respectively. The dopant concentrations as measured by secondary ion mass spectroscopy (SIMS) were 1.5×10^{19} cm^{-3} (Si), 3.6×10^{17} cm^{-3} (Be), and 7.8×10^{18} cm^{-3} (Be) for the n^{++}, p^{+}, and p^{++} layers, respectively. The junction depths at 10^{18} cm^{-3} of the U19 and U44 samples, as measured by SIMS, were 19 and 44 nm, respectively (cf. Fig. 5).

The samples were characterized by the VDP technique and conventional Hall effect measurements on 1 cm^2 square samples and by M4PP and micro Hall effect measurements near a cleaved edge. For VDP and conventional Hall effect measurements, Ohmic contacts were formed close to each of the four sample corners by deposition of In dots on the top surface without annealing, and the magnetic flux density was 163 mT normal to the sample surface. M4PP sheet resistance measurements were performed on the CAPRES microRSP-M150 system[5] at zero magnetic flux density with an electrode pitch of 10 μm using either straight cantilevers (standard) or high aspect ratio L-shaped cantilevers (cf. Fig. 6) for sliding contact and static contact,[6] respectively. The micro Hall effect measurements were performed on a modified CAPRES microRSP-M150 system, with a nominal magnetic flux density of 500 mT normal to the sample surface, unless otherwise is stated. For micro Hall effect measurements, Au coated straight cantilever M4PPs with an electrode pitch of 20 μm were used.

IV. RESULTS

Sheet resistances of 18 different samples of types IA and IB, with different implant and annealing conditions, were measured by M4PP and VDP to correlate the two methods. M4PP measurements were performed inside the 1 cm^2 samples used for the VDP measurements and no significant R_S variations were observed. The result is summarized in Fig. 7 and shows good linear agreement of the two techniques.

To support the measurement analysis for the USJ type U samples, we performed a high resolution sheet resistance area scan of the U19 sample, which showed no sign of large R_S nonuniformities (cf. Fig. 8). For this initial test, we used L-shaped cantilevers to exclude potential mechanical surface damage of the soft InGaAs material. From the R_S measurements in Fig. 8 the measurement repeatability of M4PP can be calculated be $< 0.65\%$. Furthermore, we performed sheet resistance wafer maps, each with 361 measurement points (cf. Fig. 9). The R_S variation of the U19 sample was found to be 4.3% (relative standard deviation) with an average R_S of

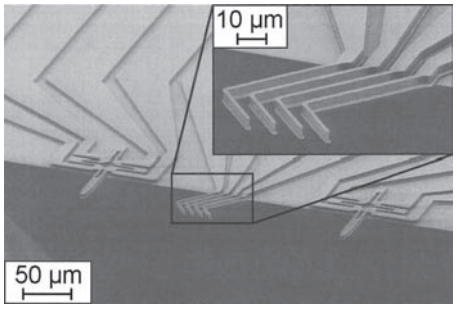

FIG. 6. M4PP with L-shaped cantilevers for static contact and strain gauge for surface detection.

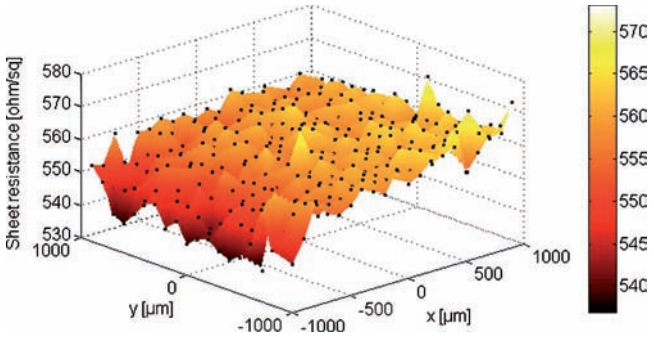

FIG. 8. (Color online) 20 × 20 points R_S area scan of the U19 sample (19 nm junction depth). The scan was performed with an L-shaped cantilever M4PP and the measurement points were measured in a random sequence.

TABLE III. Hall carrier mobility measured on the U19 sample at three different magnetic flux densities.

B_z (mT)	μ_H [cm^2/(V s)]
56.2	1675 ± 42
102	1633 ± 159
488	1974 ± 83

533.1 Ω/sq. The wafer map of the U44 sample was much more uniform with just 0.9% variation and with an average R_S of 105.5 Ω/sq.

Hall effect measurements were then compared for two of type IB and two type U samples. For type IB samples, the measured Hall carrier mobility was found to be 20%–25% higher using the micro Hall effect method than with the conventional Hall effect method. The micro Hall effect measurements on type U samples were repeated 51 times with relative standard deviations on R_S and μ_H of 0.6% and 3% for U44 and 0.7% and 4% for U19. In Table II, the results of the Hall effect measurements are summarized and the only obvious difference in measurement condition was the magnetic flux density.

In an attempt to explain the difference in the measured Hall carrier mobility, the magnetic field was reduced and micro Hall effect measurements confirmed a significant reduction in Hall carrier mobility when reducing the magnetic flux density (cf. Table III).

V. DISCUSSION

In this section we analyze the reliability of the two measurement techniques. For the data analysis, we shall assume a scattering factor of unity. This is in good agreement with theoretical calculations for 10^{19} cm^{-3} doped n-type InGaAs.[7]

The importance of using the modified position error suppression method as opposed to not including magnetoresistance is best evaluated at high carrier mobility and high magnetic flux density. For the U44 sample, errors of 1.5%, −6.2%, and 5.1% would have been induced on the sheet resistance, sheet carrier density, and carrier mobility, respectively, without correcting for the geometrical magnetoresistance in the position error suppression method. For the U19 sample, the errors would have been 0.9%, −4.1% and 3.3%, respectively, due to the lower carrier mobility affecting the magnetoresistance to the power of 2.

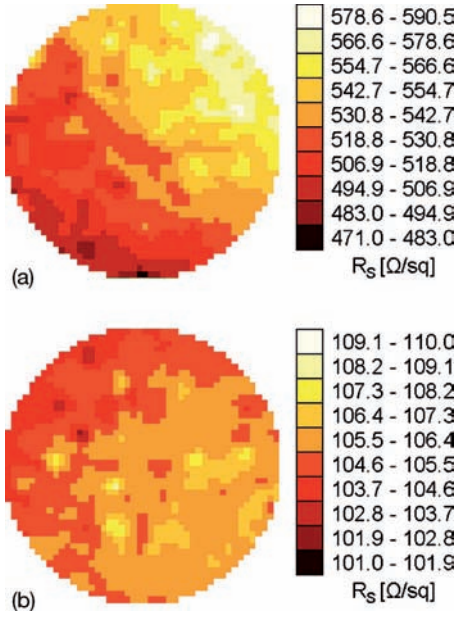

FIG. 9. (Color online) 361 points sheet resistance wafer maps of the U19 (a) and U44 (b) samples performed with standard M4PP. The average wafer sheet resistances were calculated to be 533.1 Ω/sq ± 4.3% and 105.5 Ω/sq ± 0.9%. For both measurements, the points were measured in a random sequence.

On the IA and IB samples, VDP measured, on average, 3.4% lower R_S than M4PP. It is well known that positioning of electrical contacts near the corners of a square sample is critical for precise sheet resistance measurements when using VDP. A geometrically induced measurement error of −3.4% will result when the four contacts are placed on the diagonals of an $L \times L$ square at a distance of roughly $0.25 \times L$ from the corners.[8] However, such a large position error does not appear to be a general trend for the measured samples. For the M4PP measurements, we first notice that the measured sheet resistance is independent of the use of sliding contact or static contact. Also, the repeatability was found to be $< 0.65\%$ on the U19 sample which shows the largest sample variation. This is in good agreement with previous results, which showed a repeatability and reproducibility of M4PP measurements on Si USJ to be $< 0.1\%$.[9] The average differ-

TABLE II. Comparison of Hall effect measurements performed with conventional Hall effect method and micro Hall effect method on four different samples.

	Hall effect–square sample				Micro Hall effect			
Sample name	B_z (mT)	R_0 (Ω/sq)	N_{HS} (10^{13} cm^{-2})	μ_H [cm^2/(V s)]	B_z (mT)	R_0 (Ω/sq)	N_{HS} (10^{13} cm^{-2})	μ_H [cm^2/(V s)]
IB1 (600 °C, 60 s)	163	44.0	7.34	1931	500	44.55	6.03	2323 ± 62
IB2 (600 °C, 600 s)	163	42.4	7.70	1911	500	43.36	5.99	2402 ± 21
U19	163	363	1.33	1288	488	556.8	0.588	1974 ± 83
U44	163	95.1	3.72	1770	488	106.3	2.37	2473 ± 73

ence of 3.4% between the two measurement techniques is, however, not necessarily an inherent measurement error but could be attributed to calibration errors such as different resistance reference, temperature difference, or time between measurements.

Although conventional Hall effect and micro Hall effect methods measure the same sheet resistance on type IB sample, the Hall sheet carrier density and Hall carrier mobility clearly differs by 20%–25%. However, a difference of ~16% between micro Hall effect measurements at 500 mT and 50–100 mT is also seen (cf. Table III), which indicates a dependency on the magnetic flux density and could be the result of a change in the Hall scattering factor. For both methods, the sheet carrier density measured for the ion implanted IB1 and IB2 samples is only 6%–8% of the implanted dose (10^{15} cm^{-2}). However, this is in very good agreement with the results previously obtained by Penna *et al.*[10] In the light of these results, we assume that both methods do, in fact, measure Hall effect correctly on type IB sample.

On the USJ type U samples, we see a clear difference in the measured sheet resistance for VDP and M4PP. We note that the VDP measurements were performed on two structures of each sample, and that the results were reproduced within expected experimental uncertainty; also the results were independent of the measurement current. Likewise, the M4PP measurements were reproducible and independent of the measurement current as well as electrode pitch. From our previous work with p^{++}/n^{+} Si USJ,[1] we know that high leakage current leads to a reduced measured sheet resistance. Such explanation fits well with the results of the U44 and U19 samples, for which a reduced R_S of 11% and 35% is seen for the 44 and 19 nm films, respectively, as compared to M4PP. At this time the origin of leakage current is unknown; i.e., leakage current can occur either beneath the In contacts or as a general n^{++}/p^{+} junction leakage as described in Ref. 11.

Leakage current will also reduce the measured Hall sheet resistance R_H, which results in an apparent increase in Hall sheet carrier density as they are inversely proportional; we recall that $N_{HS}=ZB_z/(eR_H)$. The Hall carrier mobility depends both on the measured R_S and R_H ($\mu_H=R_H/(ZB_zR_0)$) and thus in the presence of leakage current, the calculated mobility will also be incorrect, although the error cancels out to some unknown extent.[12]

To complete the analysis of measurement reliability, we note that whereas M4PP R_S measurements were straightforward, a higher than normal standard deviation in measurement repeatability was observed for U19 ($<0.65\%$) as compared to normally $<0.1\%$ for Si USJ.[9] However, the increase in measurement standard deviation for the U19 sample could be related to the extremely low sheet carrier density (cf. Table II) and carrier fluctuations. For instance, if we assume a box profile with the carrier concentration of $n=1.5\times10^{19}$ cm^{-3} as found by SIMS; then the average number of carriers N within a cube of dimensions d^3 will be on the order of $N=nd^3=n_Sd^2=n_S^3/n^2\approx1$, where d is defined by the electrical junction depth and n_S is the sheet carrier density. Thus, the average number of carriers in a cube is so low that it can result in discontinuities of the conductive n^{++} surface layer,[13] which may affect measurement repeatability.

The carrier mobility measured for the most shallow junction, U19, is 18% lower compared to the average of the U44, IB1, and IB2 samples. This could be the result of increased surface scattering, i.e., the electron mean free path approaches the conductive layer thickness. The electron mean free path may be estimated as $\lambda=\mu v_{\mathrm{th}}m^*/e\approx6$ nm, where v_{th} is the thermal carrier velocity, m^* is the effective electron mass, e is the unit charge, and the carrier mobility measured for the U44 sample is used. In addition, the effective layer thickness is expected to be less than the metallurgical junction depth of 19 nm due to surface and junction depletion layers; thus, increased surface scattering seems to agree with the experimental results. Another possible reason is that lateral continuity may be lost in some areas due to the low sheet carrier density and carrier fluctuations. The latter agrees with the above analysis on carriers in a box.

VI. CONCLUSION

For sheet resistance characterization of InGaAs, we established a sensible linear agreement between conventional VDP measurements and M4PP measurements on n^{++}/insulating structures. However, for ultra-shallow n^{++}/p^{+} structures with junction depths of 44 and 19 nm, we find M4PP much more reliable. A significant leakage current is proposed to be the reason for the lower sheet resistance measured with VDP, which, in turn, also prevents accurate Hall effect measurements on USJ.

For micro Hall effect measurements, we have derived an approximation to the position error suppression method in order to include geometrical magnetoresistance, which is important for $(\mu_HB_z)^2\geqslant0.01$. With the micro Hall effect method, we observed a difference of ~16% between Hall carrier mobilities measured at low magnetic flux density (56 and 102 mT) and at moderate magnetic flux density (488 mT). Except for this difference, a good correlation between conventional Hall effect and micro Hall effect was found on n^{++}/insulating structures. For USJ n^{++}/p^{+} structures, micro Hall effect showed repeatabilities of 3% and 4% on carrier mobility for 44 nm and 19 nm junction depths, respectively. Finally, we observed an ~18% decrease in the carrier mobility for the 19 nm USJ as compared to the 44 nm junction. We expect this may be a scaling effect caused by increased surface scattering or lost continuity in some areas due to low sheet carrier density and carrier fluctuations.

[1] T. Clarysse *et al.*, Mater. Res. Soc. Symp. Proc. **912**, 197 (2006).
[2] D. H. Petersen, O. Hansen, R. Lin, and P. F. Nielsen, J. Appl. Phys. **104**, 013710 (2008).
[3] D. H. Petersen, O. Hansen, R. Lin, P. F. Nielsen, T. Clarysse, J. Goossens, E. Rosseel, and W. Vandervorst, *Proceedings of the 16th IEEE International Conference on Advanced Thermal Processing of Semiconductors, RTP 2008* (IEEE, New York, 2008), pp. 251–256.
[4] R. S. Popović, *Hall Effect Devices, Magnetic Sensors and Characterization of Semiconductors*, The Adam Hilger Series on Sensors (Adam Hilger, Bristol, 1991).

[5]Capres A/S, http://www.capres.com.
[6]D. H. Petersen, O. Hansen, T. M. Hansen, P. R. E. Petersen, and P. Bøggild, Microelectron. Eng. **85**, 1092 (2008).
[7]Y. Takeda and M. A. Littlejohn, Appl. Phys. Lett. **40**, 251 (1982).
[8]D. W. Koon, A. A. Bahl, and E. O. Duncan, Rev. Sci. Instrum. **60**, 275 (1989).
[9]D. Kjaer, R. Lin, D. H. Petersen, P. M. Kopalidis, R. Eddy, D. A. Walker, W. F. Egelhoff, and L. Pickert, AIP Conf. Proc. **1066**, 167 (2008).
[10]T. Penna, B. Tell, A. S. H. Liao, T. J. Bridges, and G. Burkhardt, J. Appl. Phys. **57**, 351 (1985).
[11]C. L. Petersen, R. Lin, D. H. Petersen, and P. F. Nielsen, *Proceedings of the 14th IEEE International Conference on Advanced Thermal Processing of Semiconductors, RTP 2006* (IEEE, New York, 2006), pp. 153–158.
[12]T. Clarysse *et al.*, Mater. Sci. Eng., B **154–155**, 24 (2008).
[13]D. H. Petersen *et al.*, J. Vac. Sci. Technol. B **28**, C1C27 (2010).

Paper VIII

in Proc. RTP 2009 (IEEE, New York, 2009) pp. 157-162.

PhD students contribution:

Idea for study and conceptual idea for the three MHE methods described. Supervised all experimental MHE work and data treatment except numerical conformal mapping. Major revisions to manuscript, figures and references.

17th IEEE International Conference on Advanced Thermal Processing of Semiconductors - RTP 2009

Accurate micro Hall Effect measurements on scribe line pads

F. W. Osterberg[a], D.H. Petersen[a,b], F. Wang[a], E. Rosseel[c] and W. Vandervorst[d,e] O. Hansen[a,d]
[a]DTU Nanotech - Dept. of Micro and Nanotechnology, Technical University of Denmark,
building 345 East, DK-2800 Kgs. Lyngby, Denmark
[b]CAPRES A/S, Scion-DTU, building 373, DK-2800 Kgs. Lyngby, Denmark
[c]IMEC, Kapeldreef 75, B-3001 Leuven, Belgium
[d]CINF - Centre for Individual Nanoparticle Functionality, Technical University of Denmark,
building 345 East, DK-2800 Kgs. Lyngby, Denmark
[e]Inst. voor Kern- en Stralingsfysica, K. U. Leuven, Celestijnenlaan 200D B-3001 Leuven, Belgium

***Abstract*—Hall mobility and sheet carrier density are important parameters to monitor in advanced semiconductor production. If micro Hall Effect measurements are done on small pads in scribe lines, these parameters may be measured without using valuable test wafers. We report how Hall mobility can be extracted from micro four-point measurements performed on a rectangular pad. The dimension of the investigated pad is 400×430 μm^2, and the probe pitches range from 20 μm to 50 μm. The Monte Carlo method is used to find the optimal way to perform the Hall measurement and extract Hall mobility most accurate in less than a minute. Measurements are performed on shallow trench isolation patterned silicon wafers to verify the results from the Monte Carlo method.**

I. Introduction

In processing of semiconductor devices, it is becoming increasingly important and difficult to be able to characterize material parameters such as sheet resistance, sheet carrier density and Hall mobility. These parameters can be characterized through various methods, where some require special sample preparation, and others are destructive [1], [2]. It has previously been shown that micro four-point probes are able to measure sheet resistance, sheet carrier density and Hall mobility on thin film samples with at least one insulating boundary [3].

The existing technique has been validated experimentally for samples with a single boundary, while assuming a uniform sheet resistance throughout the entire sample, which allows for position error suppression thus giving very accurate results [4].

In this paper we investigate the possibility of performing micro Hall Effect measurements in less than a minute on small (400×430 μm^2) test pads, which do not necessarily have uniform sheet resistance. Being able to extract sheet resistance, sheet carrier density and Hall mobility from small samples is a significant advantage, as these can be patterned in scribe lines on the actual wafer, thus reducing the need for expensive test wafers.

II. Theory

A. Micro Hall Effect measurements: Micro Hall Effect measurements are performed on thin film samples using a micro four-point probe. The four electrodes are placed in-line with equal distance between the probes, also called the probe pitch, s. An insulating boundary must be present and a magnetic field, B_z, applied perpendicular to the surface. The actual measurement is done by forcing a current, I, through two of the probes pins while measuring the potential difference, V, between the two remaining pins. Four different pin configurations (A, A', B, B') are used, and these are illustrated in Fig. 1.

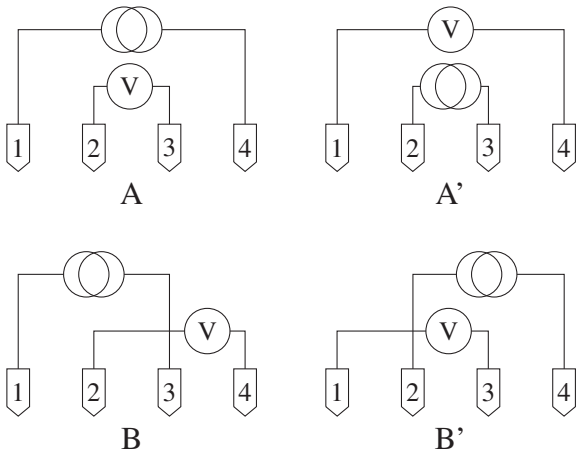

Fig. 1. The four different probe configurations (A, A', B, B') used for Hall Effect measurements.

Previous work [3] has shown the convenience of defining the resistance difference as $\Delta R_{BB'} \equiv R_B - R_{B'}$ and the mean resistance as $\overline{R_{BB'}} \equiv (R_B + R_{B'})/2$, where R_B and $R_{B'}$ are the resistances, $R = V/I$ measured in configurations B and B' respectively, similar values can be computed for the A and A' configurations. Furthermore, it has been shown that introducing a pseudo sheet resistance, R_P, greatly reduces position errors [4]:

$$\exp \frac{2\pi \overline{R_{AA'}}}{R_P} - \exp \frac{2\pi \overline{R_{BB'}}}{R_P} = 1. \quad (1)$$

Simple analytical expressions can be derived for $\Delta R_{BB'}$, $\overline{R_{BB'}}$ and $\overline{R_{AA'}}$ for homogeneous thin films with geometries such as the infinite half plane. Since (1) cannot be solved analytically for R_P, it is solved numerically. What makes R_P and $\Delta R_{BB'}$ convenient is the fact that they are proportional

987-1-4244-3815-0/09/$25.00 © IEEE

to the sheet resistance R_0 and the Hall sheet resistance R_H, respectively. This allows for expressing them in the following manner:

$$R_P = R_0 f\left(\frac{y}{s}\right), \tag{2}$$

$$\Delta R_{BB'} = R_H g\left(\frac{y}{s}\right), \tag{3}$$

where $f(x)$ and $g(x)$ are theoretically calculated functions and y is the distance to the barrier. When measurements are fitted to (2) and (3) to give R_0 and R_H, they can be used to calculate the Hall mobility μ_H:

$$\mu_H = \frac{ZR_H}{R_0 B_z}, \tag{4}$$

where Z is the sign of the carrier charge.

B. Measurement strategy: A procedure for extracting Hall mobility from measurements performed on homogeneous thin films has previously been described [4]. In short, this method dictates that two measurements should be performed with e.g. a 20 μm pitch probe; one roughly 4 μm from the boundary and the other 60 μm from the boundary. The measurements are then fitted to the theoretical expressions for the infinite half plane. This method can be performed in less than a minute, and will therefore be referred to as the "Fast - $3s$ apart" (F3S) method. The F3S method can also be applied to measurements on other geometries as long as the theoretical values used for fitting are those for the given geometry. Since a 400×430 μm^2 rectangle cannot be treated as an infinite half-plane the theoretical values used for fitting are computed using numerically conformal mapping [5]. A potential flaw with this method is that it assumes uniform sheet resistance for the sample and in particular at the two points measured. Since practical samples often have nonuniform sheet resistance a new measurement strategy will be proposed.

1) New measurement strategy: Here another fast method will be proposed, called the "Fast - with Small Separation" (FSS) method. The idea behind the new FSS method is that despite the degree of sheet resistance variation, it can be assumed constant within a significant small area. This will allow for performing two measurements with a small separation and then fitting to the theoretical expressions for a constant sheet resistance. In the following the method will be derived.

Two measurements are to be performed; the first measurement point is placed y_0 from the boundary and the second Δy further away. However, both values are assumed unknown due to the uncertainties on the actual probe positions. The two measurements will each result in a value for R_P and $\Delta R_{BB'}$, which leads to four equations with four unknowns:

For the pseudo sheet resistance:

$$R_{P1} = R_0 f\left(\frac{y_0}{s}\right), \tag{5}$$

$$R_{P2} = R_0 f\left(\frac{y_0 + \Delta y}{s}\right), \tag{6}$$

and for the resistance difference:

$$\Delta R_{BB'1} = R_H g\left(\frac{y_0}{s}\right), \tag{7}$$

$$\Delta R_{BB'2} = R_H g\left(\frac{y_0 + \Delta y}{s}\right), \tag{8}$$

where R_0, R_H, y_0, Δy are all unknowns.

By eliminating R_0 and R_H, two equations with two unknowns are obtained:

$$\frac{R_{P1}}{R_{P2}} = \frac{f\left(\frac{y_0}{s}\right)}{f\left(\frac{y_0+\Delta y}{s}\right)}, \tag{9}$$

$$\frac{\Delta R_{BB'1}}{\Delta R_{BB'2}} = \frac{g\left(\frac{y_0}{s}\right)}{g\left(\frac{y_0+\Delta y}{s}\right)}. \tag{10}$$

The two equations cannot be solved analytically and must instead be fitted numerically by using the least square method. Once y_0 and Δy are found, R_0 is found by doing least square fit of (5) and (6), while R_H is found similarly from (7) and (8).

2) Extensive measurement strategy: As a third method to extract the Hall mobility, the "All Inclusive" (AI) method will be presented. For this both a sheet resistance scan and and Hall Effect scan is required. The sheet resistance scan is used to calculated theoretical values for $\Delta R_{BB'}$ and R_P by assuming a constant Hall mobility and using the finite element method (FEM). The series of Hall Effect measurements is then fitted to the FEM calculated theoretical values, similar to the two previously described methods.

C. Monte Carlo Simulations: Monte Carlo simulations of the FSS method have been performed to determine where to measure the two points such that the Hall mobility is found most accurately. Monte Carlo simulations have been performed for 400×400 μm^2 samples with both uniform and nonuniform sheet resistance using 20 μm electrode pitch.

For the samples with uniform sheet resistance the simulated measurement data were obtained by conformal mapping in the same way as the new theoretical values were calculated, as described in [5].

The simulated data for a sample with nonuniform sheet resistance were obtained by using COMSOL FEM simulations, where the sheet resistance was defined to vary like an even fourth order polynomial in the y-direction, fitted to experimental measurement, such that the sheet resistance at the boundaries was 75% of the value at the centre. As sheet resistance is typically most strongly dependent on carrier concentration, the mobility has been assumed constant.

For the Monte Carlo simulations a normal distributed position error has been applied for each probe pin (in-line $\sigma_x = 0.5$ μm, out-of-line $\sigma_y = 0.1$ μm). Also a normal distributed error on the boundary position was applied ($\sigma_b = 0.1$ μm), and finally a normal distributed electrical error on the resistance was added [$\sigma_R = R_0/(1.5 \times 10^5)$ Ω]. 1000 simulations are used for each set of y_0 and Δy.

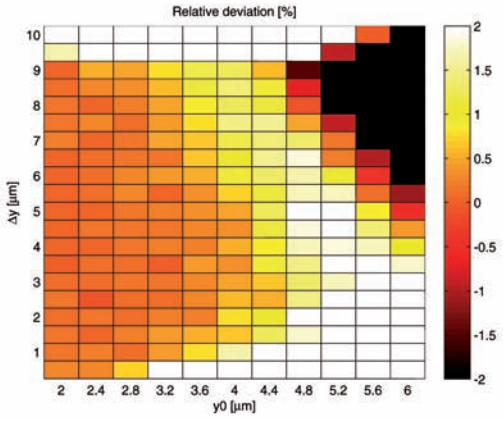

(a)

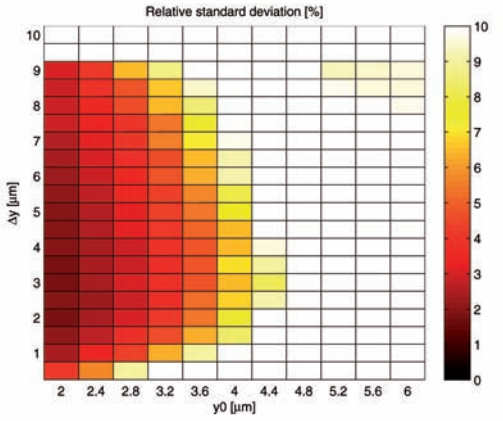

(b)

Fig. 2. Monte Carlo simulations for a sample with uniform sheet resistance, 1000 iterations are used for each point. (a) Contourplot of relative deviation in extracted Hall mobility. (b) Contourplot of relative standard deviation in extracted Hall mobility.

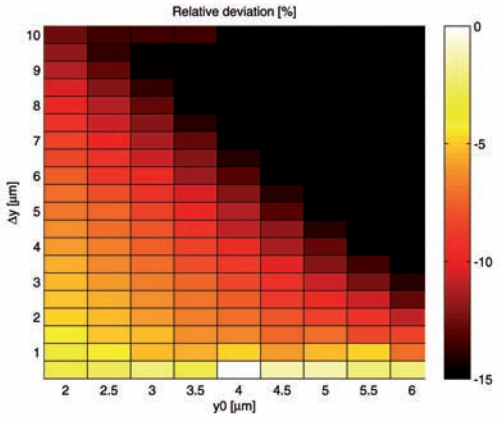

(a)

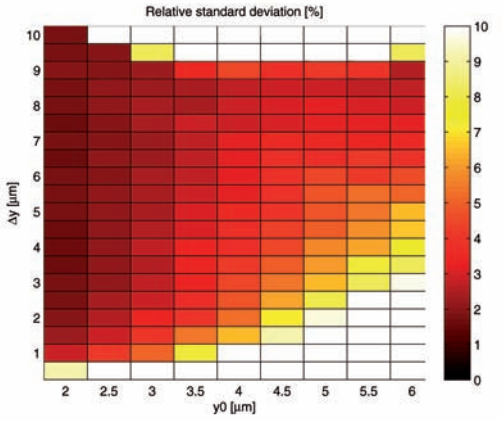

(b)

Fig. 3. Monte Carlo simulations for a sample with nonuniform sheet resistance, 1000 iterations are used for each point. (a) Contourplot of relative deviation in Hall mobility. (b) Contourplot of relative standard deviation in Hall mobility.

The results of the Monte Carlo simulations for the homogeneous sample is shown in Figs. 2(a) and 2(b). Fig. 2(a) shows the relative deviation of the calculated Hall mobility from the true Hall mobility. It is seen that in order to get correct results the measurements should be performed with y_0 as small as possible and Δy between 1 and 9 μm. In Fig. 2(b) the relative standard deviation is shown as a function of y_0 and Δy. It is seen that y_0 again should be as small as possible and Δy should be around 3 μm in order to minimize the relative standard deviation.

In Figs. 3(a) and 3(b), the results from the Monte Carlo simulation on the inhomogeneous sample are shown. From these results it is more difficult to choose which parameters are the optimal to use for real measurements, since the relative deviation is always negative for the chosen variation, which means that the Hall mobility will be estimated too low. To get the best possible value, Δy should be as small as possible, but on the other hand a small Δy results in a large relative standard deviation which is undesirable.

Even though the results of the Monte Carlo simulation indicate that different measurement procedures should be applied for homogeneous and inhomogeneous samples, it has been decided to choose one set of Δy and y_0 to use for all measurements. The reason for this is because when the measurement technique is to be applied, it is unknown whether the sample is completely homogeneous or how inhomogeneous it is. Additional measurements would be required to determine the homogeneity of the sample before performing the actual Hall Effect measurement. However, this would be more time consuming than the actual Hall measurement. The values of Δy and y_0 that will be used when performing the measurements are $y_0 \approx 4$ μm and $\Delta y = 3$ μm for a probe pitch of 20 μm.

III. Experimental

Measurements have been performed on two different shallow trench isolation (STI) patterned silicon wafers. Both are implanted at 0.5 keV with a nominal dose of 1×10^{15} cm^{-2} B, and laser annealed in an Applied Materials DSA chamber [6] at a nominal temperature of ~ 1200°C. The difference

between the two wafers is that on one of them a 400 nm thick absorber layer (AL) was deposited after the B implant, and stripped again after the laser anneal in an oxygen plasma asher. Measurements have been performed on 400×430 µm^2 pads on both wafers. The pads have been chosen with the same coordinates on both wafers to ensure that they have had similar preparation, except for the AL.

For the measurements a CAPRES microRSP-M150 system [7] has been used. For the Hall Effect measurement a permanent magnet was placed at the centre of the sample chuck. The magnetic flux density at the position of measurements was measured to 0.50 T using a calibrated Hall sensor. All the M4PP used for measurements had a strain gauge positioned next to the probe, to allow for accurate surface detection.

A. Sheet resistance scans: From the theory it is clear that the uniformity of the sheet resistance is very important when Hall mobility is to be extracted from the Hall measurements. For this reason, sheet resistance scans have been performed on the pads used for Hall measurements.

The sheet resistance scans were performed by scanning at the centre of the pad in the direction parallel to the probe pins, thus eliminating geometrical errors in proximity of the pad edges [8]. The scans are composed of two separate scans. One measured in a dense scan close to the boundary (< 50 µm) with a probe pitch of 1.5 µm and the other measured away from the boundary (> 30 µm) using a probe pitch of 10 µm.

B. Micro Hall Effect measurements: Hall measurements have been performed on the same pads as used for the sheet resistance scans. The three different approaches described in section II-B have all been used to extract the Hall mobility. Hall measurements have been performed at all four sides of the measured squares with three different probe pitches; $s = 20$ µm, $s = 30$ µm and $s = 50$ µm.

IV. Results

A. Sheet resistance scans: The results of the sheet resistance scans of the wafer processed without and with the AL are shown in Figs. 4(a) and 4(b) respectively. The measured sheet resistance is plotted as a function of the distance to the boundary orthogonal to the scan direction, which means that the centre of the pad is 215 µm from the boundary when scanning in the west - east direction and only 200 µm when scanning in the north - south direction, which is also illustrated in the inset.

B. Micro Hall Effect measurements:

1) The All Inclusive (AI) method: As it has been shown in Fig. 4(a), the sheet resistance is not uniform on the investigated samples. Since most of the sheet resistance scans are completely different, theoretical values must be computed for each sample before fitting. A set of these fits are shown for the edges north and south in Fig. 5. Here both measured $\Delta R_{BB'}$ and R_P are plotted as well as the theoretically fitted results. The corresponding sheet resistance scan from Fig. 4(a), used to compute new theoretical values, has also been plotted, and as expected it is seen that this fits the theoretical R_P in the range $50 - 350$ µm.

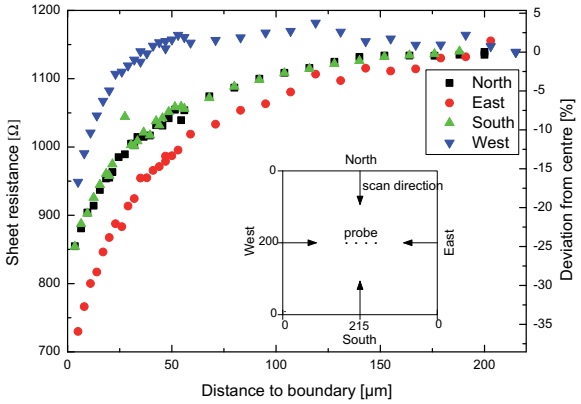

(a)

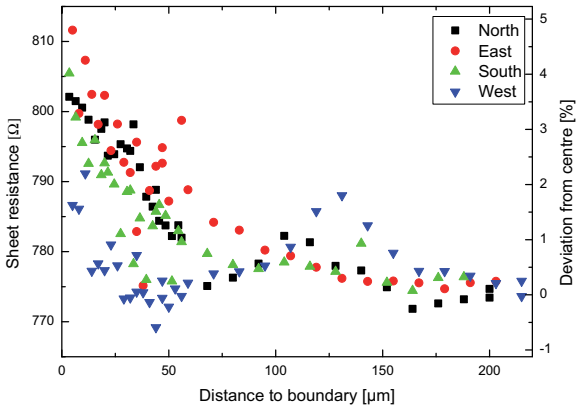

(b) With AL

Fig. 4. Sheet resistance scans on 400×430 µm^2 pads. (a) Measurements on pad processed without AL. The inset shows how the scans are performed, starting with 0 at the boundary and scanning towards the centre, the probe positioned in the middle is aligned in the west - east scan direction, for north - south it would be rotated 90°. (b) Measurements on pad processed with AL.

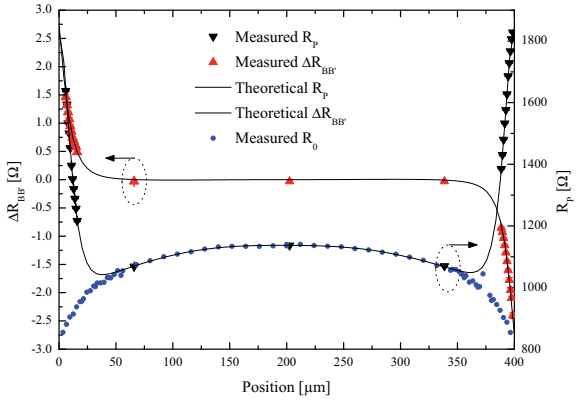

Fig. 5. Fits of theoretical values to sheet resistance and Hall Effect measurement using varying sheet resistance. Measured at north (400 µm) and south (0 µm) edges on pad processed without AL. The sheet resistance scan from Fig. 4(a) has also been plotted here.

The AI method have been applied for all four edges of the square with the three different probe pitches, resulting in twelve Hall mobility values. As the mobility is assumed to

TABLE I
MEAN HALL MOBILITIES EXTRACTED USING 20, 30 AND 50 µM PITCH.

	No AL	With AL
	$\overline{\mu_H} \pm \sigma_{\mu_H}$ [cm^{2}V^{-1}s^{-1}]	$\overline{\mu_H} \pm \sigma_{\mu_H}$ [cm^{2}V^{-1}s^{-1}]
AI	32.4 ± 0.6	31.4 ± 0.3
F3S	43.2 ± 4.5	28.5 ± 1.9
FSS	28.3 ± 1.6	30.6 ± 1.6

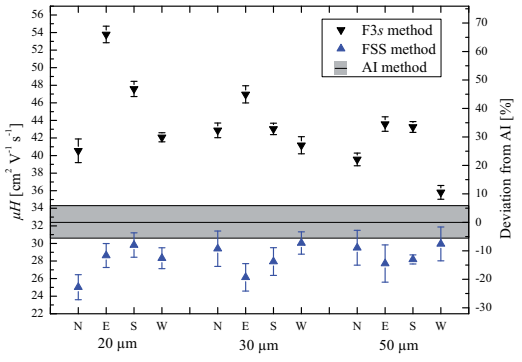

(a)

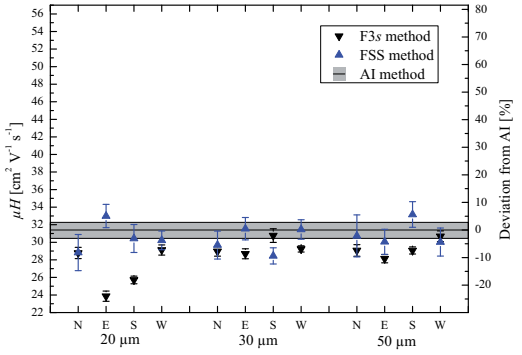

(b)

Fig. 6. Hall mobilities extracted from Hall measurements on 400x430 µm^2 pads. N, E, S and W indicates which boundary the measurement is performed at, and the numbers 20, 30 and 50 µm are the probe pitch used. The grey bands are $\overline{\mu_H} \pm 3\sigma_{\mu_H}$ found using the AI method. (a) Sample without AL. (b) sample with AL.

be uniform throughout the pad, the mean Hall mobility, $\overline{\mu_H}$, and standard deviation, σ_{μ_H}, has been found for each pad and reported in Tab. I.

2) The Fast methods: The results of the measurements using the FSS and F3S methods can be seen in Fig. 6. On the same plot the Hall mobility values from the AI method are plotted as grey bands, which corresponds to $\overline{\mu_H} \pm 3\sigma_{\mu_H}$. These bands are believed to be the true values as they are found using the most correct theoretical data and all experimental data.

V. DISCUSSION

A. Sheet resistance scans: From Figs. 4(a) and 4(b) it is seen that the change of the sheet resistance towards the edge is much larger for the wafer without AL than for the one with AL. The reason for this is believed to be related to the change in the optical reflection coefficient from oxide covered areas to noncovered areas, giving rise to a significant higher anneal temperature near the oxide edge. This difference is addressed in more detail in [9]. Whereas the sheet resistance decreases by 15-35 % toward the edge on the wafer without the AL, it increases by 2-5 % for the wafer with the AL.

B. Micro Hall Effect measurements: Based on the results from the Monte Carlo simulations of the FSS method, it is expected that the measured Hall mobility will be lower than the real value for the wafer without the AL and slightly higher for the one with the AL.

From Tab. I it is seen that the average Hall mobility extracted by the FSS method on the pad without AL is 13 % below the value found using the AI method, which is in good agreement with the Monte Carlo simulations.

Also from Tab. I it is seen that the average Hall mobility extracted from the F3S method is 33 % higher than the AI method value for the nonuniform pad processed without AL and the relative standard deviation is 10 %. Thus, the results clearly demonstrate that this method is useless for highly nonuniform samples as the results are completely wrong.

The extracted Hall mobilities for the more uniform pad processed with AL are in general placed closer to the expected value for both two point methods. On average the F3S method underestimates the Hall mobility by 9.2 %, whereas the FSS method is just 2.3% below the expected Hall mobility. From this, it is clear that when examining slightly nonuniform samples, the FSS method is preferable to the F3S method.

We conclude that with a measurement time of less than a minute, the accuracy of the FSS method is reasonable for samples with sheet resistance variations below 5 %, whereas highly nonuniform samples must be characterized with the more time consuming AI method, which in turn does yield a Hall mobility with very high confidence, and with relative standard deviations of just 1 % and 2 %, for the wafer with and without AL, respectively. However, the measurement time for the AI method is 30-40 minutes for one series of N, S, E, W measurements. The AI methods also validates the assumption of constant mobility, since it has been shown that the two pads have the same Hall mobility, while having significantly different sheet resistances.

1) Sheet carrier density: The sheet carrier density changes significantly towards the edges of the pads where the Hall mobilities are extracted. Thus, for a constant Hall mobility we find the activation degree of the implanted dose to be 14 % and 21 % in the pad centre and on average 18 % and 20 % at the pad edges for the wafer without and with AL, respectively. This is in reasonable good agreement with previously reported values for a non-patterned wafer [10].

VI. CONCLUSION

Micro Hall Effect measurements have been performed on two different pads, one with a sheet resistance change toward the edge of ≈ -25 % and the other with $\approx +5$ %. Three different methods have been used on both samples to extract

the Hall mobility. For both fast methods, it proved most difficult to extract correct values of Hall mobilities on the pad with the biggest change in sheet resistance. The proposed technique of measuring two points close to each other was shown to be more reliable than the existing method, where the two points were measured relatively far apart. Measuring two points close to each other resulted in an average Hall mobility that are around 10 % too low, when measuring on the pad with the largest variation, while only a 2.3% wrong when measuring on the test pad with least sheet resistance variation. However, when combining detailed scanning of sheet resistance and micro Hall Effect, it has been demonstrated that Hall mobility can be determined with a relative standard deviation of 1-2 $\%$, even for highly non-uniform test pads.

ACKNOWLEDGEMENTS

We are grateful for the financial support from Copenhagen Graduate School for Nanoscience and Nanotechnology C:O:N:T, the Danish Research Agency FTP. Center for Individual Nanoparticle Functionality CINF is sponsored by The Danish National Research Foundation. We thank Peter F. Nielsen and Rong Lin for continuous help and support, and Peter Bøggild for encouragement and fruitful discussions.

REFERENCES

[1] D. K. Schroder, "Semiconductor materail and device characterization", 3rd ed. (Wiley, Hoboken, NJ, 2006).

[2] T. Clarysse, J. Bogdanowicz, J. Goossens, A. Moussa, E. Rosseel, W. Vandervorst, D. H. Petersen, R. Lin, P. F. Nielsen, O. Hansen, G. Merklin, N. S. Bennett, and N. E. B. Cowern, "On the analysis of the activation mechanisms of sub-melt laser anneals", Mater. Sci. and Eng. B, 154, 24 (2008).

[3] D. H. Petersen, O. Hansen, R. Lin and P. F. Nielsen , "Micro-four-point probe Hall effect measurement method", J. Appl. Phys. 104, 013710, 2008.

[4] D. H. Petersen, O. Hansen, P. F. Nielsen, T. Clarysse, J. Goossens, E. Rosseel and W. Vandervorst, "High precision micro-scale Hall Effect characterization mehod using in-line micro four-point probes", J. Vac. Sci. Technol. B, 26(1), 2008.

[5] F. W. Osterberg, D. H. Petersen, F. Wang, E. Rosseel, W. Vandervorst and O. Hansen, to be submitted.

[6] A. Hunter, J. Zelenko and R. Mani, Proc. IEEE RTP 2007, p.13.

[7] http://www.capres.com/

[8] S. Thorsteinsson, F. Wang, D. H. Petersen, T. M. Hansen, D. Kjær, R. Lin, J. Y. Kim, P. F. Nielsen and O. Hansen, "Accurate micro four-point probe sheet resistance measurements on small samples", Review of Scientific Instruments, Vol. 80, Issue 5, pp. 053902-053902-10, 2009.

[9] E. Rosseel, D. H. Petersen, F. W. Osterberg, O. Hansen, J. Bogdanowicz, T. Clarysse, W. Vandervorst, C. Ortolland, T. Hoffmann, P. Chan, A. Salnik and L. Nicolaides, "Monitoring of local and global temperature non-uniformities by means of Therma-Probe and Micro Four-Point Probe metrology", Proc. IEEE RTP 2009.

[10] E. Rosseel, W. Vandervorst, T. Clarysse, J. Goossens, A. Moussa, R. Lin, D. H. Petersen, P. F. Nielsen, O. Hansen, N. S. Bennett, and N. E. B. Cowern, "Impact of multiple sub-melt laser scans on the activation and diffusion of shallow Boron junctions", Proc. IEEE RTP 2008.

Paper IX

J. Vac. Sci. Technol. B **28**, C1C34-C1C40 (2010).

PhD students contribution:

General idea for study. Major support in problem definition and data treatment. Significant figures, manuscript and references revisions.

Sensitivity study of micro four-point probe measurements on small samples

Fei Wang[a)]
Department of Micro- and Nanotechnology, Technical University of Denmark, DTU Nanotech, Building 345 East, DK-2800 Kgs. Lyngby, Denmark

Dirch H. Petersen
Department of Micro- and Nanotechnology, Technical University of Denmark, DTU Nanotech, Building 345 East, DK-2800 Kgs. Lyngby, Denmark and Capres A/S, Scion-DTU, Building 373, DK-2800 Kgs. Lyngby, Denmark

Torben M. Hansen, Toke R. Henriksen, and Peter Bøggild
Department of Micro- and Nanotechnology, Technical University of Denmark, DTU Nanotech, Building 345 East, DK-2800 Kgs. Lyngby, Denmark

Ole Hansen
Department of Micro- and Nanotechnology, Technical University of Denmark, DTU Nanotech, Building 345 East, DK-2800 Kgs. Lyngby, Denmark and Danish National Research Foundation's Center for Individual Nanoparticle Functionality (CINF), Technical University of Denmark, DK-2800 Kgs. Lyngby, Denmark

(Received 10 June 2009; accepted 10 August 2009; published 1 March 2010)

The authors calculate the sensitivities of micro four-point probe sheet resistance and Hall effect measurements to the local transport properties of nonuniform material samples. With in-line four-point probes, the measured dual configuration sheet resistance is more sensitive near the inner two probes than near the outer ones. The sensitive area is defined for infinite film, circular, square, and rectangular test pads, and convergent sensitivities are observed for small samples. The simulations show that the Hall sheet resistance R_H in micro Hall measurements with position error suppression is sensitive to both local carrier density and local carrier mobility because the position calculation is affected in the two pseudo-sheet-resistance measurements needed for the position error suppression. Furthermore, they have also simulated the sensitivity for the resistance difference $\Delta R_{BB'}$ of two specific configurations to clarify the effect of the calculated position, which results in an unexpected sensitivity to the local carrier mobility. © *2010 American Vacuum Society.*
[DOI: 10.1116/1.3224889]

I. INTRODUCTION

Accurate electrical characterization of ultrashallow junctions (USJs) and other advanced semiconductor structures is essential for monitoring and development of implant and annealing technologies. For decades, four-point probe measurements[1,2] have been used as a good metrology technique because of its low demand on sample preparation and high accuracy. However, the large probe pitch of conventional four-point probes can provide inaccurate results for advanced structures with microscale variation.[3] Recently, the micro four-point probe (M4PP) has been proven to be an efficient method to accurately characterize the sheet resistance of USJs.[4] The accuracy of sheet resistance measurements has been studied for small samples with dimensions comparable to the electrode pitch.[5] Using in-line M4PP and dual configuration measurements,[6,7] the sheet resistance can be measured with high accuracy on test pads like circles, squares, and rectangles without using geometry correction factors. Moreover, micro Hall effect measurements with M4PP have also been applied for characterization of semiconductor films.[8,9] With this technique, carrier mobility, sheet carrier density, and sheet resistance of ultrashallow junctions can be measured, e.g., on a cleaved nonpatterned wafer.

Interpretation of the measured data is rather straightforward on uniform samples. Real samples, however, may not be perfectly uniform and can exhibit small or even large local variations in transport properties and sheet carrier densities. In such cases, the measured data are actually mean values of the local properties in some region in the vicinity of the probes. Moreover, thus, it may conceal any variations within a nonuniform material sample. To fully understand such measurement data and evaluate the measurement error, a sensitivity study of how the measured results depend on the local variations of sample properties is important.

The sensitivity to local resistivity has previously been calculated as weighting functions for the traditional four-point probes arranged on the corners of test samples.[10,11] However, only sensitivities of measurements on infinite films or with the probes at the boundary of the sample are reported, both sample configurations are infeasible for practical USJ measurements. Some of the calculations are not accurate enough in comparison to recently developed finite element modeling

[a)]Author to whom correspondence should be addressed; electronic mail: fei.wang@nanotech.dtu.dk

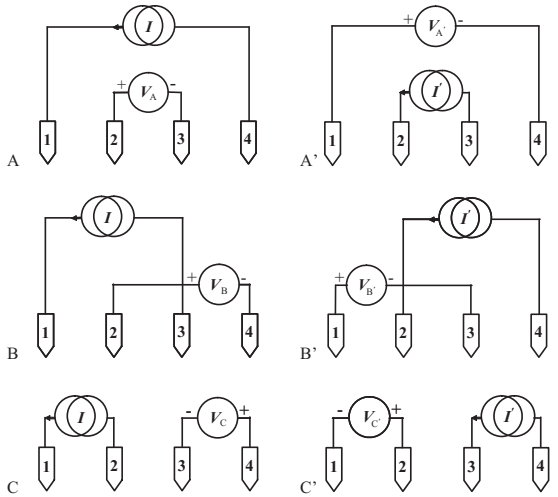

FIG. 1. A, B, and C configurations used in the four-point probe measurement. Each pair of these (A and B or A and C) can be used to calculate the dual configuration sheet resistance with van der Pauw method. With the current and the potential pins interchanged, the A′, B′, and C′ configurations are, respectively, realized.

methods. Furthermore, in-line four-point probe measurements deserve a more detailed study since they have proven to be more reliable than conventional Hall effect methods, and model based infrared spectroscopic reflectrometry.[12]

In this study, we will simulate the sensitivity of the sheet resistance measurements to the local sheet resistance variations and continue to find the sensitivity of micro Hall effect measurements to the local sheet carrier density and the carrier mobility, respectively. All calculations have been done in close agreement with the experimental measurement schemes available in practice.

II. METHOD

In four-point probe measurements, a current I is forced through the sample using two probe pins, while the resulting potential drop V across the other two probe pins is measured as illustrated in Fig. 1. Three pin configurations A, B, and C are usually used, and they can be changed to the configurations A′, B′, and C′, respectively, when interchanging the current and potential pins. The measured four-point resistance is the ratio of the measured voltage to the current $R_i = V_i/I$ (i=A, B, C, A′, B′, and C′).

In this study, COMSOL 3.4 finite element modeling is used to calculate the measurement sensitivities by simulating the four-point current transport in a thin sheet and thus the four-point resistances.[5,13] We first define a homogenous material with certain sheet resistance R_0, carrier mobility μ_0, and sheet carrier density N_0. Then, with a small change of the local properties Δt ($t=R_L$, μ_L, or N_L) in a small area ΔA, the measured values will change accordingly with ΔT ($T=R_S$, μ or N_S). Therefore, a dimensionless point sensitivity S_t^T is defined as

$$S_t^T = \lim_{\Delta t,\Delta A\to 0} p^2 \frac{\Delta T/T}{\Delta t/t}\frac{1}{\Delta A} = p^2 \frac{\partial^2 T}{\partial t \partial A}\frac{t}{T}, \tag{1}$$

where p is the probe pitch. The equation may be interpreted as follows. If there is a sheet resistance change of 100 Ω in a local area of 1 μm^2 with a constant sheet resistance sensitivity of 1, we can detect a change of 1 Ω in the measurement using four-point probes with a probe pitch of 10 μm. However, we will only detect a change of 0.01 Ω in the measurement if probes with a probe pitch of 100 μm are used.

For each point in the sensitivity simulation, the required four point resistances are calculated with and without the small area perturbation successively. The two cases are defined using exactly the same meshing elements to eliminate meshing effects. The convergence is verified by changing the size of the perturbation area and the magnitude of the perturbation.

For sheet resistance measurements, the sensitivity to the local sheet resistance is calculated using dual configuration measurements (A and B or A and C configurations in Fig. 1) for an infinite film as well as for circular, square, and rectangular test samples, respectively. When the four-probe pins are placed on the perimeter of the test sample, R_A, R_B, and R_C can be, respectively, measured with specific configurations. Moreover, the exact sheet resistance R_S can be calculated from following van der Pauw equations with the dual configuration measurements R_A and R_B or R_A and R_C,[6,7]

$$\exp\left(\frac{2\pi R_A}{R_S}\right) - \exp\left(\frac{2\pi R_B}{R_S}\right) = 1$$

or

$$\exp\left(-\frac{2\pi R_A}{R_S}\right) + \exp\left(-\frac{2\pi R_C}{R_S}\right) = 1. \tag{2}$$

Recently, we have further proved that Eq. (2) is also applicable when the probe pins are placed on the mirror plane of the test sample with one or more geometry mirror planes.[5]

Interpretation of the dual configuration sheet resistance results may be assisted by differentiation of Eq. (2) with respect to the local sheet resistance R_L which results in the following relation for the dual configuration sheet resistance sensitivity:

$$S_{R_L}^{R_S} = \frac{\frac{R_A}{R_S}\exp\left(\frac{2\pi R_A}{R_S}\right)S_{R_L}^{R_A} - \frac{R_B}{R_S}\exp\left(\frac{2\pi R_B}{R_S}\right)S_{R_L}^{R_B}}{\frac{R_A}{R_S}\exp\left(\frac{2\pi R_A}{R_S}\right) - \frac{R_B}{R_S}\exp\left(\frac{2\pi R_B}{R_S}\right)}$$

or

$$S_{R_L}^{R_S} = \frac{\frac{R_A}{R_S}\exp\left(-\frac{2\pi R_A}{R_S}\right)S_{R_L}^{R_A} + \frac{R_C}{R_S}\exp\left(-\frac{2\pi R_C}{R_S}\right)S_{R_L}^{R_c}}{\frac{R_A}{R_S}\exp\left(\frac{2\pi R_A}{R_S}\right) + \frac{R_C}{R_S}\exp\left(-\frac{2\pi R_C}{R_S}\right)}, \tag{3}$$

where the four-point resistance sensitivities follow directly from Eq. (1),

$$S_{R_L}^{R_A} = p^2 \frac{\partial^2 R_A}{\partial R_L \partial A} \frac{R_L}{R_A}, \quad S_{R_L}^{R_B} = p^2 \frac{\partial^2 R_B}{\partial R_L \partial A} \frac{R_L}{R_B},$$

and

$$S_{R_L}^{R_C} = p^2 \frac{\partial^2 R_C}{\partial R_L \partial A} \frac{R_L}{R_C}. \tag{4}$$

Specifically, when equidistant probes are used for an infinite film, Eq. (3) reduces to

$$S_{R_L}^{R_S} = \frac{4\ln(4) S_{R_L}^{R_A} - 3\ln(3) S_{R_L}^{R_B}}{4\ln 4 - 3\ln 3}$$

or

$$S_{R_L}^{R_S} = \frac{\ln(4) S_{R_L}^{R_A} + 3\ln(4/3) S_{R_L}^{R_C}}{\ln 4 + 3\ln(4/3)}. \tag{5}$$

All the calculations above will result in the same sensitivity, no matter which configuration pair (A and B or A and C) you choose.

For micro Hall effect measurements, we use the dual point four configuration measurement technique with position error suppression[8,9] on samples with a single insulating boundary. Here the four-point resistances in configurations A, A′, B, and B′ (as shown in Fig. 1) are measured with the probes parallel to the insulating boundary at two positions with a known separation Δy (e.g., $2.8p$). With a magnetic flux density B_z normal to the sample surface, the first set of measurements (R_{A1}, $R_{A1'}$, R_{B1}, and $R_{B1'}$) is carried out close to the boundary (e.g., approximately $0.2p$ from the boundary), while the second set (R_{A2}, $R_{A2'}$, R_{B2}, and $R_{B2'}$) is done remote from the boundary (e.g., approximately $3p$ from the boundary). Calculations using Eq. (1) with $(R_{Ai}+R_{Ai'})/2$ and $(R_{Bi}+R_{Bi'})/2$ representing R_A and R_B results in a pair of pseudosheet resistances R_{Pi} instead of the true sheet resistance. Using model relations[9] for R_P as a function of the distance from the boundary, the exact positions (y_1 and y_2) and the sheet resistance R_S are calculated from R_{P1}, R_{P2}, and Δy. Finally, the Hall sheet resistance R_H is calculated using the known relation[8,9] between the four-point resistance difference $\Delta R_{BB'} = (R_B - R_{B'})$, position y_1 and R_H.

Then, sheet carrier density N_S and carrier mobility μ can be calculated from the Hall sheet resistance R_H and the sheet resistance R_S,

$$N_S = \frac{\overline{r_H} B_Z}{ZeR_H} \quad \text{and} \quad \mu = \frac{ZR_H}{\overline{r_H} R_S B_Z}, \tag{6}$$

where $\overline{r_H}$ is the mean Hall scattering factor and Ze is the carrier charge ($Z = \pm 1$).

Differentiation of Eq. (6) leads to the following relation between the sensitivities of the measured Hall sheet resistance and sheet resistance, and the sensitivities of the measured sheet carrier density and carrier mobility:

$$S_t^{N_S} = -S_t^{R_H} \quad \text{and} \quad S_t^{\mu} = S_t^{R_H} - S_t^{R_S}. \tag{7}$$

Both the Hall sheet resistance and the sheet resistance are studied in this work, and their sensitivities to the local carrier mobility and local sheet carrier density are calculated. The sensitivities of the measured carrier mobility and sheet carrier density can be calculated afterwards using Eq. (7).

III. RESULTS

A. Sheet resistance measurements

Figures 2(a)–2(c) show the sensitivities of R_A, R_B, and R_C to the local sheet resistance for an infinite film, respectively. It can be seen that single configuration measurements exhibit singularities at the probe contact points and both positive and negative sensitivities are observed.[10] The sensitivity of A and C configurations gives exactly the same results as previously reported values calculated using the adjoint system method.[3]

For dual configuration measurements, the singularities are eliminated in agreement with Eqs. (5) and (6). In Figs. 3(a)–3(d), the measured sheet resistance shows a continuous and positive sensitivity to the local sheet resistance for all the four different sample geometries (infinite sheet, circle, square, and rectangle).[10] The simulations are performed with the four contacts placed in the mirror plane of the test pads, which is the ideal position for accurate measurement results.[5] For the samples, the simulated sheet resistance is seen to be more sensitive to the area close to the two inner probes. When a sensitivity threshold of 0.1 is defined, the "sensitive area" is within a radius of about $1p$ from the central point.

From Fig. 3(a), the sensitivity for the infinite sample is observed with maximum value of about 0.4 around the two inner probes. The sensitivity near the two outer probes is about 0.05. Compared to the infinite film, the sensitivities for small samples are much larger around the two inner probes while smaller around the outer probes. The maximum sensitivity is more than 0.8 for the rectangular sample with width of $2p$ and length of $5p$, as shown in Fig. 3(d). It follows that the confined insulation boundary conditions will enhance the influence near the inner probes with respect to that near the outer probes. The sensitivities of the measured dual configuration sheet resistance are always zero on the probe line (mirror plane of the samples) except at the probe points because of the symmetric current flow. For the region near the probe points shown in Fig. 3(e), we obtain a remarkable sensitivity of 0.45 for the area very close ($<0.005p$) to the inner probe points. However, the sensitive area here is extremely small ($<0.000\,025p^2$), and thus it will not affect the practical measurement result unless the local sheet resistance changes by several orders of magnitude.

B. Micro Hall effect measurements

In the calculations the dual point three configuration (A, B, and B') Hall effect measurements are assumed done at distances of $0.2p$ and $3p$ from the single edge, respectively. Figures 4(a) and 4(b) show the expected negative sensitivities of the sheet resistance to the local carrier density and the local mobility, respectively.

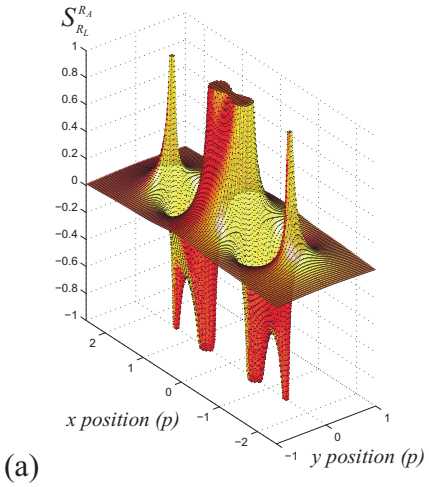

(a)

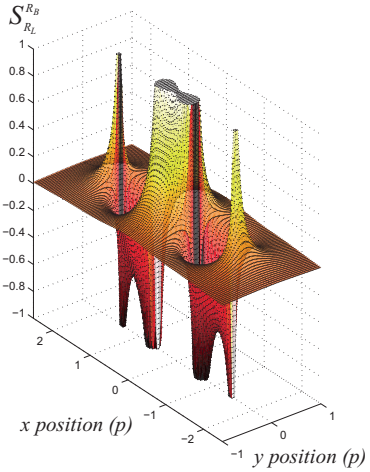

(b)

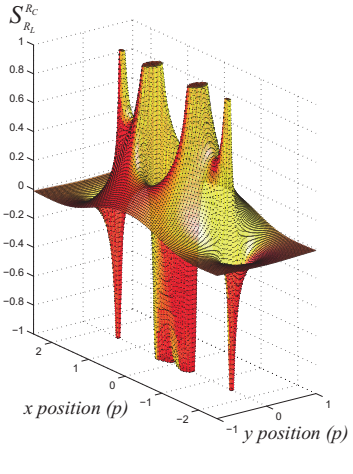

(c)

FIG. 2. (Color online) Sensitivity of the measured four-point probe resistance to local sheet resistance variations for single configuration measurements of (a) R_A, (b) R_B, and (c) R_C, respectively, on an infinite sample. The singular peaks have been truncated to show the smaller values around the probes clearly.

The negative sensitivities occur because the sheet resistance is inversely proportional to the carrier density and the mobility, $R_S \cong 1/(e\mu N_S)$ when the mobility and the magnetic flux density are sufficiently small.

The two graphs show very similar values because the carrier density and the mobility play almost the same part in the equation. The sheet resistance is seen to be far more sensitive to the area surrounding the measurement point at $3p$ while less sensitive to the measurement point at $0.2p$. In comparison to the absolute values in Fig. 3(a), it can be seen that the sheet resistance measured from micro Hall effect measurements shows a similar sensitivity to the local sheet resistance as that from a dual configuration sheet resistance measurement.

Figures 5(a) and 5(b) show the sensitivities of the measured Hall sheet resistance to the local sheet carrier density and the local carrier mobility, respectively. Unlike the sheet resistance, the Hall sheet resistance is more sensitive to the measurement point at $0.2p$ since the Hall effect signal is measured here. The negative sensitivities around measurement point at $3p$ are due to the position calculation from the two measurements, in which R_{P2} is negatively sensitive to the local sheet carrier density and the local carrier mobility. This is also the reason for the positive sensitivity to the local sheet carrier density for the measurement point at $0.2p$.

IV. DISCUSSION

To clarify the effect of the calculated position for the Hall sheet resistance measurement, we additionally analyze the sensitivity of $\Delta R_{BB'}$, which is defined as the resistance difference of configurations B and B′. Considering a four-point probe on a region Ω with an insulating boundary, an adjoint network analysis with an applied magnetic flux density results in the following expressions for the four-point resistances R_B and $R_{B'}$:

$$R_B = \frac{1}{I^2}\left[\int_\Omega R_S \mathbf{J_S}\cdot\mathbf{J'_S}d\Omega + \int_\Omega R_H(\mathbf{J_S}\times\mathbf{J'_S})\cdot\frac{\mathbf{B}}{B}d\Omega\right], \quad (8)$$

$$R_{B'} = \frac{1}{I^2}\left[\int_\Omega R_S \mathbf{J_S}\cdot\mathbf{J'_S}d\Omega - \int_\Omega R_H(\mathbf{J_S}\times\mathbf{J'_S})\cdot\frac{\mathbf{B}}{B}d\Omega\right]. \quad (9)$$

where $\mathbf{J_S}$ and $\mathbf{J_{S'}}$ are the sheet current densities for $\mathbf{B}$ and $\mathbf{B'}$ configurations, respectively. From these two equations, $\Delta R_{BB'}$ and its sensitivity are calculated as

$$\Delta R_{BB'} = R_B - R_{B'} = \frac{2}{I^2}\int_\Omega R_H(\mathbf{J_S}\times\mathbf{J'_S})\cdot\frac{\mathbf{B}}{B}d\Omega, \quad (10)$$

$$S_t^{\Delta R_{BB'}} = p^2\frac{\partial^2\Delta R_{BB'}}{\partial t\partial A}\frac{t}{\Delta R_{BB'}}$$

$$= \frac{2p^2 t}{I^2 B\Delta R_{BB'}}\frac{\partial}{\partial t}[R_H(\mathbf{J_S}\times\mathbf{J'_S})\cdot\mathbf{B}]. \quad (11)$$

From Eqs. (10) and (11), we can see that $\Delta R_{BB'}$ depends on both the Hall sheet resistance R_H and cross product of the sheet current densities $\mathbf{J_S}$ and $\mathbf{J_{S'}}$. Therefore, $\Delta R_{BB'}$ will be sensitive to any variation in local properties which can influence the Hall sheet resistance or the cross product. From Eq. (6), we know that the Hall sheet resistance R_H is inverse proportional to the carrier density, which results in the nega-

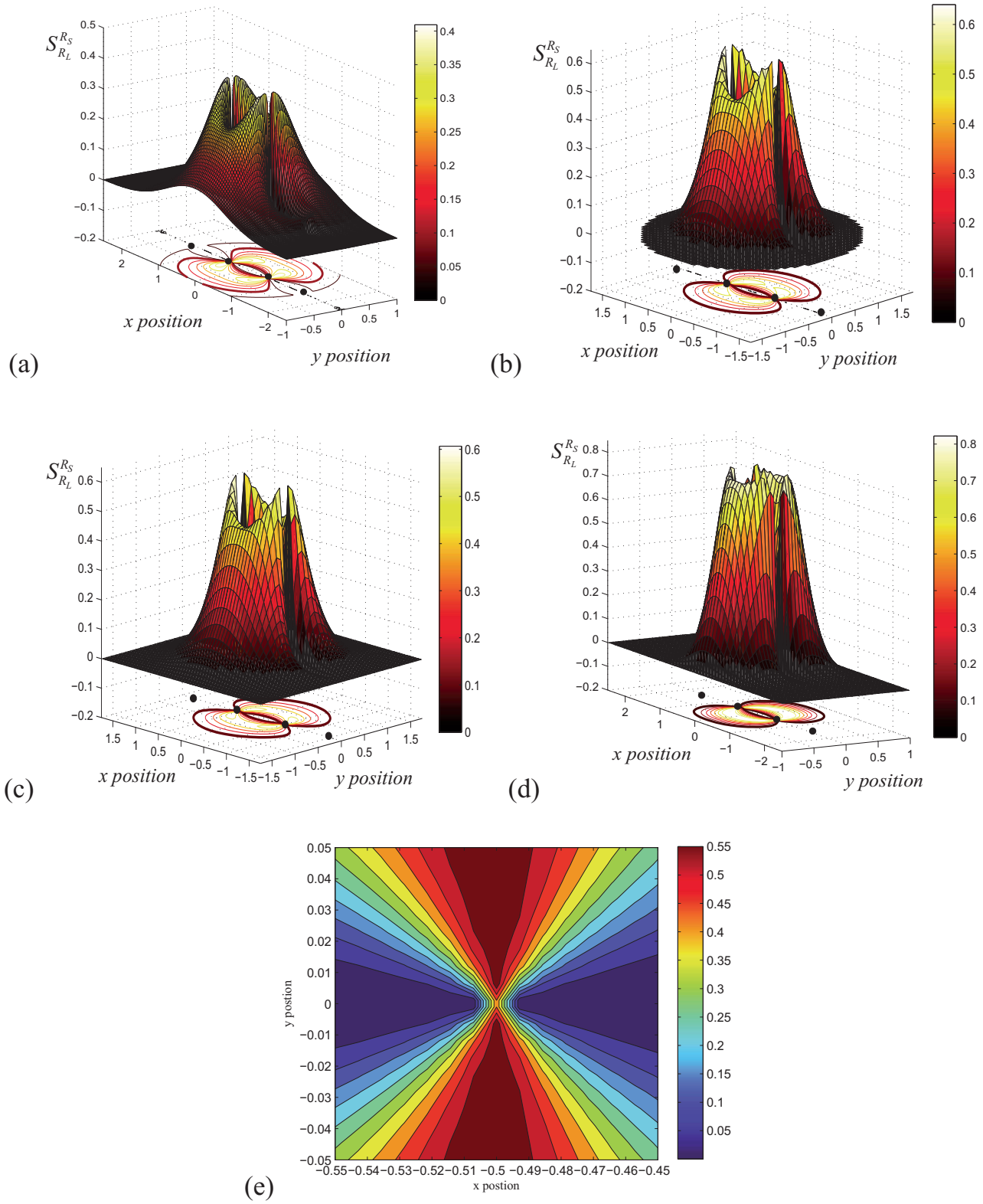

FIG. 3. (Color online) Sensitivity of dual configuration sheet resistance measurements to local sheet resistance variations for (a) part of an infinite film, (b) a circular sample with diameter of $3.5p$, (c) a square sample with side length of $3.5p$, and (d) a rectangular sample with width of $2p$ and length of $5p$. The bold lines indicate the sensitivity value of 0.1, and the black full circles indicate the contact positions. A closeup view of the area around one of the inner probes from (c) is shown in (e). All the x, y positions are normalized with probe spacing p.

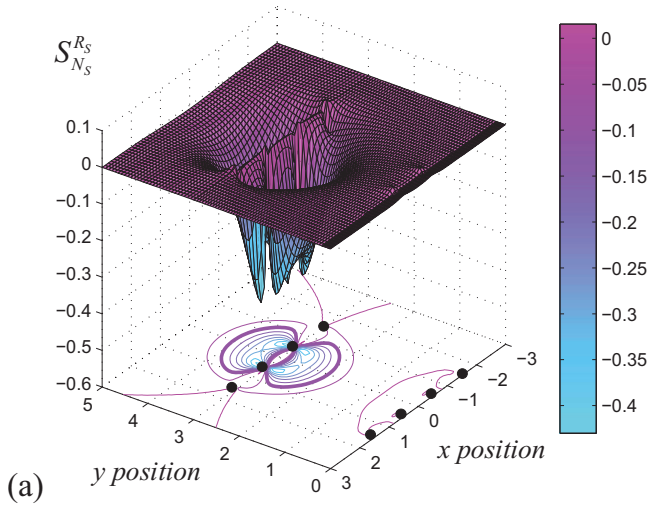

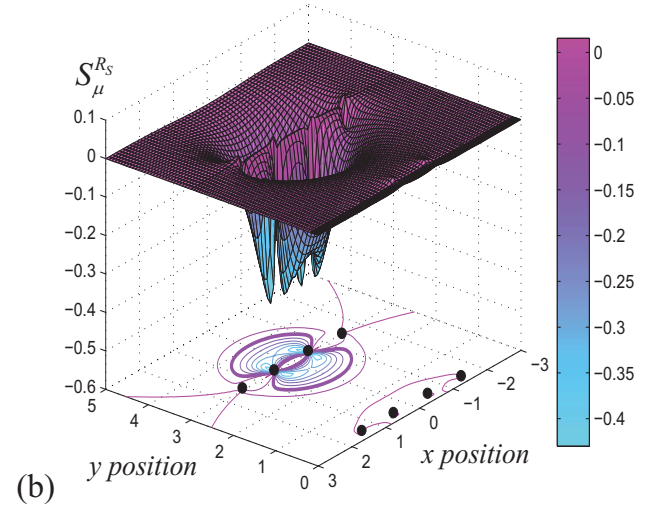

FIG. 4. (Color online) Sensitivities of the measured sheet resistance in a micro Hall effect measurement to variations in (a) local sheet carrier density and (b) local carrier mobility. The bold lines indicate the sensitivity value of −0.1, and the black full circles indicate the contact positions. All the x, y positions are normalized with probe spacing p.

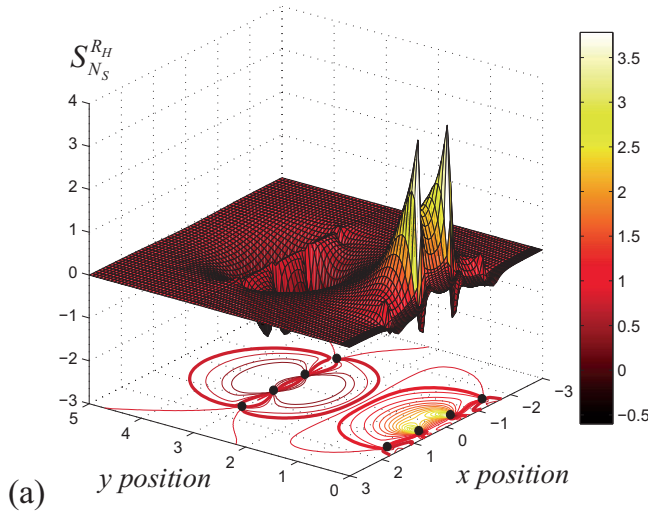

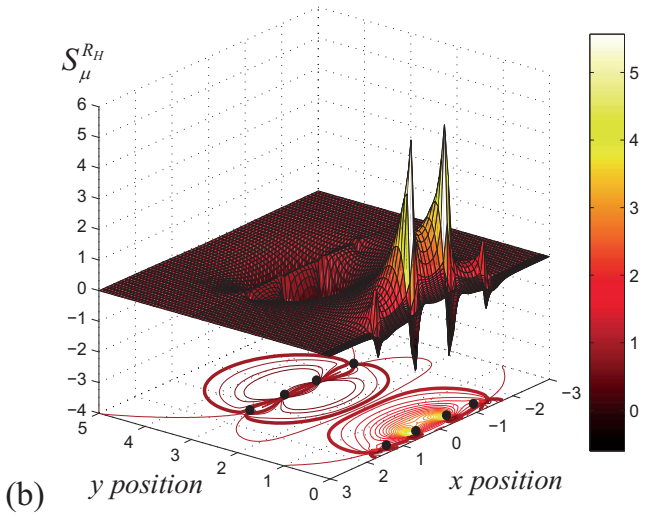

FIG. 5. (Color online) Sensitivities of the measured Hall sheet resistance in a micro Hall effect measurement to (a) local sheet carrier density and (b) local carrier mobility. The bold lines indicate the sensitivity values of ±0.1, and the black full circles indicate the contact positions. All the x, y positions are normalized with probe spacing p.

tive sensitivity of $\Delta R_{BB'}$ in Fig. 6(a). Although R_H is insensitive to the mobility, the simulation also shows a remarkable sensitivity of $\Delta R_{BB'}$ to the local carrier mobility in Fig. 6(b). This is due to the fact that the variation of local carrier mobility may affect the sheet current densities $\mathbf{J_S}$ and $\mathbf{J_{S'}}$, which finally changes the cross product and makes the $\Delta R_{BB'}$ sensitive to the local carrier mobility. An in-depth study of this effect on sheet current density will be performed in the near future. Singularities are also observed in Fig. 6(b), which is because only B-type configurations are used here as in Fig. 1(b).

Finally, when a homogenous sample is considered, the overall integral of the sensitivity may be deduced as $\Sigma_t^T = \int_\Omega S_t^T / p^2 d\Omega$, which represents the sensitivity of the measured parameter T to the global variation of the material parameter t. It may take the value of 1, −1, or 0, depending on whether the measured parameter T is proportional to, inversely proportional to, or independent of the parameter t in question. From the calculated sensitivities, we find agreements with expectations $\Sigma_\mu^{R_S} = \Sigma_{N_S}^{R_S} = \Sigma_{N_S}^{R_H} = \Sigma_{N_S}^{\Delta R_{BB'}} \cong -1$, $\Sigma_{R_L}^{R_S} \cong 1$, and $\Sigma_\mu^{R_H} = \Sigma_\mu^{\Delta R_{BB'}} \cong 0$.

V. CONCLUSION

In this article, we have shown a sensitivity study for sheet resistance measurements and micro Hall effect measurements using micro four-point probes. For an infinite film and small circular, square, and rectangular samples, dual configuration sheet resistance measurements always provide a continuous positive sensitivity to local sheet resistance. The simulations prove that the measured sheet resistances are more sensitive to the area near the two inner probes while insensitive to the central position, which is usually considered the "measurement point." In addition, when a sensitivity threshold of 0.1 is defined, the "sensitive area" is within a

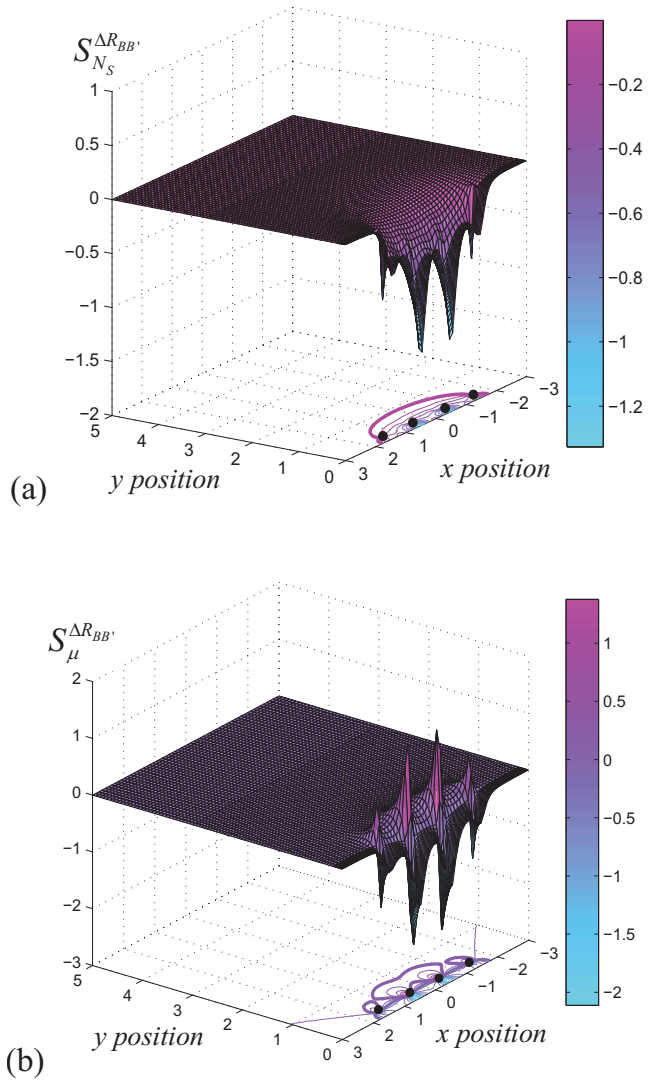

FIG. 6. (Color online) Sensitivities of $\Delta R_{BB'}$ in a micro Hall effect measurement to (a) local sheet carrier density and (b) local carrier mobility. The bold lines indicate the sensitivity values of ± 0.1, and the black full circles indicate the contact positions. All the x, y positions are normalized with probe spacing p.

radius of about $1p$ from the central point. It is also observed that the sensitivity is larger and more confined for smaller samples.

In micro Hall effect measurements, we use the position error suppression method to compare with the practical measurement. The measured sheet resistance has similar sensitivities as in the dual configuration method to the local sheet carrier density and the local carrier mobility for the remote measurement point at $3p$, while the sensitivities are negligible for the measurement point at $0.2p$. The Hall sheet resistance exhibits more complicated sensitivities compared to sheet resistance. Variations in the local sheet carrier density and the local carrier mobility will affect the position calculation from the two measurements. This effect makes the measured Hall resistance sensitive to both measurement points and causes a positive sensitivity to the local sheet carrier density around the measurement point at $0.2p$. To clarify the effect of the calculated position, the four-point resistance difference $\Delta R_{BB'}$ is also studied. The calculations show an unexpected sensitivity of $\Delta R_{BB'}$ to the local carrier mobility, and we speculate that the sensitivity is due to sheet current density changes caused by the local carrier mobility variation.

ACKNOWLEDGMENTS

The authors are grateful for the financial support from Copenhagen Graduate School for Nanoscience and Nanotechnology (C:O:N:T), the Danish Research Agency (FTP), and Danish National Advanced Technology Foundation. Center for Individual Nanoparticle Functionality (CINF) is sponsored by The Danish National Research Foundation.

[1]L. B. Valdes, Proc. IRE **42**, 420 (1954).
[2]F. M. Smits, Bell Syst. Tech. J. **37**, 711 (1958).
[3]D. H. Petersen, R. Lin, T. M. Hansen, E. Rosseel, W. Vandervorst, C. Markvardsen, D. Kjær, and P. F. Nielsen, J. Vac. Sci. Technol. B **26**, 362 (2008).
[4]T. Clarysse *et al.*, Doping Engineering for Device Fabrication (Materials Research Society Symposium Proceedings), Vol. 912, 197 (2006).
[5]S. Thorsteinsson, F. Wang, D. H. Petersen, T. M.Hansen, D. Kær, R. Lin, J.-Y. Kim, P. F. Nielsen, and O. Hansen, Rev. Sci. Instrum. **80**, 053902 (2009).
[6]L. J. van der Pauw, Philips Res. Rep. **13**, 1 (1958).
[7]R. Rymaszewski, J. Phys. E **2**, 170 (1969).
[8]D. H. Petersen, O. Hansen, R. Lin, and P. F. Nielsen, J. Appl. Phys. **104**, 013710 (2008).
[9]D. H. Petersen, O. Hansen, R. Lin, P. F. Nielsen, T. Clarysse, J. Goossens, E. Rosseel, and W. Vandervorst, in *16th IEEE International Conference on Advanced Thermal Processing of Semiconductors, RTP 2008* (IEEE, New York, 2008), pp. 251–256.
[10]D. W. Koon and C. J. Knickerbocker, Rev. Sci. Instrum. **63**, 207 (1992).
[11]D. W. Koon and C. J. Knickerbocker, Rev. Sci. Instrum. **64**, 510 (1993).
[12]T. Clarysse *et al.*, Mater. Sci. Eng., B, **154–155**, 24 (2008).
[13]http://www.comsol.com/.

Paper X

in Proc. RTP 2009 (IEEE, New York, 2009) pp.151-156.

PhD students contribution:

Experimental data. Major support in problem definition and ideas for study. Significant figures, manuscript and references revisions.

17th IEEE International Conference on Advanced Thermal Processing of Semiconductors – RTP 2009

Accuracy of Micro Four-Point Probe Measurements on Inhomogeneous Samples: A Probe Spacing Dependence Study

Fei Wang[1], Dirch H. Petersen[1, 2], Frederik W. Osterberg[1], Ole Hansen[1, 3]

[1] Department of Micro- and Nanotechnology, Technical University of Denmark, DTU Nanotech Building 345 East DK-2800 Kgs. Lyngby, Denmark and
[2] Capres A/S, Scion-DTU, Building 373, DK-2800 Kgs. Lyngby, Denmark and
[3] Danish National Research Foundation's Center for Individual Nanoparticle Functionality (CINF), Technical University of Denmark, DK-2800 Kgs. Lyngby, Denmark
Email: Fei.Wang@nanotech.dtu.dk

***Abstract*- In this paper, we discuss a probe spacing dependence study in order to estimate the accuracy of micro four-point probe measurements on inhomogeneous samples. Based on sensitivity calculations, both sheet resistance and Hall Effect measurements are studied for samples (e.g. laser annealed samples) with periodic variations of sheet resistance, sheet carrier density, and carrier mobility. With a variation wavelength of λ, probe spacings from 0.001λ to 100λ have been applied to characterize the local variations. The calculations show that the measurement error is highly dependent on the probe spacing. When the probe spacing is smaller than 1/40 of the variation wavelength, micro four-point probes can provide an accurate record of local properties with less than 1% measurement error. All the calculations agree well with previous experimental results.**

I. INTRODUCTION

Along with the continuous downscaling of the critical dimension in semiconductor processes, sheet materials such as ultra shallow junctions (USJ) are widely used in the process development. Characterization and monitoring of implant and annealing technologies for USJ is a significant metrology challenge. For several decades, conventional four-point probe measurement has been a useful metrology technique to characterize sheet resistance, sheet carrier density, and carrier mobility [1, 2] when combined with Hall Effect measurements [3, 4]. However, conventional four-point probes can cause large measurement errors on advanced micro or even nano-scale structures like USJ, unless the probe spacing can also be down scaled simultaneously with the devices under test [5]. Recently, in-line micro four-point probe (M4PP) measurements have been proven to be an accurate method for characterization of USJ sheet resistance [6, 7]. The accuracy of the measurements has been studied for small samples with dimensions comparable to the probe spacing [8]. Moreover, micro Hall effect measurements with M4PP have also been applied, and carrier mobility, sheet carrier density and sheet resistance of USJ have been accurately measured e.g. on cleaved non-patterned wafers [9, 10, 11].

The measurement results are actually mean values of the local properties across the measured sample which is perfect with ideally homogeneous samples. Real samples such as laser annealed junctions, however, may not be perfectly homogeneous and can exhibit local variations in electrical properties related to e.g. the stitching overlays and inhomogeneity of the laser beam (e.g. a diode array) used for annealing. Recently, we have calculated the sensitivities of micro four-point probe sheet resistance and Hall Effect measurements to small variations in the local properties [12].

In this study, the sensitivity values are used to estimate the measured variation according to periodic variations on inhomogeneous samples. Furthermore, the dependence of the measurement error on the probe spacing is studied in detail.

II. METHOD

For an inhomogeneous sample, with a small change of the local sheet resistance, R_L, the local sheet carrier density, N_L, or the local carrier mobility, μ_L, in a small area, ΔA, the measured values of the sheet resistance, R_S, and the Hall sheet resistance, R_h, will also change as a result. Therefore, the sensitivity of the measured values T (T=R_S , R_h , μ or N_S) to the local properties t (t=R_L, N_L or μ_L), can be defined as a dimensionless sensitivity variable S_t^T :

$$S_t^T = \lim_{\Delta t, \Delta A \to 0} p^2 \frac{\Delta T / T}{\Delta t / t} \frac{1}{\Delta A} = p^2 \frac{\partial^2 T}{\partial t \partial A} \frac{t}{T} \tag{1}$$

where p is the probe spacing; Δt is the local variation and ΔT is the measured variation; μ and N_S are the measured mobility and sheet carrier density, respectively. Two-dimensional (2D) sensitivity values of the sheet resistance and the Hall Effect measurements have been plotted in [12] and will be used in this study.

Based on the sensitivity definition a small 2D variation of the local property $\Delta t(x, y)$ across an inhomogeneous sample will result in a measured variation of ΔT as follows:

$$\frac{\Delta T}{T_0} = \iint_{\Omega} \frac{\Delta t(x, y)}{t_0} \cdot S_t^T / p^2 d\Omega \tag{2}$$

where t_0, and T_0 are the mean values corresponding to an

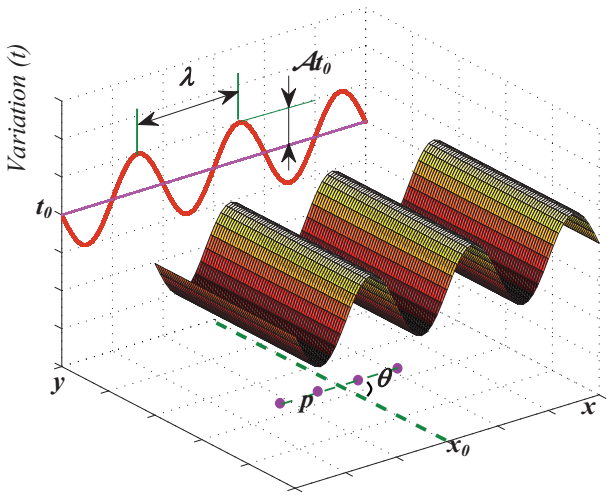

Fig. 1 Schematic view of the local property variation and the micro four-point probes for scanning measurement.

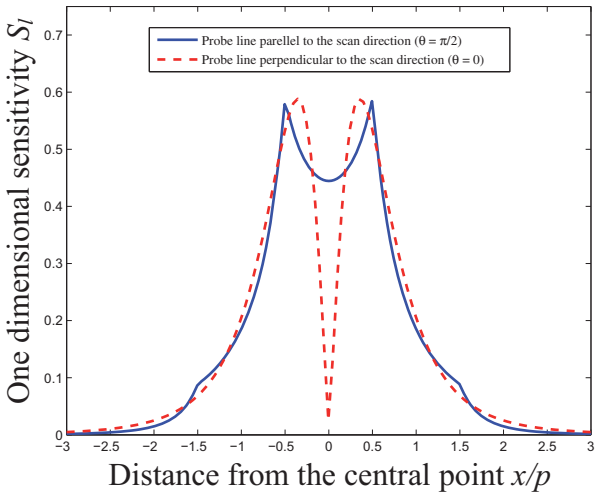

Fig. 2 1D sensitivity of the measured sheet resistance to the local sheet resistance for infinite sample.

equivalent homogeneous sample. Variations in the most sensitive area near the probes can affect the measurement results significantly while regions further away only contribute slightly.

In this study, we will study an inhomogeneous sample with a small periodic parameter variation defined by (3):

$$\frac{\Delta t(x,y)}{t_0} \equiv \mathcal{A}\sin(2\pi x/\lambda) \tag{3}$$

As schematically shown in Fig. 1, the local property t has a sinusoidal variation in the x direction with a scaled amplitude of $\mathcal{A}$ and wavelength of λ, while t does not vary in the y direction. The probes are always assumed to be scanned across the sample in the x direction to trace the local variation. As for the line of the probe, the four probes can be placed in any direction for sheet resistance measurement on an infinite film, thus forming an angle θ between the line of the probe and the y direction. For the Hall Effect measurement on a cleaved wafer, the wafer is assumed to be cleaved along the x direction, and since the line of the probe must be parallel to the cleaved boundary, the angle θ is 90 degrees in this case.

Using equations (2) and (3) the measured variation can be expressed as:

$$\frac{\Delta T}{T_0} = \int_{\Omega} \mathcal{A}\sin(2\pi x/\lambda)\cdot S_t^T \Big/ p^2 d\Omega \tag{4}$$

When the four point probes are moved along the x direction to scan the local variation, the measured variation at $x=x_0$ becomes:

$$\begin{aligned}\frac{\Delta T(x_0)}{T_0} &= \int_{\Omega} \mathcal{A}\sin(2\pi x/\lambda)\cdot S(x-x_0,y)/\,p^2 d\Omega \\ &= \int_{x} \mathcal{A}\sin(2\pi x/\lambda)\cdot S_l(x-x_0)/\,p dx\end{aligned}$$

$$= \int_{x} \mathcal{A}\sin\left[2\pi(x+x_0)/\lambda\right]\cdot S_l(x)/\,p dx \tag{5}$$

since the local property is constant in the y direction. In Equation 5, S_l is the one-dimensional (1D) sensitivity, which is defined as the line integral of the 2D sensitivity in the y direction divided by the probe pitch:

$$S_l(x) = \int_{l} S(x,y)/\,p dy \tag{6}$$

From equation (5), it follows that also $\mathcal{A}$ is periodic with the wavelength of λ,

$$\frac{\Delta T}{T_0} \equiv \mathcal{A}_m \sin(2\pi x/\lambda + \varphi_s) \tag{7}$$

with the scaled amplitude $\mathcal{A}_m$ of the measurement result and the phase shift φ_s relative to the local variation.

The sensitivity values used here were simulated with dual configuration sheet resistance measurements, while for the Hall Effect measurements the dual point three configuration method was used, just as in the practical measurements [11, 12].

III. Results and Discussion

1. Sheet Resistance Measurement

First, we calculate the 1D sensitivity of measured sheet resistance to the local sheet resistance, according to the different probe line directions. Since the line of the probe could have any angle with the scanning direction for an infinite film, we shall study two typical cases: the probe line perpendicular to the scanning direction ($\theta = 0$), and the line of the probe parallel to the scanning direction ($\theta = 90°$). The 1D sensitivities are plotted as a function the normalized distance x/p from the probe centre. As shown in Fig. 2, the 1D

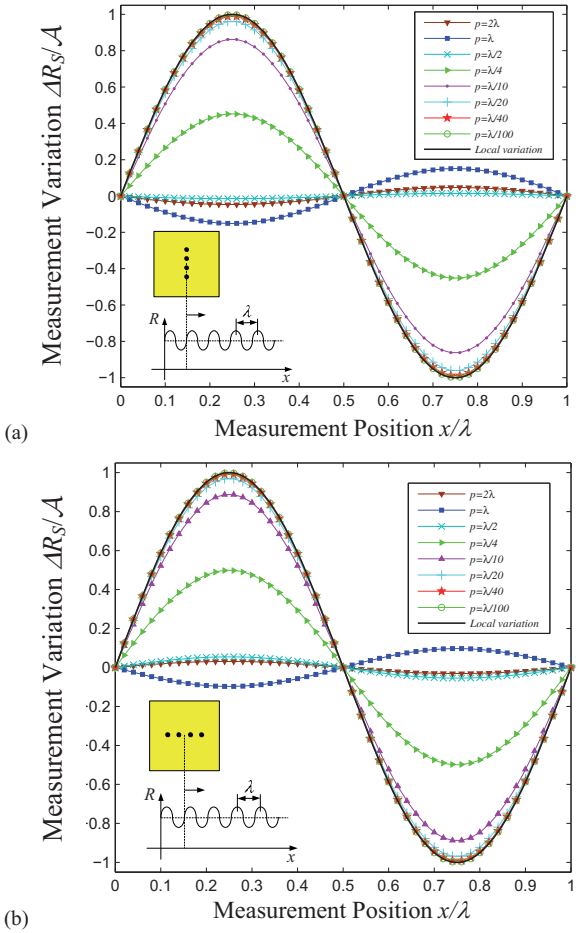

Fig. 3 Sheet resistance measurement result with different probe spacing according to a sinusoidal variation of local sheet resistance: (a) Probe line perpendicular to the scanning direction; (b) Probe line parallel to the scanning direction.

sensitivities show two peak values around 0.5p from the probe centre for both probe orientations. For the probe line parallel to the scanning direction, the sensitivity is always higher than 0.1 within a distance of 1p from the probe centre, while for the probe line perpendicular to the scanning direction, the sensitivity is almost zero at the probe centre. Thus the measured sheet resistance is not sensitive to the local sheet resistance on the probe line (except the probe points).

This canyon like distribution of sensitivity makes the measurement in the perpendicular situation less concentrated than the parallel one, which will cause a slightly larger measurement error at identical probe spacing.

Fig. 3 shows the simulated measurement result in a scan across one full wavelength of the local sheet resistance variation using eight different probe spacings. For both directions, the smaller the probe spacing used, the closer the measured result is to the local variation. About 99% of the local variation can be resolved when the probe spacing is smaller than $\lambda/40$, while less than 40% can be detected if the probe spacing is larger than $\lambda/4$. Furthermore, when a probe

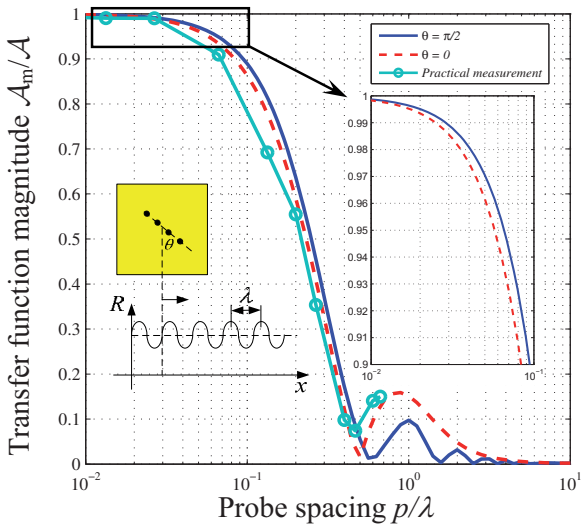

Fig. 4 The sheet resistance measurement transfer function as a function of the probe spacing p for a local sheet resistance variation with a wavelength of λ. For comparison, the previously reported measurements are included [5].

spacing approximately equal to the variation wavelength is applied, a reversal phase shift is observed because the most sensitive area is just half of the variation wavelength away from the measurement point. As discussed above, the measurement variation in Fig. 3(a) (θ = 0) is always slightly smaller than that in Fig. 3(b) (θ = 90°) when the same probe spacing is used. This is more clearly demonstrated in Fig. 4 where accuracy of the sheet resistance measurement is shown as a spatial frequency transfer function of the probe spacing. It can be seen that the measurement accuracy decreases remarkably with an increase of the probe spacing. If a measurement error of less than 1% is desired (which means a total measurement error of 0.1% for local variation amplitude of 10%, as often in the semiconductor industry), a small probe spacing of $\lambda/40$ is indispensable. This is approximately 20μm probe pitch for a typical laser inhomogeneity wavelength of 0.75mm. For comparison, Fig. 4 includes the measured variation in previously reported practical measurements [5], which agrees well with our calculations.

2. Hall Effect Measurement

Unlike the sheet resistance measurement, the Hall Effect measurement is done on a half-plane film such as a cleaved wafer using the dual point three configurations technique [11]. The probe line is parallel to the cleaved boundary which is aligned to the x direction and therefore, θ is always 90 degrees.

The measured properties studied in [12] are the sheet resistance and Hall sheet resistance, while the local variations are the local sheet carrier density and local carrier mobility. Using the sensitivity values, we can first calculate the sensitivities of the measured sheet resistance and Hall sheet resistance to local sheet carrier density (N_L) and local carrier mobility (μ_L), respectively. The four resulting 1D sensitivities

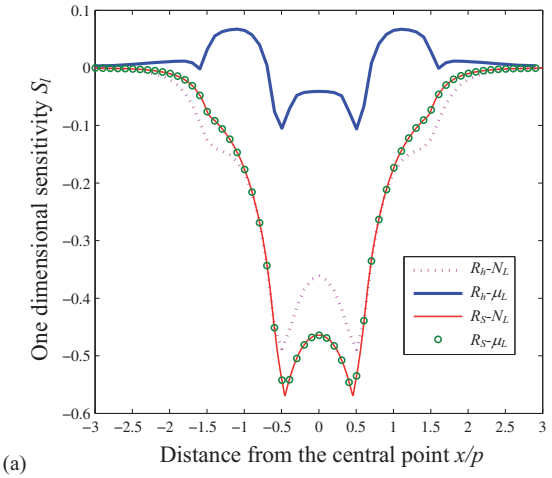

(a)

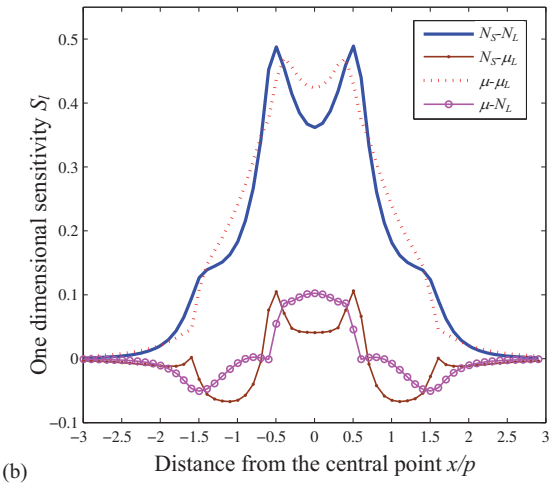

(b)

Fig. 5 1D sensitivities of (a) the sheet resistance and the Hall sheet resistance; (b) the sheet carrier density and the carrier mobility to variations of the local sheet carrier density and the local carrier mobility for Hall effect measurements on a cleaved wafer with a single boundary.

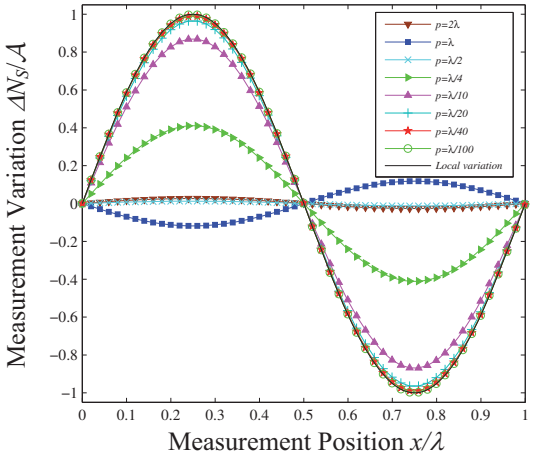

(a)

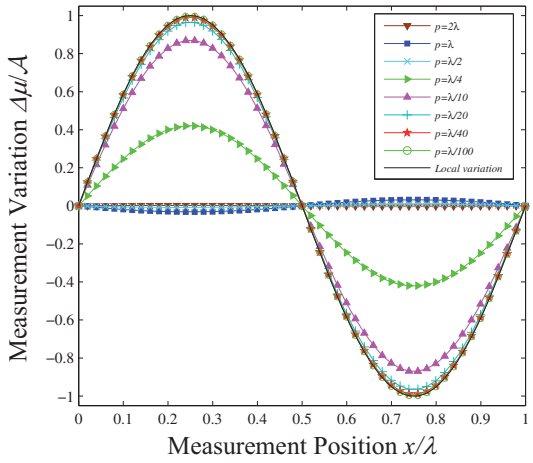

(b)

Fig. 6 (a) Variation of the measured sheet carrier density in Hall effect measurement to a sinusoidal variation of the local sheet carrier density; (b) Variation of the measured carrier mobility in Hall effect measurement to a sinusoidal variation of the local carrier mobility.

are shown in Fig. 5(a). The measured sheet resistance has almost the same sensitivity to the local sheet carrier density and the local mobility, which makes the two 1D sensitivity plots overlap each other. The two plots show similar shape as the sensitivity of local sheet resistance shown in the Fig. 2 as expected.

Using the known sensitivities of sheet resistance and Hall sheet resistance, the sensitivities of the extracted sheet carrier density and carrier mobility can also be calculated:

$$S_t^{N_S} = -S_t^{R_H} \quad \text{and} \quad S_t^{\mu} = S_t^{R_H} - S_t^{R_S} \tag{8}$$

Fig. 5(b) shows the calculated 1D sensitivity of N_S and μ to the local variations in sheet carrier density and mobility, respectively. The sensitivities of N_S-N_L and μ-μ_L has a similar shape as that of R_S-R_L shown in Fig. 2. The sensitivities in Fig. 5(b) are further used to calculate the measurement accuracy for different probe spacing. The extracted sheet carrier density and mobility are shown in Fig. 6(a) and Fig. 6(b), respectively, as a function of measurement position across a full wavelength of sheet carrier density and mobility variation. Local variations can be accurately traced when the probe spacing is as small as 1/40 of the variation wavelength.

Fig. 5(b) also shows the relatively small cross sensitivity values N_S-μ_L and μ-N_L for extracted mobility to sheet carrier density and extracted sheet carrier density to mobility, respectively. The cross sensitivities are mainly caused by the position error suppression calculation when two measurement points are used [11, 12]. As a result, the measurements for the sheet carrier density and the carrier mobility are not totally independent of each other. Fig. 7 for instance, shows a variation of the measured carrier mobility when a sinusoidal variation of the local sheet carrier density is assumed, even though the local carrier mobility is constant across the sample. The scaled amplitude of the local variation of N_S is set to 10% and this results in a maximum variation of 1.2% for the measured mobility when the probe spacing is 1/4 of the variation wavelength while at other probe spacings the cross sensitivity is smaller. The cross sensitivity is a source of measurement error which should be controlled well during a

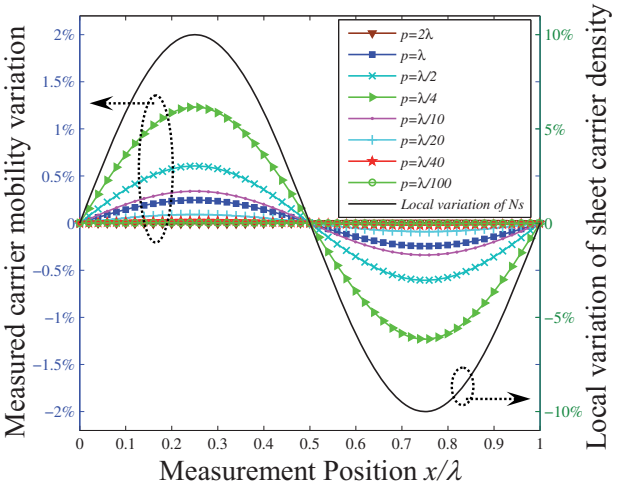

Fig. 7 Variation of the measured carrier mobility to a sinusoidal variation of the local sheet carrier density.

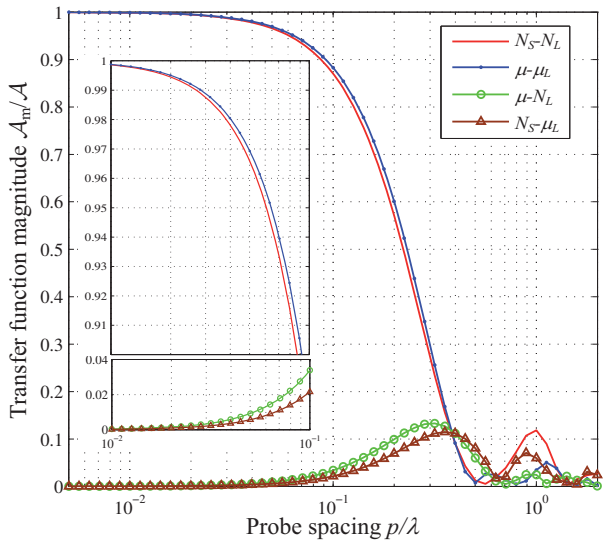

Fig. 8 The accuracy of Hall effect measurements as a function of the probe spacing p for a local sheet resistance variation with a wavelength of λ.

practical measurement.

Fig. 8 shows the four spatial frequency transfer functions of measured sheet carrier density and mobility from sample sheet carrier density and mobility, respectively, as a function of the probe spacing for the micro Hall Effect measurements. It follows that 99% of the local variation is resolved when the probe spacing is smaller than $\lambda/40$, while at the same time the cross sensitivity is reduced to less than 1%.

3. Measurement with square variation

The calculation method is also applicable for a square wave parameter variation. The square wave may easily be analyzed using a Fourier series. Here, however, we calculated the measured result directly using the 1D sensitivity and the square wave variation. For instance, a local square wave sheet resistance variation with the wavelength of λ is assumed on an

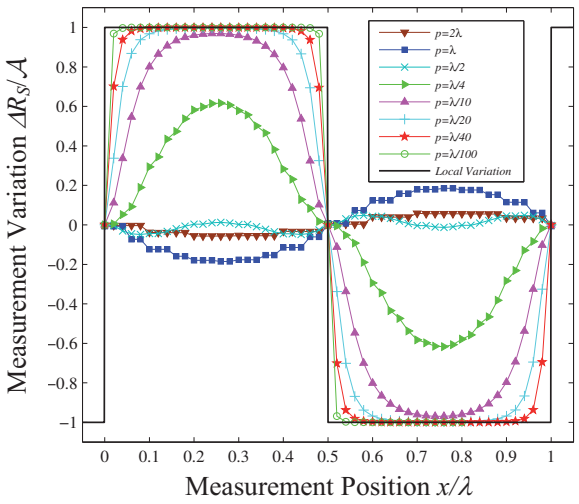

Fig. 9 The measured variations of the sheet resistance with different probe spacing, according to a local sheet resistance variation of square wave with a wavelength of λ.

infinite sample. The measured sheet resistance variations shown in Fig. 9 were calculated with eight different probe spacings. When the probe spacing is larger than $\lambda/4$, the measured variation is similar to a sinusoidal wave. When the probe spacing is smaller than 0.1λ, the measured variation becomes a square wave with a rounded corner which represents the ambiguous response to the shifting boundary. When the probe spacing is as small as 0.01λ, the square wave variation is well reproduced.

IV. Conclusion

We have studied the accuracy of M4PP measurement on inhomogeneous samples as a function of the probe spacing using calculations based on previously reported sensitivities. For both sheet resistance and micro Hall Effect measurements, the measured results are calculated at different probe spacings. We have proved that the measurement accuracy decreases significantly with increasing probe spacing. For local sinusoidal variation with wavelength of λ, the probe spacing must be less than $\lambda/40$ when 1% measurement error is desired. The cross sensitivity from mobility to sheet carrier density and from sheet carrier density to mobility is also well controlled with small probe spacing for Hall Effect measurements. The calculations prove that the measured sheet resistance, sheet carrier density and carrier mobility accurately reflect the sinusoidal variations when the probe spacing is smaller than $\lambda/40$. For the square wave variation, however, the absolute measurement accuracy is a function of the chosen probe spacing, the spatial frequency transfer function and the spatial Fourier frequencies.

Acknowledgment

We are grateful for the financial support from Copenhagen Graduate School for Nanoscience and Nanotechnology

(C:O:N:T), the Danish Research Agency (FTP), and Danish National Advanced Technology Foundation. Center for Individual Nanoparticle Functionality (CINF) is sponsored by The Danish National Research Foundation. We would also like to thank Erik Rosseel and Wilfried Vandervorst from IMEC for their continuous support and good discussions.

REFERENCES

[1]. L. B. Valdes, "Resistivity measurements on germanium for transistors," *Proc. IRE*, 42, pp. 420-427, 1954.

[2]. F. M. Smits, "Measurement of sheet resistance with the four point probe," *Bell Syst. Tech. J.* 37, pp. 711-718, 1958.

[3]. E.H. Hall, "On a new action of the magnet on electric currents," *Am. J. Math.*, **2**, pp. 287–292, 1879.

[4]. L. J. van der Pauw, "A method of measuring the resistivity and Hall coefficient on Lamellae of arbitrary shape," *Philips Res. Rep.*, vol. 13, p. 1, 1958.

[5]. D. H. Petersen, R. Lin, T. M. Hansen, E. Rosseel, W. Vandervorst, C. Markvardsen, D. Kjær, and P. F. Nielsen, "Comparative study of size dependent four-point probe sheet resistance measurement on laser annealed ultra-shallow junctions," *J. Vac. Sci. Technol. B* 26, pp. 362-367, 2008.

[6]. T. Clarysse, A. Moussa, F. Leys, R. Loo, W. Vandervorst, M. C. Benjamin, R. J. Hillard, V. N. Faifer, M. I. Current, R. Lin, and D. H. Petersen, "Accurate sheet resistance measurement on ultra-shallow profiles," *Mater. Res. Soc. Symp. Proc.* 912, pp. 197-203, 2006.

[7]. www.capres.com.

[8]. S. Thorsteinsson, F. Wang, J-Y. Kim, D. H. Petersen, T. M. Hansen, D. Kjær, R. Lin, P. F. Nielsen, and O. Hansen, "Accurate microfour-point probe sheet resistance measurements on small samples," *Rev. Sci. Instrum.* 80, 053902(8pp), 2009.

[9]. D. H. Petersen, O. Hansen, R. Lin, and P. F. Nielsen, "Micro-four-point probe Hall effect measurement method," *J. Appl. Phys.* 104, 013710 (10pp), 2008.

[10]. T. Clarysse, J. Bogdanowicz, J. Goossens, A. Moussa, E. Rosseel, W. Vandervorst, D.H. Petersen, R. Lin, P.F. Nielsen, O. Hansen, G. Merklin, N.S. Bennett, and N.E.B. Cowern, "On the analysis of the activation mechanisms of sub-melt laser anneals," *Mater. Sci. and Eng. B*, 154, 24 (2008)

[11]. D. H. Petersen, O. Hansen, R. Lin, P. F. Nielsen, T. Clarysse, J. Goossens, E. Rosseel, and W. Vandervorst, "High precision micro-scale Hall effect characterization method using in-line micro four-point probes," *in 16th IEEE International Conference on Advanced Thermal Processing of Semiconductor (RTP' 2008)*, pp. 251-256, 2008.

[12]. F. Wang, D. H. Petersen, T. M. Hansen, P. Bøggild, and O. Hansen, "Sensitivity study of micro four-point probe measurements on small samples," *J. Vac. Sci. Technol. B* , in press.

Paper XI

in Proc. RTP 2009 (IEEE, New York, 2009) pp. 129-134.

PhD students contribution:

Idea for collaborative study. Experimental M4PP measurements and data treatment in collaboration with F.W. Osterberg. Discussion of results and significant contributions to manuscript and figures.

17th IEEE International Conference on Advanced Thermal Processing of Semiconductors – RTP 2009

Monitoring of local and global temperature non-uniformities by means of Therma-Probe and Micro Four-Point Probe metrology

Erik Rosseel[a,1], Dirch H. Petersen[b,c], Frederik W. Osterberg[b], Ole Hansen[b], Janusz Bogdanowicz[a,d], Trudo Clarysse[a], Wilfried Vandervorst[a,d], Claude Ortolland[a], Thomas Hoffmann[a], Philip Chan[e], Alex Salnik[e], Lena Nicolaides[e]

[a]*IMEC, Kapeldreef 75, B-3001 Leuven, Belgium*
[b]*DTU Nanotech - Dept. of Micro and Nanotechnology, Technical University of Denmark, building 345 East, DK-2800 Kgs. Lyngby, Denmark,*
[c]*CAPRES A/S, Scion-DTU, building 373, DK-2800 Kgs. Lyngby, Denmark*
[d]*Instituut voor Kern- en Stralingsfysika, KU Leuven, Celestijnenlaan 200D B-3001 Leuven, Belgium*
[e]*KLA-Tencor Corp., One Technology Drive, Milpitas, California 95035, USA*

***Abstract*- The introduction of millisecond annealing in advanced CMOS process flows turns out to generate considerable temperature variations which can enhance the device dispersion. In the present work we report on the use of in-line Therma-Probe (TP) and Micro Four-Point Probe (M4PP) metrology to assess these temperature variations on shallow trench isolation (STI) wafers with and without absorber layer after sub-melt laser anneal (λ_{laser} = 808 nm). By calibrating the DC probe reflectance obtained during TP or the M4PP sheet resistance against the laser peak temperature on a blanket wafer with calibration stripes, the peak temperature variation on the patterned wafer can be determined at a global and local scale. By a direct comparison on the same structures we demonstrate the equivalence of both techniques and validate the contactless TP measurements. We also demonstrate the advantage of the use of absorber layers during laser anneal.**

I. Introduction

To comply with the ultra shallow junction requirements for the 32 nm CMOS technology node and beyond, millisecond annealing techniques are being introduced. As a result of the short timescales and the interaction of the electromagnetic waves with the pattern layout and wafer stacks, local (within-die) and global (within-wafer) temperature variations occur which can result in unwanted device variability [1-4]. In the present work we investigate the use of in-line Therma-Probe (TP) and Micro Four-Point Probe (M4PP) metrology to assess the temperature variations on sub-melt laser annealed patterned wafers. As it is not the intention of this work to make a systematic study of the contributions from the different technological building blocks, but rather to assess the capabilities of the aforementioned metrologies, we restricted ourselves to shallow-trench-isolation (STI) patterns.

II. Experimental

For the study of the temperature variation, 300 mm N-type device wafers with and without STI patterns were implanted with a Boron 0.5 keV, $1x10^{15}$ at/cm^2 ion beam and subjected to laser anneal. A standard CMOS 65nm technology was used for the STI flow and a mask set was chosen which had a sufficient number of active area measurement pads distributed over the die, as well as different pad sizes. On some wafers, a standard absorber layer (AL) was deposited prior to laser anneal and removed after anneal in an oxygen plasma. Laser annealing itself was performed in a system from Applied Materials [5] using a 808 nm diode bar laser. Wafers without AL were annealed at 150 mm/s while those with the AL were annealed at 300 mm/s. The Therma-Probe measurements were done in a Therma-Probe 630XP (TP) system from KLA-Tencor, while the M4PP measurements reported in this work were performed at DTU Nanotech and CAPRES A/S in a CAPRES microRSP-M150 M4PP system [6,7].

III. Therma-Probe measurements

Photo-Modulated Optical Reflectance (PMOR) or Therma-Probe (TP) measurements have actually been used for more than two decades to monitor dose levels in implanted wafers. The technique measures the time-dependent changes in surface reflectance of a laser beam (probe beam) caused by an increase in excess carrier concentration and temperature induced by an intensity-modulated pump beam [8]. In the case of the 630 XP system, a probe beam of 670 nm is used together with a 790 nm pump beam which is modulated at 1 MHz. In contrast to conventional measurements we used the TP method to measure wafers after anneal and focus on the application of this technology to the extraction of temperature and sheet resistance variations.

A. Process set-up and TP on blanket wafers

Before patterned wafers are subjected to laser anneal, the uniformity of the annealing process and the power targets are typically optimized using implanted blanket wafers. During the optimization procedure these blanket wafers are annealed, measured using either standard four point probe (4PP) or TP and finally laser process parameters are changed to obtain the best uniformity and achieve the desired temperature. From a previous study [9], we know that for the junction conditions

under consideration, the DC reflectances for the probe and pump beams which are measured at the same time as the classical modulated signal $\Delta R/R$ show a systematic correlation to the sheet resistance. It was demonstrated that this systematic correlation is present both on blanket wafers as well as "product" wafers and is caused by the free carrier or so-called Drude contribution to the reflectance. In the following we will further exploit this fact and use the DC probe reflectance to obtain information on sheet resistance and temperature variations. Although this procedure always requires calibration to a known temperature or sheet resistance it has the advantage of being a high resolution technique

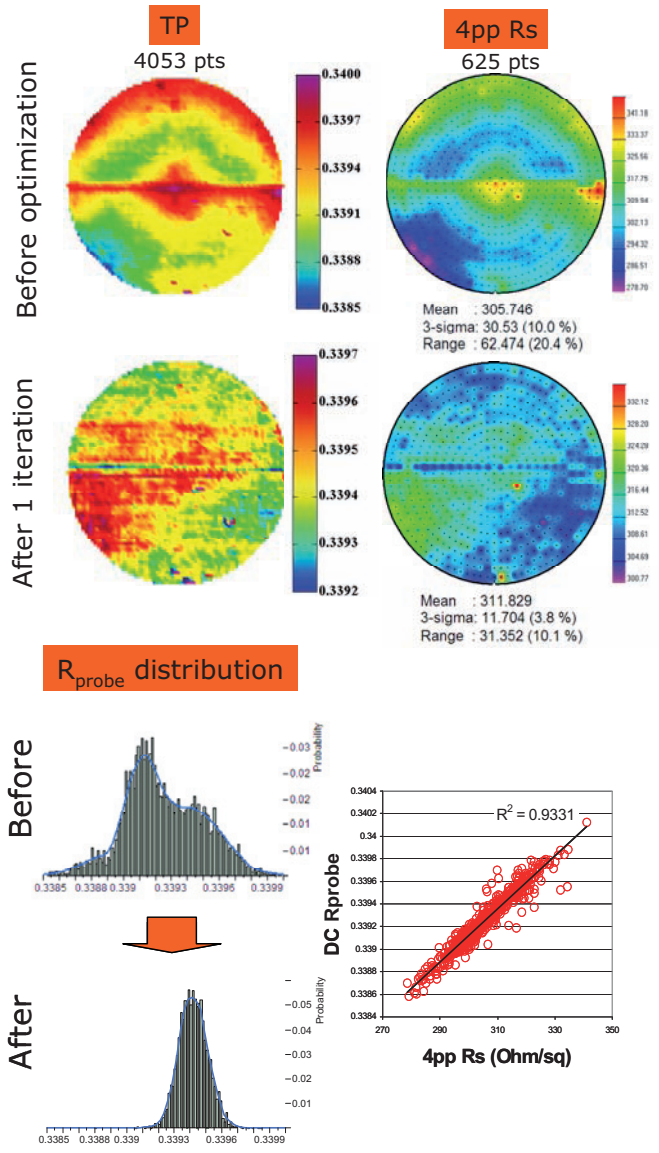

Fig. 1. Laser anneal uniformity optimization on blanket B 3kev, $1x10^{15}$ at/cm^2 implanted wafers using TP measurements for the input. T_p = 1200°C. Top left part contains shows the 4053 points probe reflectance contour maps while the right side shows the corresponding 625 points 4PP sheet resistance contour map. Top row of contour plots are before optimization, bottom row shows the maps after one iteration. At the bottom on the left we show the narrowing of the probe reflectance distribution after optimization and the bottom right shows the point-to-point correlation for the probe reflectance to the sheet resistance (bef.).

during which high point densities can be obtained in relatively short times. Figure 1 shows a typical example of a global anneal uniformity optimization using TP as an input for the laser power compensation. The corresponding sheet resistance maps before and after one iteration are shown on the top right. Without optimization, a sheet resistance variation of 10% (3σ) is obtained on a 625 points map. After one optimization cycle, the non-uniformity decreased to 3.8% (3σ). Further iterations are known to decrease the non-uniformity below 3% (3σ). The related probe reflectance distribution plots and the distribution narrowing can be seen at the bottom left of the figure. Finally at the bottom right, we show the point to point correlation plot of the probe reflectance versus the sheet resistance before optimization. As was already clear from the contour plots, both quantities are nicely correlated allowing to use the higher density TP maps as an input to the laser system.

B. TP on patterned wafers

To gather information with respect to temperature or sheet resistance variations on patterned wafers, the TP signal needs to be calibrated upfront using blanket wafers. For this purpose, a blanket wafer was illuminated with a set of laser stripes with varying peak temperatures. As the sheet resistance or TP signal can vary as well with the number of laser overlaps [10,11] a triple overlap (3x) was used which is also used for uniform illuminations. From the standard sheet resistance at the center of these stripes and peak temperatures measured by the in-situ pyrometer, a calibration curve can be built.

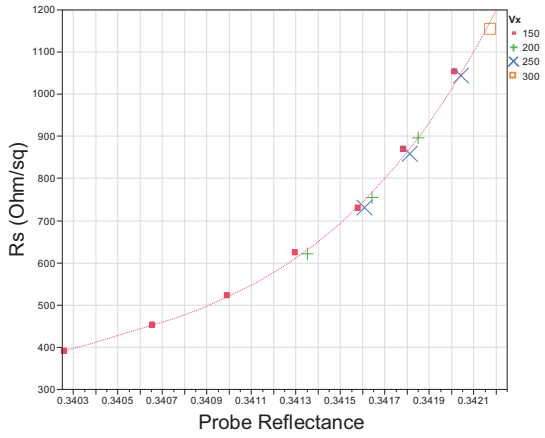

Fig. 3. $R_s(R_{probe})$ calibration curve obtained on a blanket B 0.5 keV, $1x10^{15}$ at/cm^2 implanted wafer for different scan velocities. The dashed line represents a fit with a fourth-order polynomial.

In Fig. 3, we show a $R_s(R_{probe})$ calibration curve for different laser scan velocities as an example. For 150 mm/s, the corresponding temperatures range from ~ 1300°C down to ~ 1160ºC. Note that the relation between the sheet resistance and probe reflectance is not necessarily linear over a larger R_s range or temperature interval.

After the $R_s(R_{probe})$ and $R_s(T_p)$ calibrations, we exposed the implanted STI wafers with and without absorber to the "uniform" laser anneal process, targeting a peak temperature of 1200°C. The wafers were annealed in an open loop mode, so the applied power was automatically scaled before anneal

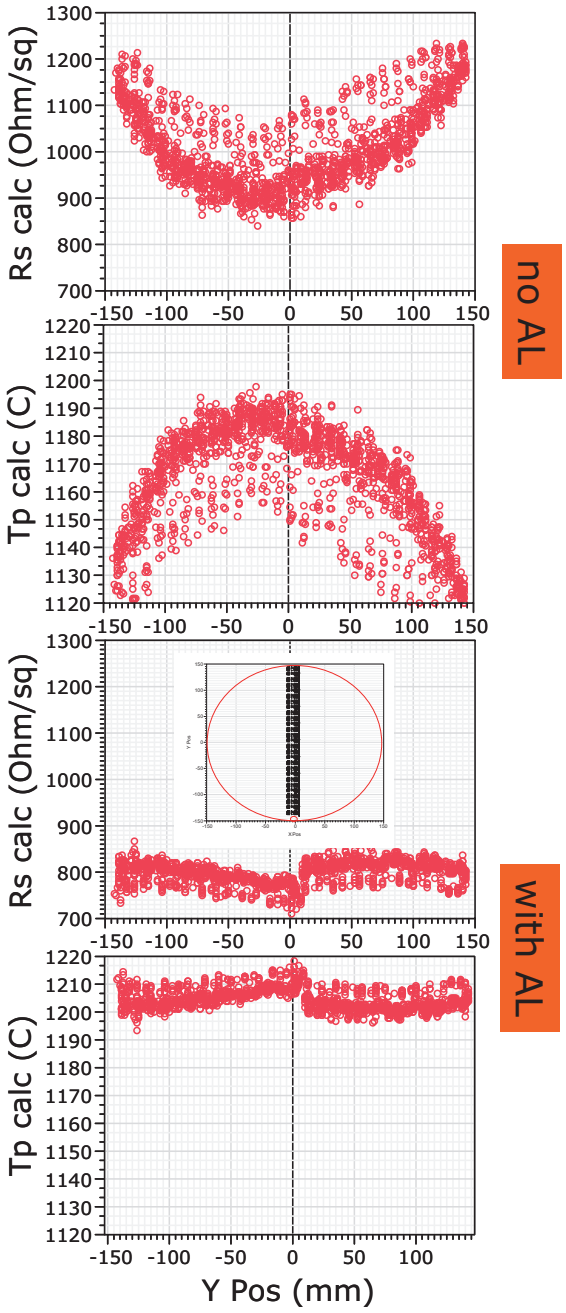

Fig. 4. Calculated sheet resistances and temperatures based on the measurement of the probe reflectance for STI wafers with and without absorber layer. The inset shows the positions of the measurements on the wafer. AL and no-AL graphs have the same scale for comparison.

based on the reflection measurement in the laser system but was not changed during the processing itself based on an in-situ *T*-measurement. To have an idea about the intra-die and intra-wafer temperature variation, we defined a set of ~244 measurement positions in each die along the central die column at X = 0 (assuming right-handed Cartesian coordinates with origin at the wafer center and notch at Y = -150), yielding a total of 1592 measurements per wafer. For all measurements, the TP beams were positioned in the center of 100 × 100 μm^2 active area pads. From the graphs it becomes clear that substantial variations are present when the laser

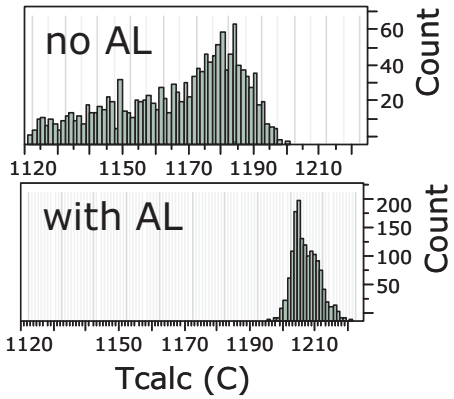

Fig. 5. Temperature distributions for STI wafers with and without absorber layer.

annealing is performed without AL. For the chosen measurement positions, within-die temperature variations of about ~50ºC can be found while an even larger global variation is obtained of ~ 80ºC. As observed from the graphs in Fig. 4 and the corresponding temperature distributions in Fig. 5, the use of an absorber layer clearly helps in narrowing the distribution. With AL, the total variation is about 20ºC which is a 4x improvement !

Although the within-die variation was expected for the case without absorber due to the sensitivity to the STI density [12], the global "parabolic" back-ground is rather unexpected. The origin of this variation turns out to be caused by the sensitivity of the local temperature to the local STI oxide thickness. As

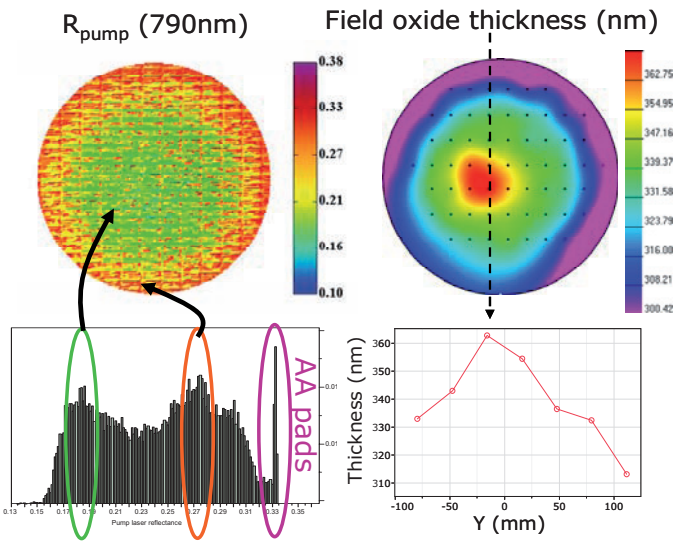

Fig. 6. Top left : high resolution TP map (pitch 1 mm) of the pump laser reflectance (790 nm). Top right : contour plot of the STI oxide thickness. Bottom left : probability distribution of the pump reflectance map. Bottom right : variation on the STI oxide thickness along the dashed line.

can be seen in Fig. 6, the (room temperature) reflectance at 790 nm measured using the high resolution TP mapping option, changes considerably over the wafer. A total range of ~0.2 is obtained with a center part of the wafer reflecting about 35% less than the edge of the wafer. As can be seen

from the optical simulation [13] shown in Fig. 7 and the contour plot of the STI oxide thickness on the right side of Fig. 6, the total range of the STI oxide varies considerably (60 nm range at a mean value of 330 nm) which can indeed give rise to a reflectance variation of ~ 0.2 without absorber while it is reduced to 0.02 with absorber present (dashed line in Fig. 7). The above indicates how non-uniformities in the STI module, which are still compatible with a correct device operation, affect the temperature uniformity over the wafer. As it is not always straightforward to reduce the STI oxide

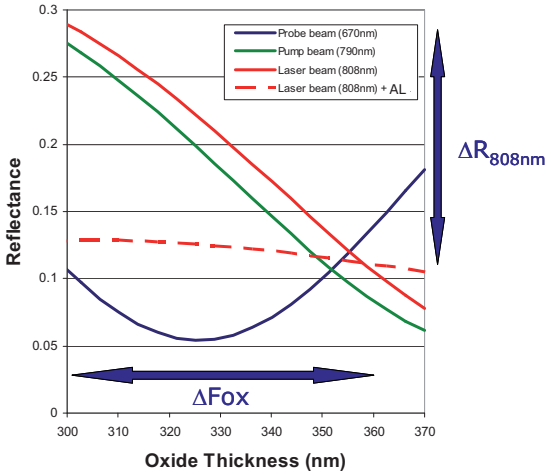

Fig. 7. Optical simulation of the reflectance of Si/SiO_2 and $Si/SiO_2/AL$ stacks for relevant wavelengths at room temperature. The experimental STI oxide variation and resulting reflectance variation at 808 nm is shown with thick arrows.

thickness variation due to interaction with other module constraints, it is definitely something to take into account. Only by using closed-loop temperature control, absorber layers or much larger wavelengths these global effects can be kept under control.

IV. M4PP MEASUREMENTS

As the TP results in the previous section were based on R_s or T_p extrapolation using a calibration on different bare wafers, we compared our results to real measurements by the M4PP probe.

In order to compare with the TP data and to build up an understanding of the response, M4PP was first carried out on the largest active area pad available on the design which is the SIMS pad (430 × 400 µm^2). Both 1D scans and 2D maps were taken. The 1D scans were performed along the center of the pad in X and Y directions (whereby X is the laser scanning direction or fast axis and Y is the stepping direction of the laser or slow axis during laser anneal). Both scans have been carried out by measuring 31 points, 12 µm apart, with a 10 µm pitch probe resulting in measurement ranges of -180 µm to 180 µm. The 2D maps were measured with 25x31 points and a spacing in the X-direction of 15 µm and 12 µm in the Y-direction. This results in the same measurement ranges as for the line scans. More information w.r.t. the measurement procedure on small samples can be found in [14]. The positioning of the probe pins and an example of the probe positioning during measurement of a 10 × 10 µm^2 pad are shown in Fig. 8. For the line scans along the X-direction the probe pins are positioned perpendicular to the measurement direction, while they are parallel for the measurements in the Y-direction. The magnification in the left part of Fig. 8 emphasizes the presence of the 2 × 2 µm^2 dummy active areas on square grid of 4 µm side which are required for chemical mechanical polishing (CMP) uniformity. These dummies are

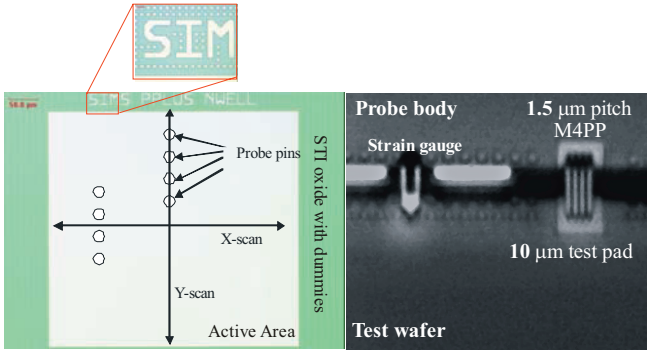

Fig. 8. Left : microscope picture of the 430 × 400 µm^2 SIMS pad together with X/Y directions and probe pin orientations. Note that the schematic drawing is magnified w.r.t. reality (probe pitch 10 µm). Magnified part shows the 2 × 2 µm^2 dummy active areas embedded in the STI-oxide reqion required for chemical mechanical polishing (CMP) purposes. Right : microscope picture of a 1.5 µm pitch probe during measurement of a 10 × 10 µm^2 pad.

present in the STI regions all over the wafer and are typically covered with a gate plate at a later stage of the process flow.

Fig. 9 shows the M4PP line scans along X and Y directions measured for SIMS pads along different Y positions in the central die column (X ~ 0) on the wafer without AL. Also shown is a temperature converted 2D map using the blanket calibration data. While the scans in the Y direction are symmetric with respect to the center of the pad, the scans in X clearly aren't and display a maximum in R_s is shifted from the center in a direction which depends on the scan direction.

The higher sheet resistance values and hence lower temperatures in the center of the pad can be understood by the higher reflectance of the Si and the lower effective temperature. Due to the limited thermal diffusion length :

$$L_d \approx \sqrt{\frac{4 \cdot \kappa \cdot \tau}{\rho C_p}} \approx 140 \mu m$$

for annealing at 1200ºC (with thermal conductivity κ = 23 J·s^{-1}·m^{-1}·K^{-1}, specific heat C_p = 990 J·kg^{-1}·K^{-1} density ρ = 2320 kg· m^{-3}, dwell time τ = 0.5 ms) the influence of the hotter STI environment is not washed out and a clear gradient can be observed. The reason for the asymmetry along the scan direction can be understood based on qualitative arguments : as the 75 µm wide laser beam heats one side of the STI pattern and enters the bare silicon, the temperature is steadily decreasing from the value on the STI oxide towards the value on bare Si. Before a saturation is reached however, the 75 µm

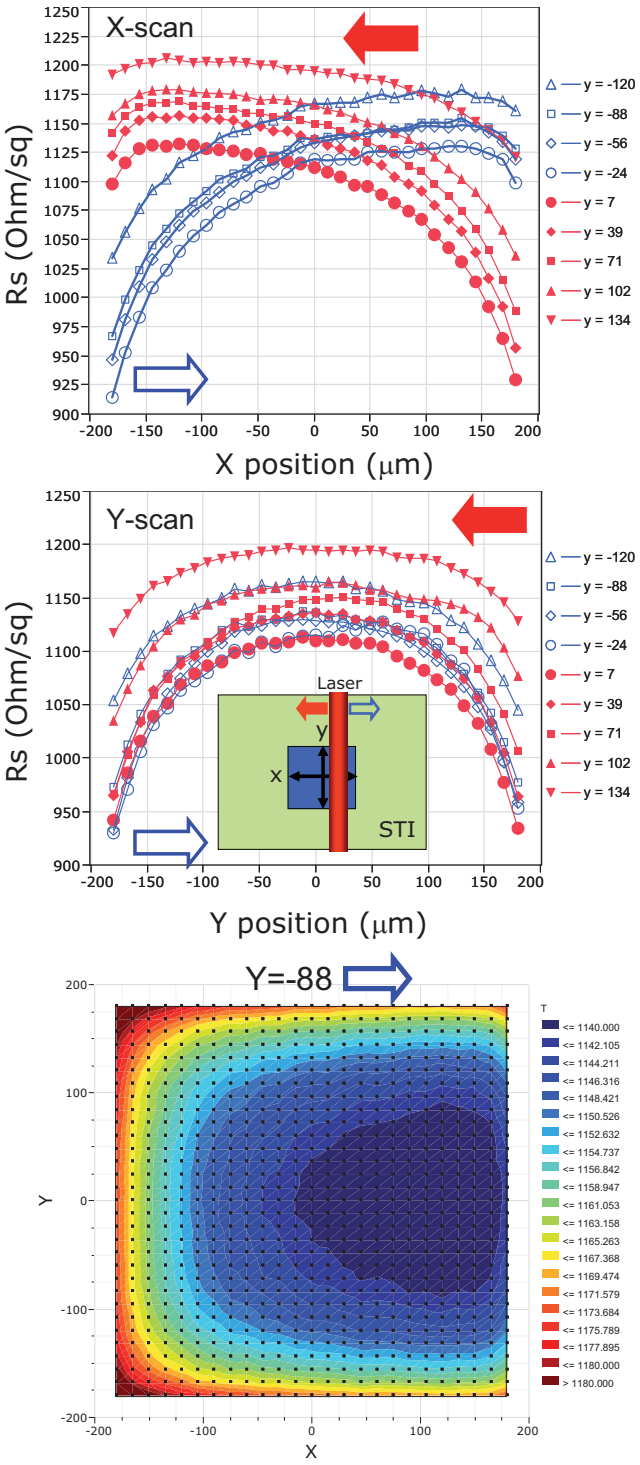

Fig. 9 case without AL; Top : 1D scans along X and Y directions of the SIMS pads at different Y positions along the central die column. Full red symbols correspond to scans on the top wafer half at which the laser moves from right to left. Open blue symbols are for Y positions on the bottom wafer half at which the laser moves from right to left. Arrows indicate the direction of laser scanning during anneal. Bottom figure gives a 2D M4PP map converted to temperature using the calibration on a blanket wafer.

wide beam starts to heat the opposite edge of the STI and the temperature starts to rise again. More detailed thermal simulations are underway to confirm this behavior and calculate the impact of the different laser parameters. It should be noted that asymmetries along the scan direction were

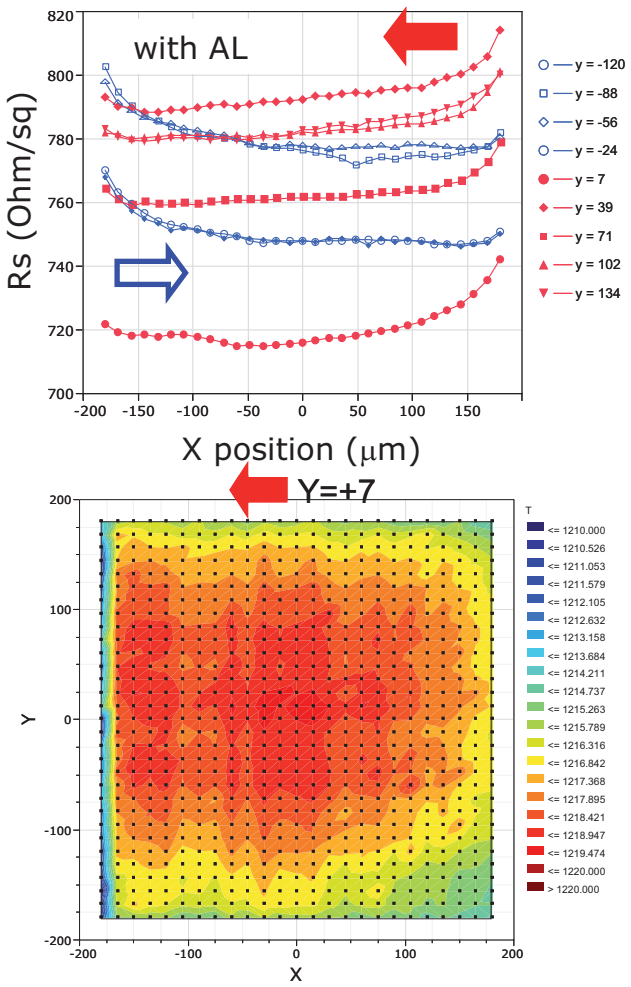

Fig. 10 case with AL; Top : 1D scans along the X of the SIMS pads at different Y positions along the central die column. Full red symbols correspond to scans on the top wafer half at which the laser moves from right to left. Open blue symbols are for Y positions on the bottom wafer half at which the laser moves from right to left. Arrows indicate the direction of laser scanning during anneal. Bottom figure gives a 2D M4PP map converted to temperature using the calibration on a blanket wafer. The map is slightly off-center resulting in a small measurement error of the points at X = - 180 μm.

previously observed by Kubo *et al.* using LSA [2]. They detected a temperature increase of about 50ºC as the laser progressed on a 100 μm pad while we clearly see a decrease.

Fig. 10 shows the corresponding case for a wafer covered with the AL during anneal. A scan direction related asymmetry remains present but the total temperature variation on the considered map is limited to only 10ºC. In this case, edges are cooler than the center and the asymmetry is now inverted compared to the case without AL. Reason is that the reflectance of the bare/AL stack is still somewhat lower than that of a Si/SiO_2/AL stack although the difference is much smaller than for the case without AL. At the same time the R_s curves saturate faster which might be due to the higher scan speed and shorter thermal diffusion length. The absorber layer thus clearly reduces the AA/STI contrast and homogenizes the temperature distribution.

From the above we observe that a maximum ΔT variation of ~65ºC is measured over the pad in case without AL. If measurements are taken at the center point, it is clear that

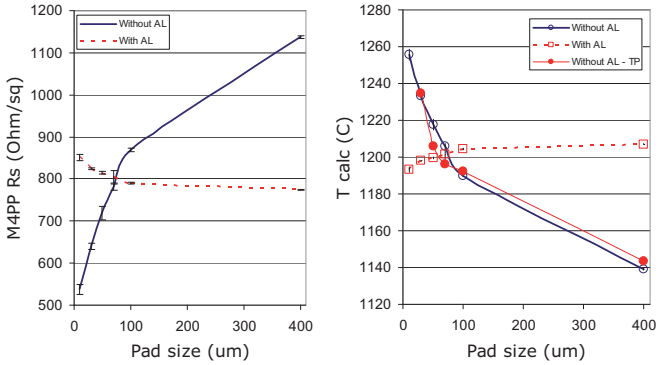

Fig. 11. Left : M4PP R_s measurements versus pad size for wafer with and without AL. Right : conversion to temperature and comparison to TP. Error bars for M4PP on the right side are smaller than the symbol size.

these must depend on the size of the pad. If an absolute environmental temperature needs to be probed, the pad size should be kept as small as possible. Fig. 11 shows the sheet resistance versus pad size, for a pad size ranging from 400 µm down to 10 µm. The sheet resistance is the average of 3 measurements performed with a 1.5 µm pitch M4PP positioned close to the center/mirror line of the pads (all data taken on one specific die and structures not further than 1 mm apart). The ±1σ error bars (not exceeding 2.3 %) are dominated by sheet resistance variations as the measurements are not performed at the exact same position (e.g. for the 10 µm pads all within a distance of 1.5 µm from the mirror line of the pad). This is supported by a thorough theoretical analysis on measurement precision [14] and a sensitivity study to local sheet resistance variations on small pads [15]. On the right side of the figure, the calculated temperature is shown based on the blanket calibration and found in agreement with TP data for pads of 30 µm and above. Although the TP data on small pads should be treated with care and more analysis should be done to confirm the validity of the technique for those dimensions, the close similarity to M4PP is encouraging. The observed dependence on the pad size indicates that the absolute temperature in the STI regions is larger than expected based on the measurement of the 100 × 100 µm^2 pads discussed in Fig.4. The difference is about 50ºC and the total variation can become as large as 100ºC.

Comparison M4PP-TP

When performing the scans on the SIMS pads using TP, and plotting the calculated R_s the curves (not shown) basically look very similar as those in Figs. 9 and 10. To compare both techniques, we plot in Fig. 12 the values obtained in the center of each pad versus the Y coordinate on the wafers with and without AL. The correlation in terms of temperature is depicted on the right side of each figure.

If we compare the absolute measured and extrapolated sheet resistances, we notice that the TP extrapolation method overestimates R_s by about 75 Ohm/sq. The variation of the sheet resistance is however very much comparable. In the case of the wafer with AL, the variation and correlation of both techniques is very good and might indicate that the somewhat worse correlation for the wafer without AL, is at least partly related to positioning differences within the pads whose impact is larger on the wafer without AL. For the temperature extrapolation it turns out that the temperature calculated using the M4PP is ~ 5ºC higher in the case without AL and ~ 15ºC in the case with AL. Overall, it can be concluded that both techniques are in good agreement with each other and can be used to extract temperature variations on product wafers.

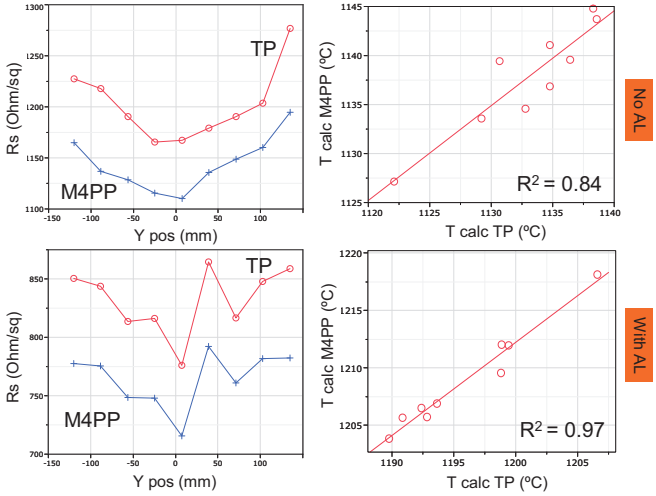

Fig. 12. Comparison M4PP/TP for corresponding measurements at the center of the SIMS pads. Top : case without AL. Bottom :case with AL.

Conclusions

In the present work we used Therma-Probe (TP) and M4PP measurements to assess the temperature non-uniformity on wafers with an STI pattern after sub-melt laser anneal with a diode bar laser system. We find that both techniques can be used to determine the temperature and sheet resistance non-uniformity at a local and global scale and hereby validate the contactless TP technique. The probe pad size turns out to be an important parameter for a correct absolute temperature determination. Besides local temperature variations caused by STI density fluctuations we also identified an important contribution from the STI oxide thickness variation. All variations are strongly reduced when an absorber layer is used.

Acknowledgement

The authors would like to thank the IMEC FAB team and Peter F. Nielsen and Rong Lin at Capres A/S for their support.

References

[1] R. Beneyton et al., Proc. IEEE RTP 2008, p.183.
[2] T. Kubo, T. Sukegawa and M. Kase, Proc. IEEE RTP 2008, p.195.
[3] H. Ohno, T. Itani and H. Yoshinori, Proc. IEEE RTP 2008, p.103.
[4] P. Morin et al., to be published at ESSDERC'09.
[5] A. Hunter, J. Zelenko and R. Mani, Proc. IEEE RTP 2007, p. 13.
[6] See http://www.capres.com for more information
[7] D.H. Petersen et al., Proceedings of the Insight'09 conference, p. 68.
[8] A. Salnick and J. Opsal, J. Appl. Phys., **91** (2002), p. 2874.
[9] E. Rosseel et al., Proceedings of the Insight'09 conference, p. 218.
[10] D.H. Petersen et al., Journal of Vacuum Science & Technology **B 26(1)**, (2008) 362.
[11] W. Vandervorst et al., MRS 2008.
[12] A. Colin et al., Mat. Sc. And Eng. B 154-155 (2008) 31-34.
[13] Using the IMD simulator (version 4.1.1.), written by D. Windt (2000).
[14] S. Thorsteinsson et al., Rev. Sci. Instr. **80**, pp.053902-053902-10, 2009.
[15] F. Wang et al., Proceedings of the Insight'09 conference, p.253.

Paper XII

Mater. Sci. and Eng. B **154**, 24 (2008).

PhD students contribution:

Experimental MHE and M4PP sheet resistance measurements. Significant discussions on measurement accuracy and reliability for van der Pauw and MHE measurements. Some manuscript revisions.

Materials Science and Engineering B 154–155 (2008) 24–30

Contents lists available at ScienceDirect

Materials Science and Engineering B

journal homepage: www.elsevier.com/locate/mseb

On the analysis of the activation mechanisms of sub-melt laser anneals

T. Clarysse[a,*], J. Bogdanowicz[a], J. Goossens[a], A. Moussa[a], E. Rosseel[a], W. Vandervorst[a,b], D.H. Petersen[c,d], R. Lin[d], P.F. Nielsen[d], Ole Hansen[c,e], G. Merklin[f], N.S. Bennett[g], N.E.B. Cowern[g]

[a] IMEC, Kapeldreef 75, B-3001 Leuven, Belgium
[b] KU Leuven, Department of Physics-IKS, Celestijnenlaan 200D, B-3001 Leuven, Belgium
[c] DTU Nanotech - Department of Micro and Nanotechnology, Technical University of Denmark, 2800 Kgs. Lyngby, Denmark
[d] CAPRES A/S, Scion-DTU, Building 373, DK-2800 Kongens Lyngby, Denmark
[e] CINF – Centre for Individual Nanoparticle Functionality, NanoDTU, DTU, b-345 East, DK-2800 Kgs. Lyngby, Denmark
[f] AMS, Advanced Metrology Systems LLC, 12 Michigan Drive, Natick, MA 01760, USA
[g] School of Electrical, Electronic and Computer Engineering, University of Newcastle upon Tyne, Newcastle upon Tyne NE1 7RU, UK

ARTICLE INFO

Article history:
Received 16 May 2008
Received in revised form
17 September 2008
Accepted 23 September 2008

Keywords:
Si
Mobility
Sheet resistance
Sheet carrier density
Sub-melt laser anneal

ABSTRACT

In order to fabricate carrier profiles with a junction depth (~15 nm) and sheet resistance value suited for sub-32 nm Si-CMOS technology, the usage of sub-melt laser anneal is a promising route to explore. As laser annealed junctions seem to outperform standard anneal approaches, a detailed assessment of the basics of laser induced activation seem appropriate. In this work the electrical activation is studied from a comparison between the dopant profiles as measured by Secondary Ion Mass Spectrometry, and the electrically active fraction as extracted from sheet resistance and mobility measurements. The latter is based on a large variety of techniques. For the sheet resistance we use conventional Four-Point Probe (FPP), Variable Probe Spacing (VPS), contactless junction photo voltage (JPV), Micro Four-Point Probe (M4PP) and an optical technique, namely Model Based Infra-red spectroscopic Reflectrometry (MBIR). For the sheet carrier density and sheet mobility extraction we use conventional Hall (without clover-leaf van der Pauw patterning, to reflect the need for fast turn-round sheet measurements), MBIR, and a recently developed new Hall-like capability using M4PP. By recognizing the interaction between the various parameters as they are not completely independent, it is possible to test the consistency of the various methods and to identify potential short comings. This concept is applied to the activation behavior of low and high implanted Boron doses and indicates that the obtained electrically active concentration level as well as the concurrent mobility is dependent on the dopant concentration level. This implies that the activation of B through the laser anneal process in the explored temperature–time space is governed by kinetic processes (i.e. the dissolution of B–I pairs) and not by the (temperature related) solid solubility.

1. Introduction

One of the major challenges in sub-32 nm technologies [1] is the formation of highly active source and drain regions combined with a very well controlled overlap between junction and gate. As conventional ion implantation followed by rapid thermal annealing results in excessive dopant diffusion and limited electrical activation levels, high temperature millisecond annealing is considered as an alternative approach to reach very high dopant activation with minimal dopant diffusion [2]. Furthermore, as more and more shallow structures need to be characterized, the accuracy of the latter becomes also more and more challenging [3].

In this work we present a systematic study of the electrical activation level of a series of low energy Boron implants activated through sub-melt laser anneal. In a subsequent publication we will also address the impact of a pre-amorphisation implant (PAI) with Ge and the co-implant of carbon. We compare in detail the sheet resistance, sheet carrier density and mobility values obtained on these structures through different techniques, among which several Hall-based ones and an optical technique and attempt to derive a consistent interpretation of these results (among others in terms of their maximum electrically active concentration level) as they are all interrelated. We then determine the dependence of the activation level for different implanted doses and anneal cycles and demonstrate that the activation in the explored temperature–time

* Corresponding author at: IMEC, AMPS/MCA Group, Kapeldreef 75, B-3001 Leuven, Belgium. Tel.: +32 16 281480; fax: +32 16 288500.
E-mail address: trudo.clarysse@imec.be (T. Clarysse).

0921-5107/$ – see front matter © 2008 Elsevier B.V. All rights reserved.
doi:10.1016/j.mseb.2008.09.038

Table 1
Summary of the low energy Boron implants studied (in lowly doped substrate) and their corresponding sheet resistances. Average R_s of 3.65 mm M4PP line scans is available for all structures. The data is equally similar to JPV and Hall–Capres. NA = not available.

Wafer ID	Nominal dose (at./cm^3)	SIMS dose (at./cm^3)	Laser anneal scan	Sheet resistance (ohm/sq)						
				JPV	FPP	VPS	MBIR	Hall–Capres	Hall–Newcastle	Hall–Imec
D02	1E+15	9.70E+14	3 × 150	559	597	614	667	553	642	553
D02	1E+15	9.70E+14	3 × 250	550	603	623	675	557	NA	562
D03	7E+14	NA	3 × 150	649	685	NA	741	620	NA	NA
D03	7E+14	NA	3 × 250	665	704	NA	804	660	NA	NA
D04	5E+14	4.75E+14	3 × 150	778	836	881	886	782	799	707
D04	5E+14	4.75E+14	3 × 250	770	825	900	865	781	NA	792
D05	3E+14	NA	3 × 150	1111	1232	NA	1123	1108	NA	NA
D05	3E+14	NA	3 × 250	1100	1200	NA	1147	1129	NA	NA
D06	1E+14	1.00E+14	3 × 150	3000	3484	3216	1775	3056	2419	2844
D06	1E+14	1.00E+14	3 × 250	3205	3537	3729	1800	3158	NA	NA

space is governed by the dissolution rate of the B–I interstitials and not by the solid solubility.

2. Structures and techniques

As listed in Table 1, low energy, 0.5 keV, B implants with doses varying from 10^{14} up to 10^{15} at./cm^2 have been made. Subsequently, sub-melt laser anneals [4,5] were performed in an Applied Materials DSA chamber which uses a 808-nm diode bar laser and has a spot size of ∼11 mm × 75 μm. Three overlapping scans at a pitch of 3.65 mm were applied, with two different scan speeds, namely 150 and 250 mm/s (dwell times of 0.5 and 0.3 ms). These two scan speeds were performed at two different (relative) laser power settings of 80% and 100%, such that the final temperature was nearly the same (where 100% relates the melting point of Si at 150 mm/s). Based on the pyrometer data the two power settings led to a temperature of 1221 and 1228 °C (±10 °C) respectively for the 150 and 250 mm/s scans. Hence the difference in the two recipes primarily leads to a different dwell time at the peak temperature.

For the determination of the sheet resistance, sheet carrier density and mobility (and subsequently the active concentration/resistivity levels) of these layers, conventional Four-Point Probe (FPP), Variable Probe Spacing (VPS), contactless junction photo voltage (JPV), Micro Four-Point Probe (M4PP), Model Based Infra-red spectroscopic Reflectrometry (MBIR) and three different sets of Hall measurements were undertaken (Newcastle, Capres, Imec).

FPP was done on an RS100 commercial tool with an electrode pitch of 1 mm (D-probe, 100 g load, 20 mil tip). VPS used an optimized Spreading Resistance Probe tool from Solid State Measurements (SSM350), with a 5-g load, separations between 40 and 1000 μm, a contact size of about 1 μm, and a penetration estimated to be about 5 nm [6]. The JPV measurements were done with an RsL 100 tool from Frontier Semiconductor (FSM) with red light to make sure a sufficient amount of excess carriers were created beyond the internal electrical junction (lowly doped substrate) [7]. The JPV wafer maps were used to verify that the sheet resistance differences of the symmetric laser anneal patterns on the top and bottom parts of the wafers (pieces of which were send to the different laboratories) were within a few percent. MBIR data were obtained using an AMS IR3100N tool, by fitting the obtained infra-red spectra with the Drude model for the sheet carrier density (assuming a box profile and a relative effective mass of 0.26) and optical carrier scattering factor (gamma) [8]. At Imec and Newcastle conventional macroscopic Hall measurements were done on 1 cm × 1 cm square pieces of material with mm-sized contacts close to the corners [9]. At Newcastle an eutectic was used for the contacts, omitting the cloverleaf structure usually used. At Imec clamps were used, also without van der Pauw patterning. Furthermore, the Newcastle data were corrected for corner effects. Finally, the Micro Four-Point Probe Hall Effect method combines zero probe penetration [10] and high spatial resolution [11] with a van der Pauw-like measurement technique [12]. Hall sheet carrier density, Hall mobility and sheet resistance are simultaneously measured by performing a series of four-point resistance measurements in a moderate magnetic flux density, B = 500 mT, and in proximity of a cleaved or lithographically defined edge. The M4PP Hall effect measurements were performed with an electrode pitch of 20 μm and a current set-point ranging from 17 to 120 μA depending on sample sheet resistance. The magnetic flux density used for the conventional Hall measurements were respectively, 330 mT at Newcastle and 200 mT at Imec.

3. Dopant profiles

Let us first take a closer look at the dopant profiles as obtained by Secondary Ion Mass Spectrometry (SIMS), as shown in Fig. 1. As can be seen from Table 1 the measured implanted doses match quite well the nominal ones. Furthermore, we can observe that the dopant profiles from the 3 × 150 and 3 × 250 mm/s scans are quite close to each other (depth difference less than 0.6 nm). The former were systematically deeper, most probably as a result of the longer dwell time and a corresponding lower effective heating 'ramp rate'. The marginal differences may indicate that for millisecond anneals, the diffusion is more controlled by the maximum temperature rather than the anneal time. Alternatively, this may be an illustration that during the early stages of heating TED dominates.

4. Sheet resistance

A first important technological parameter is the sheet resistance. Table 1 and Fig. 2 summarize the obtained sheet resistance results. In Fig. 2, the JPV data have been used as a reference since earlier work [10] has shown this is a reliable reference for this type of work.

The Hall–Capres results are in excellent agreement with JPV (less than 2% deviation). A reasonably good agreement is also found with the Hall–Imec dataset (<9%). Note that the repeatability of the latter data was within a few percent. A systematic deviation of about 10–15% is observed for FPP and VPS (too high), which may be related to probe penetration issues (local removal of material under the probes). A non-systematic deviation with approximately 15% uncertainty is observed for the Hall–Newcastle data. We attribute this large variation to the omission of cloverleaf van der Pauw structures in this experiment, combined with Newcastle's use of eutectic contacts for leakage minimization. The MBIR data display an apparently systematic trend with differences ranging from 20 to −40%. The latter are obtained from the sheet carrier density (which is directly fitted to the measured spectra) through the mobility. We will come back to this issue in Section 8.

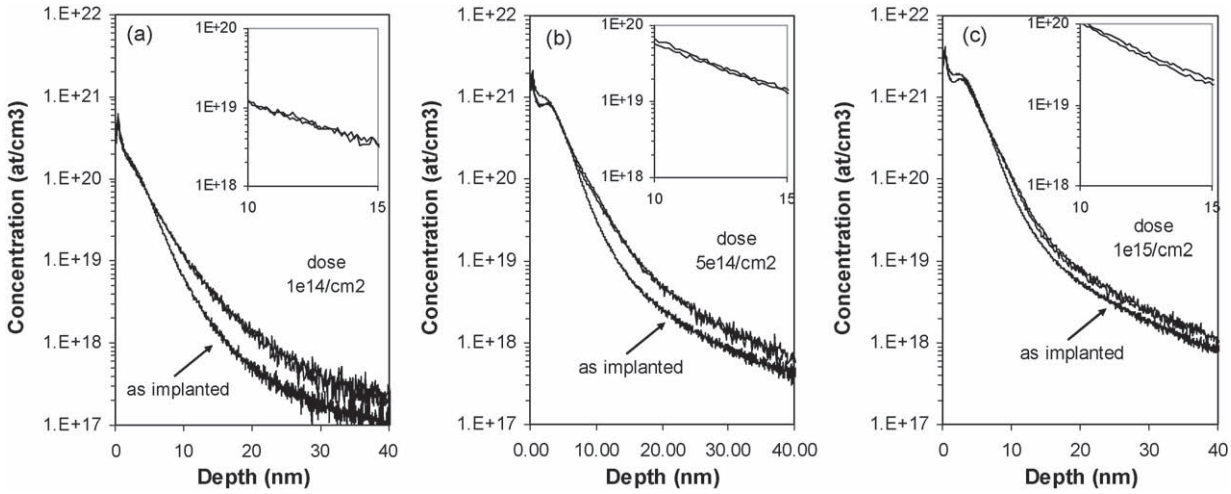

Fig. 1. SIMS dopant profiles for (a) D02, (b) D04 and (c) D06, listed in Table 1, for both scan speeds (top two almost coinciding curves, part of which is magnified in the insets) versus respective as implanted profiles.

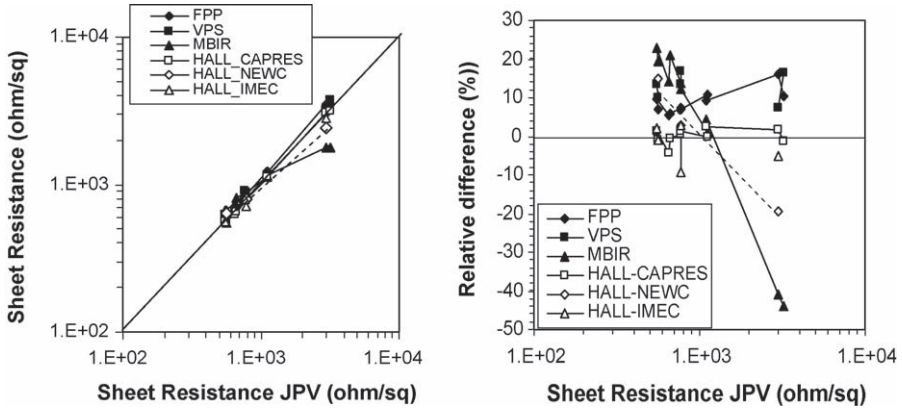

Fig. 2. Sheet resistance results versus JPV data and their relative differences.

For the higher doses and the more reliable techniques, only very small sheet resistance differences are observed between the two different laser anneal conditions (<2%). For the lowest dose, this difference grows towards 6%, with a slightly higher sheet resistance for the 3 × 250 mm/s scan (in agreement with SIMS).

As discussed previously [5,11] the Hall–Capres tool is able to resolve the small localized variations in R_s across one laser stripe. These variations are typically in the order of magnitude of 5% and increase up to 8% in the areas of the laser stitching. Present results obtained with the Hall–Capres tool indicate that a similar local variation in sheet carrier density can be observed as well. It is clear that macroscopic Hall techniques will measure an average of these local values.

5. Sheet carrier density

All Hall based techniques and MBIR can extract the sheet carrier density directly. The obtained results are shown in Table 2 and Fig. 3. Note that the output of the Hall measurements, referred to as Hall sheet carrier density, has to be multiplied with the Hall scattering factor (r_H), to obtain a sheet carrier density comparable with the output from MBIR. A Hall scattering factor $r_H = 0.8$ (p-type mate-

Table 2
Summary of the used structures and corresponding sheet carrier densities. NA = not available.

Wafer ID	Nominal dose (at./cm³)	SIMS dose (at./cm³)	Laser anneal scan	Sheet carrier density (cm⁻²)				Activation (%)			
				MBIR	Hall–Capres	Hall–Newcastle	Hall–Imec	MBIR	Hall–Capres	Hall–Newcastle	Hall–Imec
D02	1E+15	9.7E+14	3 × 150	2.34E+14	2.90E+14	2.57E+14	3.78E+14	23	29	26	38
D02	1E+15	9.7E+14	3 × 250	2.59E+14	2.90E+14	NA	3.53E+14	26	29		35
D03	7E+14	NA	3 × 150	2.08E+14	2.46E+14	NA	NA	30	35		
D03	7E+14	NA	3 × 250	2.09E+14	2.34E+14	NA	NA	30	33		
D04	5E+14	4.75E+14	3 × 150	1.74E+14	1.85E+14	1.87E+14	2.46E+14	35	37	37	49
D04	5E+14	4.75E+14	3 × 250	1.66E+14	1.89E+14	NA	2.15E+14	33	38		43
D05	3E+14	NA	3 × 150	1.34E+14	1.25E+14	NA	NA	45	42		
D05	3E+14	NA	3 × 250	1.35E+14	1.24E+14	NA	NA	45	41		
D06	1E+14	1E+14	3 × 150	7.52E+13	3.71E+13	5.16E+13	4.40E+13	75	37	52	44
D06	1E+14	1E+14	3 × 250	7.31E+13	3.66E+13	NA	NA	73	37		

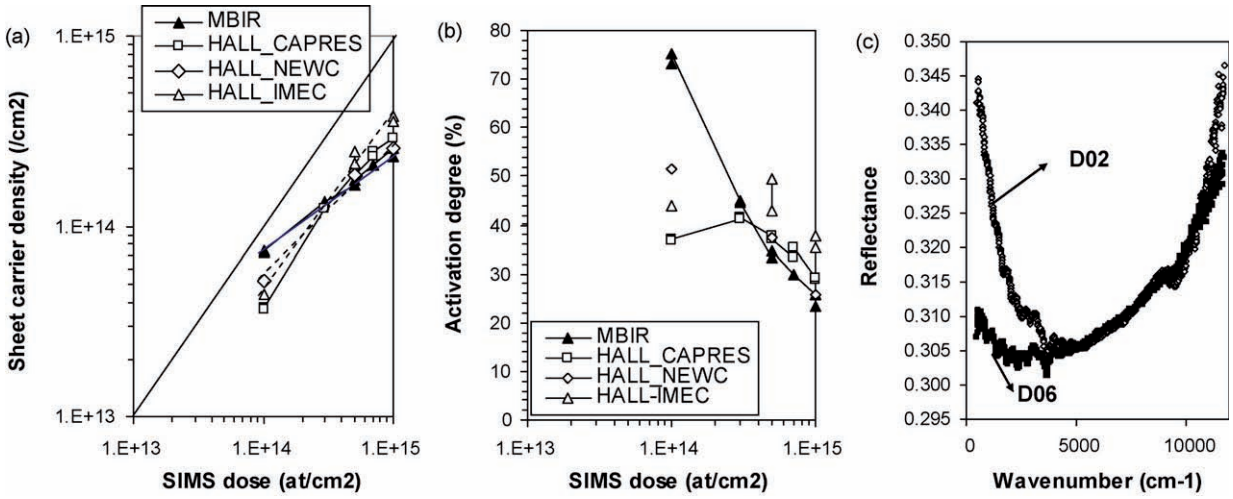

Fig. 3. (a) Sheet carrier density results versus SIMS dose and (b) the corresponding activation degrees. (c) MBIR spectra for high (D02) and low dose (D06) case.

rial) has been used systematically in this work, based on literature [13].

Opposite to the sheet resistance case, there is not directly a reliable reference at hand to compare the obtained sheet carrier density values against. As can be seen from Fig. 3a and b, the Hall–Capres and Hall–Imec results show a similar behavior, but the macroscopic Hall–Imec data give consistent higher values 14–33%. The latter is likely mainly due to a geometrical error caused by positioning of the electrode clamps a distance from the corners [14] and for the lower dose an additional error caused by leakage current due to the larger sampling volume (this is supported by the sheet resistance values where the macroscopic Hall–Imec data give lower values). Both of these errors result in a higher measured sheet carrier density. The repeatability of the Hall–Imec results was within 5–15% (worse for the lowest dose), whereas the repeatability of the Hall–Capres results was within 0.6–2.4%.

For the higher doses (5×10^{14} and 10^{15} at./cm^3) MBIR obtains sheet carrier densities close to the Hall–Capres results. Note that if a Hall scattering factor of 0.7 is chosen the difference between MBIR and Hall–Capres is just a few percent. However, for the lowest dose, differences up to 40% are observed for the MBIR case. This is probably to be related to the lower dynamic range of the MBIR spectra in the 500–3000 cm^{-1} wave number range for the lowest dose (Fig. 3). Note that the latter leads to a significant difference in activation degree of a factor of two. Hall–Newcastle lies between the Capres and MBIR results.

Given the fact that Hall–Capres gives the best overall agreement for sheet resistance and sheet carrier density, we will assume from here on that this is the more reliable data set. As illustrated in Fig. 3, the activation degree decreases with increasing implanted doses from 40% down to 30%. Note that this does not imply that the peak concentration level itself also decreases, as discussed in the next section. The results indicate that dopants are not systematically activated up to their solubility limit (since then the lowest dose should be 100% active), and that other activation mechanisms are dominant, such as the finite reaction probability for the dissolution of B–I (Boron–Interstitial) clusters. As the dose increases, and a larger amount of clusters are formed, a higher active concentration level is to be expected (see further on).

6. Carrier concentration

Starting from the SIMS dopant profiles and the above discussed sheet carrier densities it is possible to estimate the carrier depth profiles and corresponding peak carrier concentrations by removing the top part of the SIMS profile until the integrated dose (of the

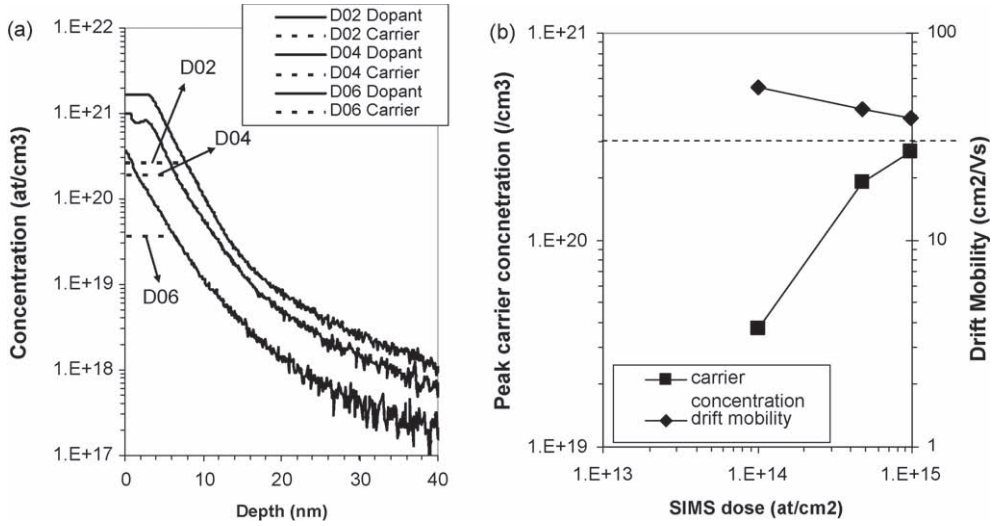

Fig. 4. (a) Carrier concentration depth profiles and (b) peak carrier concentration and drift mobility as extracted from Hall–Capres data versus SIMS dose.

active part) matches the measured sheet carrier density. Here, we made this exercise using the Hall–Capres data. The obtained carrier depth profiles are shown in Fig. 4.

It follows, that the peak carrier concentration increases from $3.71 \times 10^{19}\,\mathrm{cm}^{-3}$ for the lowest implanted dose up to $2.69 \times 10^{20}\,\mathrm{cm}^{-3}$ for the highest one, for the 3×150 mm/s anneal scan speed (Fig. 4b). The difference with the 3×250 mm/s speed (and different power) is negligible. The overall standard deviation on the extracted peak carrier concentration level is expected to be less than 5% based on the underlying SIMS and Capres–Hall accuracy. The drift mobility, to be discussed into more detail further on, decreases from 55 to 38 $\mathrm{cm}^2/\mathrm{V\,s}$ for increasing dose (Fig. 4b).

7. Resistivity

Next, starting from the above obtained carrier depth profiles, it is possible to compute the underlying resistivity depth profiles by applying an appropriate mobility model. The main requirement for this mobility model is that the sheet resistance calculated from the extracted resistivity depth profile needs to agree with the above discussed experimental sheet resistance values. Again we will use the Hall–Capres data here as a reference.

As the basis of our mobility model we will take the Thurber mobility model (ASTM F723-88). In order to compensate for a significant amount of impurity scattering due to inactive dopants, we however introduce for active dopant levels above $10^{18}\,\mathrm{cm}^{-3}$ a dopant scattering factor, named d_s, which controls our scaled Thurber mobility model through the following formula:

$$\mu_{\mathrm{scaled}} = \left(\frac{10^{18}}{n}\right)^{d_s} \mu_{\mathrm{Thurber}}(n) \tag{1}$$

where n is the active dopant concentration. It proved possible to fit the sheet resistance for all the studied doses within 2%, with a value of d_s in a narrow range between 0.06 and 0.08. The difference between the conventional Thurber and scaled Thurber model (for $d_s = 0.07$) is shown in Fig. 5a. This scaled line is in good agreement with experimental Hall measurements made by Sasaki et al. [13]. The corresponding resistivity depth profiles consistent with the measured Capres sheet resistance values are shown in Fig. 5b.

It is found that the resistivity in the highest doped region is about 6.5×10^{-4} ohm cm for the highest implant dose (10^{15} at./cm^{-2}), and about 4×10^{-3} ohm cm for the lowest implant dose (10^{14} at./cm^{-2}).

8. Mobility

Finally, the last technological parameter to be considered is the mobility. Note that the output of Hall measurements, referred to as Hall mobility, has to be divided with the Hall scattering factor (r_H), to obtain the drift mobility. The same Hall scattering factor $r_H = 0.8$ (p-type material) as above has been used.

During the subsequent discussion it is useful to keep in mind that for any structure the following relation always holds

$$\mu_{\mathrm{drift}} = \frac{1}{qR_s n_s} \tag{2}$$

where μ_{drift} is the drift (sheet) mobility (kind of average over the whole layer), R_s is the sheet resistance, n_s is the sheet carrier density and q is the elementary charge. Note that the Hall (and hence also the corresponding drift) mobility, which is a relatively small number, is obtained on the basis of quite large values going up to 10^{20}. This is numerically not advantageous, since any errors in either R_s or n_s which may be less visible on a logarithmic scale, may become more apparent in the mobility when plotted on a linear scale. On the other hand, the presence of a substrate leakage current will increase n_s and decrease R_s and therefore basically cancel out from the mobility relation (Eq. (2)) provided the relative leakage current is the same for both Hall and sheet resistance measurement. This should in principle give a lower systematic error in the mobility than in either n_s or R_s. The geometrical error caused by the positioning of contacts a distance from the sample corners can be significant and will result in smaller mobility values for the Imec results.

Table 3 and Fig. 6 show the obtained drift mobility values plotted versus the scaled Thurber mobility value taken at the peak carrier concentration of the corresponding structure. In doing so we assume that the Hall (and drift) mobility of the whole structure is

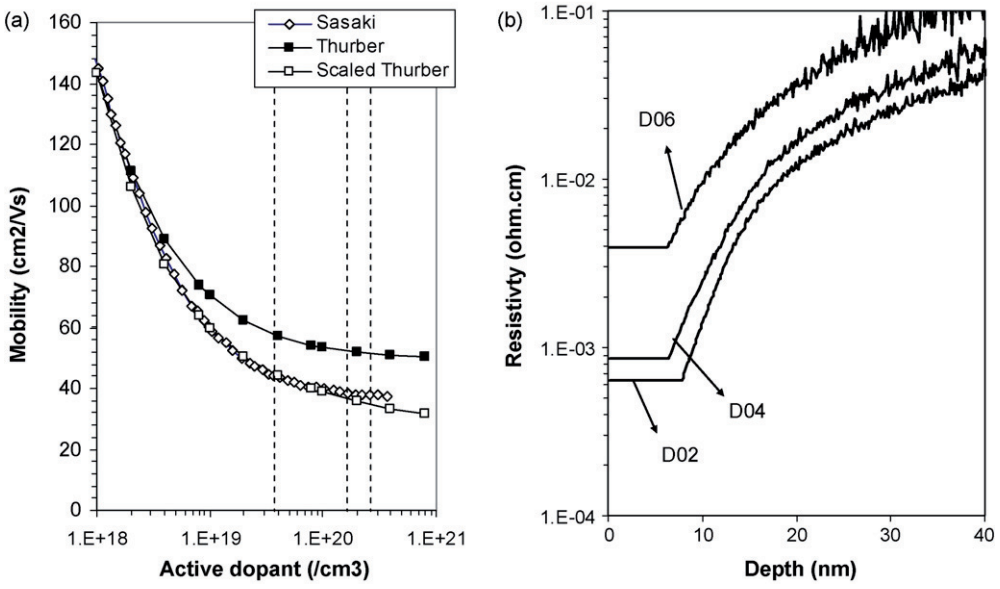

Fig. 5. (a) Conventional Thurber versus Sasaki et al. [13] and scaled Thurber model using a dopant scattering factor of 0.07 (dashed lines indicate the peak active dopant levels of respectively the 1E+14, 5E+14 and 1E+15 cm^{-2} implants) and (b) corresponding resistivity depth profiles.

Table 3
Drift mobilities obtained for the different techniques and structures.

Wafer ID	Nominal dose (at./cm^3)	SIMS dose (at./cm^3)	Laser anneal scan	Thurber	Scaled Thurber	Drift mobility (cm^2/V s)			
						MBIR	Hall–Capres	Hall–Newcastle	Hall–Imec
D02	1E+15	9.70E+14	3 × 150	52	34.7	39.0	38.9	37.8	29.9
D02	1E+15	9.70E+14	3 × 250	52	34.7	35.6	38.8	NA	31.3
D03	7E+14		3 × 150			40.5	40.9	NA	NA
D03	7E+14		3 × 250			37.9	40.5	NA	NA
D04	5E+14	4.75E+14	3 × 150	53	35.9	40.3	43.1	41.8	36.0
D04	5E+14	4.75E+14	3 × 250	53	35.9	42.4	42.4	NA	36.6
D05	3E+14		3 × 150			41.2	45.0	NA	NA
D05	3E+14		3 × 250			40.3	44.6	NA	NA
D06	1E+14	1.00E+14	3 × 150	58	44.8	49.1	55.0	50.1	50.0
D06	1E+14	1.00E+14	3 × 250			47.0	54.1	NA	NA

mainly dominated by the mobility of the highest doped part of the layer.

The largest difference between the results of the three Hall based techniques is about 30% (for the highest dose). The Capres and Newcastle results agree more closely to within about 10%, even though the Newcastle sheet resistance and sheet carrier density values had higher uncertainties due to the omission of cloverleaf van der Pauw structures in this study. This agreement illustrates the cancelling out mechanism discussed above. Likewise, the mobilities obtained from MBIR are also within 10%.

Overall, the Capres data seem to have the most credibility, especially due to their very good agreement in sheet resistance with the JPV data set. Part of this advantage with respect to the larger area Hall measurements may be due to the fact that the latter did not utilize the usual van der Pauw approach in this study. However, part could also be associated with the reduction in measurement area in the Capres technique, which minimizes vertical junction leakage between the implanted layer and the substrate. Note that with increasing implanted dose (decreasing mobility), the deviation between the experimental drift mobilities and the original Thurber model increases due to the increase of interstitial Boron atoms.

Note that we assume here that the Hall scattering factor remains meanwhile constant, for the following reason: the mobility is $\mu = e\langle\tau_m\rangle/m^*$, where e is the unit charge, m^* the effective carrier mass and $\langle\tau_m\rangle$ the momentum relaxation–time average, thus the mobility is directly affected by addition of more scattering centres or scattering processes. The Hall scattering coefficient, however, is $r_H = \langle\tau_m^2\rangle / \langle\tau\rangle^2$, and we use the working hypothesis that it is therefore not affected by the addition of more scattering centres unless the addition of these scattering centres substantially alters the energy dependency of the momentum relaxation–time $\tau_m(E)$. To a first approximation we may thus assume that r_H is unaffected by the presence of inactive Boron, whereas the mobility is affected.

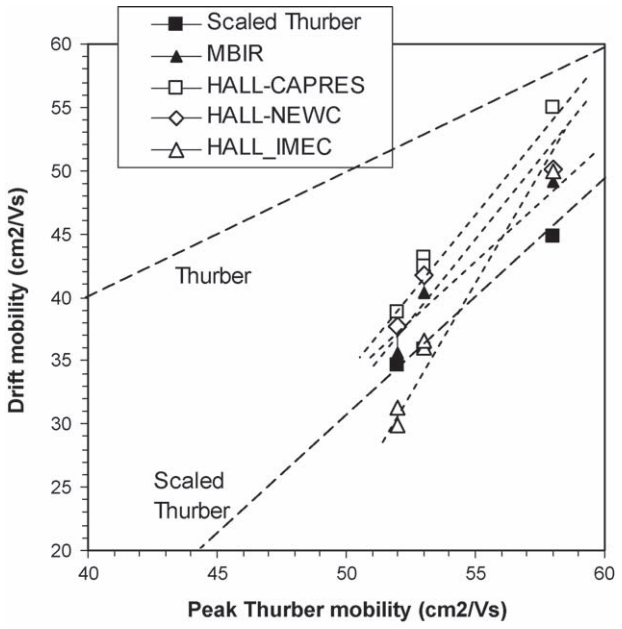

Fig. 6. Drift mobilities obtained through the different techniques for the different doses and through the scaled Thurber model versus the corresponding original Thurber mobility calculated at the peak carrier concentration.

In principle one does not expect a perfect agreement of the experimental mobility values with the scaled Thurber trend line in Fig. 6, as both axis basically refer to different values for the mobility (peak versus sheet mobility). It may however be interesting to note that such an agreement can easily be achieved for example for the Capres data set, by using a slightly different Hall scattering factor, namely 0.75.

9. Conclusions

In this work we have studied the sheet resistance, sheet carrier density and drift mobility of low energy (0.5 keV) Boron implants, with doses ranging from 10^{14} up to 10^{15} at./cm^2, and subsequently activated with sub-melt laser anneals (DSA) with two different dwell times and laser powers (but the same thermal budget). Besides a series of conventional characterization techniques (FPP, VPS, JPV), three different Hall setups and an infra-red reflectrometry tool were studied.

Overall the microscopic Hall–Capres tool seems to give the most reliable results for all the involved technological parameters. In conventional Hall measurements care must be taken to minimize geometrical error and the substrate leakage current. The more reliable parameter from MBIR is the sheet carrier density, provided a sufficient dynamic range is available in the relevant part (500–7000 cm^{-1}) of the measured spectrum. The extracted mobility proofs to be the parameter the least susceptible to problems.

The little differences observed between the 3 × 150 and the 3 × 250 mm/s indicate that the dwell time is less important than the peak temperature during the anneal. In both cases the maximum activation level that could be established was 2.69×10^{20} cm^{-3} (assuming a Hall scattering factor of 0.8). Furthermore, an increase in activation level could be clearly resolved for increasing implanted doses. It is suggested that this is evidence that during laser anneal the activation level, at the considered temperature and dwell times, is controlled by the B–I dissolution reaction and not by the solid solubility at the peak temperature.

Acknowledgement

The authors would like to thank B. Parmentier for the VPS measurements (Imec).

References

[1] ITRS roadmap, http://www.itrs.net/.
[2] P. Timans, et al., Mat. Res. Soc. Symp. 912 (2006) C1.1.
[3] W. Vandervorst, T. Clarysse, N. Duhayon, P. Eyben, T. Hantschel, M. Xu, T. Janssens, H. De Witte, T. Conard, J. Deleu, G. Badenes, International Electron Devices Meeting (IEDM) 2000, Technical Digest IEDM, 2000, p. 429.
[4] A. Hunter, et al., 15th IEEE International Conference on Advanced Thermal Processing of Semiconductors–RTP2007, 2007, p. 13.
[5] W. Vandervorst, E. Rosseel, T. Clarysse, J. Goossens, R. Lin, D. Petersen, T.M. Hansen, P.F. Nielsen, MRS 2008 Spring Meeting, 2008.
[6] T. Clarysse, D. Vanhaeren, I. Hoflijk, W. Vandervorst, Mater. Sci. Engin. Rep. 47 (2004) 123.
[7] V.N. Faifer, M.I. Current, T.M.H. Wong, V.V. Souchkov, J. Vaccin. Sci. Technol. B 24 (2006) 414.
[8] C.A. Duran, A.A. Maznev, G.T. Merklin, A. Mazurenko, M. S Gostein, IEEE/SEMI Advanced Semiconductor Manufacturing Conference, Stresa Italy, June 2007, p. 232.
[9] D.K. Schroder, Semiconductor Material and Device Characterization, second edition, John Wiley & Sons, Inc., New York, 1998, p. 510.
[10] T. Clarysse, A. Moussa, F. Leys, R. Loo, W. Vandervorst, M.C. Benjamin, R.J. Hillard, V.N. Faifer, M.I. Current, R. Lin, D.H. Petersen, Mater. Res. Soc. Symp. Proc. 912 (2006) 197.
[11] D.H. Petersen, R. Lin, T.M. Hansen, E. Rosseel, W. Vandervorst, C. Markvardsen, D. Kjær, P.F. Nielsen, J. Vacuum Sci. Technol. B: Microelectron. Nanometer Struct. 26 (2008) 362.
[12] D.H. Petersen, O. Hansen, R. Lin, P.F. Nielsen, J. Appl. Phys. 104 (2008) 013710.
[13] Y. Sasaki, K. Itoh, E. Inoue, S. Kishi, T. Mitsiushi, Solid State Electron. 31 (1) (1988) 5.
[14] L.J. van der Pauw, Phil. Res. Rep. 13 (1958) 1.

Paper XIII

in Proc. RTP 2008 (IEEE, New York, 2008) pp.135-140.

PhD students contribution:

Experimental Micro Hall Effect measurements. Data treatment assisted by O. Hansen. Discussions on M4PP, MHE, cloverleaf and conventional 4PP results, and minor revisions to manuscript.

Impact of multiple sub-melt laser scans on the activation and diffusion of shallow Boron junctions

E. Rosseel[a], W. Vandervorst[a,b], T. Clarysse[a], J. Goossens[a], A. Moussa[a]
R. Lin[c], D.H. Petersen[c,d], P.F. Nielsen[c], O. Hansen[d], N.S. Bennett[e], N.E.B. Cowern[e]

[a]*IMEC, Kapeldreef 75, B-3001 Leuven, Belgium*
[b]*KU Leuven, Dept. of Physics-IKS, Celestijnenlaan 200D, B-3001 Leuven, Belgium*
[c]*Capres A/S, Scion-DTU, Building 373, DK-2800 Kongens Lyngby, Denmark*
[d] *DTU Nanotech - Dept. of Micro and Nanotechnology, Technical University of Denmark, B-345 East, DK-2800 Kgs. Lyngby, Denmark*
[e]*School of Electrical, Electronic and Computer Engineering, Newcastle University, Newcastle upon Tyne NE1 7RU, UK*

Sub-melt laser annealing is a promising technique to achieve the required sheet resistance and junction depth specifications for the 32 nm technology node and beyond. In order to obtain a production worthy process with minimal sheet resistance variation at a macroscopic and microscopic level, careful process optimization is required. While macroscopic variations can easily be addressed using the proper spatial power compensation it is more difficult to completely eliminate the micro scale non-uniformity which is intimately linked to the laser beam profile, the amount of overlaps and the scan pitch. In this work, we will present micro scale sheet resistance uniformity measurements for shallow 0.5 keV B junctions and zoom in on the underlying effect of multiple subsequent laser scans. A variety of characterization techniques are used to extract the relevant junction parameters and the role of different implantation and anneal parameters will be explored. It turns out that the observed sheet resistance decrease with increasing number of laser scans is caused on one hand by a temperature dependent increase of the activation level, and on the other hand, by a non-negligible temperature and concentration dependent diffusion component.

INTRODUCTION

An important challenge for advanced CMOS technologies is the formation of highly active shallow source/drain extension junctions. As a classical spike Rapid Thermal Annealing (sRTA) results in excessive dopant diffusion and limited electrical activation, high temperature millisecond annealing (MSA) eventually combined with a soft sRTA is considered as the activation method of choice [1-3]. While considerable progress as been made with the integration of MSA in advanced CMOS process flows [4] some manufacturability aspects still require further attention [5]. One of these is the micro-scale sheet resistance (Rs) variation observed for sub-melt laser annealing [5-7]. These micro-scale Rs variations are caused by the overlapping or "stitching" of the laser beam during subsequent laser scans and appear as a result of the local response of the junction to multiple laser illuminations. As these effects occur on a short length scale (mm to sub-mm) dedicated metrology is required to visualize these effects and to make a correct assessment of their magnitude [6]. In the present paper, the focus will be on the response of shallow 0.5 keV B junctions to multiple laser illuminations which is key to understand the resulting stitching pattern.

EXPERIMENTAL

To emphasize the role of multiple subsequent laser illuminations, we prepared two sets of wafers with a different scanning pattern. On a first type of wafers (type "S") a number of zones where irradiated with the laser using a standard stepping distance *d* "stitching period" of 3.65 mm between subsequent scans. As the laser beam has a width of ~ 11 mm, each point in those zones is effectively annealed by 3 subsequent temperature pulses. On a second type of wafers (type "NS") zones were defined where the laser was scanning for a number of consecutive times (1x-7x) without stepping. These are the so-called "non-stitching" scans.
In both cases, 300 mm n-type wafers of device quality were used. The different wafers received a basic clean before implant, and all required implants were done on a low energy Quantum X implanter from Applied Materials. Wafers were prepared with different B doses ($1x10^{15}$ at/cm^2 down to $1x10^{14}$ at/cm^2) while the energy was kept fixed at 0.5 keV. On selected wafers a

preceding Ge Pre Amorphization Implant (PAI) was applied (Ge, 12 keV, $5x10^{14}$ at/cm^2) and in some cases an intermediate C implant was given (C, 3 keV, $1x10^{15}$ at/cm^2). All implants were single quadrant implantations with zero tilt and twist, and the 0.5 keV B implants where obtained by deceleration from a 2 keV beam. Laser annealing was done in a Applied Materials DSA chamber [8] which uses a 808 nm diode bar laser and has a spot size of ~ 11 mm x 75 μm. For all reported measurements in this paper, a fixed scan speed of 150 mm/s is used corresponding to a dwell time of ~ 0.5 ms. The wafer peak temperature (T_p) was monitored during each scan with an integrated pyrometer [9]. For the S-wafers a fixed temperature of 1220°C was applied while conditions with 1220°C and 1300°C were chosen for the NS-wafers. All wafers were annealed in a pure N_2 ambient.

For the determination of the sheet resistance, sheet carrier density and mobility of these layers, conventional Four-Point probe (4PP), Micro Four-Point Probe (M4PP) and three different sets of Hall measurements were undertaken (Newcastle, Capres, Imec). Note that the NS-wafers were evaluated by a larger set of characterization techniques for which we refer to [10]. 4PP was done on an RS100 commercial tool with an electrode pitch of 1 mm (D-probe, 100g load, 20 mil tip). At Imec and Newcastle, conventional macroscopic Hall measurements were done on 1x1 cm^2 square pieces of material with contacts close to the corners. At Newcastle an eutectic was used for the contacts and the samples were patterned into a cloverleaf structure. At Imec, clamps were used for the contact without van der Pauw patterning. Finally, the micro four-point probe (M4PP) Hall Effect method from Capres combines zero probe penetration [11] and high spatial resolution [6] with a van der Pauw like measurement technique [12]. Hall sheet carrier density, Hall mobility and sheet resistance are simultaneously measured by performing a series of four-point resistance measurements in a moderate magnetic flux density B = 500 mT and in proximity of a cleaved or lithographically defined edge. The M4PP Hall effect measurements were performed with an electrode pitch of 20 μm and a current set-point ranging from 17 to 120 μA depending on the sample sheet resistance. The magnetic flux density used for the conventional Hall measurements were respectively 330 mT at Newcastle and 200 mT at Imec.

SHEET RESISTANCE

In Figure 1a, we show a part of the M4PP scans on the S-wafers for fixed scan velocity of 150 mm/s, T_p = 1220°C and varying B doses ($1x10^{15}$, $7x10^{14}$, $5x10^{14}$at/cm^2). For a nominal dose of $1x10^{15}$ at/cm^2, the

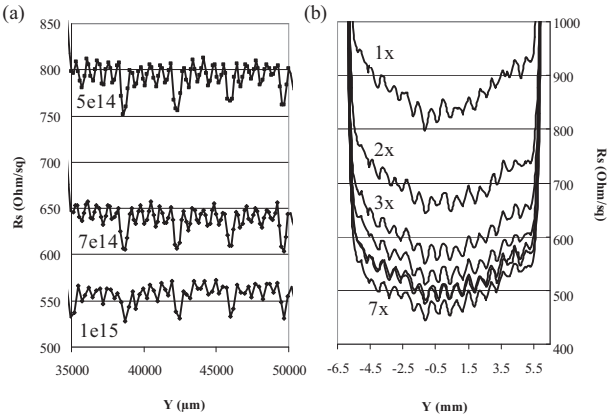

Figure 1. (a) M4PP traces for S-wafers with different B doses ($1x10^{15}$, $7x10^{14}$, $5x10^{14}$ at/cm^2). (b) M4PP traces for a NS-wafer through laser scans with varying overlaps (1x-7x). B dose $1x10^{15}$ at/cm^2 and T_p = 1220°C.

Rs span due to stitching is about 36 Ω/□ which corresponds to a variation of ~ 6%. In Figure 1b, we show the M4PP Rs on the NS-wafer with a dose of $1x10^{15}$ at/cm^2 for varying laser overlaps (1x-7x) and a Corresponding peak temperature of 1220°C. The Rs traces clearly reveal the size of the laser beam along the slow axis and explain the origin of the sub-stitching minima on the S-wafers. As previously reported [7] these sub-stitching minima are related to intensity variations within the laser spot, and can be removed by an improved laser design. When the number of overlaps is increased from 1x to 7x, the Rs drops systematically as we will discuss later in more detail. The spatial Rs variation of the standard stitching scans is the result of the integrated spatio-temporal response of the substrate on the impinging laser radiation. If we evaluate the Rs for a triple overlap at the center of the beam we find Rs values which are very comparable to the ones obtained for the corresponding stitching scans. This proves experimentally that most of the wafer area sees indeed a 3x laser illumination. The magnitude of the Rs drop for the stitching scans is also comparable to the drop in Rs when going from a 3x to a 4x trace on the NS-wafer. This shows that the large dips in the Rs traces in Figure 1a are indeed caused by local (3+1)x overlap. The stitching variation can thus be understood if the mechanism behind the Rs(n) dependence can be unraveled (with n the number of laser scans).

Figure 2 summarizes the Rs traces for the NS-wafers versus the number of subsequent laser scans at two different peak temperatures. Rs was determined as the average of the central minima in the across beam scans shown in Figure 1b. The nominal B dose is listed next to the curves. The short dashed lines are for a B 0.5 keV,$1x10^{15}$ implant preceded with a Ge PAI, while the

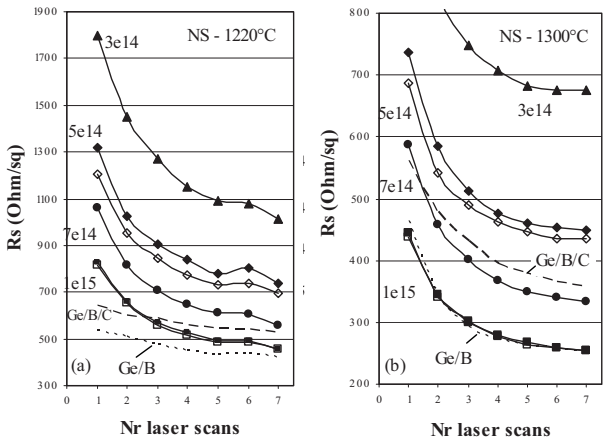

Figure 2. Sheet resistance of the NS-wafers versus the number of subsequent laser scans for (a) 1220°C and (b) 1300°C. Filled symbols are standard 4PP measurements while open symbols are M4PP measurements. Curves with short dashed lines are for the Ge/B implant, long dashed lines for Ge/C/B.

long dashed lines are for a Ge/C/B combination. Globally we observe a decrease in Rs with increasing number of subsequent laser scans as well as B dose. The shape of the curves looks similar for the two temperatures and mainly differs in absolute values. The higher temperature has clearly a beneficial effect in lowering Rs. For a B dose of $1x10^{15}$, both the M4PP and the standard 4PP gives nearly identical results. For lower doses (and larger sheet resistances) the difference becomes somewhat larger and the M4PP seems to give systematically the lowest result (which agrees with the larger spot size of the 4PP resulting in a higher average Rs cfr Fig. 1b). When a PAI is implemented before the B implant, the shape of the curves is clearly different at 1220°C compared to 1300°C. Finally, it is clear that C co-implantation also increases the Rs.

DOPANT PROFILES

To gain more insight in the dopant distribution, Secondary Ion Mass Spectrometry (SIMS) was carried out. In Figure 3, SIMS spectra are shown as a function of the number of subsequent laser scans for three different B implants (B doses $1x10^{15}$ at/cm^2, $5x10^{14}$ at/cm^2, $1x10^{14}$ at/cm^2) and T_p = 1300°C. The as - implanted profile in the crystalline Si (c-Si) is characterized by an immobile peak at ~ 2.6 nm depth, which is typically associated with the presence of Boron and Boron Interstitial Clusters (BICs) [13]. When the dose decreases the peak magnitude decreases and becomes hardly distinguishable at the lowest dose of $1x10^{14}$ at/cm^2. At the first laser scan a Transient Enhanced Diffusion (TED) takes place whose magnitude seems to be relatively independent of the B implant dose. For subsequent annealing, a kink appears in the concentration profile at a depth ~ 6 nm separating the immobile peak from a pronounced diffusing tail. As the B dose decreases, the extent of this diffusing tail is strongly reduced which clearly points towards a Boron Enhanced Diffusion [14]. With increasing number of scans the B dose in the immobile peak reduces and at the same time the edge of the diffused profile moves deeper into the substrate. When the dose is kept at $1x10^{15}$ at/cm^2 but the temperature is reduced to 1220°C (Figure 4a), the situation looks identical but the diffusion distances are now reduced due to the lower thermal budget.

The phenomenology is comparable for the wafer which received a Ge PAI (see Figure 4b with T_p = 1300°C). The as-implanted profile is shallower compared to the c-Si case due to the absence of channeling and the difference wrt the shift of the profile after the 1st laser scan is larger in case of PAI. The reason for this is twofold : there is a more pronounced End Of Range (EOR) damage due to the PAI leading to a larger interstitial flux during TED and the diffusion in the amorphous Si (α-Si) is larger compared to c-Si [16]. Similar observations were recently reported by Lerch et al. in case of multiple flash pulses [15].

Figure 4c, shows the case for which a C co-implantation is carried out after the PAI. It is interesting to note that the addition of C is effective in reducing the B diffusion during the subsequent laser scans as observed for classical RTA [16,17]. Besides suppression of classical TED, C reduces the interstitial-mediated B diffusion which takes place during the BIC dissolution. This can clearly be seen in Figure 5, where we plot the profile shift at the steep edge of the diffusing tail ([B] = $5x10^{19}$/cm^3) versus the number of laser overlaps.
At 1300°C the C introduction reduces the profile shift with ~ 3 nm for 3x and ~ 6 nm for 7x. Similar behavior can be observed at lower temperatures but the difference is smaller. Compared to the wafer with PAI, the C-co implant yields the steepest profiles and gives the best Rs-Xj trade-off.

HALL MEASUREMENTS

Now we understand the impact of multiple laser scans on the B profile, we still need to find out what portion of the profile is active and how this evolves. In a previous study on the S-type wafers [10], different Hall approaches where compared. From that study, it appeared that the Micro Hall probe gave the most

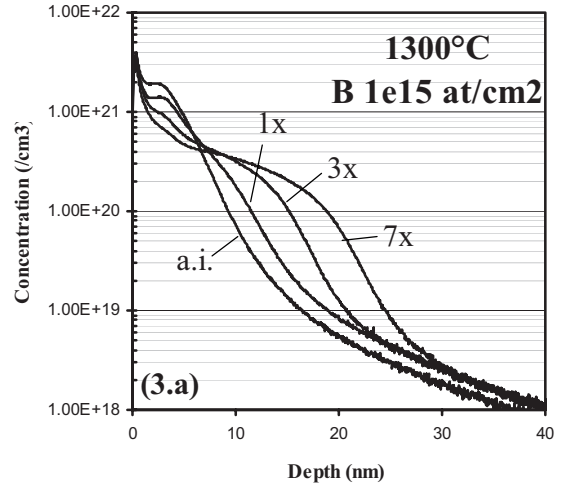

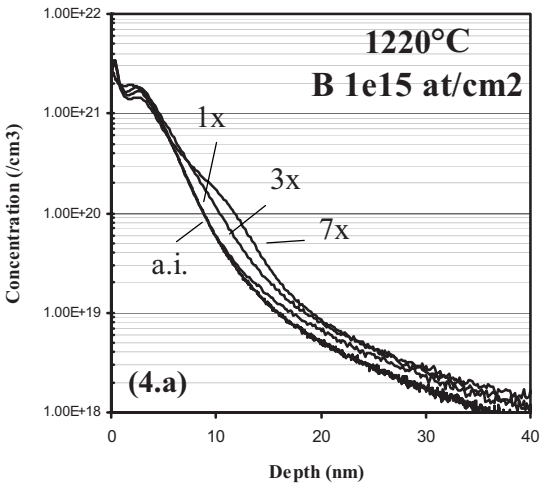

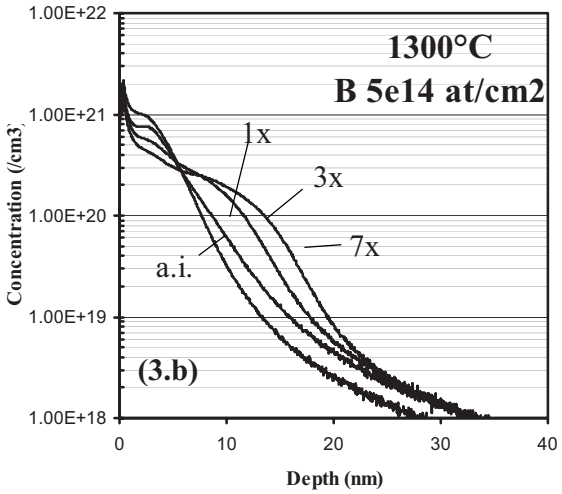

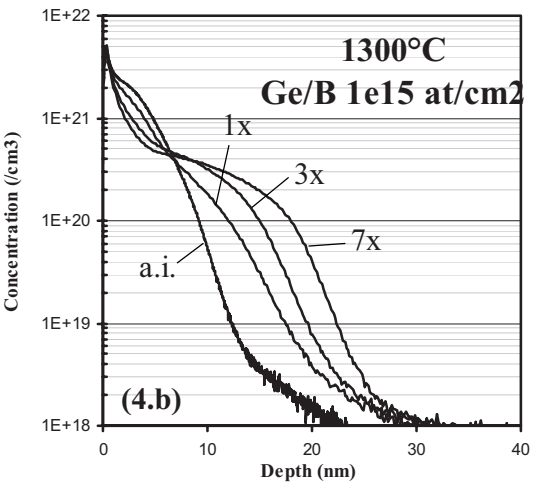

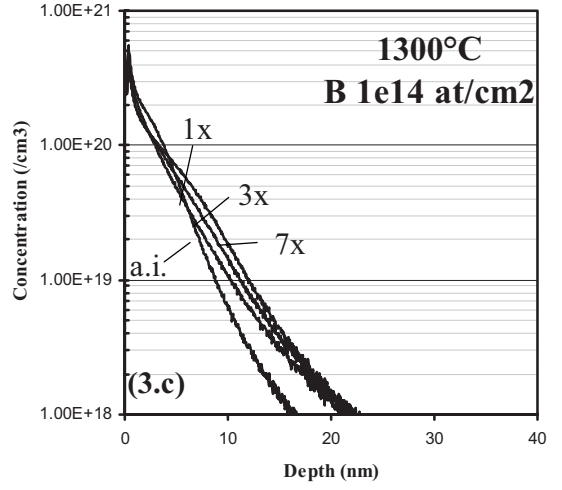

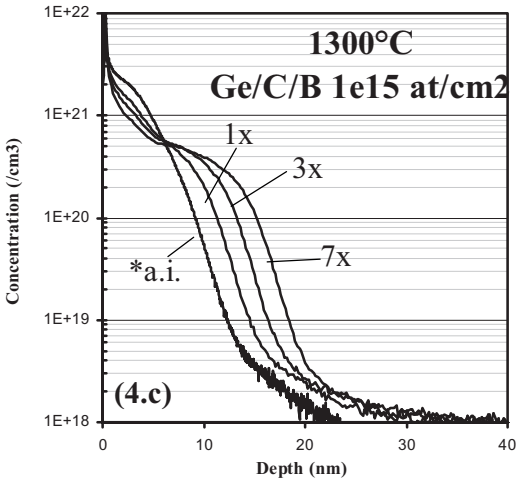

Figure 3. SIMS curves for different B 0.5 keV implants in c-Si receiving a varying number of laser scans. B dose reduces from top to bottom (a) $1x10^{15}$ at/cm^2, (b) $5x10^{14}$ at/cm^2, (c) $1x10^{14}$ at/cm^2. T_p =1300°C

Figure 4. SIMS curves for different B 0.5 keV implants receiving a varying number of laser scans.
(a) B,$1x10^{15}$ at/cm^2, T_p =1220°C
(b) Ge/B,$1x10^{15}$ at/cm^2, T_p =1300°C
(c) Ge/C/B,$1x10^{15}$at/cm^2, T_p =1300°C (*a.i. from Ge/B)

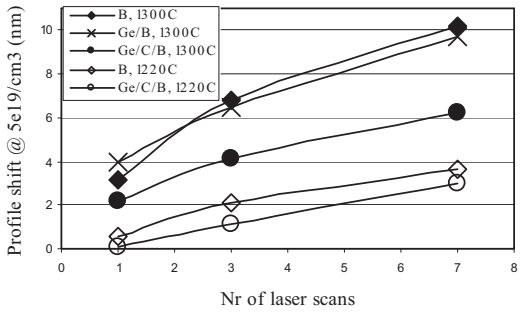

Figure 5. Profile shift taken at a B concentration of $5x10^{19}/cm^3$ versus the number of laser scans. The arrows indicates the effect of C addition.

consistent results while the classical macroscopic methods gave more deviating results. In the mean time some samples were patterned at Newcastle with a cloverleaf structure and these are reported in Figure 6, together with the original results. With the Hall measurements, one can measure the sheet resistance Rs and the Hall sheet carrier density n_{Hs} and determine the sheet carrier density from $n_s = n_{Hs}.r_H$ where r_H is the Hall-scattering factor which is assumed to be 0.8 (for p-type) based on literature [18]. Finally, the drift mobility is found from $\mu_{drift} = 1/qR_s n_s$.

If we take a look at the dependence of the sheet carrier density versus dose at 1220°C (Figure 6a) we observe a sublinear increase of n_s with increasing dose which indicates that we have more carriers at higher implant doses but that the degree of activation is decreasing (as can be seen in Figure 6b) due to the fact that more candidate acceptors are trapped in B clusters and BICs. From a measurement point of view, it is good news that the Micro Hall results and the results on cloverleaf samples are now in a good agreement. The Imec data taken on macroscopic square samples without patterning, give a systematic over estimation between 20-30%, but are nevertheless reproducible and indicate the right trend. For the data points with PAI at a B dose of $1x10^{15}$ at/cm^2 both measurements seem to confirm that the PAI also results in an improved activation. Finally, in the bottom graph (Figure 6c) we show the the drift mobility versus dose.The decreasing mobility with increasing dose seems a consistent trend with absolute values which are very reasonable [10].

Figure 7 shows the sheet carrier density, degree of activation versus the number of overlapping scans for the NS-type wafers at a B dose of $1x10^{15}$ and 1300°C The circles and triangles are the measurements with Micro Hall probe while the other datapoints were taken with the macroscopic method at Imec. If we zoom in on

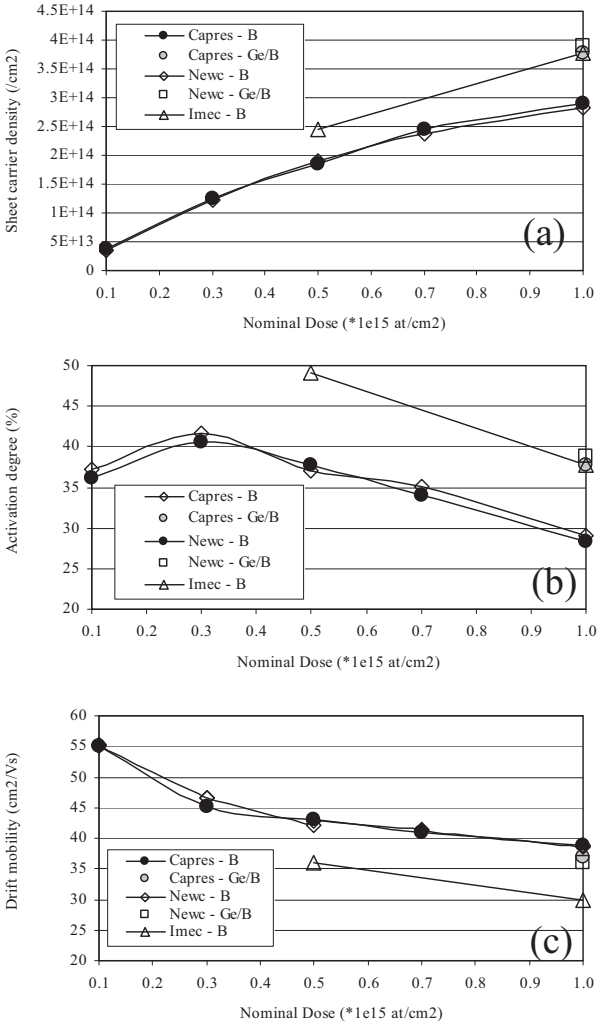

Figure 6. Hall data for the S-wafers at 1220°C versus implant B implant dose. (a) sheet carrier density; (b) activation degree; (c) drift mobility

the sheet carrier density, we notice that the Micro Hall probe predicts an increase at the first laser scans followed by a saturation above ~ 4x. The behavior for the macroscopic method follows more or less the same trend but is again overestimating the active carrier portion by 20-30%. The 1x-2x transition for the macroscopic method is clearly more abrupt and not present for the PAI case. More measurements are required however to find out if this is a systematic trend or a variation of that measurement point. The triangle represents the Micro Hall measurement on the S-wafers (3x, 1220°C). The location of this point confirms the obvious fact that the activation (and diffusion) increases with temperature.

The bottom graph shows again the mobility. For all samples, the mobility increases steadily with the

number of scans, which might indicate that the temperature pulses anneal out clusters and defects arising from the EOR, which results in a lower scattering and larger mobility. The systematic underestimation of the mobility in case of the macroscopic measurement method remains present.

CONCLUSIONS

In the present work we have analyzed the mechanisms behind the observed sheet resistance variation due to laser beam stitching on shallow B junctions. The variations are resulting from the response of the junction to the subsequent laser scans. The subsequent laser scans dissolve the B and B-I clusters in the surface region and release as such B atoms and self-interstitials which can take part in the diffusion process. This diffusion process results in a deeper profile, and hence a lower sheet resistance. By introducing C close to the zone of the dissolving clusters, the diffusion of the B can be diminished resulting in more shallow profiles. At the same time the activation of carrier profile increases with the number of scans and seems to saturate after 4-5 scans (at 1300°). Finally, these multiple laser scans also increase the mobility, most likely due to a dissolution of defects which contribute to the carrier scattering.

ACKNOWLEDGEMENTS

The authors are grateful to Imecs' FAB team and Samir Bouchema, Shankar Muthukrishnan, Abhilash Mayur, Robert Schreutelkamp from Applied Materials for their kind support.

REFERENCES

[1] A. Pouydebasque et al., IEDM'05, p.679
[2] T. Hoffmann et al., IWJT'07, p.137
[3] T. Noda et al., IEDM'06, p.377
[4] C. Ortolland et al., VLSI'08, p.186
[5] J.O.Borland, Y. Kawasaki, J. Halim, B. Chung, Solid State Technology, July 2008.
[6] D.H.Petersen et al., JVST **B 26(1)**, (2008) 362.
[7] W. Vandervorst et al. MRS 2008
[8] A. Hunter, J. Zelenko and R. Mani, Proc. IEEE RTP 2007, p. 13.
[9] B. Adams et al., Proc. IEEE RTP 2005, p. 105.
[10] T. Clarysse et al., eMRS 2008, Symposium I.
[11] T. Clarysse et al., MRS Soc. Proc. 912, p. 197 (2006).
[12] D. H. Petersen, O. Hansen, R. Lin, and P. F. Nielsen, J. Appl. Phys. 104, 013710 (2008).
[13] L. Pelaz, M. Jaraiz, G. Gilmer, J. Gossmann, C. Rafferty, D. Eaglesham and J. Poate, Appl. Phys. Lett. **70**, 2285 (1997).

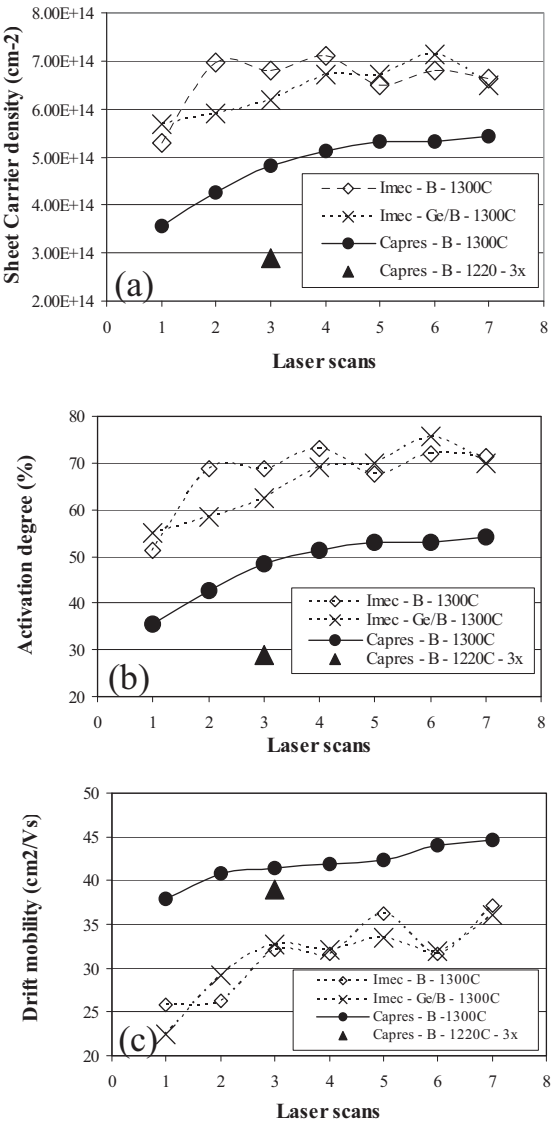

Figure 7. Hall data for the NS-wafers at 1300°C versus nr of laser scans (a) sheet carrier density; (b) activation degree; (c) drift mobility

[14] A. Agarwal, H. Gossmann, D. Eaglesham, S. Herner, A. Fiory and T. Haynes, Appl. Phys. Lett. **74**, 2435 (1999).
[15] W. Lerch et al., eMRS 2008, Symposium I.
[16] V. Moroz, Y.-S. Oh, D. Pramanik, H. Graoui, M. Foad, Appl. Phys. Lett. **87**, 51908 (2005).
[17] R. Duffy et al., Appl. Phys. Lett. **84**, 4283 (2004).
[18] Y. Sasake, K. Itoh, E. Inoue, S. Kishi, T. Mitsiushi, Solid-State Electron. 31 (1) (1988) 5.

Paper XIV

J. Vac. Sci. Technol. B **26**, 317-321 (2008).

PhD students contribution:

Supporting calculations and discussions. Experimental M4PP carrier profiling and data treatment together with R. Lin. Some manuscript revisions.

Advanced carrier depth profiling on Si and Ge with micro four-point probe

Trudo Clarysse,[a] Pierre Eyben, Brigitte Parmentier,
Benny Van Daele, and Alessandra Satta
IMEC, Kapeldreef 75, B-3001 Leuven, Belgium

Wilfried Vandervorst
IMEC, Kapeldreef 75, B-3001 Leuven, Belgium and Electrical Engineering Department, KU Leuven, INSYS, Kasteelpark Arenberg 10, B-3001 Leuven, Belgium

Rong Lin
CAPRES A/S, Scion-DTU, Building 373, DK-2800 Kongens Lyngby, Denmark

Dirch Hjorth Petersen
MIC-Department of Micro and Nanotechnology, NanoDTU, Technical University of Denmark, b-345 East, DK-2800 Kgs. Lyngby, Denmark and CAPRES A/S, Scion-DTU, Building 373, DK-2800 Kongens Lyngby, Denmark

Peter Folmer Nielsen
CAPRES A/S, Scion-DTU, Building 373, DK-2800 Kongens Lyngby, Denmark

(Received 31 May 2007; accepted 1 October 2007; published 31 January 2008)

In order to reach the ITRS goals for future complementary metal-oxide semiconductor technologies, there is a growing need for the accurate extraction of ultrashallow electrically active dopant (carrier) profiles. In this work, it will be illustrated that this need can be met by the micro four-point probe (M4PP) tool. M4PP sheet resistance measurements taken along beveled Si and Ge blanket shallow structures will be investigated. From the differential sheet resistance changes, the underlying carrier profile can be reconstructed without the need to rely on a complicated contact modeling, i.e., M4PP carrier profiling is an absolute carrier depth profiling technique. On Si, it is found that the more sensitive a structure is to carrier spilling along the bevel, the better the M4PP system performs relative to conventional spreading resistance probe (SRP) due to its much lower probe pressure in combination with its sensitivity to what happens around the probes (and not underneath them). Also for Ge, the same issues change significantly the apparent carrier spilling behavior and improve the final accuracy obtained relative to SRP. © *2008 American Vacuum Society.*
[DOI: 10.1116/1.2802101]

I. INTRODUCTION

Recently, a new approach to carrier depth profiling based on the usage of a micro four-point probe (M4PP) tool along a beveled surface has been proposed.[1] The measurement setup itself is quite similar to conventional spreading resistance probe (SRP) profiling, i.e., the micromachined four probes (positioned at about 1.5 μm separation) are aligned with the edge of a beveled surface and stepped down the bevel toward the substrate generating a resistance versus depth profile from which the underlying resistivity (and carrier) profile can be extracted. A major difference between M4PP and SRP is that the former gives absolute data values, i.e., there is no calibration step needed to convert the raw data toward resistivity values.[1] After a smoothing step, the subsequent M4PP calculations to extract the carrier profile are extremely simple relative to the tedious SRP contact modeling approach.[1]

In this work, we further explore the capabilities of M4PP for carrier depth profiling. First, we discuss the impact of some experimental issues on the measurement quality, such as bevel surface roughness, starting point definition, depth resolution, and reproducibility of the raw data. Next, we will mainly focus on the so-called carrier spilling phenomenon for junction isolated structures. We will consider both Si-based and Ge-based diodes and compare SRP, M4PP, and scanning spreading resistance microscopy (SSRM) behaviors in the neighborhood of the junctions.

II. EXPERIMENTAL ISSUES

Previously, the required bevels were obtained through standard SRP beveling techniques, based on mechanical polishing on a rotating roughened glass plate.[2] Alternatively, SSRM based polishing techniques used to obtain low roughness cross sections can also be applied for beveling purposes.[3] In this work, both techniques have been used. In the future, it is recommended to use only the SSRM approach, since this results in a better bevel surface with a rms roughness of about 0.3 nm (versus about 2 nm for the SRP way).[3] It should be noted that, in practice, the limiting factor is the peak to peak roughness rather than the rms roughness. The former should ideally be less than 0.5 nm.

Previously, it was found that the determination of the starting point was not easy to do in practice on the small angles (a few minutes) needed for ultrashallow junction pro-

[a]Electronic mail: trudo.clarysse@imec.be

filing. As we start using SSRM bevels instead of SRP bevels, this is expected to become even more difficult due to enhanced bevel rounding of the former procedure. Hence, there is a need to systematically deposit a low temperature oxide on the samples, such that the transition from the high resistance oxide toward the low resistance semiconductor material can be determined more easily.

It has been verified that M4PP profiling has a good reproducibility within 10%. It should, for completeness, be mentioned that there are still some lifetime problems with the probes (maximum of 100 data points) which need further work.

Presently, a depth resolution of about 1 nm is achievable. In order to obtain this depth resolution, an on-bevel step size of 1 μm needs to be combined with a bevel angle of a few minutes. Note that the probes themselves have virtually zero penetration depth.[4] A higher depth resolution may be feasible in the near future by using etched bevels with magnifications as large as a factor of 5000,[5] leading to subnanometer depth resolution.

For completeness, it should be mentioned that with the present electronics, a good electrical contact can only be established in the case of a low enough contact resistance (less than 500 kΩ). The latter implies that more lowly doped profiles cannot be measured at this moment. Work is in progress to improve on this situation.

When discussing the M4PP sensitivity to carrier spilling and surface roughness, it is important to realize that the area of sensitivity is fundamentally different from SRP and SSRM. Whereas SRP and SSRM are most sensitive to the resistivity directly underneath the contact point, the M4PP measures the sheet resistance in proximity of the probe position and is virtually insensitive to the sheet resistance at the contact points.[6] For this reason, the M4PP is highly sensitive to deep scratches (e.g., >2 nm) that can result from the bevel preparation. When approaching the on-bevel electrical junction, even smaller scratches (e.g., <2 nm) may prevent the current to flow in a direct path between the two current probes, resulting in a sheet resistance value higher than for the ideal case, consequently reducing the measured junction depth. Thus, whereas surface roughness results in noise for SRP and SSRM, it should be included in the M4PP model for completeness (not yet the case) or ideally be reduced to zero. Finally, one must consider other geometrical effects that can occur near the on-bevel electrical junction and at the bevel starting point.[7]

III. SILICON PROFILING

Although the mechanical depth resolution of M4PP may be adequate for structures developed in the near future, its electrical depth resolution may be worse due to the impact of carrier spilling. We discuss this issue now in more detail first for silicon and in the next section for germanium material.

Carrier spilling causes the on-bevel, electrical carrier profile to be different from the underlying vertical carrier profile as well as from the dopant profile (assuming 100% activation), i.e., the electrical on-bevel junction, the vertical electrical junction, and the metallurgical junction can all be different.[2] A minimal amount of carrier spilling caused by the presence of the bevel, i.e., the removal of highly doped surface material as one moves down the bevel, is unavoidable. Earlier work has illustrated that the bevel angle, probe pressure, and roughness related surface state density along the beveled surface all play a role in the amount of carrier spilling. Enhanced carrier spilling can occur under the probe contacts due to a high contact force, which locally results in significant band gap narrowing and a substantially increased dielectric constant.[2] Thus, the experimental on-bevel electrical carrier profile as measured along a beveled surface with high pressure probes may be different from the geometrically induced on-bevel carrier profile. For larger probes such as those used in SRP (micrometer contact size) the pressure seems to be the dominating issue (β-tin transformation).[2] For smaller probes, as used in SSRM (using nanometer contact sizes), the surface states become more important (depletion/inversion layers near the surface that have an impact on the results for lowly doped regions). Here, we take a closer look at the carrier spilling behavior of the M4PP technique (50 nm contact size).

Figure 1(a) compares the SRP and M4PP carrier profiles obtained for a n^+p 50 nm deep structure. It follows that for this rather steep profile on a lowly doped substrate ($5\times10^{14}/\mathrm{cm}^3$), there is apparently little difference in carrier spilling between both techniques. On the other hand, Fig. 1(b) illustrates a dramatic difference for a 34 nm thick top layer (p^{++}) in a $p^{++}n^+n$ structure (thickness of n^+ layer is about 20 μm), where the respective dopant levels were 2×10^{19} cm^3 for the p^{++} layer, $8\times10^{17}/\mathrm{cm}^3$ for the n^+ layer, and $1\times10^{15}/\mathrm{cm}^3$ for the n substrate. Whereas SRP suffers from a huge amount of carrier spilling pushing the electrical on bevel junction so far toward the surface that it is no longer visible, the M4PP electrical junction remains reasonably close to the metallurgical [secondary ion mass spectroscopy (SIMS)] junction (junction depth difference of only about 9 nm). Note that this reduced M4PP carrier spilling behavior has been observed both on bevels made with the SRP and the SSRM procedure. The measurements shown in Fig. 1(b) were done on a structure with a 100 nm capping oxide to obtain a precise starting point definition. This difference in apparent carrier spilling behavior can be understood through a reduction in sensitivity due to surface roughness (scratches) close to the junction and the fact that M4PP uses lower pressure than SRP (no β-tin phase necessary) and is more sensitive to what happens in the proximity of the probes than directly underneath them. For completeness, it should be mentioned that the oscillatory behavior of the M4PP profile [Fig. 1(b)] is probably related to local depth variations, probe positioning, and geometrical effects not yet taken into account properly (lack of topographic feedback information).

Figure 1(c) illustrates the impact of different local stress models underneath the probes through one-dimensional Poisson simulations for a 40 nm structure (using earlier developed software[8]) taking into account different vertical stress

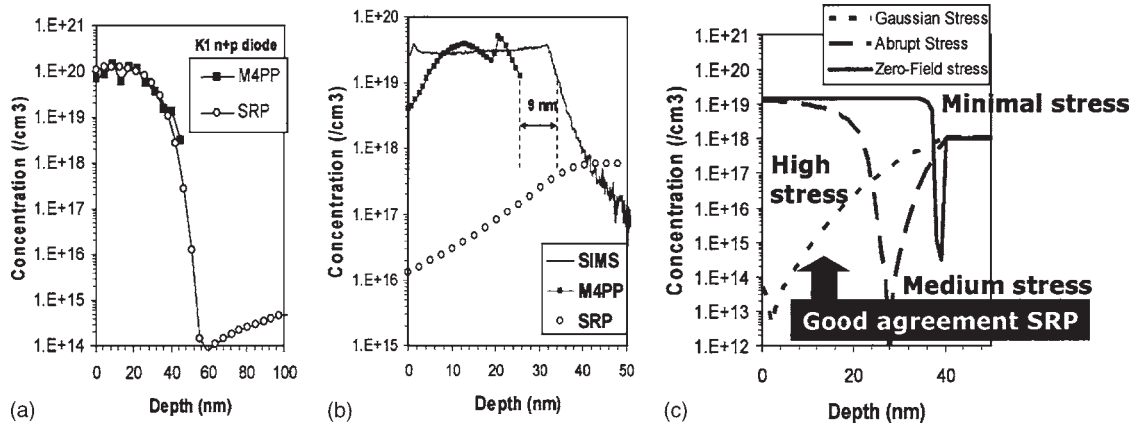

FIG. 1. Comparison of SRP and M4PP on bevel carrier depth profiles with (a) similar and (b) highly different amounts of carrier spilling behavior vs (c) on-bevel Poisson simulations with different stress levels for case (b) illustrating that a "high stress" model prediction (assuming significant band gap narrowing and increase of the dielectric constant) agrees well with the experimental SRP data. Case (a) has a lowly doped substrate (SRP bevel), while case (b) has an $8\times10^{17}/\mathrm{cm}^3$ doped opposite-type (n-type) underlying layer (SSRM bevel). (a) Without capping oxide and (b) with capping oxide.

distributions through modified depth-dependent, band gap, and dielectric constant variations.[2] The high stress carrier spilling simulations are clearly in good agreement with experimental SRP data (dominated by pressure under probes). The medium stress simulations, although resembling the experimental data, are not directly comparable to the M4PP data, because M4PP is not dominated by what happens underneath the probes (as long as the latter have near zero penetration) but by the current flowing in between them. Actually, in theory, the zero-field simulation should be the one in best correspondence with M4PP, if there were no other problems such as surface roughness.

IV. GERMANIUM PROFILING

Recently, the interest in the carrier depth profiling of germanium implanted and annealed structures has been growing among others for improved carrier mobility reasons. Earlier, we have reported on the capabilities of SRP/SSRM to profile germanium material[9] based on a new contact model. This model is able to explain why one systematically measures with SRP/SSRM a clear junction cusp on n^+p diodes but not on p^+n diodes.

Figure 2(a) compares the raw resistance data as obtained by SRP and M4PP for a P doped germanium structure (n^+p). Immediately, one can see that the on-bevel junction depths (locations of maximum resistance) are very different. For M4PP the (electrical) junction depth is only 130 nm, while it is about 370 nm for SRP. Taking into account that the metallurgical (SIMS) junction in this case is at 125 nm, it is clear that the M4PP profile once again has significantly less carrier spilling than SRP. Figure 2(b) shows the quantified resistivity depth profiles for M4PP and SRP. Note that the sheet resistance from the M4PP measurement is in good agreement with variable probe spacing (VPS) measurements done with SRP.

The reduced M4PP carrier spilling can most likely again be correlated with the reduced pressure of the probes. Recently, we succeeded in making transmission electron microscopy (TEM) cross-sectional images through SRP imprinted areas. As shown in Fig. 3, after removal of the SRP probes a significant amount of defects remains visible up to considerable depths (several hundred nanometers). The amount of defects is actually worse than in silicon.[2] It cannot be excluded that these defects have a non-negligible impact

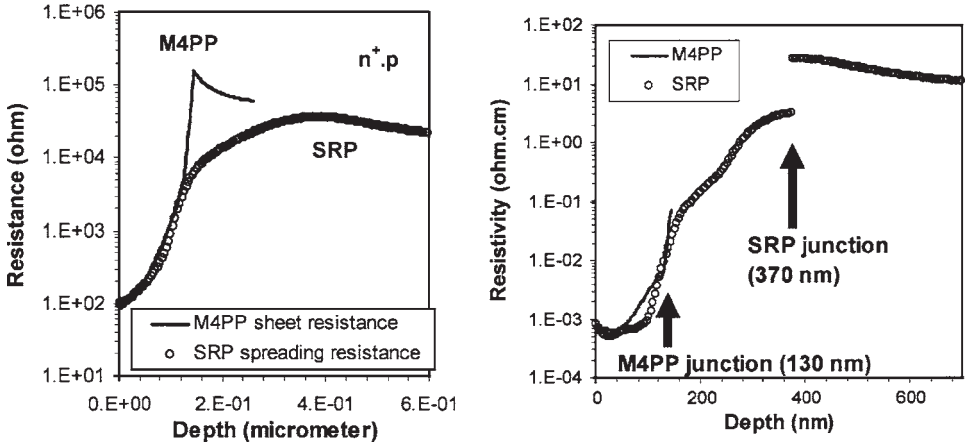

FIG. 2. Comparison of SRP vs M4PP raw resistance and calculated resistivity profiles for P, 40 keV, $1\times10^{15}/\mathrm{cm}^2$, 500 °C, 60 s, annealed implant into germanium (n^+p). SSRM bevel procedure.

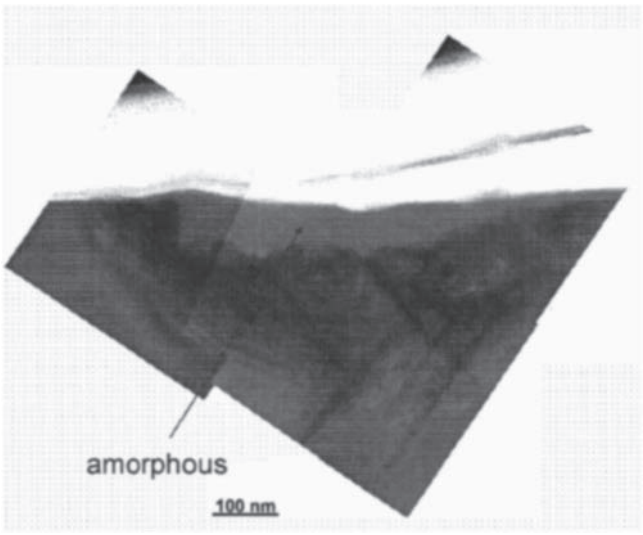

FIG. 3. TEM cross section of SRP imprint on germanium material.

on the carrier spilling behavior of SRP. Up to now no such TEM images are available for the M4PP imprints (work in progress).

Figure 4(a) compares the raw resistance data as obtained by SRP and M4PP for a B doped germanium structure (p^+n). Here, we observe that similar to SRP/SSRM, the M4PP technique does not see a junction cusp in the raw data, therefore, the junction position is also difficult to localize with M4PP on p^+n structures. This is in agreement with the earlier derived germanium contact model,[9] and can be mainly attributed to the presence of surface states (which create a thin p-type inversion layer on top of the lowly doped n-type substrate, hence, apparently converting the p^+n structure close to the surface toward a p^+p structure without junction).

It follows that M4PP can be used successfully for profiling germanium structures, but that a clear junction depth determination is only possible for n^+p structures. Note that the data discussed above were obtained on samples without a capping oxide. The position of the starting point was determined through alignment of the steepest slope in the rear portion of the profile with SIMS. It is assumed that this has no impact on the basic conclusions of this work. Further work is in progress to do similar measurements on germanium structures with a capping oxide.

V. CONCLUSIONS

There will always be a need for reliable carrier depth profiling. As SRP is running out of steam for sub-100-nm structures for many reasons, among others, the problem of profile distortions due to carrier spilling, there is a need for new measurement technologies. M4PP uses a micromachined four-point-probe head (with 1.5 μm separations) to measure a differential sheet resistance versus depth (raw data) profile along a beveled surface. Its geometrical depth resolution ultimately depends on the bevel magnifications that can be reached (subnanometer achievable).

M4PP has many advantages over SRP. First, M4PP is an absolute technique, i.e., it needs no calibration samples. Furthermore, it is a virtual zero-penetration technique, it needs no probe conditioning, and the calculational algorithm to extract the underlying resistivity/carrier profile is extremely simple (provided a powerful smoothing algorithm is used, and bevel rounding is avoided, for example, through an oxide capping layer). Also, good reproducibility and sensitivity could be observed.

Finally, due to the lower contact pressure (no β-tin and virtually zero penetration) in combination with a sensitivity to what happens around and not underneath the probes, the amount of carrier spilling on both silicon and germanium material is found to be *significantly* less with M4PP than with SRP. The remaining apparent carrier spilling can be partially (or completely) due to a reduction of sensitivity caused by scratches (blocking the current path) close to the junction. Also, geometrical effects (lateral current flow distortions near boundaries) may play a role. The impact of surface states on the results due to the beveling process (presence/absence junction cusp on Ge diodes) can only be reduced partially by using low roughness polishing procedures (such as used for SSRM), but not completely eliminated.

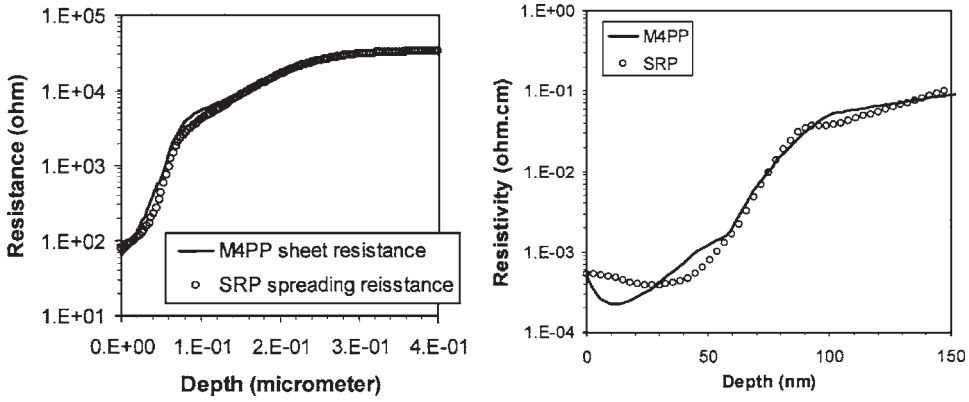

FIG. 4. Comparison of SRP vs M4PP raw resistance and calculated resistivity profiles for B, 4.5 keV, $1 \times 10^{16}/\text{cm}^2$, 500 °C, 60 s, annealed implant into germanium (p^+n) SSRM bevel procedure.

ACKNOWLEDGMENTS

The authors would like to acknowledge the TEM work of Olivier Richard and Hugo Bender.

[1]T. Clarysse, W. Vandervorst, R. Lin, D. H. Petersen, and P. F. Nielsen, Nucl. Instrum. Methods Phys. Res. B **253**, 136 (2006).
[2]T. Clarysse, D. Vanhaeren, I. Hoflijk, and W. Vandervorst, Mater. Sci. Eng., R. **R47**, 123 (2004).
[3]P. Eyben, D. Alvarez, T. Clarysse, and W. Vandervorst, AIP Conf. Proc. **683**, 685 (2003).
[4]T. Clarysse *et al.*, Mater. Res. Soc. Symp. Proc. **912**, 197 (2006).
[5]S. Fearn, Ph.D. thesis, Imperial College, London, 2000.
[6]D. H. Petersen, R. Lin, T. M. Hansen, E. Rosseel, W. Vandervorst, C. Markvardsen, D. Kjær, and P. F. Nielsen, J. Vac. Sci. Technol. B (submitted).
[7]T. Clarysse, M. Caymax, and W. Vandervorst, Appl. Phys. Lett. **80**, 2407 (2002).
[8]IMECPROF, a professional SRP analysis package, Imec, Belgium.
[9]T. Clarysse *et al.*, J. Vac. Sci. Technol. B **24**, 381 (2006).

Paper XV

Microelectron. Eng. **85**, 1092-1095 (2008).

PhD students contribution:

Conceptual idea, probe design and fabrication. Experimental M4PP measurements was assisted by P.R.E. pPetersen. Data treatment was assisted by T.M. Hansen. Draft manuscript.

Co-authors contribution:

Supporting L-beam design calculations by O. Hansen. Significant revisions to manuscript by O. Hansen and P. Bøggild. The measurement standard deviation resulting from position errors was formulated by T.M. Hansen. Minor revisions of manuscript by T.M. Hansen and P.R.E. Petersen.

The paper is based on patent application by D.H. Petersen, T.M. Hansen and P.R.E. Petersen.

Available online at www.sciencedirect.com
ScienceDirect
Microelectronic Engineering 85 (2008) 1092–1095
MICROELECTRONIC ENGINEERING
www.elsevier.com/locate/mee

Static contact micro four-point probes with <11 nm positioning repeatability

Dirch H. Petersen [a,b,*], Ole Hansen [a,c], Torben M. Hansen [a,b], Peter R.E. Petersen [b], Peter Bøggild [a]

[a] Department of Micro and Nanotechnology, NanoDTU, DTU, Oersteds Plads build.345E, 2800 Kgs. Lyngby, Denmark
[b] CAPRES A/S, Scion-DTU, Build.373, 2800 Kgs. Lyngby, Denmark
[c] CINF-Centre for Individual Nanoparticle Functionality, NanoDTU, DTU Oersteds Plads build.345E, 2800 Kgs. Lyngby, Denmark

Received 7 October 2007; received in revised form 16 December 2007; accepted 27 December 2007
Available online 15 January 2008

Abstract

In recent years micro four-point probes (M4PP) have proved a powerful tool for electrical characterization of thin film due to a high surface sensitivity and spatial resolution. However, a common problem is the probe lifetime which is limited mainly due to mechanical wear of the electrode material on the cantilever tips. In this paper we present a three-way flexible M4PP that enables static contact upon surface contact. We experimentally demonstrate that the static contact results in little or no frictional wear of the electrode material. In addition we investigate the repeatability of the effective spatial electrode position and find that the standard deviation of each electrode position is more than one order of magnitude smaller than the length scale of the tip contact area.

Keywords: Tribology; Wear; Micro four-point probe; Sheet resistance; Static contact

1. Introduction

Micro four-point probes (M4PP) are used as a metrology tool for electrical characterization of conducting and semi-conducting thin film and multi-layered structures [1,2]. Cantilever based M4PP consisting of four straight collinear cantilevers have previously been demonstrated by various groups [3–5].

A fundamental problem in micro four-point measurements is the electrical contact between the electrode tips and the surface to be measured. Thus the M4PP have a limited lifetime due to mechanical wear.

The cantilever design concept presented here overcomes some of the problems on wear observed for conventional M4PP. With conventional straight cantilever M4PP, the tips slide along the surface in the length direction of the cantilever, as the electrode tips are brought into contact with a surface. The frictional wear of the electrode material causes the contact area to increase over time and poor tip positioning repeatability necessitates the use of dynamic position error correction for reliable sheet resistance measurements [2,6].

To reduce this mechanical wear we have designed a M4PP with three-way flexible cantilevers to obtain a static mechanical contact upon surface contact. When the cantilever tip is deflected a distance, d, in the z-direction, see Fig. 1, the force acting on the tip is given by a generalized Hooke's law.

$$\begin{bmatrix} F_x \\ F_y \\ F_z \end{bmatrix} = - \begin{bmatrix} k_{11} & k_{12} & k_{13} \\ k_{21} & k_{22} & k_{23} \\ k_{31} & k_{32} & k_{33} \end{bmatrix} \begin{bmatrix} 0 \\ 0 \\ d \end{bmatrix}$$

Here F is the force and k is the cantilever spring constant. To obtain static contact, the force acting in the surface

* Corresponding author. Address: Department of Micro and Nanotechnology, NanoDTU, DTU, Oersteds Plads build.345E, 2800 Kgs. Lyngby, Denmark. Tel.: +45 30342408.
E-mail address: dhp@mic.dtu.dk (D.H. Petersen).

0167-9317/$ - see front matter © 2008 Elsevier B.V. All rights reserved.
doi:10.1016/j.mee.2007.12.077

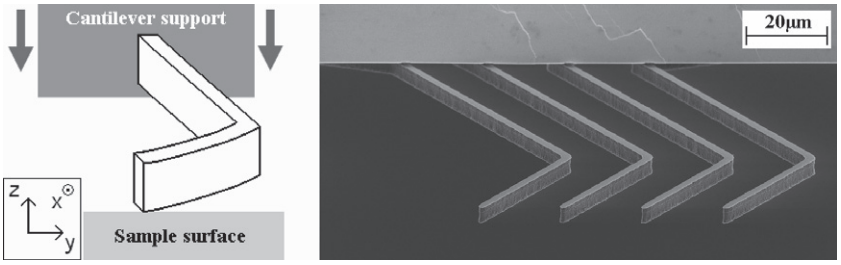

Fig. 1. (Left) Illustration of the deflection of a high aspect ratio L-shaped cantilever when engaged on a surface. (Right) SEM micrograph of a M4PP with L-shaped cantilevers. The cantilevers extend from the edge of a silicon support.

plane must be lower than the product of the normal force, $N = F_z$, and the friction coefficient, μ_S, and it can be shown that static contact is achieved when

$$\mu_S \geqslant \frac{\sqrt{k_{13}^2 + k_{23}^2}}{k_{33}}$$

One way to achieve this is with a high aspect ratio L-shaped cantilever design as illustrated in Fig. 1, where k_{13} and k_{23} are very small compared to k_{33}.

In this work we demonstrate experimentally a considerably reduced electrode wear obtained with a static contact M4PP, compared to conventional M4PP with dynamic contact. We further investigate the spatial positional repeatability of the electrode tips.

2. Experimental

The static contact M4PP used in these experiments consists of micro-machined cantilever electrodes extending from the edge of a silicon support. The cantilevers consist of 5 μm thick polysilicon coated with a 10 nm Ti adhesion layer and a 200 nm Au thin film. Fabrication of the probes is done essentially as by Petersen [3], but the cantilevers were defined by reactive ion etching (SF_6/O_2) in a 5 μm thick LPCVD polysilicon film. The cantilever design aimed at a spring constant of $k_{33} = 20$ N/m, for comparison with commercially available M4PPs. A scanning electron microscope (SEM) image of a static contact M4PP is shown in Fig. 1.

The four-point measurements were carried out on a CAPRES microRSP-M150 using lock-in technique. The current set-point was 200 μA and the frequency 987 Hz.

3. Results and discussion

3.1. Lifetime experiment

The probe lifetime was investigated on a 50 nm ruthenium thin film. A multi-cantilever probe with seven cantilevers was engaged on the ruthenium surface and four-point sheet resistance was measured without position correction using different combinations of four cantilevers, such that all cantilevers sequentially were used as current electrodes. The sample time for each configuration was 45 s resulting in a total contact time of 3 min per engage. The probe was disengaged from the surface, moved 100 nm and engaged again repeatedly to perform a continuous line scan. The experiment was terminated after 2000 engages and an accumulated surface time of 100 h.

It should be noted that due to hand mounting of the probe chip on the carrier, the probe was slightly misaligned with the surface. Thus, the two outermost cantilevers had an order of magnitude difference in contact force throughout the experiment, which corresponds to an engage depth of approximately 0.5 μm and 6 μm, respectively. This difference resulted in a contact area, which was estimated from SEM micrographs to be between ~0.02 μm^2 (0.1 μm by 0.2 μm) for a contact force of roughly 10 μN and ~0.24 μm^2 (0.4 μm by 0.6 μm) for a contact force of roughly 120 μN, see Fig. 2.

The observed Au deformation is in agreement with the expected deformation due to contact pressure, and thus no frictional wear is visible. In a similar lifetime experiment using straight cantilevers, the Au tip as well as the polysilicon beneath was excessively worn after 2000 engages; here

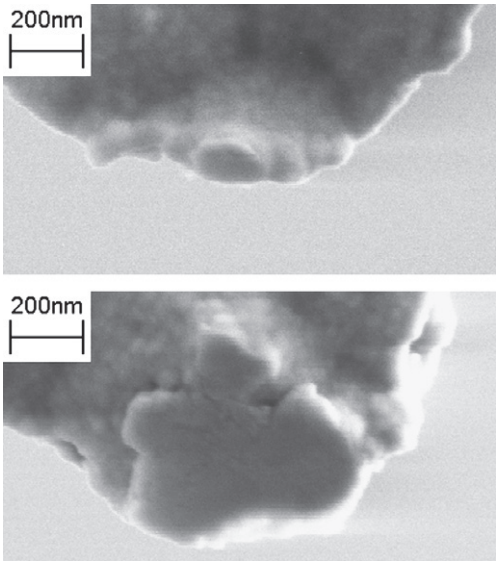

Fig. 2. SEM micrographs showing the contact area of two L-shaped cantilever tips after 2000 engages and 100 h of contact time. The contact area is the flat region in the centre. The two tips were engaged with a force of 10 μN (top) and 120 μN (bottom).

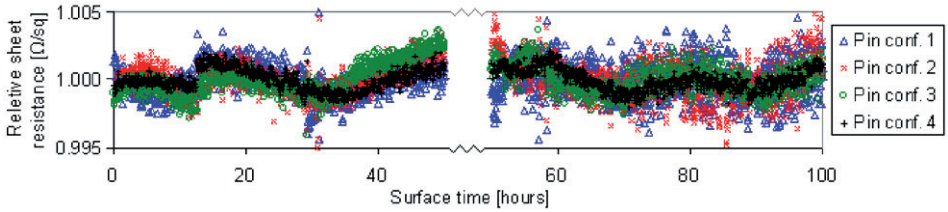

Fig. 3. Resistance repeatability measurement for 2000 surface engages and four different configurations of a seven cantilever probe. The accumulated surface contact time was 100 h. Three outliers with a relative sheet resistance of 0.981 Ω/sq, 0.983 Ω/sq and 1.007 Ω/sq are outside the scale of the graph.

the contact area was ~1.6 μm^2 of which the Au was completely removed from an area of ~0.7 μm^2.

3.2. Position repeatability

The measured sheet resistance is plotted against surface time in Fig. 3. From the measured resistance variation it is possible to calculate the effective spatial positioning repeatability of the cantilever tips. We assume the electrical noise to be zero, the sheet resistance to be perfectly homogeneous and the periodic variation to be mainly temperature dependent (day and night). Thus, we restrict the calculation to a stable period (between 15 h and 25 h).

The measured four-point resistance is given by [7]

$$R_{4PP} = \frac{V}{I} = \frac{R_S}{2\pi} \ln\left(\frac{(x_3 - x_1)(x_4 - x_2)}{(x_2 - x_1)(x_4 - x_3)}\right)$$

R_S is the sheet resistance and x_N ($N = 1, 2, 3, 4$) is illustrated in Fig. 4. The relative standard deviation of measured resistance due to variations of the effective spatial tip positions then becomes.

$$\sigma^{\text{rel}}_{R_{4PP}} = \frac{1}{R_{4PP}} \sqrt{\sum_{N=1}^{4} \left(\frac{\partial R_{4PP}}{\partial x_N}\right)^2 \sigma^2_{x_N}}$$

Assuming that the absolute standard deviation is the same for each tip position, σ_{x_N}, we find the standard deviation of the effective spatial tip positioning to be 10.5 nm, 11.0 nm, 11.8 nm and 23.9 nm for the four cantilever sets, respectively. This is more than an order of magnitude smaller than the length scale of the contact area of each tip.

3.3. Lifetime experiment 2

An accelerated lifetime experiment was performed using the same probe, but with a sample time of 4 s and only one configuration. After 12,000 engages one cantilever showed sign of deterioration in measurement repeatability due to increased contact resistance.

3.4. Processability

The cantilevers are defined by an SF_6/O_2 based reactive ion etch which is the most critical step in the fabrication process. To obtain static contact the cantilever line-width and morphology must be well controlled such that the spring constant coefficients k_{13} and k_{23} become close to zero. This sets high demands on the process uniformity and reproducibility, which can be difficult to achieve in high aspect ratio silicon etching. For imperfect cantilevers with reduced cantilever width a bi-stable contact has been observed in which a cantilever tip in static contact suddenly skids to a new position. This can result in unwanted measurement error. Alternative materials and/or fabrication process may be considered to implement high yield wafer-scale fabrication.

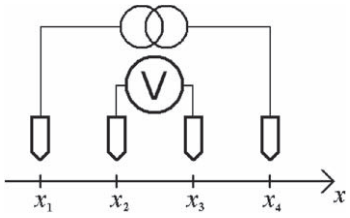

Fig. 4. Illustration of the four-point tip positioning.

4. Conclusion

The proposed concept of a static contact M4PP has been proven experimentally with minute or no frictional wear. This should be seen in relation to the electrode wear of conventional straight cantilever M4PP, which after a few hundred engages can show significant changes in the electrode tip morphology. In addition, the standard deviation of the effective spatial tip position has been shown to be more than one order of magnitude smaller than the length scale of the contact area of each tip.

Acknowledgement

We are grateful for the financial support from Copenhagen Graduate School for Nanoscience and Nanotechnology (C:O:N:T), the Danish Research Agency (FTP), and acknowledge valuable discussions with Rong Lin and Kristian Mølhave. Center for Individual Nanoparticle Functionality (CINF) is sponsored by The Danish National Research Foundation.

References

[1] D.C. Worledge, P.L. Trouilloud, Appl. Phys. Lett. 83 (1) (2003) 84.

[2] D.H. Petersen, R. Lin, T.M. Hansen, E. Rosseel, W. Vandervorst, C. Markvardsen, D. Kjær, P.F. Nielsen, in: INSIGHT 2007, San-Francisco, US.
[3] C.L. Petersen, T.M. Hansen, P. Boggild, A. Boisen, O. Hansen, T. Hassenkam, F. Grey, Sens. Actuators A 96 (2002) 53.
[4] H. Shin, P.J. Hesketh, Am. Soc. Mech. Eng. 5 (2003) 283.
[5] S. Keller, S. Mouaziz, G. Boero, J. Brugger, Rev. Sci. Instrum. (2005) 76.
[6] R. Rymaszew, J. Phys. E: Sci. Instrum. 2 (1969) 170.
[7] F.M. Smits, Bell Syst. Technol. J. 37 (1958) 711.

Paper XVI

Microelectron. Eng. **86**, 987–990 (2009).

PhD students contribution:

Problem definition and idea for study. The paper is based on a student project supervised by the PhD student. Supporting calculations and supporting manuscript writing.

Co-authors contribution:

Calculations and manuscript writing by T. Ansbæk and O. Hansen. Calculations by J.B. Larsen and T.M. Hansen. Manuscript and references revisions by P. Bøggild.

Microelectronic Engineering 86 (2009) 987–990

Contents lists available at ScienceDirect

Microelectronic Engineering

journal homepage: www.elsevier.com/locate/mee

Fundamental size limitations of micro four-point probes

Thor Ansbæk [a], Dirch H. Petersen [a,b,*], Ole Hansen [a,c], Jakob B. Larsen [a], Torben M. Hansen [a], Peter Bøggild [a]

[a] Department of Micro- and Nanotechnology, Technical University of Denmark, DTU Nanotech, Building 345E, DK-2800 Kgs. Lyngby, Denmark
[b] CAPRES A/S, Scion-DTU, Building 373, DK-2800 Kgs. Lyngby, Denmark
[c] Centre for Individual Nanoparticle Functionality, Technical University of Denmark, Building 345E, DK-2800 Kgs. Lyngby, Denmark

ARTICLE INFO

Article history:
Received 30 September 2008
Received in revised form 5 November 2008
Accepted 17 November 2008
Available online 3 December 2008

Keywords:
Four-point probes
Sheet resistance
Surface conductivity
NEMS
MEMS

ABSTRACT

The continued down-scaling of integrated circuits and magnetic tunnel junctions (MTJ) for hard disc read heads presents a challenge to current metrology technology. The four-point probes (4PP), currently used for sheet resistance characterization in these applications, therefore must be down-scaled as well in order to correctly characterize the extremely thin films used. This presents a four-point probe design and fabrication challenge. We analyze the fundamental limitation on down-scaling of a generic micro four-point probe (M4PP) in a comprehensive study, where mechanical, thermal, and electrical effects are considered. We show that the most severe limits on down-scaling from a state of the art M4PP are set by electromigration, probe fracture or material strength, and thermal effects. Compared to current state of the art probes, however, there is still room for down-scaling.

1. Introduction

Four-point probe (4PP) characterization is a standard method for measuring the electrical properties of solids and thin films in material science and in the semiconductor industry. The typical arrangement is four conducting tips placed in a row, where the current is passed through the sample via two electrodes, and the potential difference measured across the two other electrodes, allowing the resistivity or sheet resistance to be determined with minimal influence of contact resistance. To measure accurately on thin conductors localized at or near the surface, such as ultra-thin films [1] and surface states [2], the electrode pitch must be reduced to microscale dimensions [2,3]. Another advantage of reducing the electrode pitch is the possibility of spatial mapping of sub-millimeter domains with micro-scale resolution [4]. The most notable approaches towards sub-micron pitch are four-point scanning tunnel microscopes with independent control of four conducting tips [5,6], and micro-fabricated cantilever arrays, so-called micro four-point probes (M4PP) [1]. Several other attempts have been made to further reduce the pitch and thereby improve the sensitivity to the surface or sub-surface conductance. High aspect ratio nano-tips were deposited on micro-cantilevers using electron beam deposition to arrive at 300 nm pitch [7], while a 500 nm pitch was achieved by milling metal coated nano-cantilevers using a focused ion beam milling [8]. Also, a multi-point mono-cantilever probe with a 500 nm pitch has been used to measure the properties of a range of surfaces in ultra high vacuum [9]. The M4PP manufactured by CAPRES is, however, becoming the preferred tool for surface characterization as it is (i) simple, with only one manipulator required for positioning, (ii) cheap, as it is batch-fabricated and (iii) reproducible, since the fixed cantilever spacing and long durability make highly accurate and consistent interpretation possible [3]. Recently, even high precision Hall effect characterization using M4PP's was demonstrated [10,11]. With current nano-lithography it is possible to down-scale the existing M4PP further to a pitch considerably below 1 μm. This paper addresses the question of feasibility of such down-scaling, and identify the probe parameter space limitations on cantilever length and width set by fundamental mechanical, thermal, and electrical effects.

2. Fundamental limitations

The generic probe type considered here is a M4PP consisting of four collinear cantilever beams contacting the sample at an inclination angle $\phi = \pi/6$ as shown in Fig. 1. The inclination angle ϕ is defined as the angle between the x, y-plane of the beams and the x', y'-plane of the sample surface. The cantilever beams of width W and length L may consist of either a single conducting layer or a bi-layer structure of total height H. The bi-layer structure combines advantageously a low resistivity metal of height H_m with a high Young's modulus (E_b) base material of height H_b. The ratio of the layer thicknesses is $\gamma = H_m/H_b$, and we use $\gamma = 1/5$ in bi-layer beam

* Corresponding author.Department of Micro- and Nanotechnology, Technical University of Denmark, DTU Nanotech, Building 345E, DK-2800 Kgs. Lyngby, Denmark. Tel.: +45 45255901.
E-mail address: dirch.petersen@nanotech.dtu.dk (D.H. Petersen).

0167-9317/$ - see front matter © 2008 Elsevier B.V. All rights reserved.
doi:10.1016/j.mee.2008.11.029

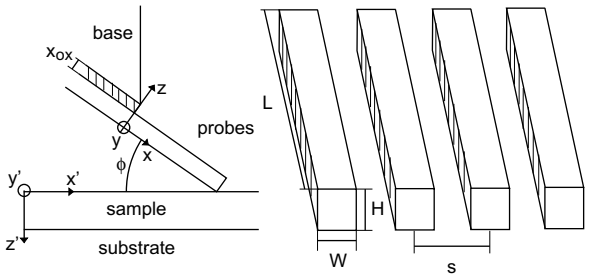

Fig. 1. Schematic drawing of the generic M4PP model system. Left: probe cantilever, sample, and support structure seen from the side. Right: probe cantilevers and their dimensions.

calculations. In both cases the (effective) Young's modulus is E. The probes protrude from a significantly larger silicon support, and they are electrically isolated by a silicon dioxide dielectric, see Fig. 1.

2.1. Mechanical limitations

The cantilever probe is modelled as a clamped-free beam with a point shear load $F = N\cos(\phi)$, where N is the force normal to the sample surface. The cantilevers are characterized by their spring constants K_z and K_y in the z and y-direction, respectively. The spring constants

$$K_z = EWH^3/(4L^3),\ K_y = EHW^3/(4L^3) \propto \lambda, \tag{1}$$

both decrease with the linear scaling factor λ, thus the cantilevers becomes softer for a simple linear scaling of L, W and H. In order to minimize lateral deflection of the cantilevers during engagement K_y should ideally be as large as possible compared to K_z, but since $K_y/K_z = (W/H)^2$ this condition affects the achievable probe pitch for a given cantilever thickness. Empirically, contact between adjacent probes is avoided, proper electrical contact to the sample is ensured, and a reasonable probe pitch achieved if an optimal ratio of height to width $H/W = 3/2$ is chosen. Down-scaling aims at minimizing the probe pitch s, however lithography and measurement accuracy considerations restricts the pitch to $s = 2W$. We shall adopt these two restrictions on the probe geometry in what follows.

In a practical measurement the electrical position of the probe tips will be different from the intended position. If the standard deviation σ_y of the tip positions is assumed identical for all probe tips then the relative standard deviation of the measured resistance, $\sigma_{R_{4PP}}/R_{4PP}$ becomes [12]

$$\frac{\sigma_{R_{4PP}}}{R_{4PP}} = \frac{\sqrt{5}}{2\ln 2}\frac{\sigma_y}{s} \propto \lambda^{-1}, \tag{2}$$

where the dependency on probe spacing has been experimentally verified [13].

The shear force F_S in the engaged cantilever is dependent on the cantilever geometry and is proportional to the end deflection angle θ_L which is a design parameter we keep fixed

$$F_S = \theta_L EWH^3/(6L^2) \propto \lambda^2. \tag{3}$$

If alternatively, the force was fixed the strain in down-scaled probes would rapidly increase beyond the linear-elastic limit and the contact area would grow in relative magnitude. At a constant end deflection θ_L, the stress in the cantilever increases with reduced cantilever length, thus the yield strength σ_Y of the cantilever materials sets a lower limit on the cantilever length L to avoid fracture,

$$L \geqslant EH\theta_L/\sigma_Y. \tag{4}$$

To ensure proper electrical contact to the sample we assume that plastic deformation of the probe material is necessary. We estimate the contact area A using Vickers hardness H_V of the probe material

$$A = \pi a^2 = \theta_L EWH^3/(6\cos(\phi)H_V L^2) \propto \lambda^2, \tag{5}$$

where a is an equivalent radius of the contact. The exact mechanism of probe contact area formation may be disputed. Empirical results indicate that also wear caused by sliding of the probe during engagement with the sample plays a major role. This is more difficult to quantify and is more an effect related to multiple use of the probe. The leftmost cantilever probe in Fig. 2 (lower left) shows a typical probe contact area after more than 100 engages.

2.2. Thermal limitations

At least two thermal effects must be considered: (i) electromigration in the probe metal layer and Joule heating of the probe combined form a serious failure mechanism, which sets an upper limit on the current density and the allowable increase in probe temperature. (ii) Joule heating affects the sample temperature near the voltage probes, and may cause measurement accuracy problems if the sample properties are temperature dependent.

The mean time to failure (MTTF) of the probes is limited by electromigration and has been shown to be inversely related to the current density squared [14]. The allowable current density J_{max} for a constant probe current I sets a lower limit on the cantilever width W to ensure a reasonable MTTF,

$$W \geqslant \sqrt{2I(1+1/\gamma)/(3J_{max})}. \tag{6}$$

A current density range $J_{max} = 1 - 100$ mA/μm^2 results in an estimated active MTTF from 500 to 5000 min. Fig. 2 left shows an example of probe failure by a combination of electromigration and probe heating.

Joule heating of the cantilevers is an increasingly severe problem when the probes are down-scaled, since the total current remains constant. Probe heating will contribute to a decrease in MTTF. Empirically, the temperature rise of the cantilever should be less than $\Delta T = 50$ °C to ensure a reasonable probe life. In a worst case thermal scenario the cantilever has electrical contact to the sample while the thermal contact is poor. Then the temperature rise ΔT_{max} in the cantilever results

$$\Delta T_{max} = \frac{L^2}{2}\frac{\rho_{eff}}{\kappa_{eff}}\left(\frac{I}{HW}\right)^2\left[1 + 2\frac{\ell}{L} + 2\frac{\ell^2}{L^2}\right] \propto \lambda^{-2}, \tag{7}$$

where ℓ is a characteristic length scale for heat transport to the silicon support through the insulating oxide, $\ell^2 = H\,x_{ox}\,\kappa_{eff}/\kappa_{ox}$, where x_{ox} is the thickness and κ_{ox} the thermal conductivity of the dielectric between probe and support. Assuming $\ell \ll L$, the thermal restriction on the cantilever length L becomes

$$L \leqslant \sqrt{9\Delta T\kappa_{eff}W^4/(2\rho_{eff}I^2)}, \tag{8}$$

where $\kappa_{eff} = (\gamma\kappa_m + \kappa_b)/(\gamma + 1)$ is the effective heat conductivity and $\rho_{eff} = (\gamma + 1)/(\gamma/\rho_m + 1/\rho_b)$ the effective resistivity of the cantilever.

Joule heating of the sample, with thermal conductivity κ_s and sheet resistance $R_\square$, is primarily due to the contact resistance characterized by the specific contact resistivity ρ_c and the contact area A. Joule heating will cause a measurement error if the temperature in proximity of the voltage probes is allowed to increase significantly. The temperature at the current probes is easier to calculate, and we estimate it assuming isotropic heat transport away from the current probes. The total temperature increase at the current probes ΔT_{14} is modelled as the sum of the temperature increases due to the contact resistance and spreading resistance of a disc of radius a,

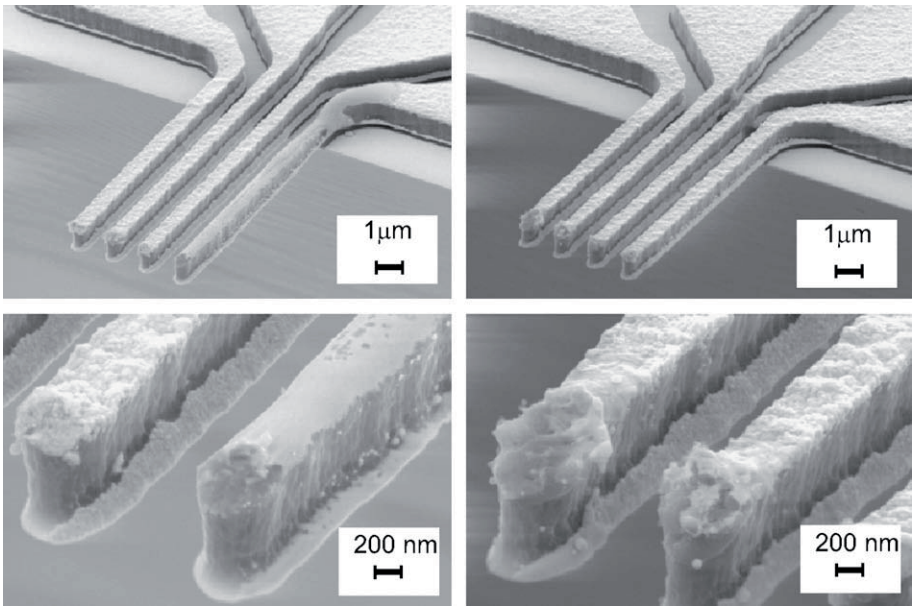

Fig. 2. SEM images of M4PP's with $s = 1.5$ μm pitch; these probes are Ni coated silicon cantilevers. Upper left image: probe failure due to thermal heating and/or electromigration. Lower left image: close-up showing that Ni has melted and sintered with Si. Upper and lower right images: different failure mode where thermo-electromigration is assisted by abrasive removal of the Ni electrode.

$$\Delta T_{14} = \frac{4}{3}\frac{R_\square}{a\kappa_s}\left(\frac{I}{2\pi}\right)^2\left[1+3\frac{\rho_c}{a^2R_\square}\right] \propto \lambda^{-3}. \tag{9}$$

As a worst case estimate of the temperature rise at the voltage probes we set $\Delta T_{23} = \Delta T_{14}/4$. Using the expression for the contact area A, Eq. 5, the following restriction on probe geometries results

$$\frac{WH^3}{L^2} \geqslant \frac{6\pi\cos(\phi)H_V}{E\theta_L}\left(\frac{4\rho_c}{\Delta T_{23}\kappa_s}\left(\frac{I}{2\pi}\right)^2\right)^{2/3}. \tag{10}$$

2.3. Electrical limitations

The applied voltage V_B is limited by impact ionization and arching in the air around the probe which will cause catastrophic failure of the probe. To prevent impact ionization the voltage between probe pins must be kept below approximately $V_B = 15$ V. At a constant measurement current the total resistance in the current path sets the applied voltage. The total series resistance R_{tot} of the system is the sum of the probe resistance, contact resistance, and sample resistance

$$R_{tot} = 2\frac{\rho_{eff}L}{HW} + 2\left(\frac{\rho_c}{\pi a^2} + \frac{R_\square}{8\pi}\right) + \frac{R_\square}{\pi}\ \text{arccosh}\left(\frac{3s}{2a}\right). \tag{11}$$

The contact resistance is modelled as that of a disc of radius a including spreading resistance, while sample resistance is modelled as the resistance between two parallel cylinders of radius a and pitch $3s$ [15]. Contact resistance is dominant when probes are scaled down.

The total voltage across the current probe pins is dominated by the voltage drop across the contacts when the probe is scaled down, and the following geometric restriction results,

$$H^3W/L^2 \geqslant 12H_V\cos(\phi)\rho_c I/(E\theta_L V_B). \tag{12}$$

3. Results and discussion

The scaling trends presented here applies to the generic M4PP with four cantilever electrodes contacting the sample at an inclination angle ϕ. For down-scaling of a more conventional probe system with probe pins normal to the sample other effects, e.g. beam buckling and surface destruction, have to be considered. The cantilever system has, however, proved to be the preferred method for M4PP and we believe it will remain the system of choice for the near-future down-scaling of 4PP's.

Fig. 3 shows the down-scaling restrictions for a probe with Ni metal and Si base layers. The restrictions on L are shown as a function of s for the different physical effects considered. In this particular case beam fracture, contact resistance, and the electromigration related maximum current density are seen to limit the design space. The dimensions of three different existing probes from CAPRES (♦) fit into the design space and are seen to follow the necessary scaling trend. Also, the geometry of an existing probe with Au metal and SiO_2 base layers is included (■).

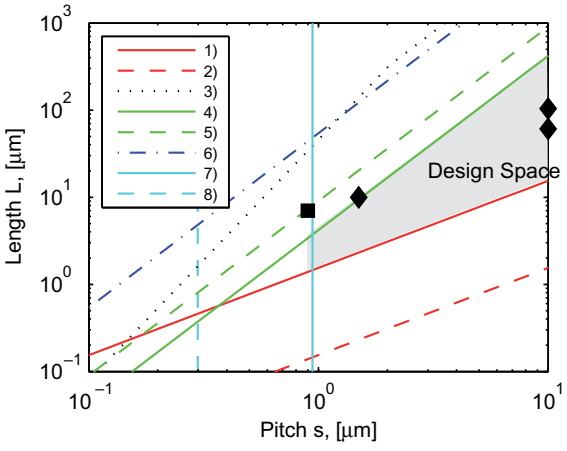

Fig. 3. Scaling restrictions for a probe with Ni metal and Si base layers. Existing probes are marked with (♦) while a probe with a SiO_2 base is marked with (■). The legends are: (1) and (2) Cantilever fracture $\theta_L = 5°$ and 0.5°, respectively. (3) Probe heating $\Delta T = 50$ K. (4) and (5) Sample heating $\Delta T_{23} = 1$ °C and 10 °C, respectively. (6) Breakdown $V_B = 15$ V. (7) and (8) Electromigration $J_{max} = 9$ mA/cm^2 and 90 mA/cm^2, respectively. A Si yield strength of 7 GPa, Young's modulus of 180 GPa, Ni Vickers hardness of 3 GPa, specific contact resistivity of $\rho_c = 10^{-8}$ Ωcm^2, a current of 0.5 mA, and NiSi sample with $R_\square = 10$ Ω were used.

Electromigration sets the lower limit on the cantilever width and is in Fig. 2 left seen to be a catastrophic failure mode; the fundamental physics behind electromigration is still disputed [16], and the interaction between thermal effects, mechanical stress, and current density on electromigration make predictions for other material combinations difficult.

The fracture limit due to the stress at the clamped point exceeding the yield strength is well understood for simple beams similar to this generic probe. However, material characteristic may change as the dimensions are scaled down and therefore usual bulk values may not apply. High-quality single crystal silicon with its high Young's modulus and high yield strength seems promising for further down-scaling.

The contact resistance proves to become of more concern as the probe is down-scaled. The main effect is sample heating and therefore a loss of measurement accuracy that has to be compared to other sources of measurement error such as position errors and electrical noise. Here the measurement current (0.5 mA) was assumed constant; this assumption has a strong effect on sample heating, but was considered necessary since the required current density for a fixed sample sheet resistance cannot be reduced without severe effects on measurement errors due to electrical noise [17].

4. Conclusion

Using a set of physical models for unwanted effects in micro four-point probing we have identified limitations on down-scaling of M4PP's. We show that the minimum pitch is 950 nm limited by electromigration, probe fracture and sample heating due to contact resistance. These results may serve as a guide to successful down-scaling and help to identify limitations on probe performance in measurement problems where a very small probe pitch is required.

Acknowledgement

We thank Helle Vendelbo Jensen and DTU Danchip for M4PP fabrication. Center for Individual Nanoparticle Functionality (CINF) is supported by The Danish National Research Foundation.

References

[1] C.L. Petersen, T.M. Hansen, P. Bøggild, A. Boisen, O. Hansen, F. Grey, Sens. Actuators A 96 (2002) 53.
[2] S. Hasegawa, I. Shiraki, T. Tanikawa, C.L. Petersen, T.M. Hansen, P. Bøggild, F. Grey, J. Phys.: Condens. Mater. 14 (2002) 8379–8392.
[3] D.H. Petersen, R. Lin, T.M. Hansen, E. Rosseel, W. Vandervorst, C. Markvardsen, D. Kjær, P.F. Nielsen, J. Vac. Sci. Technol. B 26 (2008) 362.
[4] P. Bøggild, F. Grey, T. Hassenkam, D.R. Greve, T. Bjørnholm, Adv. Mater. 12 (2000) 947.
[5] S. Yoshimoto, Y. Murata, K. Kubo, K. Tomita, K. Motoyoshi, T. Kimura, H. Okino, R. Hobara, I. Matsuda, S. Honda, M. Katayama, S. Hasegawa, Nano Lett. 7 (2007) 956–959.
[6] O. Guise, H. Marbach, J.T. Yates Jr., M.-C. Jung, J. Levy, J. Ahner, RSE 76 (2005) 045107.
[7] P. Bøggild, T.M. Hansen, O. Kuhn, F. Grey, T. Junno, L. Montelius, Rev. Sci. Instrum. 71 (2000) 2781.
[8] M. Nagase, H. Takahashi, Y. Shirakawabe, H. Namatsu, Jpn. J. Appl. Phys. 42 (2003) 4856–4860.
[9] L. Gammelgaard, P. Bøggild, J.W. Wells, K. Handrup, Ph. Hofmann, M.B. Balslev, J.E. Hansen, P.R.E. Petersen, Appl. Phys. Lett. 93 (2008) 093104.
[10] D.H. Petersen, O. Hansen, R. Lin, P.F. Nielsen, J. Appl. Phys. 104 (2008) 013710.
[11] T. Clarysse, J. Bogdanowicz, J. Goossens, A. Moussa, E. Rosseel, W. Vandervorst, D.H. Petersen, R. Lin, P.F. Nielsen, O. Hansen, G. Merklin, N.S. Bennett, N.E.B. Cowern, Mater. Sci. Eng. B 154–155 (2008) 24–30.
[12] D.H. Petersen, O. Hansen, T.M. Hansen, P.R.E. Petersen, P. Bøggild, Microelectron. Eng. 85 (2008) 1092–1095.
[13] C.L. Petersen, D. Worledge, P.R.E. Petersen, Mater. Res. Soc. Symp. Proc. 738 (2003) 157–162.
[14] J.R. Black, Proc. IEEE (1969) 1587–1594.
[15] W.R. Smythe, Static and Dynamic Electricity, vol. 234, McGraw-Hill, New York, 1950.
[16] D.G. Pierce, P.G. Brusius, Microelectron. Reliab. 37 (1997) 1053–1072.
[17] L.K. J Vandamme, G. Leroy, Fluct. Noise Lett. 6 (2006) L161–L178.

Paper XVII

Nanotechnology **21** (40), 405304 (2010).

PhD students contribution:

Conceptual idea for fast NEMS prototyping. Fabrication of template chips with Y. Gyrsting. Initial FIB prototyping proof of concept in collaboration with Ö.S. Sukas and A. Lei. Supervisor for A. Lei. Significant manuscript revisions.

Nanotechnology **21** (2010) 405304 (6pp) doi:10.1088/0957-4484/21/40/405304

Customizable *in situ* TEM devices fabricated in freestanding membranes by focused ion beam milling

Anders Lei[1], Dirch Hjorth Petersen[1], Timothy John Booth[1], Lasse Vinther Homann[1], Christian Kallesoe[1], Ozlem Sardan Sukas[1], Yvonne Gyrsting[2], Kristian Molhave[1] and Peter Boggild[1]

[1] DTU Nanotech, Department of Nano- and Microtechnology, Technical University of Denmark, DK-2800 Kongens Lyngby, Denmark
[2] DTU Danchip, National Center for Micro- and Nanofabrication, Technical University of Denmark, DK-2800 Kongens Lyngby, Denmark

E-mail: Anders.Lei@nanotech.dtu.dk

Received 25 May 2010, in final form 2 August 2010
Published 10 September 2010
Online at stacks.iop.org/Nano/21/405304

Abstract
Nano- and microelectromechanical structures for *in situ* operation in a transmission electron microscope (TEM) were fabricated with a turnaround time of 20 min and a resolution better than 100 nm. The structures are defined by focused ion beam (FIB) milling in 135 nm thin membranes of single crystalline silicon extending over the edge of a pre-fabricated silicon microchip. Four-terminal resistance measurements of FIB-defined nanowires showed at least two orders of magnitude increase in resistivity compared to bulk. We show that the initial high resistance is due to amorphization of silicon, and that current annealing recrystallizes the structure, causing the electrical properties to partly recover to the pristine bulk resistivity. *In situ* imaging of the annealing process revealed both continuous and abrupt changes in the crystal structure, accompanied by instant changes of the electrical conductivity. The membrane structures provide a simple way to design electron-transparent nanodevices with high local temperature gradients within the field of view of the TEM, allowing detailed studies of surface diffusion processes. We show two examples of heat-induced coarsening of gold on a narrow freestanding bridge, where local temperature gradients are controlled via the electrical current paths. The separation of device processing into a one-time batch-level fabrication of identical, generic membrane templates, and subsequent device-specific customization by FIB milling, provides unparalleled freedom in device layout combined with very short effective fabrication time. This approach significantly speeds up prototyping of nanodevices such as resonators, actuators, sensors and scanning probes with state-of-art resolution.

(Some figures in this article are in colour only in the electronic version)

1. Introduction

Fast prototyping of advanced freestanding structures with dimensions in the sub-100 nm range is a great advantage in developing better nanoelectromechanical systems (NEMS), including nanosensors [1], relays [2], nanoresonators [3] and high-aspect ratio scanning probe tips [4]. In virtually all areas of microelectromechanical systems (MEMS) the trend is further miniaturization, to increase performance and reduce costs. This presents two major challenges.

First, the difficulty of fabricating nanostructures, long turnaround time and the considerable equipment costs comprise a serious bottleneck for research and development. Top-down approaches for fabrication of structures in this size range typically employ electron-beam lithography (EBL) [5]. However, freestanding structures with sub-100 nm features

still remain challenging to fabricate even with EBL, and the chip fabrication itself is time consuming, significantly slowing down the prototyping process. Bottom-up structures such as carbon nanotubes [6] and epitaxial nanowires [7, 8] have been used successfully in such applications, however, planar integration of these on a large scale is still a considerable challenge. For prototyping applications, focused ion beam milling is a powerful technique, as it allows direct etching of thin membranes with resolution down to 10 nm [9]. Focused ion beam milling, however, induces considerably more damage than conventional etching techniques, affecting its usability for fabrication of devices that depend on the structural integrity.

Second, the characterization of the devices, in particular in operating conditions, is very difficult since even high resolution scanning electron microscopes (SEM) do not have sufficient resolution. While the transmission electron microscope (TEM) is capable of assessing the size, shape, crystal structure and even dynamic behaviour [10] with atomic resolution, TEM imposes two considerable constraints; firstly, standard TEM holders only admit samples of a few cubic millimetres due to lens and holder design. Secondly, the structures must be suspended and should preferably have a thickness of a few hundred nanometres or less to allow imaging in TEM.

Here we present a simple approach in an attempt to address these two challenges. The basic idea is that of a configurable highly doped, single crystal silicon membrane suspended at the edge of a silicon chip.

By separating device-specific focused ion beam (FIB) nanostructuring of the suspended membrane from trivial batch-level microfabrication of generic chip templates with auxiliary electrical connections, the total fabrication time from layout to finished device is effectively reduced to 20 min, as the fabrication of the template chips can be done without knowledge of the specific device geometry. Due to the thinness of the membranes, the common problems of redeposition [11, 12] and long writing times for FIB lithography are greatly reduced.

We observe that the focused ion beam milling leads to near total amorphization of sub-300 nm structures with an at least two orders of magnitude increase in resistivity. The bulk resistivity can, however, be nearly recovered by controlled current annealing, which allows the use of sub-100 nm conducting structures. The dynamics of the annealing process was found to be highly dependent on the degree of amorphization, with both gradual and sudden changes of the crystal structure and the resistivity.

The prototyping concept is demonstrated with a device for obtaining high temperature gradients either across or near a conducting silicon nanobridge depending on the chosen current path, allowing for imaging of coarsening dynamics of a thin gold film inside a TEM with on-chip local heating.

2. Method

The TEM microchip with outer dimensions of 3.5 mm × 1.7 mm was fabricated from a smart cut silicon-on-insulator (SOI) wafer, with a buried oxide layer of 400 nm and

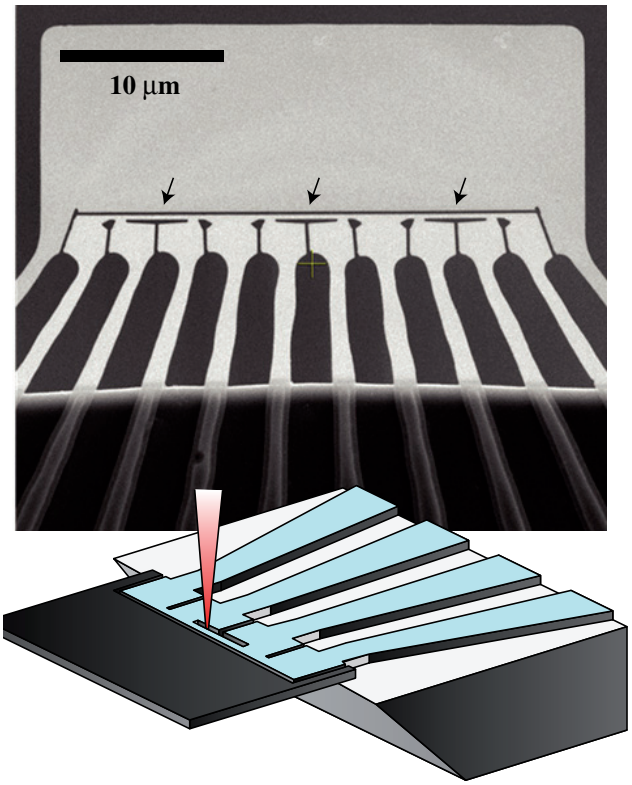

Figure 1. Top: SEM image of a structure with three nanowires in series, used for testing electrical conductivity of the milled membrane structures. Arrows indicate the nanowires. Bottom: schematic representation of the generic template chip during patterning with FIB milling.

an original highly B-doped (nominally $\sim 10^{20}$ atoms cm^{-3}) silicon device layer of 340 nm, see figure 2(a). The silicon device layer was then thinned by sequential wet oxidation and etching in buffered hydrofluoric acid (BHF). The membrane, leads and contact pads were defined using photolithography followed by reactive ion etching (RIE), see figure 2(b). After conformal deposition of silicon nitride (figure 2(c)), the backside was patterned by a second photolithography and RIE step (figure 2(d)), followed by membrane release in a potassium hydroxide (KOH) etch (figure 2(e)). After removal of the silicon nitride in hot phosphoric acid, the oxide beneath the released silicon membrane was etched in BHF (figure 2(f)).

The FIB milling was performed using an FEI Quanta 3D dual-beam microscope with a 30 keV Ga ion beam (30 pA beam current, nominal beam width: 50–75 nm). The milling was done using a raster-scan strategy. In some cases the milling of different parts had to be ordered to minimize the effects of unidirectional drift of the FIB–SEM. As the actual milling was typically performed in a few minutes, drift was in most cases insignificant. No polishing or cleaning processes were employed after the milling process.

A series of nanowires was milled in a four-terminal configuration, cf. Figure 1, in order to measure the electrical resistance whilst accounting for contact and lead resistance. A Keithley 2400 SourceMeter was used to pass a DC current through the two outer leads of the nanowires, while the

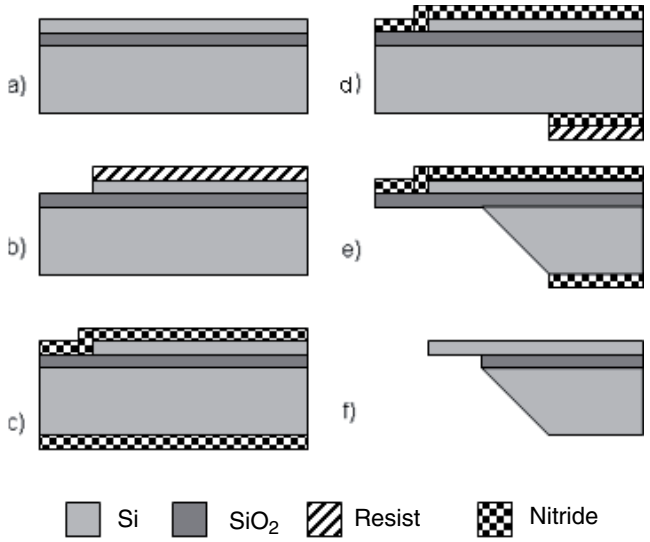

Figure 2. Processflow of TEM microchip: (a) SOI wafer. (b) Silicon device layer patterned by photolithography and RIE. (c) Conformal deposition of silicon nitride. (d) Backside silicon nitride opened using photolithography and RIE. (e) Chip and membrane released by KOH etch. (f) Removal of silicon nitride and buried oxide.

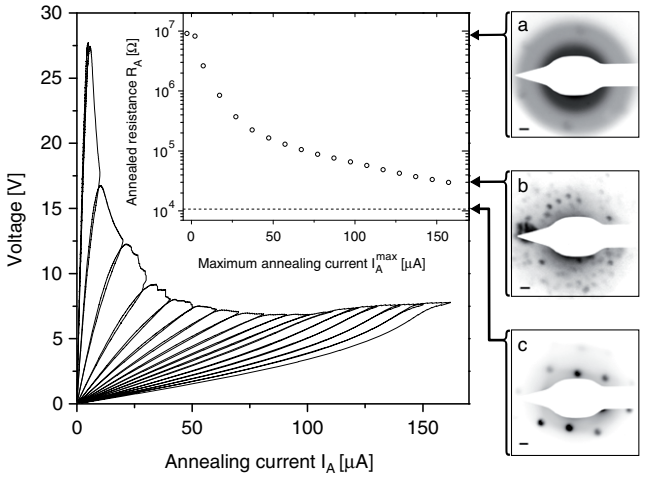

Figure 3. Current annealing of FIB-defined nanowire structures (measured dimensions: width 290 nm, length 4170 nm and nominal thickness 135 nm). Sweeping the applied annealing current I_A enables stepwise annealing of the resistance to a desired value. Inset: resistance of annealed nanowire versus maximum annealing current applied—control of nanowire resistance is possible over three orders of magnitude. ((a)–(c)) Diffractograms (scale bar: 1 $Å^{-1}$) showing the crystal structure of the wire at given annealing stages: (a) as-produced amorphous FIB-defined nanowire, (b) fully annealed nanowire—amorphous silicon has been recrystallized into polysilicon (c) pristine silicon. Representative resistance of each structure is indicated by solid arrows. Dashed line indicates the FEM simulated resistance of a single crystalline silicon structure with the same geometry as the nanowire.

potential across the inner two leads was measured using a Keithley 2000 Multimeter. van der Pauw (vdP) measurements of the resistivity of the pristine silicon prior to milling yielded ∼2.5 mΩ cm. Finite element method simulations were used to derive the ideal resistance of a structure using COMSOL software. In these simulations the damage induced by the focused ion beam was not taken into account.

Gold layers of 5 nm nominal thickness were deposited using electron-beam evaporation resulting in gold clusters. *In situ* inspection was performed in a FEI TECNAI T20 TEM, with a TEM sample holder allowing for electrical contact to the membrane chips. Electrical contact was achieved using wire bonding from chip to holder, and an oxygen plasma cleaning of the holder was performed before TEM insertion. A Keithley 2400 SourceMeter was used to pass an increasing DC current through the structures and the behaviour was observed with a image frame rate of 0.66 Hz.

3. Current annealing of nanowires

We investigated 25 silicon nanowires such as shown in figure 1. The IV characteristic of all measured nanowires was found to be linear up to at least 100 nA, allowing us to estimate the electrical resistance. The measured resistance of all annealed nanowires was initially found to be at least two orders of magnitude higher than the FEM simulated values based on vdP measurements and TEM images. We looped the current between zero and stepwise larger maximum values, and used the linear part of the IV characteristic for each loop to extract the low current resistance. The duration of the annealing loops was between two and four minutes, with no observable differences in behaviour between these annealing rates. Figure 3 shows the measured voltage drop across three nanowires in series. In this case the stepwise annealing leads to a highly controllable reduction of the resistance. For the other nanowires the stepwise annealing continued up to a point where multiple, sudden jumps in the voltage were observed, in a few cases destroying the sample.

The nanowires annealed in figure 3 were imaged in an FEI TECNAI T20 TEM before and after the resistive heating process. While the diffractogram of a non-FIB irradiated region (figure 3(c)) displays long-range crystal order, the FIB-defined region (figure 3(a)) shows nearly complete amorphization. After annealing with a current up to 160 μA a clear recrystallization was observed (figure 3(b)). Well-defined diffraction spots here indicate that the structure is polycrystalline silicon.

The annealing process was studied using *in situ* TEM, see figure 4. The sample thickness is in this case 235 nm, which still allows the crystal structure to be monitored. In this case the diffractogram reveals both a single crystalline and amorphous structure before the annealing process, see figure 4(a) and inset in figure 4(c). Up to a current of 54 μA little visible change of the structure was observed. At this current, however, the wire abruptly changes to a polycrystalline structure, see figure 4(b). Figure 4(c) shows the IV characteristics, with insets showing the diffractograms at the beginning of the process as well as right after the sudden change.

In a number of annealing experiments we observed even more radical changes. Figure 4(d) shows the IV characteristics of two nanowires, where the voltage drops instantly to a value corresponding to the final, near-bulk resistivity value, at a

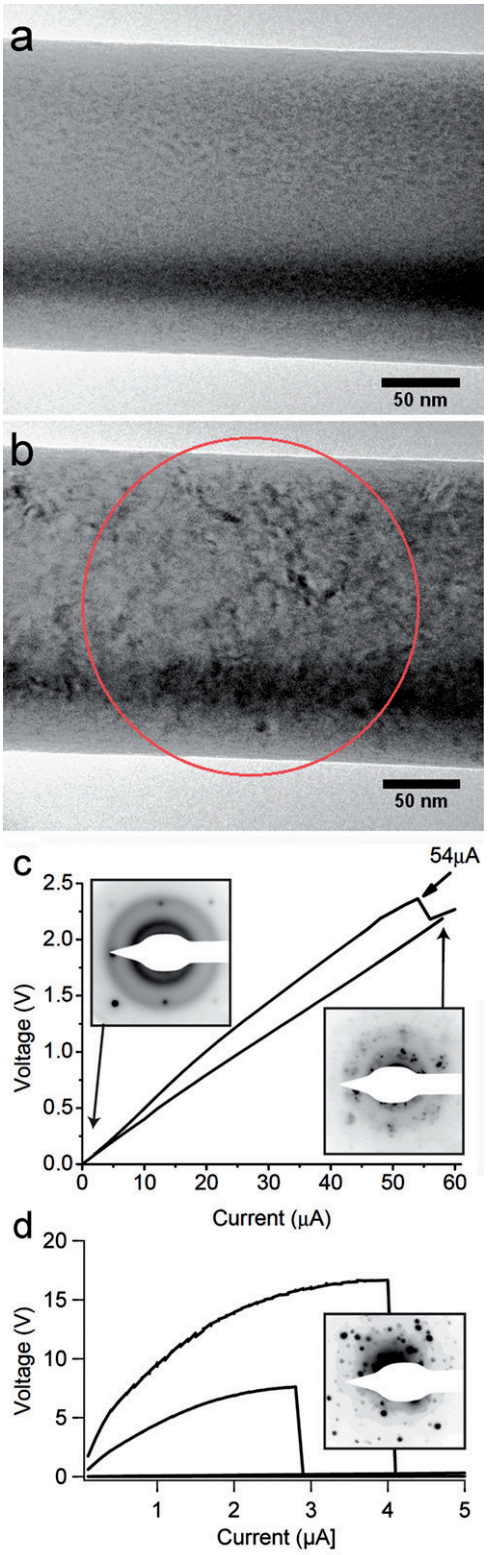

Figure 4. (a) TEM image of a nanowire (measured dimensions: width 200 nm and thickness 235 nm) before current annealing. (b) Immediately after a sudden change of the crystal structure occurring at 54 μA. (c) IV characteristics showing the sudden decrease of the measured voltage. (d) IV characteristics of two nanowires with a thickness of 135 nm showing an instant drop in voltage, which corresponds to a near complete recovery of the resistance. The diffractogram after this event shows a polycrystalline structure.

comparatively low annealing current, 3–4 μA. Further current annealing did not change the resistivity, until the nanowire was ultimately destroyed by high current. The corresponding diffractogram recorded after annealing, as shown in figure 4(d), shows polycrystalline structure, similar to that seen for the continuously annealed sample, see figure 3.

4. Local temperature gradients

We defined a number of test structures consisting of a thin bridge connected at one end to a resistive heater loop and at the other end to a large plane acting as a thermal reservoir on a floating potential. An overview of the structure is seen in figure 5(a). A finite element calculation using COMSOL (figure 5(b)) shows that for the case of the current running in the heating loop as indicated by the arrow, the temperature gradient is expected to be localized across the nanobridge.

The current through the gold covered structures was slowly ramped up from 0 to 320 μA while monitoring the structure *in situ* in the TEM, see figures 5(c)–(f). In figure 5(d) larger gold clusters are starting to form at the lower part of the heating loop, while in figure 5(e), the as-evaporated discontinuous gold films have coarsened into 100 nm size facetted islands. Between two TEM frames (1.5 s) the particles simultaneously achieve a spherical shape, see figure 5(f). The gold film on the thermal reservoir above the nanobridge shows almost no sign of change (figure 5(f)), indicating that the temperature gradient is localized across the bridge, as seen in figure 5(b). In figures 5(g)–(j), the current is passed directly through the nanobridge. As the current increases, the 5 nm gold layer agglomerates into larger particles, as seen in figure 5(h). Further increase of the current results in a reduced contrast of the gold on the thin wire, as seen in figure 5(i). In figure 5(j) the bridge is finally destroyed.

5. Discussion and conclusion

In our case the resolution of the milled structures seems to be limited by the focused ion beam diameter, as structures with comparable dimensions to the beam diameter can routinely be produced. The thinness of the membrane and the short FIB write-time counteracts common problems such as redeposition and drift. FIB milling systems can have ion beam diameters in the sub-10 nm range [9], suggesting that the lateral dimensions of the membrane devices presented here could be reduced significantly with a narrower beam spot size.

The ion damage from the FIB milling of the silicon nanowires was found to cause an increase in resistance of at least two orders of magnitude, and diffractograms showed a nearly complete amorphization of the nanowires. Our Monte Carlo-based SRIM simulations of gallium ion penetration depth in silicon suggest a value of 30–50 nm, indicating that a major part of the inner core of the nanowire should be intact after the ion irradiation. Even considering proximity effects from the three sides irradiated with ions, i.e. top and two sides, the apparent complete amorphization is surprising. For the thicker nanowires studied *in situ* (figure 4(d)) a smaller resistance change is observed upon annealing, but the change is

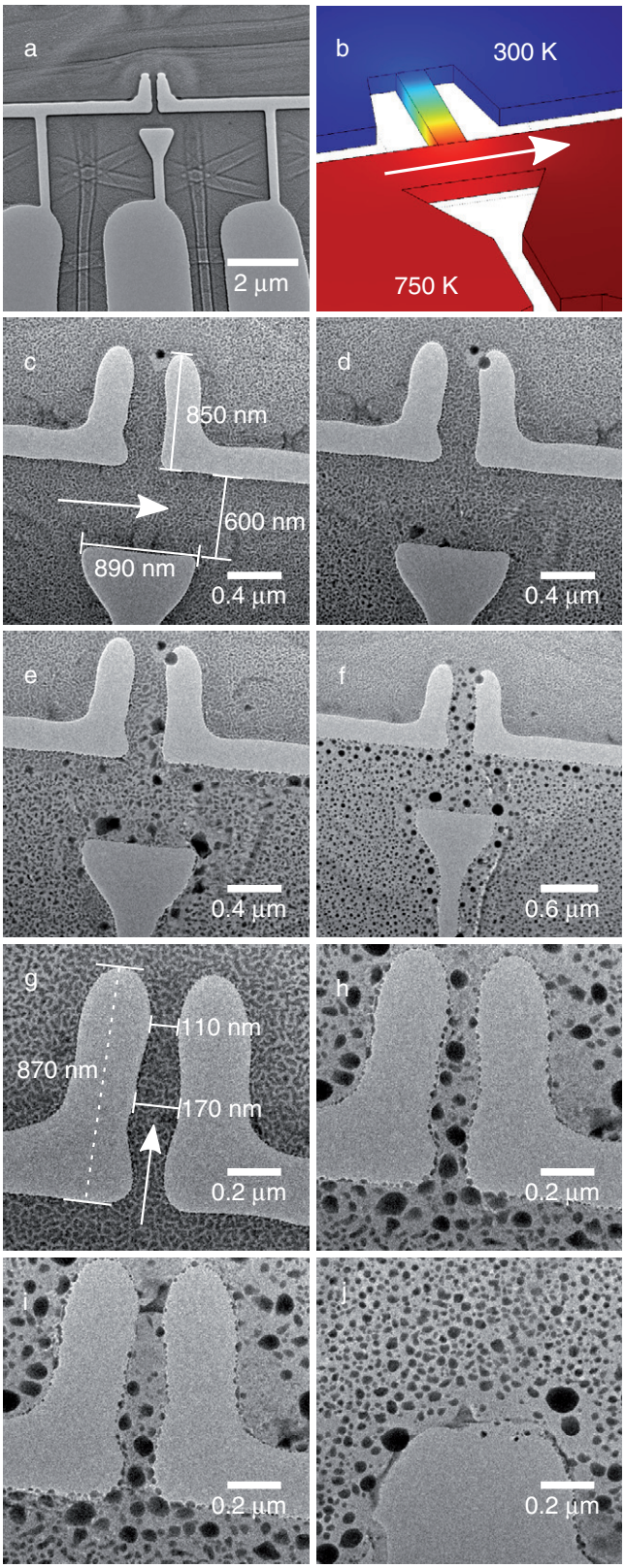

Figure 5. (a) Overview of heater structure. (b) Finite element calculation of the temperature distribution at a current of 420 μA. ((c)–(f)) Sequential images from the heating process. The current is passed through the two bottom contacts, corresponding to (c) 0 μA, (d) 120 μA, (e) 255 μA, (f) 320 μA. ((g)–(j)) Sequential images of the bridge with increasing current passing through, (g) 0 μA, (h) 265 μA, (i) 275 μA, (j) 290 μA. White arrows indicate the direction of the applied current.

still significantly higher than the calculated penetration depth supports. One explanation could be channelling of the ions in the Si single crystal [13], which result in far larger penetration depths and a lower sputter yield along some crystallographic directions than predicted by SRIM models which neglect crystal symmetry. *In situ* TEM experiments of single crystals with other orientations would be highly interesting to elucidate this question.

Resistive heating was used to reduce the resistance of FIB milled structures by three orders of magnitude to values close to the nominal bulk resistance of the silicon wafer. Since no change in outer dimensions was observed during the heating process, the reduced resistance R should correspond purely to a reduction in resistivity $\rho = R(\text{area}/\text{length})$. We find this to be related to recrystallization caused by the current annealing, leaving a polycrystalline structure. After the annealing, TEM studies revealed crystal grains with sizes up to 100 nm for the nanowires with annealed resistance closest to the table value. The grain sizes are observed to be larger in the centre of the wire, as anticipated from the modelled parabolic temperature distribution of the nanowire.

Gallium implantation will affect both mechanical and conductive properties of the FIB milled structures. Heating is reported to cause implanted gallium to migrate to the surface [14]. It is therefore assumed that the gallium will not contribute significantly to the resistivity of the highly doped silicon after annealing has occurred. Future work will investigate the effect of ion implantation on the mechanical properties. During annealing, pronounced irregular behaviour was observed, with major changes in the crystal structure occurring between individual measuring points. In some cases the structure changed from amorphous to a stable polycrystalline structure at comparatively low current values, with a final resistivity close to the value for pristine bulk silicon. This rich, unstable behaviour suggests a complex interplay between the crystal structure and the thermal and conducting properties which may be revealed through further TEM investigations of FIB milled nanowires.

Theoretical calculation of the exact temperature generated by a specific external current in the annealing is made difficult by the fact that, during the process, the crystal structure (and hence resistivity and thermal properties) of the silicon comprising the nanowires is changing. Since it is known from the literature that Si regrowth commences around 800 K [15], we used FE simulations to estimate the required current for reaching the regrowth temperature, assuming a completely amorphous structure up to this temperature. These calculations predict a much higher onset current than observed experimentally. These preliminary studies suggest that either the thermal conductivity in our system is much lower than we predict for thin, amorphous silicon, or that the regrowth mechanism does not account for the observations. Further work is needed to clarify this issue.

A significant difference in the IV characteristics is observed for the two nominally identical nanowires in figure 4(d). This was observed in several other pairs of nanowires, and cannot be explained just by geometrical differences induced by the focused ion milling. We speculate

that statistical fluctuations in the structural damage resulting from the focused beam milling might account for this; we generally observed a rather wide spread in initial electrical resistance.

We have used the TEM nanodevice to monitor the coarsening of a thin gold film on top of the silicon structures with nanometre resolution *in situ* TEM as the structures were gradually heated by an electrical current. Since the temperature can be varied within fractions of a second as a result of the small heat capacity of the structure, the melting point of the larger nanoparticles could be used as a rough indication of the absolute temperature. The relatively small gold particles with mean diameters of less than 100 nm, seen in the first *in situ* heating experiment (figure 5(f)), indicate that the molten gold cannot move freely on the surface. This can be attributed to the native oxide layer on the membrane, as SiO_2 is known to prevent surface migration of gold [16].

We also observed indications that a Si–Au eutectic forms, despite the native oxide layer and the lack of mixing from the metal deposition. This was seen as a reduced contrast of some of the gold particles [17] or as growth of small wires adsorbing silicon from the surroundings. Furthermore, the presence of gallium from the FIB milling process can potentially result in a Si–Au–Ga eutectic with a lowered melting point compared to silicon. By increasing the oxide diffusion barrier, or by depositing a different metal, the temperature could be inferred, taking into account melting point depression [18].

Both numerical and experimental results suggests that the temperature gradient can be localized to a very small region; there are few reports in literature of strong, well controlled temperature gradients *in situ* TEM [19] as the temperature is normally defined globally by the sample holder. Moreover, the devices allow very high temperature experiments to be carried out in an ordinary high vacuum TEM, providing a highly convenient platform for studying migration, annealing, thermal expansion and coarsening effects on a nanoscale level.

References

[1] Cui Y, Wei Q, Park H and Lieber C M 2001 Nanowire nanosensors for highly sensitive and selective detection of biological and chemical species *Science* **293** 1289–92

[2] Chen Y *et al* 2003 Nanoscale molecular-switch crossbar circuits *Nanotechnology* **14** 462–8

[3] Naik A K, Hanay M S, Hiebert W K, Feng X L and Roukes M L 2009 Towards single-molecule nanomechanical mass spectrometry *Nat. Nanotechnol.* **4** 445–50

[4] Carlson K *et al* 2007 A carbon nanofibre scanning probe assembled using an electrothermal microgripper *Nanotechnology* **18** 345501–8

[5] Li M, Tang H X and Roukes M L 2007 Ultra-sensitive NEMS-based cantilevers for sensing, scanned probe and very high-frequency applications *Nat. Nanotechnol.* **2** 114–20

[6] Martinez J, Yuzvinsky T D, Fennimore A M, Zettl A, Garcia R and Bustamante C 2005 Length control and sharpening of atomic force microscope carbon nanotube tips assisted by an electron beam *Nanotechnology* **16** 2493–6

[7] Tay A B H and Thong J T L 2004 High-resolution nanowire atomic force microscope probe grown by a field-emission induced process *Appl. Phys. Lett.* **84** 5207–9

[8] Patolsky F, Zheng G and Lieber C M 2006 Nanowire sensors for medicine and the life sciences *Nanomedicine* **1** 51–65

[9] Gierak J *et al* 2007 Sub-5 nm FIB direct patterning of nanodevices *Microelectron. Eng.* **84** 779–83

[10] Kuzumaki T and Mitsuda Y 2006 Nanoscale mechanics of carbon nanotube evaluated by nanoprobe manipulation in transmission electron microscope *Japan. J. Appl. Phys.* **45** 364–8

[11] Utke I, Hoffmann P and Melngailis J 2008 Gas-assisted focused electron beam and ion beam processing and fabrication *J. Vac. Sci. Technol.* B **26** 1197–276

[12] Tseng A A 2004 Recent developments in micromilling using focused ion beam technology *J. Micromech. Microeng.* **14** R15

[13] Kempshall B W, Schwarz S M, Prenitzer B I, Giannuzzi L A, Irwin R B and Stevie F A 2001 Ion channeling effects on the focused ion beam milling of Cu *J. Vac. Sci. Technol.* B **19** 749–54

[14] Xie D Z, Ngoi B K A, Zhou W and Fu Y Q 2004 Fabrication and thermal annealing behavior of nanoscale ripple fabricated by focused ion beam *Appl. Surf. Sci.* **227** 250–4

[15] Plummer J D, Deal M D and Griffin P B 2000 *Silicon VLSI Technology Fundamentals, Practice and Modeling* (Englewood Cliffs, NJ: Prentice-Hall)

[16] Hannon J B, Kodambaka S, Ross F M and Tromp R M 2006 The influence of the surface migration of gold on the growth of silicon nanowires *Nature* **440** 69–71

[17] Molodtsov S L, Laubschat C, Shikin A M and Adamchuk V K 1992 Effects of adatom concentration on Au/Si(111) and Si/Au interface formation *Surf. Sci.* **269/270** 988–94

[18] Buffat P and Borel J 1976 Size effect on the melting temperature of gold particles *Phys. Rev.* A **13** 2287

[19] Kallesoe C 2010 *Small* doi:10.1002/smll.200902187

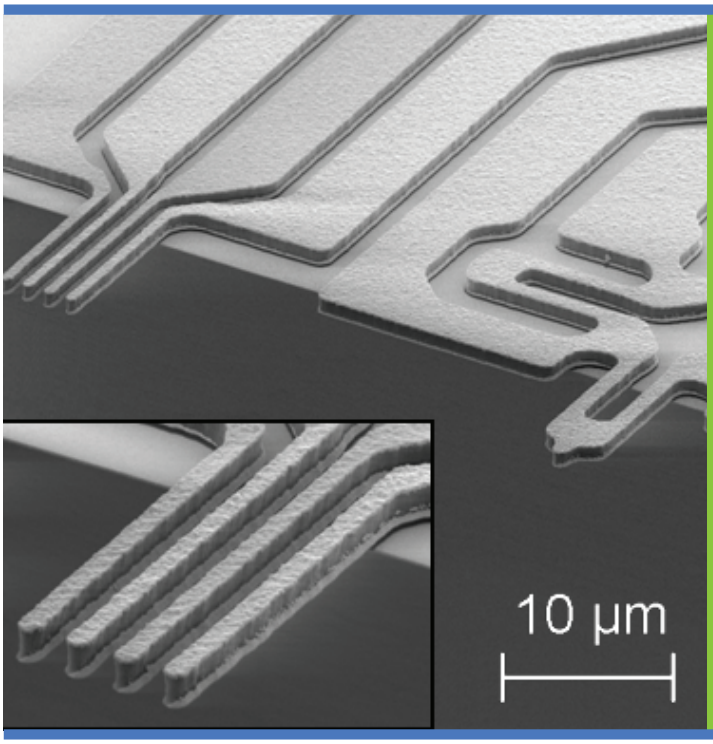

ISBN: 978-87-91797-43-9

Awarded
`Best Dissertation at DTU in 2010´
by the Dean of Research

Published by:
DTU Nanotech
Department of Micro- and Nanotechnology
Technical University of Denmark
Ørsteds Plads, building 345 B
DK-2800 Kgs. Lyngby

Printed in Denmark by Schultz Grafisk

DTU Nanotech
Department of Micro- and Nanotechnology